UQAC
Université du Québec
à Chicoutimi

Numerical and Experimental Investigation of the Design of a Piezoelectric De-Icing System for Small Rotorcraft

Par

Eric Villeneuve

Sous la direction de Christophe Volat, Sébastian Ghinet et Jean Perron

Thèse présentée à l'Université du Québec à Chicoutimi en vue de l'obtention du grade de Doctorat (Ph. D.) en Ingénierie

Soutenue le 19/11/2020

Jury :

Ali Saeidi, Professor, UQAC, Président du Jury

Eric Chen, Research Officer, NRC, Membre externe

Lyne St-George, Professor, UQAC, Membre interne

Christophe Volat, Professor, UQAC, Directeur

Sebastian Ghinet, Research Officer, NRC, Co-Directeur

Québec, Canada

RÉSUMÉ

Le givrage en vol diminue grandement les performances des hélicoptères pouvant mener à l'écrasement de l'appareil. Le système de dégivrage électrothermique, seul système présentement développé pour ces véhicules, consomment beaucoup trop d'énergie pour les petits et moyens appareils ne laissant aucune autre alternative à ceux-ci que de demeurer cloué au sol lors de ces événements. Afin de palier à ce problème, un système à faible énergie basé sur la vibration créée par des actuateurs piézoélectriques est étudié. L'objectif de ce projet de recherche peut être divisé en quatre sous-objectifs. Le premier étant de développer un système de dégivrage piézoélectrique intégré à un montage expérimental d'une plaque plane encastrée ainsi que son modèle numérique et sa effectuer sa validation expérimentale. L'intégration des actuateurs doit être optimisée afin que le montage permette le bris de glace. En second lieu, il faut utiliser ce même montage expérimental pour investiguer l'excitation des actuateurs piézoélectriques à l'aide de balayage fréquentiel et analyser la vibration transitoire. De cette façon des informations sur l'excitation optimale des actuateurs seront obtenues pour la suite du projet. En troisième lieu, il faut ajouter une couche de glace au modèle numérique initial et effectuer une seconde validation expérimentale du modèle modifié. Ensuit le modèle validé sera utilisé pour étudier et prédire numériquement les contraintes pour différents bris de glace. Comme preuve de concept, des bris de glace seront prédits avec le modèle. Finalement, les résultats issus de la plaque plane seront transposés à une structure de pale de queue d'hélicoptère pour des essais en soufflerie.

En premier lieu, des analyses numériques préliminaires ont été réalisées pour obtenir les concepts de bases permettant l'intégration du système piézoélectrique à la plaque plane pour l'étude du dégivrage par vibration. Les résultats de ces analyses ont permis l'optimisation du positionnement des actuateurs sur une plaque plane ainsi que le phasage d'excitation du signal de commande de ces derniers. Des essais expérimentaux avec le montage expérimental final de la plaque plane ont été réalisés au Conseil National de Recherches Canada (CNRC) à l'aide d'un vibromètre laser pour mesurer précisément les différents modes de résonnance. Les résultats expérimentaux ont ainsi permis de valider le modèle numérique

développer sous Abaqus lorsque la plaque était excitée optimalement avec une erreur moyenne de 20% et maximale de 43%.

Le montage expérimental de la plaque plane a ensuite été utilisé pour étudier la vibration transitoire obtenue lors de balayages fréquentiels. L'accélération pendant les différents balayages fréquentiels effectués a été mesurée à l'aide d'un accéléromètre positionné directement sur la plaque plane. Les résultats obtenus ont démontré que le profil de vibration était le même quel que soit la vitesse de balayage et la bande fréquentielle utilisées. Cependant, l'amplitude de chaque mode de résonance augmente avec une diminution de la vitesse de balayage. Des balayages fréquentiels effectués autour de différents modes de résonance ont permis de montrer qu'à mesure que la vitesse de balayage tend vers zéro, l'amplitude de vibration tend vers la valeur en régime établi pour ce même mode. Comme aucun autre effet transitoire n'a été mesuré, cela signifie que le régime établi est l'excitation optimale pour un mode de résonance. Pour valider cette hypothèse, le montage de la plaque plane a été installé en chambre climatique où des couches de glace ont été accumulées sur cette dernière. Des balayages fréquentiels à haut voltage ont été effectués et synchronisés à une caméra afin de déterminer les fréquences d'excitation pour lesquelles les bris dans la glace sont obtenus. Des essais en régime établi ont été effectués aux mêmes modes obtenus lors des balayages et ont permis d'obtenir les premiers bris de glace en régime établi, confirmant les résultats obtenus lors de l'étude transitoire. Ils ont aussi permis d'identifier les désavantages de l'excitation en régime établi, c'est-à-dire de pouvoir identifier les modes susceptibles de briser la glace numériquement et de déterminer avec exactitude la fréquence de ces modes. Les résultats ont ainsi permis de démontrer que des balayages fréquentiels correctement déterminés peuvent être utilisés pour se substituer au régime établi.

Afin de pouvoir valider le modèle numérique avec présence d'une couche de glace cinq accéléromètres ont été installés sur la plaque plane pour mesurer l'accélération lors des différents essais en chambre climatique. La validation expérimentale de la réponse vibratoire du modèle numérique de la plaque avec la glace a ainsi permis de déterminer les contraintes mécaniques nécessaire pour engendrer la fissuration ou la délamination de la couche de glace. Cela a ainsi permis de défini un critère de limite de contrainte pour les deux types de bris. Ces critères ont ensuite été utilisés dans des simulations numériques pour identifier les modes susceptibles de provoquer un bris dans la glace ainsi que les niveaux de tension des actuateurs piézoélectriques requis, valeurs qui ont été validées expérimentalement.

Pour la dernière étape, le concept de la plaque plane équipée des actuateurs piézoélectriques a été transposé à la structure d'une petite pale, et ce, autant numériquement qu'expérimentalement. Les limitations du système de mesure ont permis d'effectuer une validation partielle du modèle numérique. De plus, les tests expérimentaux ont permis d'obtenir un dégivrage complet de la pale entraînée en rotation dans une soufflerie givrante. La puissance nécessaire pour ce dégivrage était inférieure de près de 25% à celle des systèmes thermiques présentement utilisés. Cependant, la configuration de petite pale n'était pas jugée optimale pour le système, limitant ces capacités à réduire la consommation de puissance. Ces limitations n'étant pas les mêmes pour une pale de rotor de queue réelle, le concept a donc été extrapolé numériquement a une pale de rotor de queue complète d'hélicoptère pour estimer les bénéfices potentiels d'un tel système sur la consommation de puissance nécessaire au dégivrage de cette dernière. Les résultats, bien que préliminaire, ont confirmé que la réduction de puissance pourrait être de loin supérieur que celle obtenue avec la petite pale, avec une réduction par rapport aux systèmes électrothermiques supérieure à 90%.

ABSTRACT

Aircraft in-flight icing is an important problematic in the aerospace industry, especially for small helicopters. All rotorcraft currently habilitated to fly under icing conditions are equipped with electrothermal systems. They are not fitted to small and even medium size helicopters, which cannot provide the high power required and bear the additional weight of those systems. As an alternative, this research investigates the use of piezoelectric actuators to develop a low-energy vibration based ice protection system that could be implemented on small rotorcraft. The objective of this project was divided in four parts: (1) to design a piezoelectric actuator-based de-icing system integrated to a flat plate experimental setup and develop a numerical model of the system with experimental validation, (2) use the experimental setup to investigate actuator activation with frequency sweeps and transient vibration analysis, (3) add ice layer to the numerical model and predict numerically stresses for different ice breaking with experimental validation, and (4) bring the concept to a blade structure for wind tunnel testing. First, preliminary numerical analysis was performed to gain basic guidelines for the integration of piezoelectric actuators in a simple flat plate experimental setup for vibration-based de-icing investigation. The results of these simulations allowed to optimize the positioning of the actuators on the structure and the optimal phasing of the actuators for mode activation. A numerical model of the final setup was elaborated and an experimental setup was fabricated faithful to the numerical model at the laboratory with piezoelectric actuator patches bonded to a steel flat plate. The experimental setup was brought at the National Research Council Canada (NRC) for testing with a laser vibrometer to validate the numerical results. The experimental results validated the model when the plate is optimally excited with an average of error of 20% and a maximal error obtained of 43%. However, when the plate was not efficiently excited for a mode, the prediction of the numerical data was less accurate. This was not a concern since the numerical model was developed to design and predict optimal excitation of structures for de-icing purpose.

The experimental setup was used to study transient vibration occurring during frequency sweeps. Acceleration during different frequency sweeps was measured with an accelerometer on the flat plate setup. The results obtained showed that the vibration pattern was the same for the different sweep rate (in Hz/s) tested for a same sweep range. However, the amplitude of each resonant mode increased with a sweep

rate decrease. Investigation of frequency sweeps performed around different resonant modes showed that as the frequency sweep rate tends towards zero, the amplitude of the mode tends toward the steady-state excitation amplitude value. Since no other transient effects were observed, this signifies that steady-state activation is the optimal excitation for a resonant mode. To validate this hypothesis, the flat plate was installed in a cold room where ice layers were accumulated. Frequency sweeps at high voltage were performed and a camera was used to record multiple pictures per second to determine the frequencies where breaking of the ice occur. Consequently, the resonant frequencies were determined from the transfer functions measured with the accelerometer versus the signal of excitation. Additional tests were performed in steady-state activation at those frequencies and the same breaking of the ice layer was obtained, resulting in the first ice breaking obtained in steady-state activation conditions as part of this research project. These results confirmed the conclusions obtained following the transient vibration investigation, but also demonstrated the drawbacks of steady-state activation, namely identifying resonant modes susceptible of creating ice breaking and locating with precision the frequencies of the modes, which change as the ice accumulates on the structure. Results also show that frequency sweeps, if designed properly, can be used as substitute to steady-state activation for the same results.

An ice layer was added to the numerical model. Five accelerometers were installed on the flat plate to measure acceleration. Validation of the vibration amplitude predicted by the model is performed experimentally and the stresses calculated by the numerical model at cracking and delamination of the ice layer are determined. A stress limit criteria is then defined from those values for both normal stress at cracking and shear stress at delamination. As a proof of concept, the numerical model was then used to find resonant modes susceptible of generating cracking or delamination of the ice layer within the voltage limit of the piezoelectric actuators. The model also predicts a voltage range within which the ice breaking occurs. The experimental setup is used to validate positively the prediction of the numerical model.

Finally, the concept was brought to a small blade structure both numerically and experimentally. Limitations of the measurement systems limited the validation of the numerical model. However, partial validation was still done and complete de-icing was successfully obtained in rotation in wind tunnel. The concept was

extrapolated numerically to a full tail rotor structure showing the potential benefit in power reduction of the system.

TABLE OF CONTENTS

LIST OF TABLES

LIST OF FIGURES

DÉDICACE

Je voudrais dédicacer ma thèse à toute ma famille et amis qui m’ont grandement supporté dans cette grande étape de ma vie. À Cyndi, qui a été à mes côtés et s’est occupé de tout pour moi pendant ce long périple et à mes enfants, Félix, Marc-Antoine et Zachary, qui ont été des anges me permettant de poursuivre ce projet. À mes parents, Jean et Marie, et grands-parents, Delphine, Jean-Marc, Rosita et Jean-Paul, qui par leurs efforts avant moi m’ont permis d’atteindre cette réalisation.

AKNOWLEDGEMENT

Je tiens à remercier tout d'abord mon directeur Christophe Volat et co-directeur Sebastian Ghinet qui ont été plus que de simple aides pédagogiques durant ces quatre années. Ils ont été des mentors et des amis et sans qui je n'aurais pu atteindre cette réalisation. Merci également à mon co-directeur Jean Perron qui m'a offert cette opportunité unique de pouvoir travailler et réaliser ce projet en même temps, me permettant de subvenir à ma famille. Un énorme merci à Carol Mercier pour la réalisation de tous les montages qui ont assurés la réussite de ce projet. Merci à l'équipe du laboratoire pour leur support. Finalement, merci aux professeurs Lyne St-George et Ali Saeidi pour tous leurs conseils et aide dans ce projet.

INTRODUCTION

Aircraft in-flight icing is an important problematic in the aerospace industry, especially for small helicopters. Helicopters can be subjected to in-flight icing under different conditions and at different altitudes. When flying under these conditions, layers of ice accrete on the blades which lead to increased drag and torque requirements, decreased lift, vibration, and imbalance [1]. This can lead to hazardous situations. In order to fly into known icing conditions, rotorcraft requires an ice protection system capable of meeting the demands of various certifications for full icing clearance [2]. All rotorcraft currently habilitated to fly under icing conditions are equipped with electrothermal systems. Those systems require large energy quantity and add a lot of weight to the vehicles. They are not fitted to small and even medium size helicopters, which cannot provide the high power required and bear the additional weight of those systems. Rotorcraft are often used for their great flexibility and access to remote locations that are otherwise inaccessible. Not being able to flight under different environmental conditions is a major drawback for those vehicles

As an alternative to the standard electrothermal deicing systems, this doctoral research investigates the use of piezoelectric actuators to develop a low-energy ice protection system that could be implemented on small rotorcraft. Piezoelectric actuators are devices that generate strains when subjected to an electrical charge. In this particular study, alternating current was applied to piezoelectric devices to produce vibrations at frequencies that excited some of the resonant modes of structures. Different approaches using piezoelectric actuators have been explored in the past. First investigated by Ramanathan [3] and later by Palacios [4], resonating piezoelectric elements were used to generate ultrasonic surface waves to produce shear stress at the ice interface. The method has provided interesting results for flat and shelled structures. Venna and al. [5] used piezoelectric actuators located directly below the iced zones of a leading edge to generate both local shear strains and normal impulse forces to de-ice, however with limited results. Similar to the deicing mechanism explored in this study, Kandagal and Venkatraman [6] partially deiced a cantilevered flat plate with piezoelectric actuators by exciting resonant frequencies. Analysis of the results showed that shear stress generated at the interface was responsible for breaking the ice adhesion to the substrate.

Analysis of the literature revealed that the structure resonance methods suffered from the lack of proper design guidelines. The main goal of this project is to develop a low power piezoelectric vibration based ice protection system applied to small rotorcraft blades. In order to achieve this goal, the methodology of the project is divided in four sub-objectives. The first sub-objective consists of developing a numerical model of the vibration of a flat plate structure excited by piezoelectric actuators and perform an experimental validation. The second sub-objective consists of investigating transient vibration and actuators optimal excitation strategies by studying frequency sweeps and steady-state vibration of the flat plate structure. For the third sub-objective, an ice layer is added on the flat plate in the numerical model to study the different stresses and stress levels involved in the different ice breaking mechanism and a new experimental validation study is performed. Finally, for the last sub-objective, the concept have to be implemented to a small blade prototype replicating a Bell tail rotor to perform a proof of concept experimental testing in rotation in wind tunnel.

Therefore, in this study a numerical model of a piezoelectric system was created. The first step was to simulate the vibration of a flat plate excited by piezoelectric actuator patches. This model had to include the right piezoelectric material properties for the actuators which allowed electromechanical coupling. Proper boundary conditions had to be imposed in the analyses. This numerical model was validated experimentally with a setup that recreated the flat plate model and a laser vibrometer that measured the vibration amplitudes. The experimental setup was then used to investigate the structure’s vibration response to transient and frequency sweep excitation in order to understand and optimise operation of the system for de-icing. An ice layer was added both numerically and experimentally to the flat plate structure to perform an experimental validation of the model with the ice accumulation as well as the stresses involved in delamination and cracking of the ice layer. As a final step with the flat plate structure, the numerical model was used to find frequencies susceptible of generating ice breaking in the layer and predict the voltage range within which that breaking should occur. This work was the subject of three published papers in peer reviewed journals.

The numerical model was adapted to a tail rotor blade structure and knowledge obtained with the flat plate was used to integrate the piezoelectric actuator system to the blade. Partial validation of the model was obtained in wind tunnel for both static tests and in rotation. Complete de-icing of the blade was also achieved in rotation. Finally, the numerical model was used to extrapolate power density requirements for a full tail rotor blade, showing the potential benefits of the system. This part will be the subject on a fourth paper for the project.

This thesis was realized under the ENV702 CRIAQ project in collaboration with Bell flight and the Nation Research Council in Ottawa.

CHAPTER 1

LITERATURE REVIEW

The first chapter of this thesis consists of a comprehensive literature review of the different aspect involved in the successful realization of this project. First, a summary of the different parameters and characteristics of atmospheric ice found in the literature is presented. It also details the different failure modes possible for an ice layer which will be valuable later in this study. The second part presents the work that can be found in the scientific community on numerical modeling of ice and different ice breaking and failure. The third part presents the different ice protection systems readily available or under investigation as well as their performances, advantages and drawbacks. Finally, a summary of the literature is presented summing up the information gathered on ice protection systems and the need of a new low power system, the ice breaking mechanisms and key concepts to investigate for the design of a piezoelectric actuator based ice protection system.

1.1 ATMOSPHERIC ICING

Different types of ice can form on a structure. The resulting type of ice will depend mainly on the atmospheric conditions during ice accretion. Glaze, rime and mixed ice are the main forms that will form on rotorcraft and cause various problems. To a lesser extent, frost formation can also be problematic to aerial vehicles. Supercooled droplets suspended in the clouds impact the vehicle and solidify to form ice. Ice layers accreted on key aerodynamic surfaces, like wings and blades, significantly alter the performances of those surfaces and create hazardous situations. The type and accretion rate of the ice depend mainly on relative speed of the surface with the droplets, the median volumetric diameter (MVD) of the droplets, the liquid water content (LWC) in the cloud and the air temperature. It also depends on the size and shape of the surface which define the collection coefficient, the ratio of droplets that impact the surface [7]. Rime formation occurs when a supercooled water droplet completely freeze as it hits the surface, before the impact of a new supercooled water droplet. This is called a dry accretion regime. When this happens, air gets trapped inside the ice matrix, causing the white appearance and rough surface of the ice. This also causes the low density of the ice, usually between 500 and 850 kg/m^3, and low cohesion. The rapid solidification occurring in the formation of this type of ice creates an ice layer that will tend to match the shape of the profile on which it accretes, like the ice formed towards the root of the blade shown at Figure 1.1:1. However, for longer or more severe accumulation, the ice layer can end up changing the structure geometry.

Figure 1.1:1 – Rime accretion on SRB blade

Glaze ice is formed under a wet accretion regime. This accretion regime occurs when the rate of solidification of water droplets is too slow to allow the freezing of the droplets when it impacts the surface. Only a fraction of a droplet becomes solid before a new droplet impacts. The fraction of water that solidifies is called the solid fraction and range from 0 to 1. The water fraction that is trapped in the ice gives the glaze ice its translucent appearance and smooth surface. It is also the reason for its higher density, from 900 to 999 kg/m³, and higher cohesion. Water that does not freeze at impact can flow further down the surface causing the resulting layer of ice to have a completely different shape than the surface on which it is accreted. On an aerodynamic profile, this can result in a double horn ice shape (Figure 1.1:2). This type of ice is the most problematic in aeronautic due to the ice shape which alters the airflow around the aerodynamic surfaces.

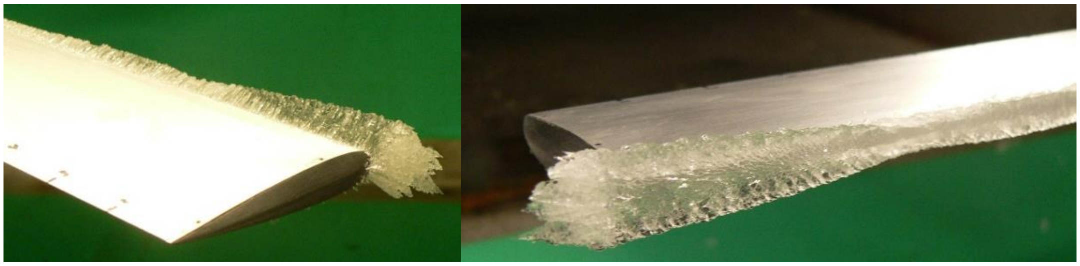

Figure 1.1:2 – Glaze formation on SRB blade

1.1.1 CRYSTAL STRUCTURE

Ice exists in 12 different crystal structures and two amorphous states. When surrounding pressure is low, the ice stabilize in phase called ice I [8]. Two close variants of ice I are hexagonal ice Ih, with a crystal symmetry in shape of snowflakes (Figure 1.1:3), and cubic ice Ic. Freezing water at ambient pressure leads to an Ih structure while low temperatures (-130°C) vapor deposition creates Ic structure. Ice Ih is also termed ordinary ice and is the common form in nature. Amorphous states are obtained by the compression of ice Ih at liquid nitrogen temperature and by vapor deposition at lower temperatures than ice Ic.

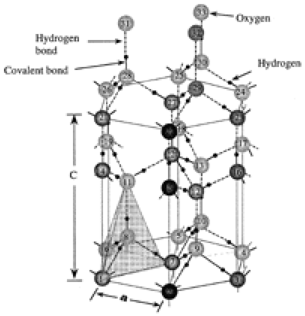

Figure 1.1:3 – Schematic of the crystal structure of hexagonal ice Ih [8]

For ice Ih, H_2O molecules have four neighbors shaped like a regular tetrahedron. Oxygen atom in the molecule is bonded covalently with two hydrogen atoms. Molecules are bonded to each other with a weak covalent bond. Unit cell of ice Ih is open with a packing factor less than 0.34, explaining why ice is less dense than water.

1.1.2 ELASTIC MODULUS AND POISSON’S RATIO

Elasticity of isotropic material can be described by two constants, the young’s modulus and Poisson’s ratio. Those two constants allow determining of other constants such as Lame’s constant, shear modulus and bulk modulus. Main methods for measuring elastic modulus include measuring propagation velocity of longitudinal and transverse elastic waves as well as the Hook’s law method. The former being dynamic, and the later static. Gold [9] used plates of polycrystalline ice submitted to biaxial bending to measure elastic modulus and Poisson’s ration. Young’s modulus was measured between 9.7 and 11.2 GPa and Poisson’s ratio between 0.29 and 0.32. Fletcher [10] determined that near the melting point, the young’s modulus of single crystals has a variation of less than 30%, starting from 12 GPa parallel to the c-axis, which is the least compliant direction, down to 8.6 GPa inclined to the c- and a-axes. For polycrystals oriented randomly, typical Young's modulus is 9.0 GPa and Poisson's ratio 0.31.

1.1.3 TENSILE AND COMPRESSIVE STRENGTH

Tensile and compressive strength of atmospheric ice are important parameters when it comes to predicting and modeling ice shedding phenomenon. Not many studies have been published for atmospheric ice properties such as tensile and compressive strength. Ambient environmental conditions during accretion and substrate structural parameters have a significant impact on the properties of atmospheric ice. Lots of parameters can influence ice strength like accretion temperature, wind speed, liquid water content, median volumetric diameter, strain rate, porosity, etc.

In his review of the mechanical properties of ice and snow, Petrovic states that tensile strength for atmospheric icing in the literature typically range from 0.7 to 3.1 MPa, with an average value of 1.43 MPa between -20°C and -10°C [11]. For compressive strength, the values range from 5 to 25 MPa. Main variables that impact ice strength raised in literature includes temperature, strain rate, tested volume and grain size.

Studies indicate that both the tensile and compressive strength of ice increases with decreasing temperature (Figure 1.1:4). Compressive strength dependence to temperature is related to ice dislocation and grain boundary sliding phenomena and varies by a factor 4 from 0°C to -40°C. Tensile strength shows less dependence to temperature, with a factor of 1.3 over the temperature range obtained in literature [12], which can be explained by the localization of stress-accommodating mechanisms at the tips of tensile flaws.

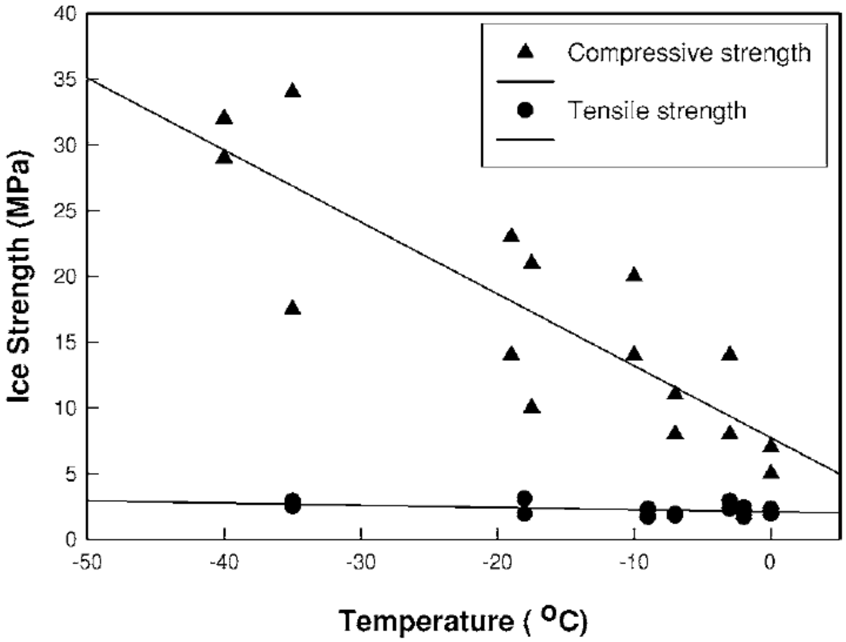

Figure 1.1:4 – Tensile and compressive strength of ice as a function of temperature [12]

Research showed that the effect of strain rate is significant for compressive strength, but less important for tensile strength (Figure 1.1:5). For tensile strength, the stress-strain curves investigated demonstrated a ductile behavior at low strain rates and brittle behavior at intermediate and high strain rates [8]. For compressive strength, brittle behavior appeared only at high strain rates. This is consistent with dislocation and grain boundary sliding deformation mechanisms.

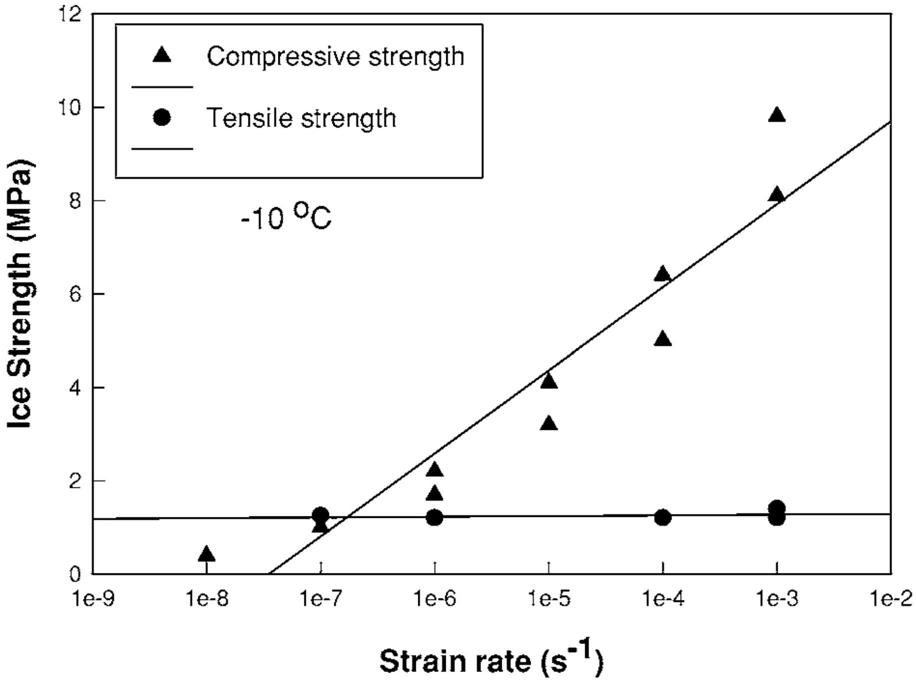

Figure 1.1:5 – Tensile and compressive strength of ice as a function of strain rate [8]

Grain size is another parameter influencing ice strength. Increasing grain diameter leads to a decrease in tensile strength (Figure 1.1:6). Hall-Petch relationship (Equation 1 [13]) describes this phenomenon, with n = -1/2, suggesting that this process is led by a stress concentration process.

$$\sigma_y = \sigma_i + kd^n \qquad (1)$$

With σ_y the yield stress, σ_i a measure of the crystal lattice's frictional resistance to slip, k a constant and d the average grain diameter. Michel [14] suggested an equation for the tensile strength in the brittle range:

$$\sigma = 7.94x10^4 \left[\left(1 - \frac{e}{0.285}\right) \frac{(1 - 0.9x10^{-3}\theta)}{d} \right]^{\frac{1}{2}} \qquad (2)$$

With e the porosity (1-ρ'/ρ), ρ the density of pure ice (917 kg/m^3), ρ' density of ice, θ temperature and d grain diameter.

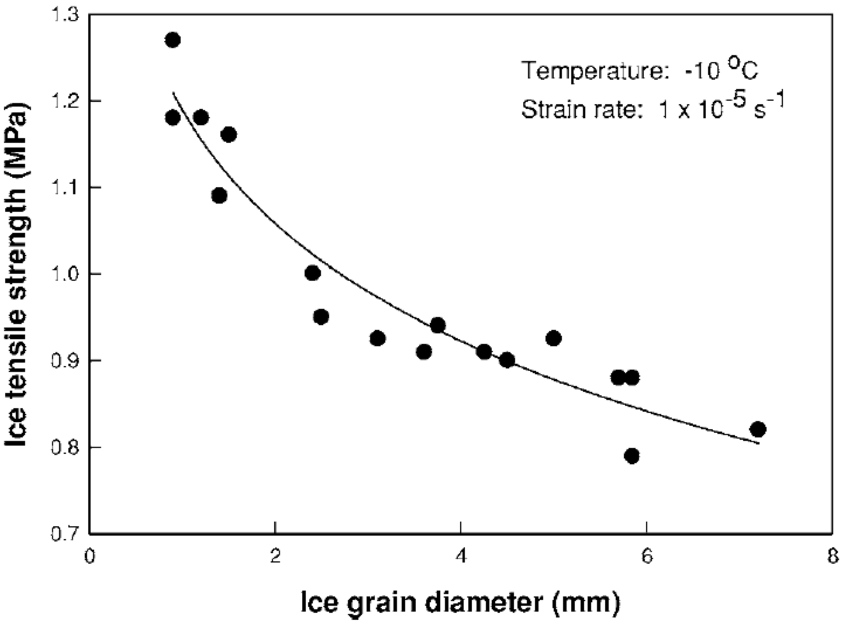

Figure 1.1:6 – Tensile strength of ice as a function of grain size [13]

The volume of the test specimen also has an impact on the tensile strength. With increasing volume comes a tensile strength decrease (Figure 1.1:7), which is usually described with a Weibull statistical approach for brittle materials [15]. The probability of the fracture is expressed by :

$$P = 1 - \exp(-\vartheta \left(\frac{\sigma}{\sigma_0}\right)^m \qquad (3)$$

With P the probability of fracture, σ the applied tensile stress, σ_0 a constant, ϑ the stressed volume and m the Weibull modulus. Equation 4 gives the volume dependence for strength of brittle materials, with the Weibull modulus estimated at 5 for ice.

$$\frac{\sigma_2}{\sigma_1} = \left(\frac{\vartheta_1}{\vartheta_2}\right)^{\frac{1}{m}} \qquad (4)$$

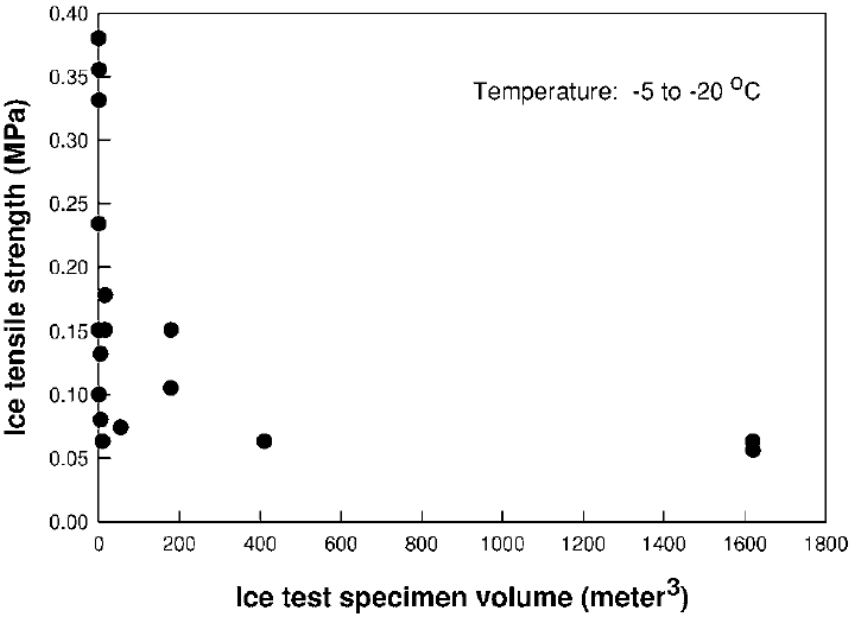

Figure 1.1:7 – Tensile strength of ice as a function of volume [16]

To determine tensile strength, two main experiments have been used up to now: the uniaxial tensile test and the ring tensile test. Tensile strength is largely dependent on strain rate, as reported by Petrovic [11]. At low strain rates, below $10^{-7}s^{-1}$, ice is in the ductile regime. Transitional domain occur between $10^{-7}s^{-1}$ and $10^{-6}s^{-1}$ and at higher strain rates, while maintaining a quasi-static regime, the brittle behavior is dominant. Mohamed et al. [17] have performed tensile testing to determine tensile strength of atmospheric icing in function of wind speed, air temperature and strain rate. Ice accumulation was performed in a wind tunnel with a median volumetric diameter (MVD) of 40 µm and a liquid water content of 2.5 g/m^3. Ice was accumulated on a rotating aluminum cylinder and dumbbell samples were carefully cut off the accumulation (Figure 1.1:8). The samples were tested with an electrohydraulic testing machine. The samples were prepared at temperatures of -5°C, -10°C and -15°C and tested at strain rates between $2.22x10^{-6}$ s^{-1} and $1.67x10^{-3}$ s^{-1}.

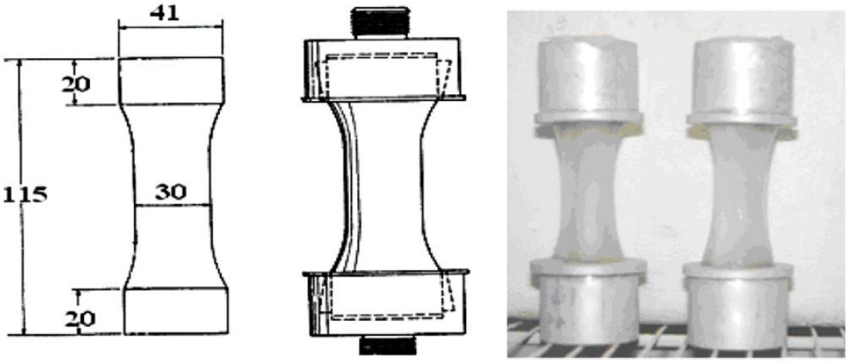

Figure 1.1:8 – Ice dumbbell specimens [17]

Statistical technique based on the two-level experimental design [18] was used to determine tensile strength dependence on those variables. The tensile strength showed an increase with increasing wind speed up to 15 m/s and then decreased up to 20 m/s. Authors believed that the reason could be the formation of hard rime or glaze at higher wind speed, which is brittle. The tensile strength increased slightly with decreasing temperature which was consistent with polycrystalline ice results detailed by Mellor et al. In return, tensile strength proved strongly influenced by strain rate. Tensile strength increased greatly with increasing strain rate up to $4.4\text{x}10^{-5}$ s^{-1} and then decreased up to the maximum strain rate tested. Ductile, ductile-brittle transition and brittle regimes could be observed: ductile regime from $2.2\text{x}10^{-6}$ s^{-1} to $1.1\text{x}10^{-5}$ s^{-1}, transition regime between $1.1\text{x}10^{-5}$ s^{-1} to $4.4\text{x}10^{-5}$ s^{-1} and brittle regime from $4.4\text{x}10^{-5}$ s^{-1} up to the maximum tested strain rate, $1.6\text{x}10^{-3}$ s^{-1}. Comparing with Kermani et al. [19], it was observed that at very low strain-rate the tensile strength and compressive strength were similar, but as transition between ductile and brittle regime occurred, a slight difference between the two could be observed. With the results obtained, a regression was developed for the ultimate tensile strength (Equation 5). Looking at the equation, it is possible to conclude that variation of the strain rate has the greater impact on the tensile strength.

$$UTS = 1.26 - 0.00858 WindSpeed - 0.0142 Temperature + 19.6 StrainRate \qquad (5)$$

Kermani et al. [19] investigated the compressive strength of atmospheric ice. Ice accumulation was generated in a wind tunnel at -20°C, -10°C and -6°C, at 10 m/s and with a liquid water content of 2.5 g/m^3 on a rotating aluminum cylinder. Ice slice specimens of 20 mm thick, 45 mm long and 40 mm high were then carefully taken from the ice accumulation. Compressive strength tests were performed at accumulation temperature, and for ice accumulated at -10°C, some samples were also tested at -20°C and -3°C. Testing was done at seven different strain rates, ranging from $3x10^{-5}$ to $3x10^{-2}$. Each test was repeated at least five times. Grain size at -6°C ranged from 0.5 to 3 mm with a 1.5 mm average. Above -10°C, nucleation of air bubbles was initiated when concentration of air dissolved in water hit a critical value. Air bubble proportion of atmospheric ice depended on the accumulation conditions like air temperature, liquid water content, droplet dimension, etc. Grain size at -10°C was smaller than at -6°C with values less than 0.5 mm, showing that grain size decreases with accumulation temperature. Density of air bubbles was also greater at that temperature than at -6°C. Data obtained was in good agreement with literature. At -20°C, the microstructure was different than for the two other temperatures, with cavities and crack caused by the high freezing rate at low temperatures preventing the liquid of filling the cavities before solidifying. The porosity at -20°C was calculated at 8.5%, compared to 2.9% at -6°C. Compressive strength increased with decrease in temperature. The strength increased with increasing strain rate up to a certain value and then decreased. Between 10^{-4} s^{-1} and 10^{-2} s^{-1} there was a transition region where compressive break could be caused either by cracking in brittle regime or because of viscous strains in ductile mode. Finally, strength increased with decreasing grain size.

Since atmospheric ice is defined by many parameters, empirical models are efficient tools to define ice parameters. Farid et al. [20] have investigated an empirical solution taking into account the strain rate, temperature and porosity of atmospheric ice. In this study, ice samples were prepared in a wind tunnel using distilled water at a wind speed of 20 m/s, a fixed liquid water content of 2.5 g/m^3 and a MVD of 40 µm. Ice was accumulated on a rotating cylinder at three different temperatures, -20°C, -15°C and -5°C. Blocks were cut from the cylinder of ice when a thickness of 60 mm was obtained and were machined into 100 mm long cylinder of 40 mm in diameter. Observation of the microstructure of the ice samples showed that the pores in the ice structure became smaller and more uniformly distributed as temperature decreases. Uniaxial compression testing was performed at four different strain rate, 10^{-4} s^{-1}, 10^{-3} s^{-1}, 10^{-2} s^{-1} and 10^{-1} s^{-1} and repeated five times for each strain rate and temperature. The compressive strength of ice increased from 10^{-4} s^{-1} to 10^{-3} s^{-1} and then decreased for every temperature, showing a ductile-brittle transition where brittle fracture is dominant and there is no plastic deformation. For each strain rate, it was shown that the compressive strength increased as the temperature decreased down to -15°C and then decreased from -15°C to -20°C due to an increase in porosities. The most influential parameter in their empirical solution was the strain rate. The compressive strength was represented by a distribution similar to the normal law with regards to the strain rate and porosity (Equation 6).

$$\sigma_c = \frac{\alpha}{f(\eta)\sqrt{2\pi}} exp\left(-\frac{1}{2}\left(\frac{log(\dot{\varepsilon}) - n}{f(\eta)}\right)^2\right) \qquad (6)$$

Parameter $\dot{\varepsilon}$ is the strain rate, η the porosity and $f(\eta)$ a linear function of the porosity and n a strain rate sensitivity factor. Parameter α depends on the temperature and was found to be close to the creep activation energy of ice. However more investigations were still required for further statement on this matter. Temperature dependence of parameter α is defined by Equation 7.

$$log(\alpha_T) = \frac{-C_1(T - T_r)}{C_2 + (T - T_r)} \qquad (7)$$

C_1 and C_2 are empirical constants, T the temperature and T_r the reference temperature on which the main curve is established. The data was validated using compressive tests performed at -10°C. The empirical solutions showed satisfying fitting, with an average relative error of 14.52%. The failure criterion was also used to predict tensile failure, using experimental data from Mohamed et al. [17]. This method was able to predict the tensile strength at -5°C, -10°C and -15°C with an error of less than 2%.

Farid and al. [21] investigated the effect of multiaxial stress on failure of atmospheric icing. As for in other publication [20], atmospheric ice samples were created in a wind tunnel on a rotating aluminum cylinder with an icing cloud liquid water content of 2.5 g/m^3 and droplets median volumetric diameter of 40 µm. Accretion temperatures were -15°C, -10°C and -5°C. A compression confinement stress was applied in two directions and in the third direction, a compression force was added to the confinement stress. The confinement pressure is applied by imposing a pressure to a fluid surrounding the sample. The additional compression force in the third direction was applied by a pusher piston. Testing included variation of the confinement pressure in relation to the compression force, variation of the strain-rate and variation of the temperature. The ice samples showed both the ductile and brittle behavior. When ductile behavior was obtained, the elastic deformation was followed by a plastic deformation and finally a hardening or softening plateau. With the brittle behavior, elastic deformation was immediately followed by a brittle failure. Example of ductile behavior and brittle behavior are presented at Figure 1.1:9 and Figure 1.1:10 respectively. Appearance of a brittle-like failure is also reported, due to presence of shear faulted failure oriented at ±45°

of shortening. Results showed that brittle fracture is dependent of the hydrostatic confinement. Increasing confinement pressure allows stress to surpass uniaxial compressive strength.

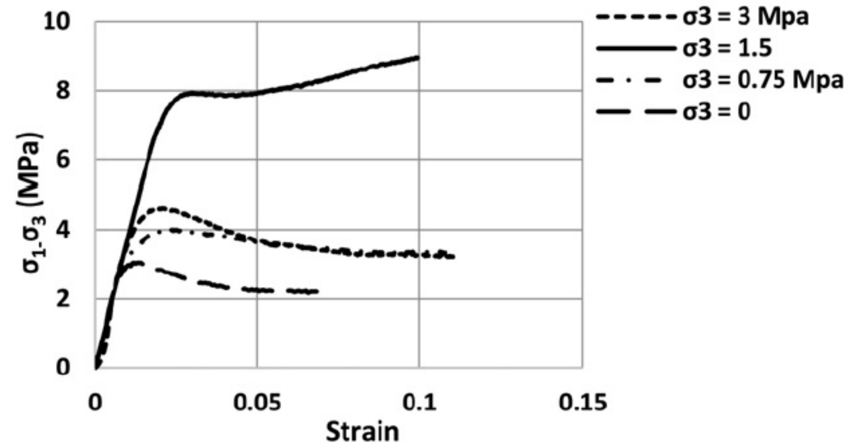

Figure 1.1:9 – Example of ductile behavior. Stress versus normalized displacement under different confinement pressures at -5°C for a strain rate of $10^{-4}s^{-1}$ [21]

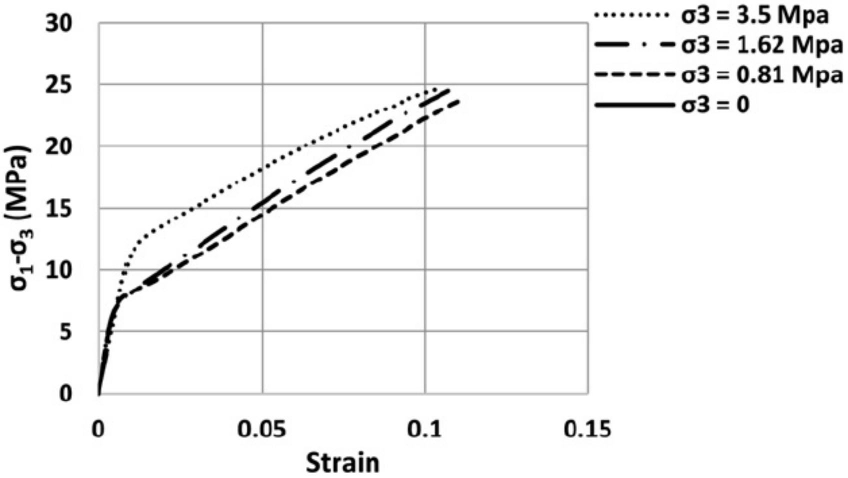

Figure 1.1:10 - Example of brittle behavior. Stress versus normalized displacement under different confinement pressures at -5°C for a strain rate of $10^{-2}s^{-1}$ [21]

At -5°C the strength increased with confinement pressure up to 1.62 MPa, and then decreased. This is attributed to confinement induced plasticity and damage. At lower temperatures, -10°C and -15°C, strength continued to increase with strain rate and confinement. At low temperatures, no ductile-brittle transition was observed. Experiment showed that, as accumulation temperature decreased, the porosity increased and grain size decreased and that it strongly influenced density of ice. It also showed that presence of pores, up to a certain point, can increase the compressive strength of ice by reducing the concentration of intergranular stresses.

At low strain rates ice is considered ductile, which can be approximated with Tresca or Von Mises criterion. At higher strain rates, its behavior is considered brittle and Mohr-Coulomb and Hoek-Brown failure theories, like in the case of rocks and soils, are considered. Farid et al. [21] used those two criteria, Mohr-Coulomb and Hoek-Brown, to represent the brittle behavior of the ice. For the Mohr-Coulomb criterion, the shear stress ($|\tau|$) through the plan of future fault is resisted by the cohesion of the material (C) and by friction. Friction can be defined by internal friction (μ) multiplied by normal stress to the plan (σ), giving Equation 8.

$$|\tau| = C + \mu\sigma \qquad (8)$$

It can also be expressed by the minimum and maximum principal stress by Equation 9, where φ is the friction angle.

$$\sigma_1 = \tan^2\left(\frac{\pi}{2} + \frac{\varphi}{2}\right)\sigma_3 + 2C\tan\left(\frac{\pi}{2} + \frac{\varphi}{2}\right) \qquad (9)$$

The Hoek-Brown empirical criterion, expressing the relationship between two principal stresses in failure was also used to represent the tendency of the ice strength to stabilize once the confinement pressure reached a certain value. The criterion is represented by Equation 10.

$$\sigma_1 = \sigma_3 + \sigma_c\left(m\frac{\sigma_3}{\sigma_c} + s\right)^{\frac{1}{2}} \qquad (10)$$

With σ_c the uniaxial compressive strength, m and s material constants to be determined experimentally. The two criteria are presented at Figure 1.1:11.

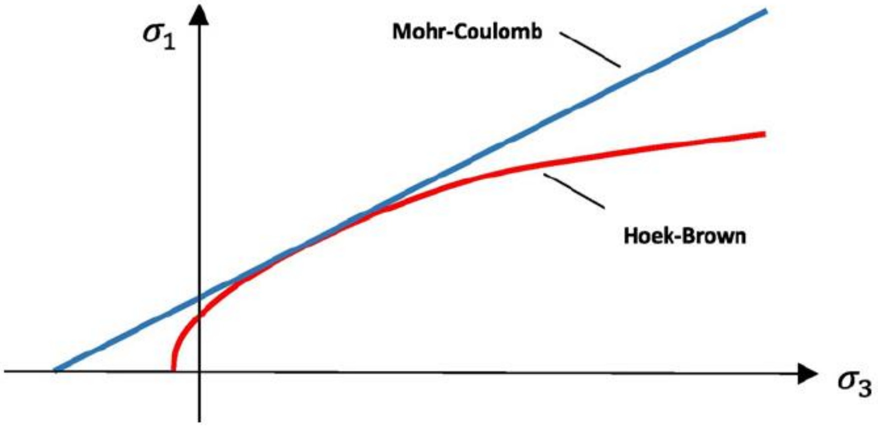

Figure 1.1:11 – Mohr-Coulomb and Hoek-Brown failure criteria in the principal stresses space [21]

The experimentation performed allowed the identification of the empirical constants for the criteria. It was found that those criteria represent well the brittle behavior of the ice samples. Results obtained with the Hoek-Brown criterion were slightly more accurate. As temperature decreased, the cohesion increased and friction angle decreased, which can be explained by the ice grain shape and morphology.

1.1.4 ADHESION

Strength of interfaces between ice and solid has been the subject of different studies. Tensile, shear and impact strength of the interface have been investigated and it was found that the techniques and conditions have a large influence on the adhesion. Before solidification, a few nanoseconds after impact, water droplets wet either partially the substrate's surface or completely when water forms a film. Chemical bonds at the molecular level can be classified in different categories, with three main ones being the covalent bonds, the ionic bonds and the Van der Waals forces. Covalent bonds, which depend greatly on the nature of the substrate, and Van der Waals forces are not considered dominant in adhesion mechanism. Ionic bonds, however, are an important parameter in adhesion forces. Ryzhkin and Petrenko [22] created a model based on electric properties of substrate and studied the important of ionic bond on adhesion force. Model showed the importance of ionic bond in ice adhesion by predicting the adhesive energy and adhesion force in function of time and temperature. A method to study hydrogen bond impact on ice adhesion was developed by Petrenko and Peng [23]. They observed that ice adhesion was dependent of the water contact angle on the surface by covering metals with hydrophobic or hydrophilic mono-molecule layers. Hydrogen bonds significantly increase ice adhesion. Type of ice, type of surface and structure at ice/substrate interface influence greatly adhesion. Depending on surface tension and water impact pressure, droplets can penetrate substrates surface cavities. When freezing, water will anchor and increase the ice adhesion [24]. Contact surface will vary for rime and glaze ice which will also impact adhesion forces.

Most of the studies are based on mechanical ice removal and few based on fundamental understanding of the process behind it. Many tests have been developed to measure ice adhesion like flat shearing tests, tensile tests, torsion tests, peeling tests, impact tests, cone method, centrifugal test, etc. Faraday [25] was the first to assume the presence of a thin liquid-like layer at ice's surface down to -30°C. Adhesion is a property of the interface and is dependent on the atomic structure and chemistry of the region. Intrinsic tensile strength or toughness can be used to characterize the interface. Fundamental interface stress-separation curve allows to link those two parameters together. Jellinek [26] studied the adhesion of snow-ice trapped between different materials with both tensile and shear loading. Loading rate, surface roughness, temperature and type of the substrate were the key parameters in defining the adhesion strength. Rice et al. [27] discovered that local stress is a combination of shear and tension when cracks exists at the interface between dissimilar substances. Scavuzzo et al. [28] and Ramanathan [3] published literature reviews of ice adhesion measurements. Their reviews show that there is a lot of variation in the adhesion values found in literature. Temperature, surface roughness, type of ice, droplet size, impact speed are all parameters that greatly influence ice adhesion. Even when conditions are highly controlled, variation in the results are found, indicating a stochastic nature for adhesion of ice [29]. Generally, adhesion increases when temperature decreases near freezing point until reaching a temperature where adhesion stops increasing. Anti-icing Materials International Laboratory (AMIL) developed a centrifuge adhesion test. Ice adhesion on aluminum beam is measured by first accumulating ice at one extremity of aluminum beams under highly controlled conditions in a cold room. Then the beams are spun in a centrifuge (Figure 1.1:12). Rotation speed is increased until ice detach under the centrifugal load. Piezoelectric devices detect the exact time at which the ice detaches. Adhesion strength at -10°C for 6061-T6 aluminum with a surface roughness of 0.7 µm has been measured at 0.51±0.04 MPa [30].

Figure 1.1:12 – Centrifuge Adhesion Testing Apparatus [30]

Another test has been developed at AMIL to measure ice adhesion. The Spinning Rotor Blade test (SRB) has been developed to mimic helicopter in-flight icing accretion and ice shedding. A scaled down helicopter rotor is installed in an icing wind tunnel when an icing cloud is created. NACA 0012 aluminum blades are spun (Figure 1.1:13). Tip speed can reach 130 m/s. Rotation is maintained at constant speed until a critical ice mass is obtained and shedding occurs. Shedding is signaled by a drastic decrease in power required to maintain the rotation speed. At -15°C for a liquid water content of 0.8 g/cm^3 and a wind speed of 15 m/s, the adhesion has been measured at 0.21±0.06 MPa [31].

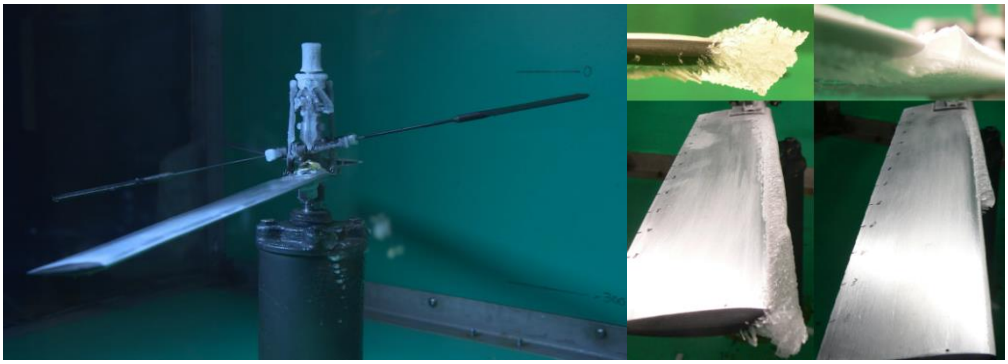

Figure 1.1:13 – Spinning Rotor Blade Apparatus [31].

Akitegetse [32] has developed a mechanical method to measure the bonding strength of atmospheric ice with PVDF film sensors installed at the ice/substrate interface. Tests were performed on aluminum beam submitted to sinusoidal stress by an electromagnetic shaker. Ice was accumulated in a cold room with supercooled water droplets sprayed on the beam. Results prove the concept of the method and the sensitivity of measurements for aluminum beam used (Figure 1.1:14). Finite element model was also developed and 12% maximum variation was obtained between model and experimental results. Measurement showed that speed of vibration amplitude had no effect on results while ice thickness of sample showed a great influence on measured adhesion. The stress decreased with an increase of ice thickness, leading to a zero stress value when the neutral axis of the composite aluminum/ice beam is positioned at the ice/substrate interface. All rupture was completely adhesive. Adhesion strengths of 0.32 MPa, 0.34 MPa and 0.37 MPa were obtained for ice thicknesses of 2.5 mm, 4 mm and 10 mm respectively.

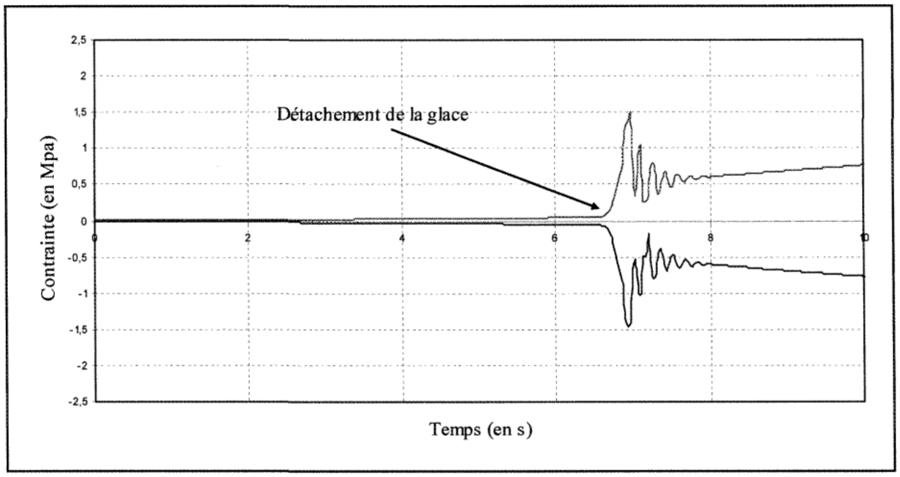

Figure 1.1:14 – Stress evolution at interface read by a PVDF film for an ice layer 10 mm thick [32]

Meuler et al. [33] investigated the relationship between advancing and receding water contact angles and ice adhesion strength for twenty-one different coatings. A goniometer was used to measure the contact angle on the coatings. Freezer ice was created on the coatings and a homemade adhesion apparatus was used to measure adhesion strength. Results showed that ice adhesion strength correlates with the works necessary to remove liquid water from the surfaces and ice adhesion was diminished by up to 4.2 for some of the coatings. Knuth [34] developed a physics-based analytical model to predict adhesion shear strength of ice on different surface morphologies. It is believed that droplets between 10 and 80 µm, when they impact on surfaces, expend and clamp to discontinuities playing a large role in ice adhesion. To calculate the forces required for the removal of this kind of ice, the model was based on the derivation of a Newtonian mechanics model. The macro-scale geometry of the surface needed to be input in the model. Before experimental validation of the model, parameters required to be input in the model were defined. First, some parameters were obtained from the literature. Relationships for temperature dependence of the Young's modulus and thermal coefficient of expansion of ice are examples. Then, the rest of the parameters, like coefficient of friction of ice, were obtained experimentally at their laboratory. Then the model was validated experimentally with the Adverse Environment Rotor Test Stand (AERTS). The AERTS is constituted of a 5.7 m rotor spinning in a cold chamber at temperatures ranging from 0°C to -25°C. 15 NASA standard icing nozzles are installed in the cold room ceiling in two circles. The angular speed can reach 1500 RPM and the system, with the 1.37 m radius blades, can reproduce full-scale helicopter tip speeds. Load cells measure loads generated by rotation and ice accumulation until ice sheds from the blade and the adhesion is calculated. Test surfaces were created for the model validation. Surface roughness ranged from 0.01 µm to 5.11 µm average roughness (R_a). Adhesion strength obtained experimentally ranged from 0.028 MPa to 0.157 MPa at -8°C and from 0.055 MPa to 0.293 MPa at -16°C. The adhesion increased with surface average roughness and compares with values obtained with the SRB tests developed at AMIL [31]. Maximum difference between experimental and numerical results was 9%.

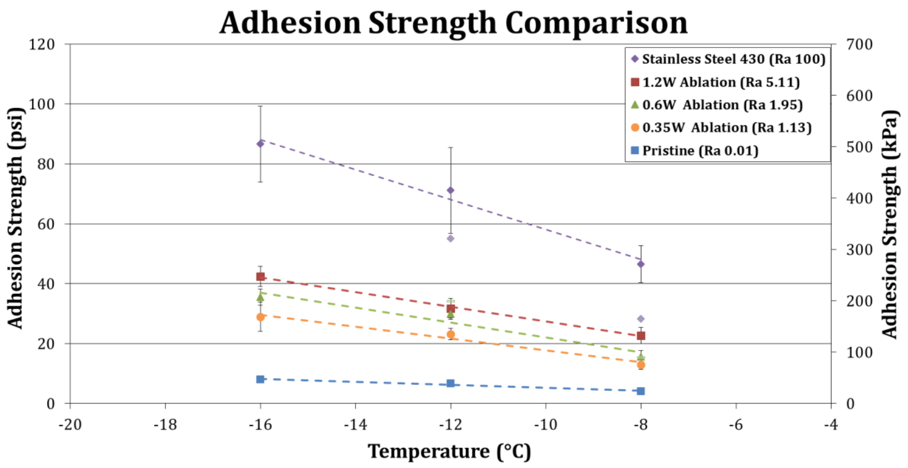

Figure 1.1:15 – Adhesion strength comparison as a function of temperature [34]

1.1.5 FAILURE MODE

1.1.5.1 DUCTILE AND BRITTLE FAILURE

As shown in Section 1.1.3, ice can be ductile or brittle depending of the formation conditions and solicitation. At low rates of deformation there is no crack that forms in the material and its behavior is ductile. At high strain rates, cracks develop in the ice and its behavior is brittle. For intermediate deformation rates, ice is brittle in tension while ductile in compression. The transition between ductile and brittle occurs at higher strain rates in compression because required stress is generated locally through crack sliding while in tension, stress opens cracks directly. Figure 1.1:16 resumes ice behavior for strain rates in tension and compression.

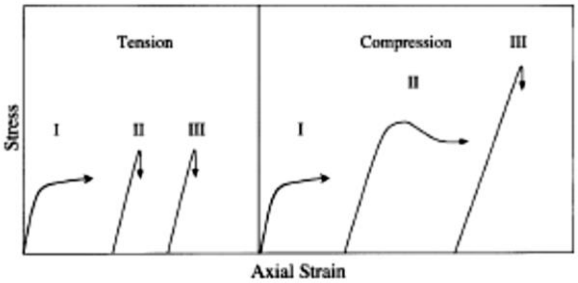

Figure 1.1:16 – Schematic stress-strain curves for ice with horizontal arrows indicating ductile behavior and vertical arrows brittle behavior for low (I), intermediate (II) and high (III) strain rates [8]

In brittle behavior, breaking occurs after lengthening of 0.01 to 0.1%. Nucleation and growth of cracks define tensile behavior, as well as grain size and fracture toughness. With small grain size, cracks are shorter at nucleation than critical size and crack propagation limits the strength and a small amount of ductility (0.1%) is observed. For larger grain size, propagation of cracks happens immediately at nucleation. In compression, sudden collapse of ice happens due to shear faulting of planes inclined at around 30° of the principal stress direction. Shortening in those cases is less than 0.5%. Compressive strength increases significantly with confinement in a Coulombic manner indicating that frictional crack sliding is important. Compressive failure is a multistep process which starts with crack nucleation at grain boundaries. Then crack density increases progressively in the body and finally sudden formation of macroscopic shear faults.

The mechanical resistance of ice σ_f, the Young's modulus E and the volume of ice V are the three factors that impact the energy required to create fracture in brittle regime. This energy is represented by Equation 11. Mechanical resistance of ice is function of temperature and microstructure of the ice, while Young's modulus is dependant of mass density.

$$U_f = \frac{V\sigma_f^2}{2E} \qquad (11)$$

With this equation, Laforte et al. [35] evaluated the energy required to break layers of ice with shocks on cylindrical conductor when adhesion force is not considered. Energy required is higher in compression than in tension and energy increases as temperature decreases. Energy calculated in Joule per kilogram ranged from 0.25 to 7.0, meaning that mechanical breaking requires 70 000 to 1 400 000 times less energy than melting.

1.1.5.2 ADHESIVE AND COHESIVE FAILURE

Two types of rupture can be observed: cohesive, which happen in the ice itself, and adhesive, which happens at the ice/substrate interface. Studies show that tensile efforts tend to create cohesive break, leaving a small layer of ice on the substrate. Shearing, on the other hand, is more inclined to lead to adhesive break with a complete removal of ice from the surface.

Jellinek [36] reported two different experiments on adhesive strength: shear and tensile. For the shear experiments, the adhesive strength increased linearly and rapidly with decreased in temperature. Pure adhesive breaks were obtained down to -13°C. Below this temperature, breaks suddenly changed to cohesive, which were almost independent from temperature. In the tensile experiments, adhesive strength in tension was at minimum 15 times greater than the one under shear experiments. Jellinek [36] explained this phenomenon by the presence of a liquid-like layer at the interface which hold the ice and substrate together by surface tension forces, adding to the overall adhesion strength. The adherence due to a pressure difference across a curved liquid-like layer-air interface can be described with Equation 12.

$$\Delta p = \gamma \left(\frac{1}{r_1} + \frac{1}{r_2}\right) \qquad (12)$$

With Δp the pressure difference, γ the interfacial tension and $r_1$and $r_2$the principal radii. Riahi [37] performed tests on layers of ice accumulated in a cold room at -10°C on aluminum beams. Aluminum beams were then submitted to centric tensile loading, applied at a constant rate. Three different thickness of ice layers were tested: 2 mm, 5 mm and 10 mm. For the 2 mm layer, cracks appeared perpendicular to the beam length, and brittle failure occurred, breaking the ice layer in multiple pieces. With the high strain rate applied of 2x10^{-4} mm/s, this mode of failure was expected. It was concluded that since the layer was thin, the interfacial forces were larger than the cohesive forces of the ice, leading to failure in the ice instead than at the interface. In other words, cohesive failure is more probable than adhesive failure for small thicknesses. For the 5mm thickness both cohesive failure (fracture within ice) and adhesive failure (removal of the ice layer from the surface) were observed. At this thickness a transition is observed between the two failure modes. Finally, at 10 mm, delamination of the ice was obtained without any break within the ice layer itself. Crack propagated at the interface and separation of the two materials occurred.

1.1.6 FRACTURE TOUGHNESS

Fracture toughness is the property of a material containing a crack to resist fracture. It quantifies the material's resistance to brittle fracture when cracking is present. When fracture toughness is high, material will fracture under ductile regime. Linear-elastic fracture toughness is obtained from the stress intensity factor representing the value at which a thin crack begins to grow. Plastic-elastic fracture toughness measures the energy to grow a thin crack. Investigation of ice fracture toughness has been limited. Values in literature range from 50 to 150 kPa $m^{1/2}$. Fracture toughness of ice depends weakly on temperature and loading rate. It is dependant of grain size, decreasing with increasing grain size (Figure 1.1:17).

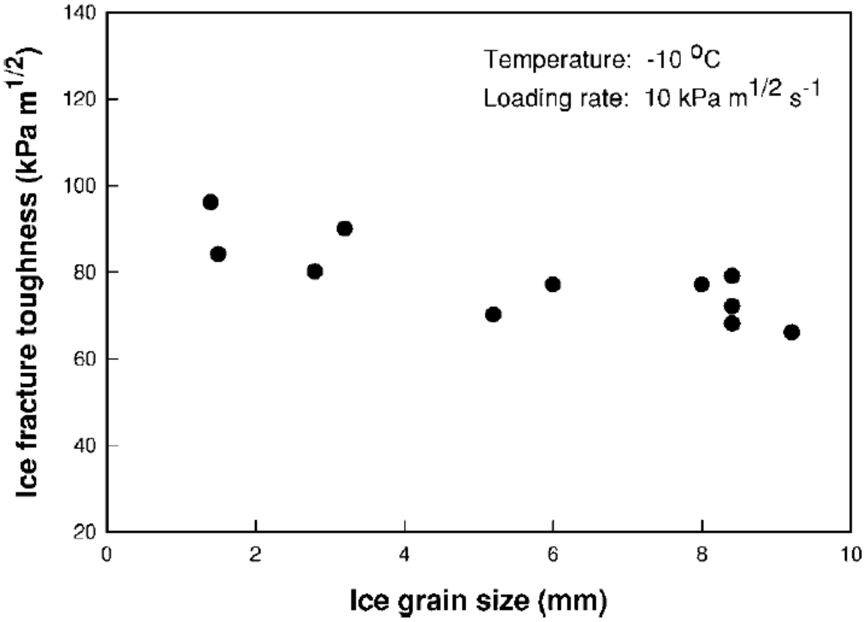

Figure 1.1:17 – Fracture toughness of ice as a function of ice grain size [38]

1.1.7 CREEP

Creep is the permanent deformation of a solid material under mechanical stress. High mechanical stresses, inferior to yield strength of material, are often the cause of creep. Creep, as shown at Figure 1.1:18, is constituted of three phases. In the first phase of creep (A to B), strain rate is high but undergoes a decrease with time. Decrease continues until reaching a constant strain rate and goes through second phase (B to C) where creep is constant. During this phase, the microstructure of the ice does not change and recovery is as important as deformation. Ice strength stays the same during the first two phases of creep phenomenon.

In the last stage, exponential raise of the strain rate happens due principally to necking, resulting in loss of strength and permanent shape changes.

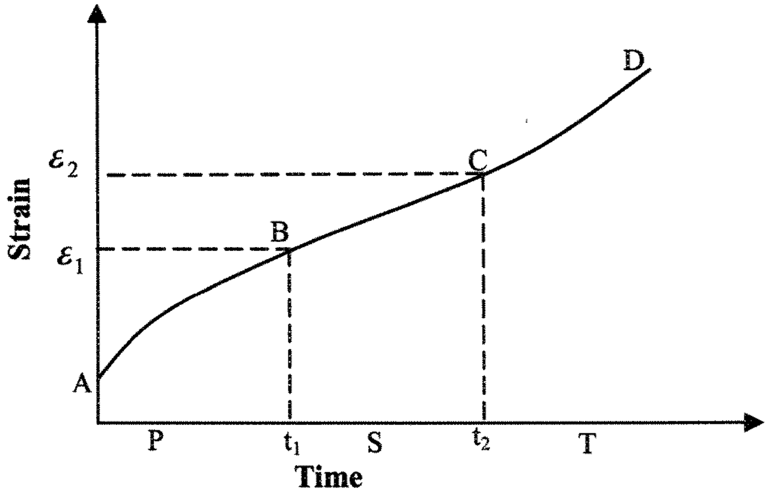

Figure 1.1:18 – Schematic creep curve for polycrystalline ice under constant load [37]

1.2 ICE NUMERICAL MODELING

Riahi [37] performed a comparison between experimental results and a mathematical model developed using the classical linear beam theory and linear description of strain tensor. This theory used the elastic properties of each material to do the computations and used the balance coefficient to model the ice/aluminum beam as a unique material. Results for the normal stress distribution and longitudinal shear stress showed that this theory could not be used to predict correctly the de-icing of the ice from the aluminum beam. The complex distribution of the shear and normal stresses at the interface preclude the utilisation of classical beam theory. Also, apparition of cracks in the ice significantly impacts the stresses distribution preventing the use of simple beam theory or any other theory ignoring presence of cracks. Riahi [37] also investigated a theory using the energy concepts, developed by Griffith [39]. This theory states that fracture is associated with the energy consumption of the system, by balancing the total potential energy of the system with the elastic energy of the uncracked plate, the increase in elastic-surface energy caused by the formation of the crack surface and decrease in the elastic energy caused by introducing the crack in the plate. At high strain rates, like the one generated by a piezo-electric de-icing system, the failure mode of the ice is brittle and deformation mostly elastic for both tension and compression. Due to the bending created by the development of anti-node during vibration excitation, both tensile and compressive strength are expected in the ice layer.

For the tensile strength of ice it was shown that at higher strain rates, limit is around 1 MPa and breaking occurs when lengthening ranges from 0.01-0.1%. [40, 41]. Grain size is another important parameter. The critical grain size corresponds to the point where the stress required to nucleate a crack is the same than the stress required for its propagation. When grain size is higher than the critical grain size, the stress to nucleate a crack is sufficient for its propagation, meaning that the failure is limited by nucleation of cracks. On the other hand, when the grain size is smaller than the critical grain size the failure is governed by crack propagation. Critical grain size is dependent on the strain rate applied, where higher strain rates lead to smaller critical grain size.

Brittle cracking model is designed for situations where tensile cracking is the primary behavior while compressive failure is negligible. In this theory, crack growth is function of energy release rate G and stress intensity factor K_I, related to mode 1. Irwin's formula (Equation 13) defines the relation between energy release rate and stress intensity factor and elastic modulus E [42].

$$G = \frac{K_I^2}{E} \qquad (13)$$

When stress intensity factor reaches fracture toughness, K_{Ic}, crack propagation begins and can be expressed by [43].

$$K_{Ic} = \sqrt{EG_f} \qquad (14)$$

where G_f is fracture energy. Values for K_{Ic} and G_f for ice can be found in literature [44].

Hilleborg and al. [45] showed that fracture mechanics can be used to explain the fundamentals for crack propagation. Development of finite element methods has given the possibility of crack growth analysis for complex cases. Using energy balance approach, they were able to get coherent results for concrete material simulations. In this approach, formation of a unit area of crack surface absorbs a quantity of energy G_c. A crack propagation occurs when energy is released and at least equal to the absorbed energy. They used the FEM to define the energy release rate, allowing them to use a mesh with large element, considerably reducing computation time. In the model proposed, crack propagation occurs when stress at crack tip equals tensile strength f_t. Once a crack opens, stress decreases with increase in crack width w. This continuous decrease in stress is explained by the crack being a microcracked zone with ligaments allowing stress transfer. The energy absorbed during crack opening per unit area can be described by :

$$\int_0^{w_1} \sigma dw \qquad (15)$$

with w_1 being the width where stress has decreased to zero.

Presence of stresses in a small displacement microcracked zone has been demonstrated in tension tests [46]. The curve presented at Figure 1.2:1 was selected to obtain equation 16, so that energy absorbed by unit crack area was equivalent to the one in the energy balance approach.

$$\int_0^{w_1} \sigma dw = G_c \qquad (16)$$

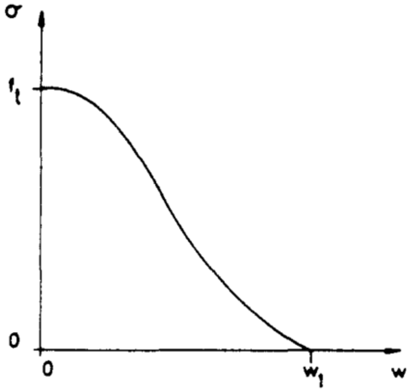

Figure 1.2:1- Assumed variation of stress o with crack width w, general case [47]

A simple mathematical relation, as those presented at Figure 1.2:2, can be used as a simplifying approximation of the curve at Figure 1.2:1. Figure 1.2:2 c) was selected in model [47]. Results obtained from tension test indicates that Figure 1.2:2 c) is the most suitable curve to describe concrete [46]. Also its simple and continuous nature makes it a suitable selection for FEM analysis. Riahi [37] also used this curve for ice material with success, arguing that the microstructure of polycrystalline ice is more uniform than concrete and the curve is unlikely to have an elongated tail, which has been successfully assumed for concrete. By resolving equation 16 with Figure 1.2:2 c), equation 17 is obtained:

$$w_1 = \frac{2G_c}{f_t} \qquad (17)$$

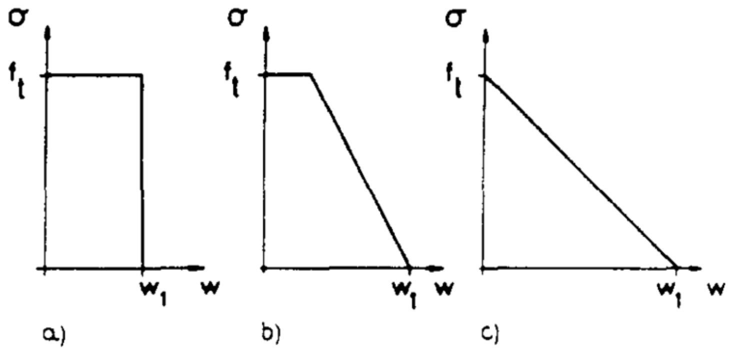

Figure 1.2:2 - Examples of possible assumptions of variation of stress with crack width w in practical applications [47]

ABAQUS brittle cracking model provides a capability for modeling concrete, as well as other brittle materials such as rocks. Riahi [37] used this method to model ice tensile failure with great success. It is designed for simulations where tensile cracking is the dominant behavior, compression is linear elastic and removal of elements based on brittle failure criterion is possible. Discontinuous brittle behavior is modeled by smeared crack modeling. In smeared crack modeling, many small cracks nucleate and linkup in a later stage of loading to form one or more dominant cracks, as compared to discrete crack modeling where the model simulates the initiation and propagation of dominant cracks directly. Presence of cracks is modeled by simulating the way the cracks affect stress and material stiffness at each point.

The model uses orthogonal cracks and limits the maximum number of cracks at a material point by the number of direct stress components: One crack in beam and truss simulations, two in shell and plane stress simulations and three in three-dimensional simulations. When a crack is generated, the component forms of all vector and tensor-valued quantities at that point are rotated to lie in the local system normal to the crack faces, the crack orientation vectors. The crack face normal vectors are kept orthogonal by the model to keep the system rectangular Cartesian.

To detect crack initiation ABAQUS [48] uses a simple Rankine criterion, which is applicable to brittle materials and specifies that failure occurs when maximum principal stress at a point is equal to tensile stress. It does not take into account the effect of the two other principal stresses. This means that detection is based on Mode I fracture considerations. However, cracked behavior following detection is based on Mode I and Mode II. The crack generated once criterion is met is normal to the direction of the maximum tensile principal stress and other cracks can form normal to the maximum tensile principal stress orthogonal to existing cracks at this point.

The model decompose strain rate into elastic and cracking strain rate as expressed by Equation 18, with $d\varepsilon^{el}$ the elastic strain rate in medium between cracks and $d\varepsilon^{ck}$ the cracking strain rate of existing cracks. The medium between cracks is considered isotropic and linear elastic while crack are modeled orthotropic.

$$d\varepsilon = d\varepsilon^{el} + d\varepsilon^{ck} \qquad (18)$$

Hillerborg et al. [47] brittle fracture concept is used as basis for the tension softening model, which correspond to the postcracked behavior in the crack surface's normal direction. In this model, the Mode I fracture energy (G_f^I) (Figure 1.2:3) is a material property defined by the function representing the tensile stress and crack opening displacement:

$$G_f^I = \int \sigma_t^I du_n \qquad (19)$$

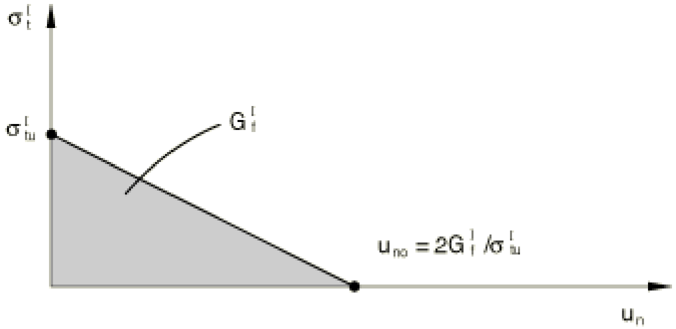

Figure 1.2:3 - Postfailure stress-fracture energy curve [48]

A more comprehensive literature study will be performed on this matter as a next step in the project. This literature study will also include cohesive elements as a tool to model ice/substrate interface and shedding and delamination of the ice.

1.3 ICE PROTECTION SYSTEMS

1.3.1 ELECTROTHERMAL AND OTHER HEAT BASED SYSTEMS

To date, all helicopters equipped with an ice protection system uses electrothermal technologies. This system converts electric energy into heat to protect the blade. For rotorcraft, heating elements are installed behind the erosion strip in the blade. Since ice accumulates solely on the first 15 to 25% of the blade chordwise [49], only this part of the blade is protected by the heated elements. Power is brought to the system via a slip ring installed on the rotor. Such a system can be used for anti-icing or de-icing. In de-icing mode, a small amount of ice is tolerated on the surface. When this amount has been reached, the system starts to operate to melt the ice at the ice/substrate interface. The aerodynamic and/or centrifugal forces are then sufficient to expel the ice layers from the surface and the system is shut down until a new ice layer reaches the maximum allowed thickness on the surface. Most helicopters will allow a maximum thickness of 1.6 mm (1/16'') on their blades. In anti-icing mode, the system is continuously working, preventing any ice from forming. The system can operate at high enough temperatures to evaporate the droplets impacting the surface or at lower temperatures to simply prevent the droplets from freezing. If the water is not evaporated, water can flow further aft of the blades and refreeze, creating runback ice. This ice accumulation can be even more problematic for the aerodynamic of the blades and needs to be taken into heavy considerations when designing and operating such systems [50]. Generally, when a small amount of ice can be tolerated, systems will operate in de-icing mode due to the difference in energy consumption in favor of this regime. Those systems are reliable and durable, but their power consumption is very high, even in de-icing mode. A value of 39 kW/m^2 (25 W/in^2) is usually used as a valid estimation for the power consumption of those systems [51]. This high amount of power is not available on most rotorcraft and necessitates a second electric power system installed on board. This second system adds a lot of weight to the vehicle and takes a lot of the free space inside the cabin making it unpractical for small rotorcraft.

With the apparition of more and more composite structures on aircraft and rotorcraft, alternate ways of melting the ice needed to be found because of the low heat conductivity and risk of overheating the composite materials. Feher and Thumm [52] studied the use of high frequency microwaves to efficiently heat carbon fiber structure. For fiberglass structures, which do not absorb those waves, the microwaves are transmitted out of the structures to the ice. A part of waves are then absorbed by the ice and melting occurs. However, risks to human health and interferences with other instruments prevent this system from being used for small rotorcraft.

1.3.2 WEEPING WINGS SYSTEM

Many other de-icing systems have been developed or investigated as alternative to the electrothermal system. The weeping wings system is a method based upon the freezing point depressant concept [53].

Fluid with low freezing point is pumped to the leading edge of the wings and other critical surfaces of aircraft, depressing the freezing point of the water impacting. This allows the water to flow off without creating ice. The first fluid based system was developed in the 30's during World War II. The system evolved in the early 80's with laser drilled holes in the surfaces, leading to an official US certification in 1987 for several aircraft [51]. For the rotorcraft industry, Bell Helicopter investigated this type of system on UH-1 in the 60's. Experiments showed that for a LWC of 0.8 g/m^3, a standard value for atmospheric icing, the system used 0.41 kg/min of fluid down to -20°C, which was considered effective. Recommendations to work further on this system were made but never followed up [49]. This system prevents any ice from forming without considerably limiting the aerodynamic properties and requiring almost no power. However the added weight for the fluid container as well as the place it requires makes it not practical for small rotorcraft.

1.3.3 PNEUMATIC BOOTS SYSTEM

Pneumatic boots is another proven system for the aircraft industry. An inflatable boot is installed on the wings of the aircraft and when a sufficient amount of ice has accreted on the surface, air is pumped and fills the boot. By inflating, the boot breaks the ice accumulation and is then deflated. The weight added and energy consumed by this system can be considered negligible. However, its application on helicopters is impossible mainly due to the damage sustained by the boots caused by the high erosion affecting the rotating blades. Also, the cyclic nature of the system allows small amounts of residual ice to accumulate, which roughness can cause significant aerodynamic losses [54].

1.3.4 MECHANICAL SYSTEMS

The electro-impulse method, which was first patented in 1937, uses high-voltage capacitors that discharged rapidly. The discharge happens through coils installed inside the leading edge (Figure 1.3:1), which generates an electromagnetic force that breaks ice accumulation. The method was tested on the NASA Twin otter aircraft both in wind tunnel and in-flight [55]. Its drawbacks were found to be electromagnetic interference, structural fatigue and noise. Only one aircraft has been certified with this system, and only for its tail. For rotorcraft application, a 3 kW system of 55 kg would be required to de-ice the main and tail rotor. The low power and weight makes it an interesting solution, however, in addition to the already mentioned drawbacks, the lack of space inside the blades and higher rigidity of the leading edge prevent this system from being used.

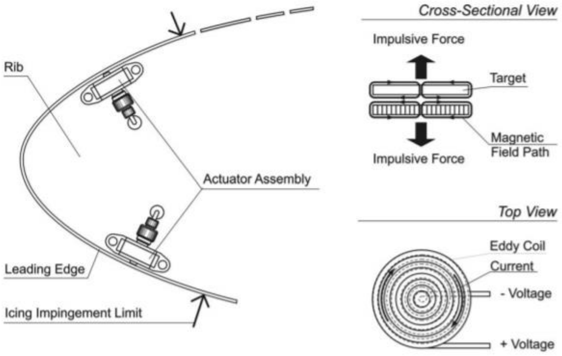

Figure 1.3:1 – Impulsive coil in a leading edge (Eddy current) [51]

Other mechanical systems have been developed or investigated like the Electro-Expulsive Separation System (EESS) and the Electro-Mechanical Expulsion Deicing System (EMEDS). The EESS replicates the pneumatic boot method with conductors. A first layer of conductors is installed in an elastomer material in the airframe surfaces. A second layer is installed on top of the first one closer to the surface (Figure 1.3:2). When current is driven into the conductors of the two layers, the resulting magnetic fields produce repulsive forces that separate the conductors and expulse the ice.

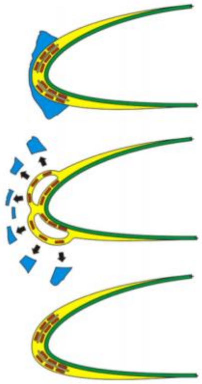

Figure 1.3:2 – Ice shattering using the Electro-Expulsive Separation [51]

The EMEDS is controlled by high current electrical pulse driven to actuators, again to generate electro-magnetic fields, that changes the shape of the actuators at fast pace. The change of shape is transmitted to the surface causing it to vibrate at high frequency and debond the ice [56]. The main drawbacks of those systems is that they are not retrofit and are not applicable to all surfaces, like engine [57].

De-icing by vibration has been studied by Bell in 1978 and financed by the American Army [49]. The entire blades were vibrated at their first modes creating high forces by two eccentric masses in rotation. De-icing was obtained from -15° to -5° by exciting the blades at 45 Hz, with resulting forces as high as 35 G for very short time, less than 2 seconds. De-icing at the tip of the blades was not possible with this method, meaning an alternated de-icing would be required for this part of the blade. Also those very large cyclic loads limited too much the lifespan of the structure.

1.3.5 PIEZOELECTRIC ACTUATOR SYSTEMS

As an alternative to the standard electrothermal de-icing systems or other methods presented previously, the current work investigates the use of piezoelectric actuators as a low-energy de-icing system that could be implemented on small rotorcraft. Piezoelectric actuators are devices that generate strains when subjected to an applied voltage. Different approaches using piezoelectric actuators have been explored in the past. First investigated by Ramanathan [3] and later by Palacios [4], resonating piezoelectric elements were used to generate ultrasonic surface waves to produce shear stress at the ice interface. Ramanthan used an aluminum plate on which a piezoelectric actuator patch was bonded. The actuator was excited with a 1 MHz frequency, the resonant frequency of the actuator, to remove an ice layer accreted a few centimeters ahead of the actuator. Delamination of the ice occurred after more than a hundred seconds and thermal energy released from the actuator played an important role in it.

The method later provided interesting results for flat and shell structures. Venna et al. [5] used piezoelectric actuators located directly below the iced zones of a NACA 0012 leading edge to generate both local shear strains and normal impulse forces to de-ice, however with limited success. Unlike Ramanathan, they used the resonant frequencies of the structure instead of the resonant frequency of the actuator. The leading edge structure was fixed spanwise at its extremities and actuators positioned at the stagnation line. Ice was accumulated in a cold room. Instantaneous de-icing wasn't observed as they forecasted. Instead de-icing was obtained after more than a minute of activation.

Similar to the de-icing mechanism explored by Venna and al., Kandagal and Venkatraman [6] partially succeeded in de-icing a cantilevered flat plate with piezoelectric actuators by exciting its resonant frequencies. Excitation of the fourth mode, at 805 Hz, resulted in instantaneous delamination of the ice at several locations on the plate, without any trace of heating from the actuators. Analysis of the results showed that shear stress generated at the interface seemed to be responsible for breaking the ice adhesion to the substrate.

Palacios [4] studied ultrasonic waves and their dispersion on a flat plate. It was showed that as the excitation frequency approached the resonant frequency of the actuator, the adhesion of the ice diminished and the plate temperature increased. The percentage of adhesion reduction due to the heating of the plate was not determined. He was able to debond an ice layer of 2.54 mm on a steel plate with a disk actuator at 28.5 kHz and 50 W, satisfying results from numerical simulations. He tried designing actuators to excite specific mode at frequencies of 200 and 500 kHz without success. His conclusion was that the frequency should be below 100 kHz since strains generated diminished with a frequency increase.

Zhu et al. [58] followed up on Palacios research by adding discontinuities on the surface of setup similar to what Palacios used. Using the same activation methods for the actuators, they hoped that the high frequency waves would be guided by the discontinuities. Numerical results were in agreement with this, predicting increases in the strain generated by up to 400% for some places on the plate. Experimental results showed diminution of power required to de-ice by more than a factor 2.

Quilan et al. [59] performed experimental testing with a thin curved aluminum surface equipped with piezo-electric actuators applied over a rotor blade shaped section. The rotor blade shaped section was built out of wood and a 2 mm rubber band was installed between the section and the thin curved aluminum surface. A total of seven actuators were bonded to the aluminum surface. Wind tunnel testing showed that the most effective method of deicing was by cascade activation. In cascade activation, two actuators were operated at once, alternating the activated piezo actuators along the span. This lead to the emission of a patent for vibrating sleeves. The small thickness of the sleeve tested and its weak strength makes it impractical for rotorcraft application. No numerical model was done during this study.

1.3.6 MODELLING OF PIEZOELECTRIC DEICING SYSTEMS

In addition to experimental testing, numerical modelling of piezo-electric deicing systems has been investigated by the scientific community. Palacios implemented a 3D finite element model and used it to design the de-icing system experimental setups. With the help of this tool, he was able to investigate in particular the impedance matching for excitation which lead to promising experimental results [60, 61].

Harvey [62] followed by Villeneuve and al. [63] showed a proof of concept for de-icing with actuator patches at resonant frequencies matching the first modes of the structures on which they were bonded. They succeeded total or partial de-icing for flat plate, a thinned Bell 206 main rotor and a Bell 206 tail rotor blade. Numerical simulations were used to predict the resonant frequencies and mode shapes to positioned the actuators and activate them (Figure 1.3:3). The actuators were positioned at anti-node positions and phased properly with the matching anti-nodes. Low power consumption was required for de-icing, as low as less than 1.5 kW/m^2 (1 W/in^2) for the flat plate, and 15.5 kW/m^2 (10 W/in^2) with a suboptimal system for the tail rotor blade.

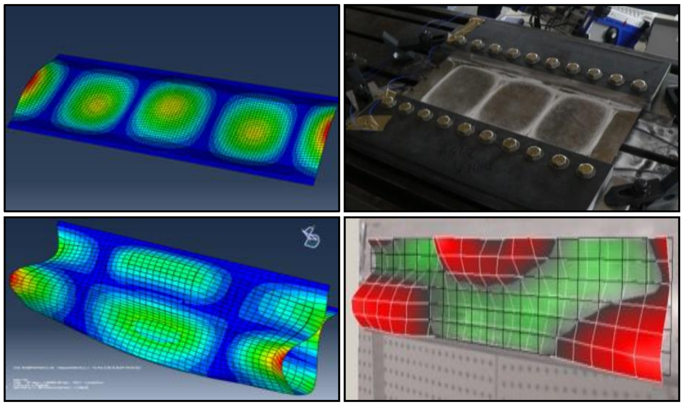

Figure 1.3:3 – Numerical simulations and experimental results of a flat plate (top) and Bell 206 thinned main rotor (bottom) [63]

Boutros [64] proposed de-icing using lightweight Macro Fiber Composite (MFC) actuators on the leading edge of a wing. He developed a numerical model for MFC actuators and validated it experimentally on cantilever beams. He then modeled resonant frequencies of the structure excited by the actuators to predict if the adhesion of ice could be overcome by the shear stress generated. He concluded that by exciting the third mode of the structure with three MFC actuators at optimal positions, he could generate more than sufficient shear stress to debond the ice. He used a fixed value of 1.6 MPa for the adhesion value of ice.

Habibi and al. [65] investigated the use of piezoelectric actuators to excite shear stresses on Carbon-Fibre-Reinfoced Polymer (CFRP) as a de-icing system. They used FEM to study the wave propagation through this material. With the results they established an optimal excitation of the system by comparing the resulting shear stress with the adhesive shear strength of ice. The obtained results will be tested experimentally in a later study.

Budinger and al. [66] started by developing an analytical model for piezoelectric de-icing using ultrasonic frequencies. The model showed that flexural modes generate more shear stress at the ice/substrate interface than extensional modes. It also showed that Langevin type actuators, piston-like, were more suitable than patches mainly due to resistance to mechanical stress and lower energy consumption. Their experimentation validated their model and showed promising results, enough to convince them to pursue their study. They also showed that using this system with the addition of an icephobic coating could significantly reduce the power consumed by the actuators and at the same time lengthen their life duration [67].

Kalkowski [68] used numerical calculations to established to shear stress at the interface generated by piezoelectric actuators and the matching power consumption of the actuators. The calculations were done with a wave model based on the semi-analytical finite element method. With experimental investigation they were able to show that the model predicted reasonably well the power requirements for ice delamination.

Yongjiu [69] performed ANSYS numerical simulations on a wing edge skin model, which revealed the feasibility to remove ice by piezoelectric ceramic actuators. Their experimentation showed that ice can be successfully removed with a voltage of 650 V and a forced frequency of 1530 Hz. This was in agreement with the results obtained with the ANSYS model.

1.4 PIEZOELECTRICITY

The interaction between the mechanical and electrical state in crystalline materials is known as the piezoelectric effect. When a mechanical stress is applied to a piezoelectric material, its asymmetrical structure creates an electrical charge. This is due either to the re-orientation of molecular dipole moments or to the reconfiguration of the dipole-inducing surrounding. If the mechanical force is inverted, the resulting electrical polarization is also inverted and if the force is removed the charge will get null. This is called the direct piezoelectric effect. The piezoelectric phenomena is a reversible process, which means that if an electrical field is applied, the material will be subject to a mechanical force. There are numerous applications to piezoelectricity, which can be classified into three categories: power applications, signal applications and ignition applications. This project is part of the power applications.

Thermal, mechanical and electrical properties of a crystal are defined by physical values such as temperature, stress, strain, electric field and induction. These values can be linked together by different relationship. Stress and strain are linked by the elasticity and electric field and electric induction by permittivity. Electric charges are proportional to stress or strain sustained by the material and the sign of the charges switch with the stress direction (Equation 20).

$$D = d * T \tag{20}$$

with D the electric induction (C/m^2), d the piezoelectric constant and T the stress (Pa). Since the effect is reversible, application of an electric field induce a proportional strain (Equation 21) with the same proportionality as the direct effect.

$$S = d * E \tag{21}$$

with S (Pa) the strain, d the piezoelectric constant and E (V/m) the electric field.

When neglecting temperature and entropy effect, the relationship between the four physical values governing piezoelectricity can be expressed by Figure 1.4:1. This shows that the determination of the strain and electric induction depends on the coupling between the stress and the electric field. Those two values are independent from each other.

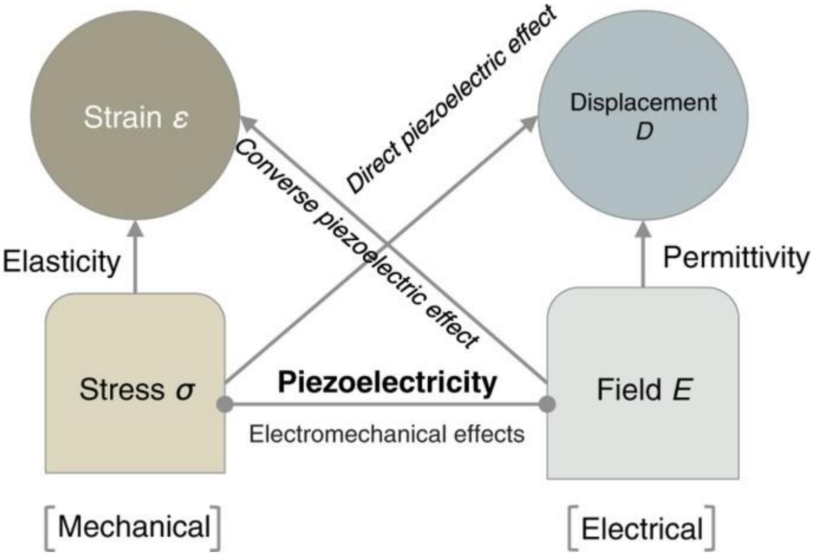

Figure 1.4:1 – Piezoelectricity relationship [70]

Piezoelectricity relationship can be expressed by the tensorial form presented at equation 22 and 23 [70]. In the first equation, the first term correspond to the elastic relationship and the second is the coupling for the direct piezoelectric effect. In the induction equation, the first term is the reverse piezoelectric effect while the second term is the dielectric relationship.

$$S_{ij} = s^{E}_{ijkl} T_{kl} + d_{kij} E_k \tag{22}$$

$$D_i = d_{ikl} T_{kl} + \varepsilon^{T}_{ij} E_j \tag{23}$$

When written under matrix form these equations become:

$$S = s^E T + d^t E \tag{24}$$

$$D = d\,T + \varepsilon^T E \tag{25}$$

with s^E (m^2/N) the constant electric field flexibility matrix, *d* (m/V) the constant stress piezoelectric coefficient and ε^T (F/m) the constant stress permittivity. These equations can be reworked to obtain the equations of stress and become:

$$T = c^E S - e^t E \tag{26}$$

$$D = e\,S + \varepsilon^s E \tag{27}$$

with c^E(N/m^2) the constant electric field stiffness matrix, *e* (N/Vm) the constant strain piezoelectric coefficient and ε^s (F/m) the constant strain permittivity. In the first equation (26), the stiffness matrix correspond to the elastic behavior of the material while the piezoelectric coefficient bring the electric field contribution to the strain. In the second equation (27) the piezoelectric coefficient correspond to the inverse piezoelectric effect and the permittivity to the dielectric behavior of the material.

For ceramic piezoelectric materials, the matrix for the permittivity and stiffness are symmetrical and square and correspond to [8]:

$$\varepsilon^T = \begin{bmatrix} \varepsilon^T_{11} & 0 & 0 \\ 0 & \varepsilon^T_{11} & 0 \\ 0 & 0 & \varepsilon^T_{33} \end{bmatrix} \tag{28}$$

$$\mathrm{c}^E = \begin{bmatrix} c^E_{11} & c^E_{12} & c^E_{13} & 0 & 0 & 0 \\ c^E_{12} & c^E_{11} & c^E_{13} & 0 & 0 & 0 \\ c^E_{13} & c^E_{13} & c^E_{33} & 0 & 0 & 0 \\ 0 & 0 & 0 & c^E_{55} & 0 & 0 \\ 0 & 0 & 0 & 0 & c^E_{55} & 0 \\ 0 & 0 & 0 & 0 & 0 & c^E_{66} \end{bmatrix} \tag{29}$$

The relationship between ε^T and ε^S is described by equation

$$\varepsilon^{s} = \varepsilon^{T} - dc^{E}d^{t} \tag{30}$$

For the constant stress piezoelectric coefficient matrix the matrix correspond to:

$$d = \begin{bmatrix} 0 & 0 & 0 & 0 & d_{15} & 0 \\ 0 & 0 & 0 & d_{15} & 0 & 0 \\ d_{31} & d_{31} & d_{33} & 0 & 0 & 0 \end{bmatrix} \tag{31}$$

The relation between d and e is described by:

$$e_{ij} = d_{ik}c_{kj}^{E} \tag{32}$$

Which results in

$$e_{31} = d_{31}(c_{11}^{E} + c_{12}^{E}) + d_{33}c_{13}^{E} \tag{33}$$

$$e_{33} = 2d_{31}c_{13}^{E} + d_{33}c_{33}^{E} \tag{34}$$

$$e_{15} = d_{15}c_{55}^{E} \tag{35}$$

These values are dependent on the piezoelectric material characteristics and can be obtained experimentally. Piezoelectric actuator manufacturers provides those values which are mandatory for numerical simulations.

ABAQUS [48] uses the e-form constitutive equations presented below (equation 36 and 37) which required the different material properties presented before. They are expressed in terms of the constant strain piezoelectric coefficient. Assumption of linear materials is utilized. With this, it is possible to couple stress and electrical field and to resolve numerical piezoelectric analysis with the finite element method.

$$\sigma_{ij} = D_{ijkl}^{E}\varepsilon_{kl} - e_{mkl}^{\varphi}E_{m} \tag{36}$$

$$q_{i} = D_{im}^{\varphi(\sigma)}g_{mjk}^{\varphi}\sigma_{jk} + D_{ij}^{\varphi(\sigma)}E_{j} \tag{37}$$

1.5 SUMMARY

The literature review has allowed first to confirm the importance of investigating a low power ice protection system for small rotorcraft, which could also apply to other aerial vehicles and that piezoelectric actuator based systems are very much worth considering. They have shown great potential in reducing power consumption, however a lot of information and design criteria are yet to be understood. The review has also provided information on the ice fracture mechanisms susceptible of generating de-icing. Two main mechanisms were found in the different works studied. The first one consist of brittle fracture and crack propagation. At a critical stress, fissure initiation is generated at the top of the ice layer. With additional energy brought to the system, crack propagation will follow through the ice layer down to the substrate, liberating energy throughout the process. This mechanism could be favorably instigated by the different flexural mode of the vibrating flat plate structure. The second mechanism is delamination of the ice layer from the flat plate. The is based on adhesive break generated at the ice/substrate interface. Depending on the conditions of accumulation and ice type, this adhesive break could move towards a cohesive break within the ice layer very close to interface, leaving a thin layer of ice on the substrate. This switch is caused by the change in relative stress limit between adhesive and cohesive bonds, the later becoming lower than the former at a certain temperature and accumulation condition. This means that the protection system must be designed to favor those shedding mechanism. The stresses at the top of the ice layer and at the ice/substrate interface must be maximized during excitation of the structure to reduce power consumption. However only partial information is known on the different stresses to optimize and to the order of magnitude to reach for de-icing. The actuator positioning and excitation are the first parameters to investigate to design an efficient experimental setup susceptible of creating different ice breaking. Then, excitation strategies need to be studied to ensure an optimal mode deployment. Finally, the stresses and their magnitude must be computed to obtain key design criteria for a piezoelectric actuator based de-icing system. The knowledge obtained in this chapter has allowed to strengthen the strategy and methodology defined for the rest of this research project.

Also, the basis for understating piezoelectricity and more precisely how to model it in numerical simulations was detailed. The theory and constitutive equations presented were used to successfully model the piezoelectric actuator patches in the flat plate numerical model used throughout this study as well as in the two blades numerical model presented in Chapter 8. Presentation on how these equations were used to build the numerical models is done at Chapter 3.

CHAPTER 2

NUMERICAL SIMULATION FOR FLAT PLATE EXPERIMENTAL SETUP DESIGN

In this chapter, a numerical model of a flat plate was created with ABAQUS software. This basic model was then used to investigate different design concept for piezoelectric actuator based de-icing system and allowed to optimally integrate the piezoelectric actuator patches to the structure. The basic model will then be used at next section to develop a more complex model including the piezoelectric actuators.

2.1 GEOMETRY

A flat rectangular plate with dimensions of 0.5 m x 0.2 m and 0.0016 m thick was modeled in ABAQUS, as shown in Figure 2.1:1-A. The plate was made of Stainless Steel 304 with a mass density of 8000 kg/m^3, a Young's modulus of 193 GPa and a Poisson's ratio of 0.27. An inherent structural damping coefficient of 0.01 was used as a standard value. This coefficient was readjusted for the assembled system when piezoelectric actuator testing was performed to obtain a more accurate value (see 5.2). As seen on Figure 2.1:1-b, a clamped boundary condition was applied to the longest sides of the plate. This configuration was used to match the experimental setup available for validation.

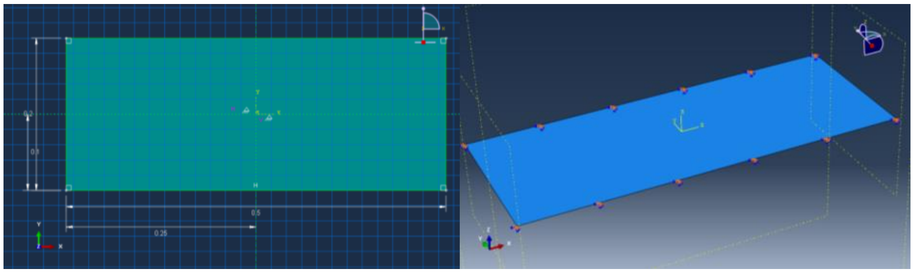

a) b)

Figure 2.1:1 – a) Sketch of the flat plate model b) Flat plate boundary conditions

2.2 MESH

Linear S4R shell elements were used to mesh the plate. A convergence study was performed in order to ensure that the numerical implementation accurately simulated the dynamic behavior of the plate. The convergence study was performed using a Frequency analysis for a frequency range of 1 to 2000 Hz. The panel was meshed with square shell elements with side dimensions of 0.02 m, 0.01 m, 0.005 m, 0.002 m and 0.001 m, resulting in a total of 250, 1000, 4000, 25 000 and 100 000 elements respectively (Figure 2.2:1).

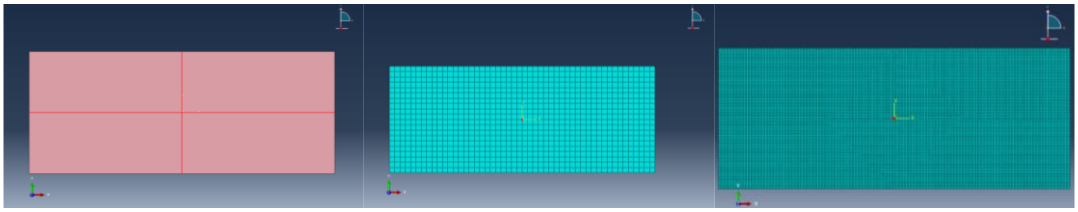

a) b) c)

Figure 2.2:1 a) Partition of the flat plate b) 0.01 m elements mesh c) 0.002 m elements mesh

The results of the frequency analysis were compared for each element size. Thirty-three resonant modes were found between 1 and 2000 Hz. Table 2.2:1 shows for each element sizes, the maximum difference with the results obtained with the most accurate element size (0.001 m). This difference dropped below 2% once the elements were 0.005 m and smaller. Figure 2.2:2 and Figure 2.2:3 show the natural frequency values for the first three modes of vibration and last three respectively, versus the total number of elements in the mesh.

Table 2.2:1 - Maximum difference for each element size for the frequency analysis on the flat plate compared to 0.001 m elements

Element size	**0.02 m**	**0.01 m**	**0.005 m**	**0.002 m**
Maximum difference with 0.001 m	26.4 %	6.4 %	1.6 %	0.2 %

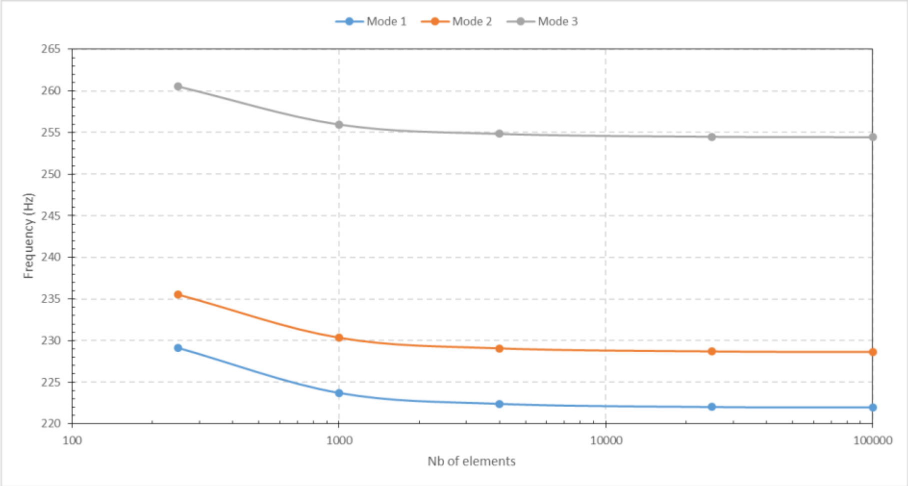

Figure 2.2:2 – Frequency in function of number of elements for Mode 1 to 3 for the flat plate

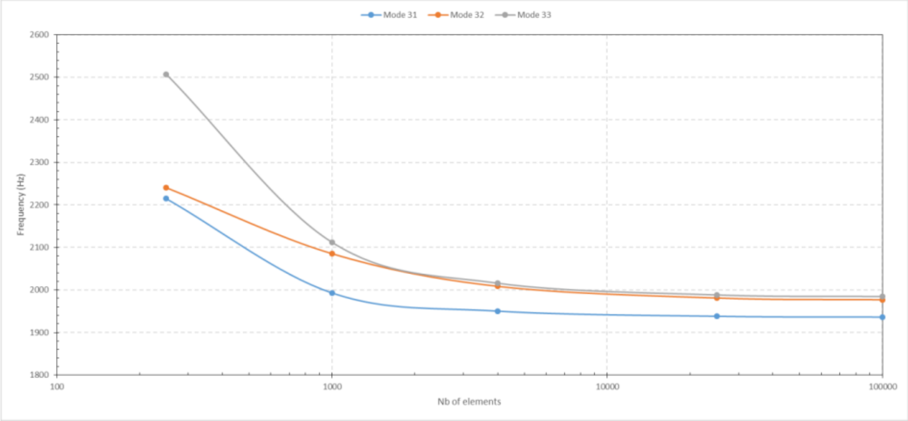

Figure 2.2:3 – Frequency in function of number of elements for Mode 31 to 33 for the flat plate

The results obtained with the modal approach showed that convergence was obtained and that element sizes of 0.005 m 0.002 m and 0.001 m were all acceptable. To save on computation time and resources, an element size of 0.005 m, corresponding to 4000 elements, was selected.

2.3 MODAL FREQUENCY ANALYSIS SIMULATION

Before performing Direct-solution Steady-State Dynamic Analysis a modal frequency analysis was performed to define the resonant frequencies of the structure. The modal frequency analysis consisted in calculating the resonant frequencies of the structure and the associated mode shapes. The frequency range selected was 1 to 5 000 Hz. Eighty-eight modes were found between 1 and 5 000 Hz. Details of the mode shapes for some of the plate resonant modes are shown in Figure 2.3:1 and Figure 2.3:2.

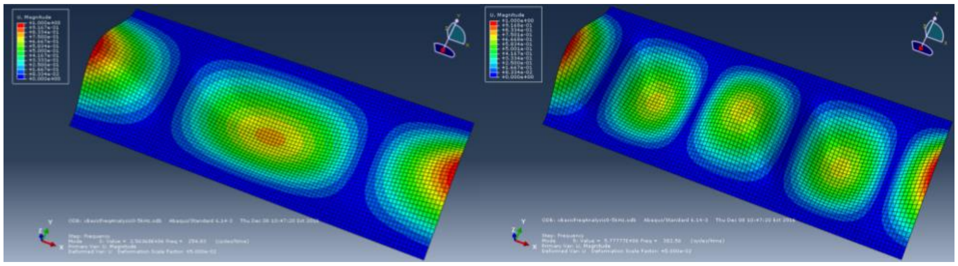

a) b)

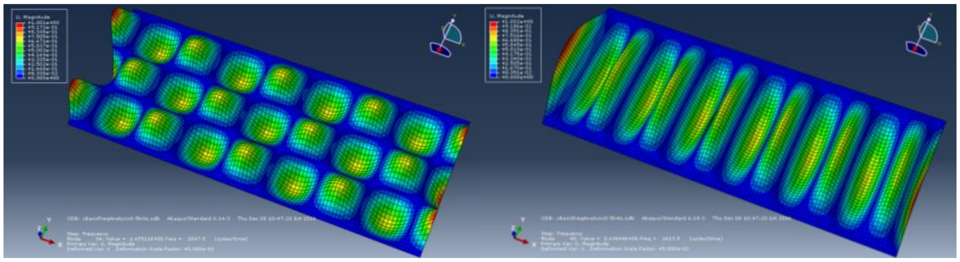

c) d)

Figure 2.3:1 – Resonant mode at A) 255 Hz B) 383 Hz C) 2048 Hz D) 2 614 Hz

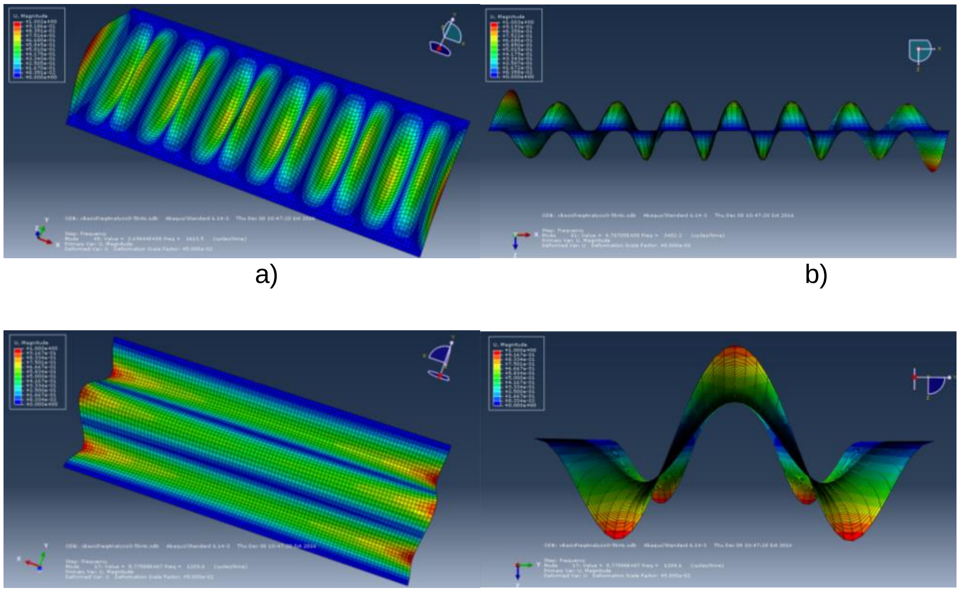

a) b)

c) d)

Figure 2.3:2 – A) Resonant mode at 2 614 Hz B) X-Z plane view of resonant mode at 2 614 Hz C) Resonant mode at 1 210 Hz D) Y-Z plane view of resonant mode at 1 210 Hz

2.4 DIRECT-SOLUTION STEADY-STATE DYNAMIC ANALYSIS

The Direct-solution Steady-State Dynamic Analysis was used to compute the amplitude of displacement and phase of a system in response to harmonic excitations at given frequencies. The numerical simulation analysis was done for one or more loads at a frequency range of interest. In this procedure, the solution of the perturbed system was obtained by linearization from the current base state. The formulation was based on the dynamic virtual work equation shown under its discretized form at Equation 38, with u and its associated derivative the displacement, velocity, and acceleration; and M^{NM} the mass matrix, $C^{NM}_{(m)}$ the mass proportional damping matrix, I^N the internal load vector, and P^N the external load vector. It was assumed that the structure undergoes small harmonic vibration to obtain the steady-state harmonic response and since it was a perturbation procedure, the change from the base state was defined by the step's load and response.

$$\delta u^n\{M^{NM}\ddot{u}^M + C^{NM}_{(m)}\dot{u}^M + I^N - P^N\} = 0 \tag{38}$$

In this step, the structural damping was used, which was defined in the model by Equation 39 with F^N_D the damping forces, *s* the structural damping, and I^N the forces caused by stressing (excitation) of the structure.

$$F^N_D = isI^N \tag{39}$$

The eigenfrequencies found in the modal Frequency Analysis Step were used to subdivide the range of 1 to 5 000 Hz. The bias parameter was set to 1 with a number of points of 5. The number of points defines the number of frequencies that are analyzed from one eigenfrequency to the next one, including the eigenfrequencies themselves. The bias parameter defines the spacing of those frequencies, as shown at Figure 2.4:1. A bias parameter of 1 means an equal spacing between each frequency. Equation for the bias is presented at equation 40. The results at the intermediate frequencies allow to plot the displacement over the whole frequency range of interest.

$$\hat{f}_k = \frac{1}{2}(\hat{f}_1 + \hat{f}_2) + \frac{1}{2}(\hat{f}_1 - \hat{f}_2)|y|^{1/p} sign(y) \tag{40}$$

where:

$$y = -1 + 2(k-1)/(n-1) \tag{41}$$

n is the number of frequency points at which results are to be given, *k* is one such frequency point, $\hat{f}_1$ is the lower limit of the frequency range, $\hat{f}_2$ is the upper limit of the range, $\hat{f}_k$ is the frequency at which the *k*th results are given, *p* is the bias parameter value and $\hat{f}$ is the frequency or the logarithm of the frequency.

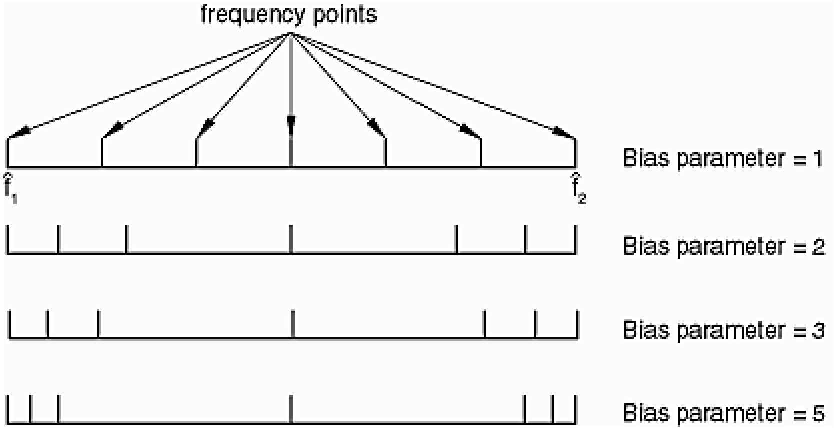

Figure 2.4:1 – Bias parameter example for a number of points of 7 [48]

2.4.1 ANALYSIS FOR EXPERIMENTAL SETUP DESIGN

2.4.1.1 INVESTIGATION OF POSITIONING WITH CONCENTRATED FORCE LOADS

With the frequency response direct steady-state dynamic analysis it is possible to apply different load configurations on the plate. The first step was to define the best actuator positions on the flat plate for the experimental setup. By comparing the results for each configuration, the optimal positioning of the actuators was determined to generate maximum displacements. Useful information was obtained at Chapter 1 on the different ice breaking mechanisms involved. However, there was a lack of information as to which stresses to optimize and the order of magnitude to reach for de-icing. Maximum displacement is investigated for the resonant modes between 0 and 1000 Hz since it is known that ice breaking can be obtained in this frequency range [71]. For a single mode, higher displacement lead to higher values for all the different stresses which means that it is a very good indicator of performances when studying mode individually. Since which mode is more susceptible to generate ice breaking and the level of stresses required are not known, and is in fact one of the object of this study, determining an actuator configuration maximizing displacement of the most modes possible in the frequency range investigate for the experimental setup will significantly increase the chances of successful ice breaking during experimentation, explaining the reason for this maximum displacement criteria used in this chapter.

A load of 1 N, defined as a concentrated force, was applied at the center of the plate in the z-axis direction (Figure 2.4:2). The 1 N value was arbitrary and facilitated comparison for each configuration. Since the direct steady-state dynamic analysis was a linear perturbation procedure, this value had no significance and the results could be extrapolate linearly to any load values. The analysis was run in the same frequency range as the frequency analysis, from 0 to 5 000 Hz, which allowed a quick computation and enough resonant mode to draw general conclusions. The displacement in the z-axis direction is calculated at the center of the plate as a function of the frequency.

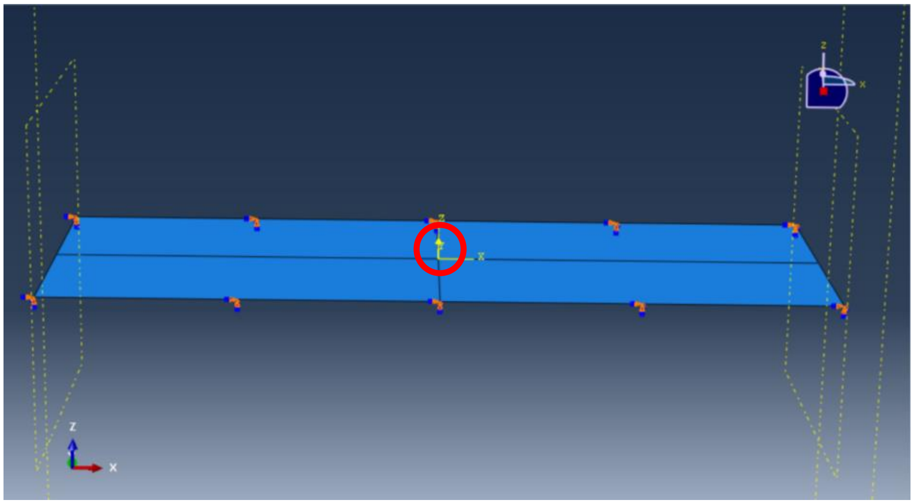

Figure 2.4:2 – 1 N load applied to the center of the flat plate

The frequency response of the plate was calculated at three hundred fifty eight frequencies: the eighty-eight resonant modes found with the modal frequency analysis and the frequencies in-between, defined by the number of points and bias set for the analysis. The displacement at the center of the plate as a function of the frequency is presented in Figure 2.4:3. Figure 2.4:4 shows the displacement at center, computed using the direct steady-state dynamic analysis, as well as the resonant frequencies, computed with the modal frequency analysis, between 0 and 1 000 Hz (Figure 2.4:4-A) and 1 000 Hz to 2 000 Hz (Figure 2.4:4-B). Only twenty-four peaks were observed with the direct steady-state dynamic analysis out of the eighty-eight natural frequencies computed with the frequency analysis.

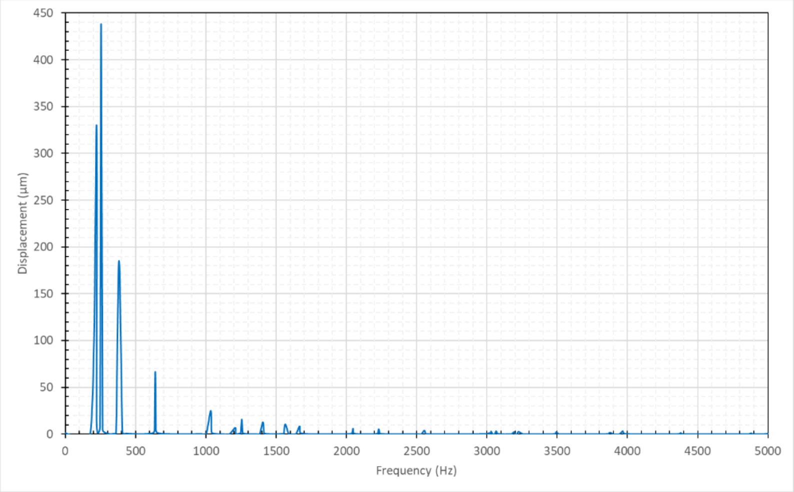

Figure 2.4:3 – Displacement at center in function of the frequency for the flat plate

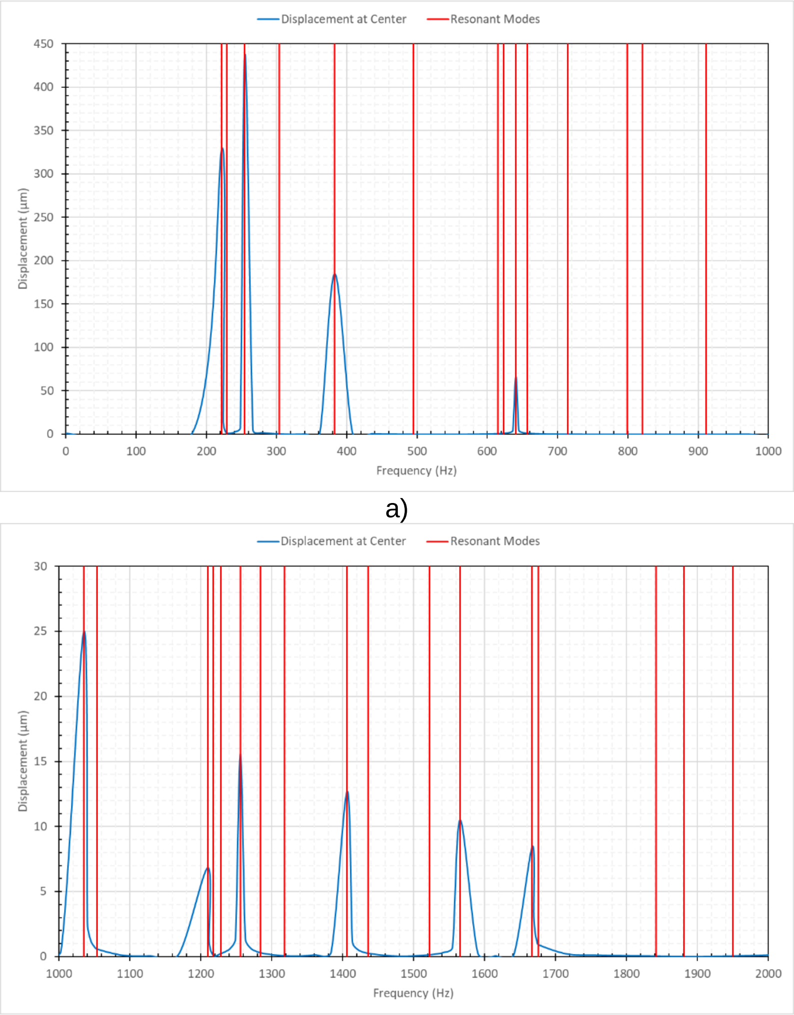

a)

b)

Figure 2.4:4 – Displacement at center and resonant modes in function of frequency for the flat plate between a) 0 and 1 000 Hz b) 1 000 and 2 000 Hz

For all the twenty-four modes observed in the direct steady-state dynamic analysis, an anti-node was located at the center of the plate, where the concentrated force load was applied. Examples of some of those modes are presented in Figure 2.4:5. On the other hand, all modes that did not have an anti-node at the center were not efficiently excited by the 1 N load and therefore resulted in negligible displacements. This explained why no peaks were obtained for these modes at Figure 2.4:4. Examples of some of those modes, and how they were excited by the concentrated force load, are shown in Figure 2.4:6. It could be concluded from this that actuators must be positioned at anti-nodes position in order to be effective.

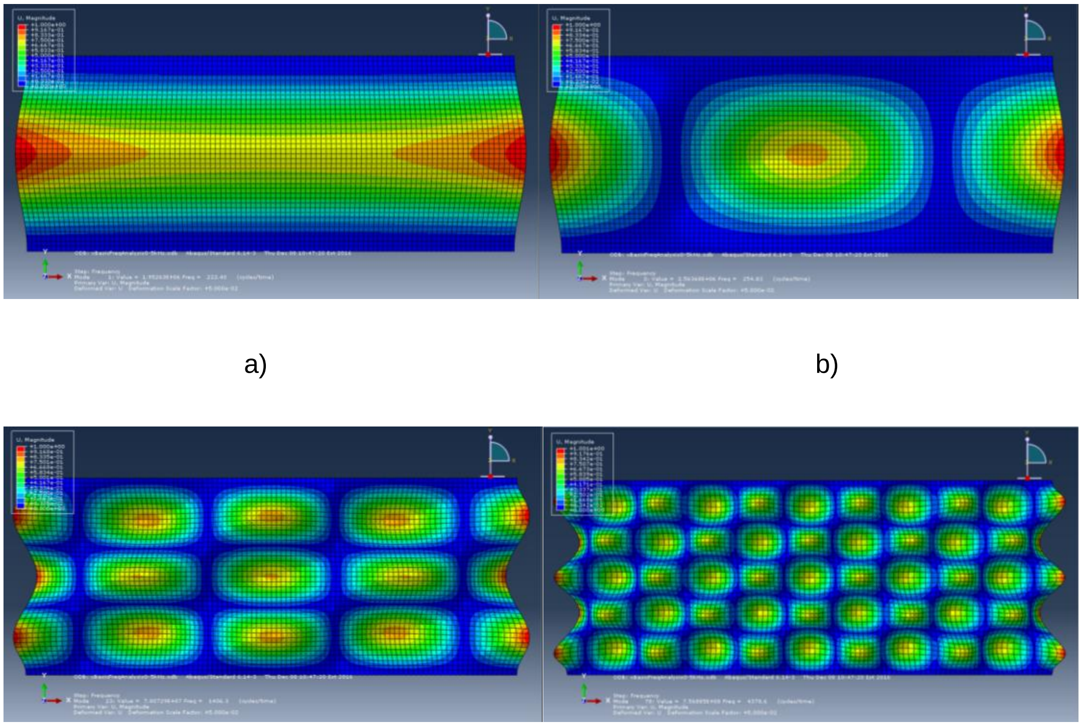

a) b)

c) d)

Figure 2.4:5 - Example of resonant modes excited by the load a) 222.4 Hz b) 254.8 Hz c) 1 406.3 Hz d) 4 378.6 Hz)

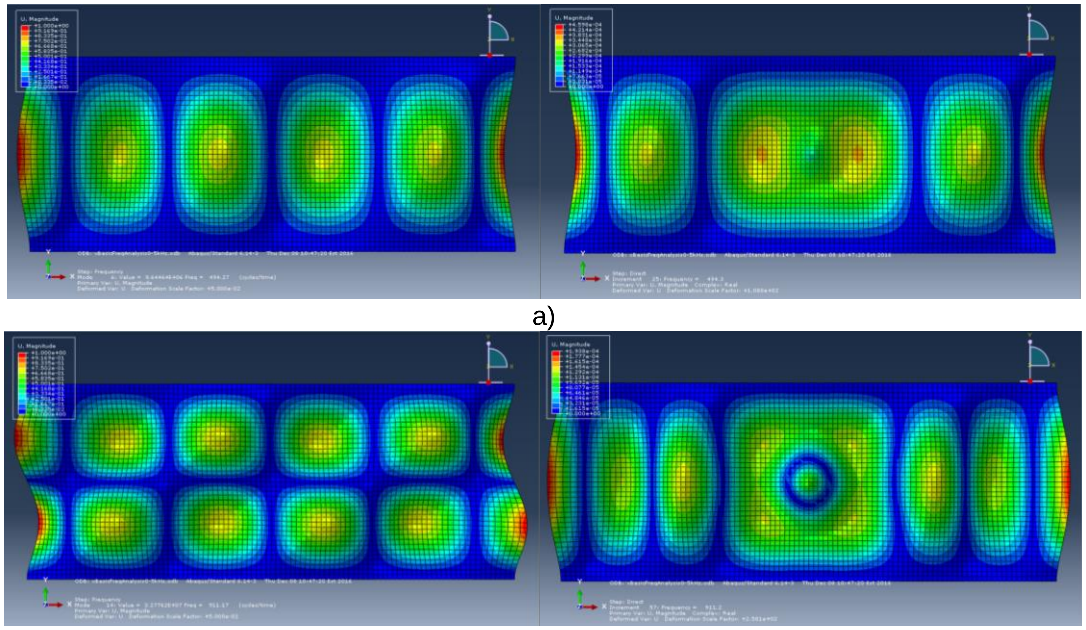

a)

b)

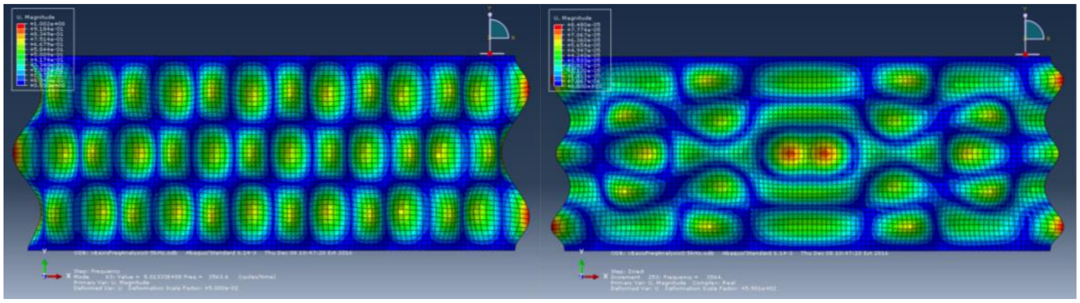

c)

Figure 2.4:6 – Example of resonant mode obtained with frequency analysis (left) and matching result for the direct steady-state dynamic analysis (right) at a) 494.3 Hz b) 911.2 Hz and c) 3 564 Hz

The 1 N load was applied on three different nodes (Figure 2.4:7) positioned on the anti-node of Mode 3 (254.8 Hz) and the displacements were computed for each load position. The first node (Node 167) was set at the edge of the anti-node, the second (Node 154) at around one third of the center of the anti-node and the last one (Node 1) at the center of the anti-node. All three nodes were at the middle of the width of the plate and consequently the middle of the width of the anti-node. Figure 2.4:8 presents the displacements of the three nodes for each of the three load positions. As the load was set closer to the center of the anti-node, computed displacements increased for each node, meaning that the center of the anti-nodes was the optimal positioning for the actuators. This was also where the maximal displacements occurred for each load positioning.

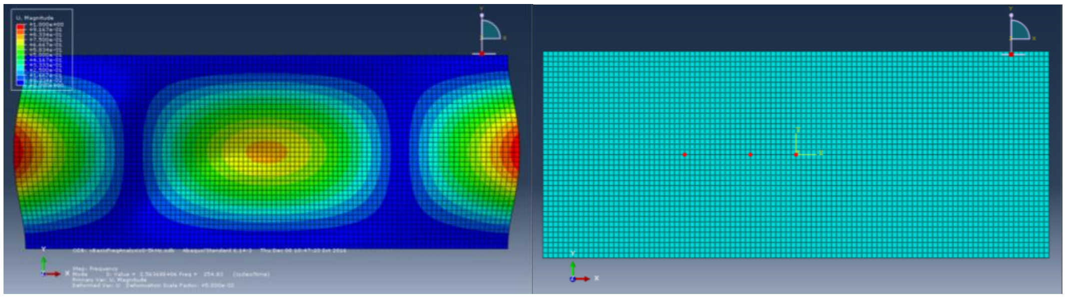

a) b)

Figure 2.4:7 – Mode 3 (a) and selected nodes for load application (b)

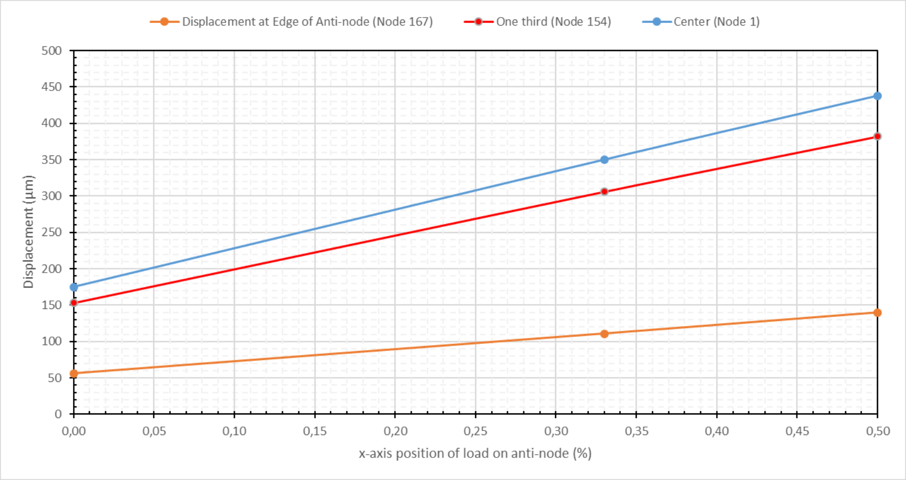

Figure 2.4:8 – Displacements for Mode 3 (254.8 Hz) in function of load position on anti-node (x-axis)

Three force load configurations were considered for a frequency of excitation of 640 Hz (Mode 9, Figure 2.4:9) under a direct-solution steady-state dynamic analysis. First, a 1 N load was applied at the center of the plate, coinciding with the center of the third anti-node. Second, a 1 N load was applied at the center of the first anti-node from the left. Third, three 0.33 N load were applied at the center of the first, third and fifth anti-nodes. Table 2.4:1 presents the displacements at anti-node 1, 3 and 5 for the three load configurations. The computed displacement for the three configurations was 66 µm ± 2%, which means the loads can be applied at the center of any anti-nodes or even split between the anti-nodes to obtain the same displacement response. This provides a great freedom when selecting the number and positions of the piezo-electric actuators. Minimum amount of actuators is ideal to reduce the cost, complexity and architecture of the system. However, more actuators allow less power to be applied for each actuator to prevent local structural damaging and excitation of the actuators out of their power and stress range. The results of these simulations show that optimal actuator positioning is at the center of the anti-nodes of the targeted mode and that the number of actuators can be divided between the different anti-nodes to reduce the burden on each actuator for the same result as fewer actuators with higher power applied, but increasing the complexity of the system.

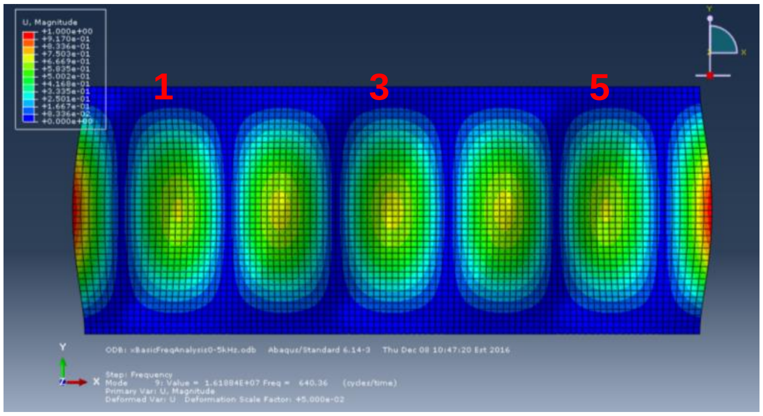

Figure 2.4:9 – Mode 9 (640.4 Hz)

Table 2.4:1 - Displacement for three load position configurations at 640 Hz (Mode 9)

Mode 9	**Displacement at center of Anti-node 1 (µm)**	**Displacement at center of Anti-node 3 (µm)**	**Displacement at center of Anti-node 5 (µm)**
1 N Load at center	67	67	67
1 N Load at anti-node 1	65	65	65
0.33 N Loads at anti-node 1,3 and 5	66	66	66

2.4.1.2 INVESTIGATION OF PHASING WITH CONCENTRATED FORCE LOADS

As it can be observed on Figure 2.3:1 and Figure 2.3:2, each antinode was out of phase with its neighboring antinodes, forming a sine wave in both dimensions of the plate. To evaluate the impact of load phasing on vibration, two load configurations were applied under a direct-solution steady-state dynamic numerical simulation analysis at 640 Hz (Mode 9, Figure 2.4:9). First, a load of 0.2 N was applied at the center of each anti-node, for a total of 1 N (Figure 2.4:10, right). The second configuration consisted of loads of 0.2 N applied at the center of anti-nodes 1, 3 and 5 and loads of -0.2 N applied at the center of anti-nodes 2 and 4 (Figure 2.4:10, left), so that each successive load was out of phase compared to the ones next to it. Table 2.4:2 presents the displacements at the center of the anti-nodes for the two configurations. When the loads were applied in opposition of phase, the computed displacements were similar to the three configurations presented in the previous section, which was expected since the same total force load was applied (Table 2.4:1). However, when all the force loads were in the same direction, the computed displacements were decreased by a factor of 5.5, meaning that some forces were acting against the optimal deployment of the mode.

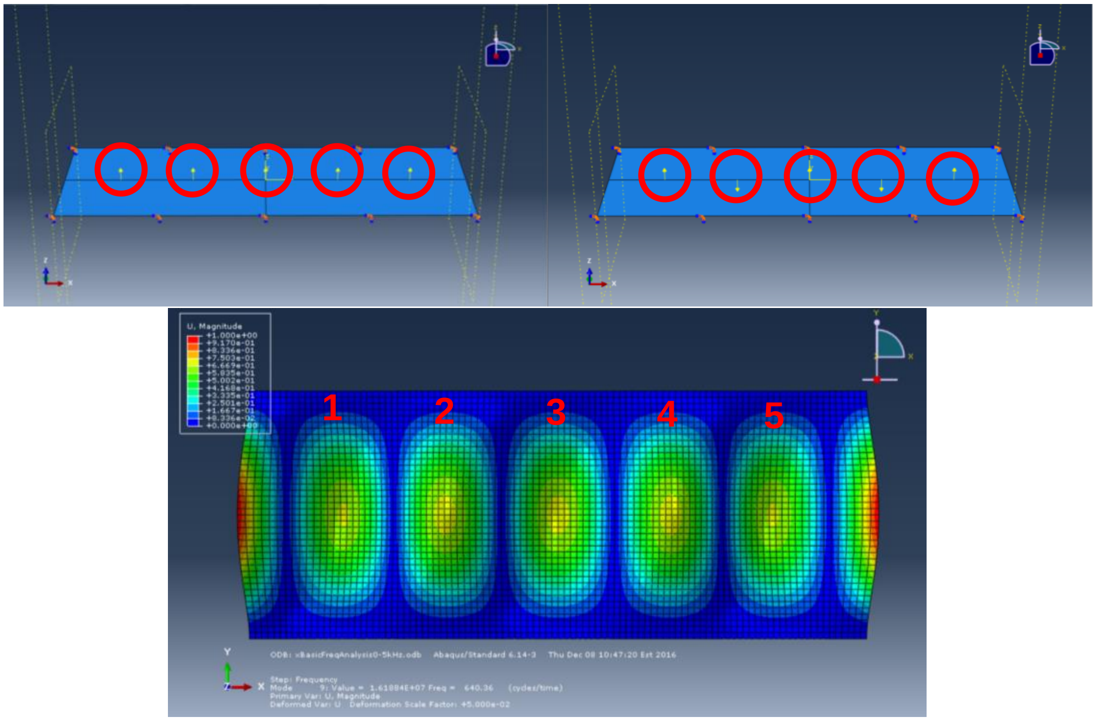

Figure 2.4:10 – Load application for load phasing simulations at 640 Hz (Mode 9)

Table 2.4:2 - Displacement for two load phasing configurations at 640 Hz (Mode 9)

Mode 9	Displacement at center of Anti-node 1 (µm)	Displacement at center of Anti-node 2 (µm)	Displacement at center of Anti-node 3 (µm)	Displacement at center of Anti-node 4 (µm)	Displacement at center of Anti-node 5 (µm)
0.2 N Load (In phase)	12	12	12	12	12
0.2 N and -0.2N Load (out of phase)	66	66	66	66	66

The same procedure was repeated for mode 10, at 657 Hz. A first simulation, with 0.5 N loads applied at the center of the top and bottom anti-nodes (Figure 2.4:11-A), and a second one, with a 0.5 N load applied at the center of the top anti-nodes and a -0.5 N load applied at the center of the bottom anti-node (Figure 2.4:11-B), were performed. Figure 2.4:12-A shows that mode 10 was excited with displacements of the same order of magnitude than the previous mode, with a maximum displacement of 73 µm at both anti-nodes, when the loads were out of phase. However, applying the force loads in phase failed to excite the mode efficiently. Mode 10 instead resulted in a low displacement response with a maximum of 1.2 µm, and deployed like a weak mode 9, instead of a mode 10 configuration (Figure 2.4:12-B).

It could be concluded that the force loading had to be applied in phase with the anti-node in order to ensure maximum displacements by exciting the mode efficiently. A load applied with the wrong phasing hindered optimal deployment of the mode and greatly reduced the displacement response of the vibrating structure.

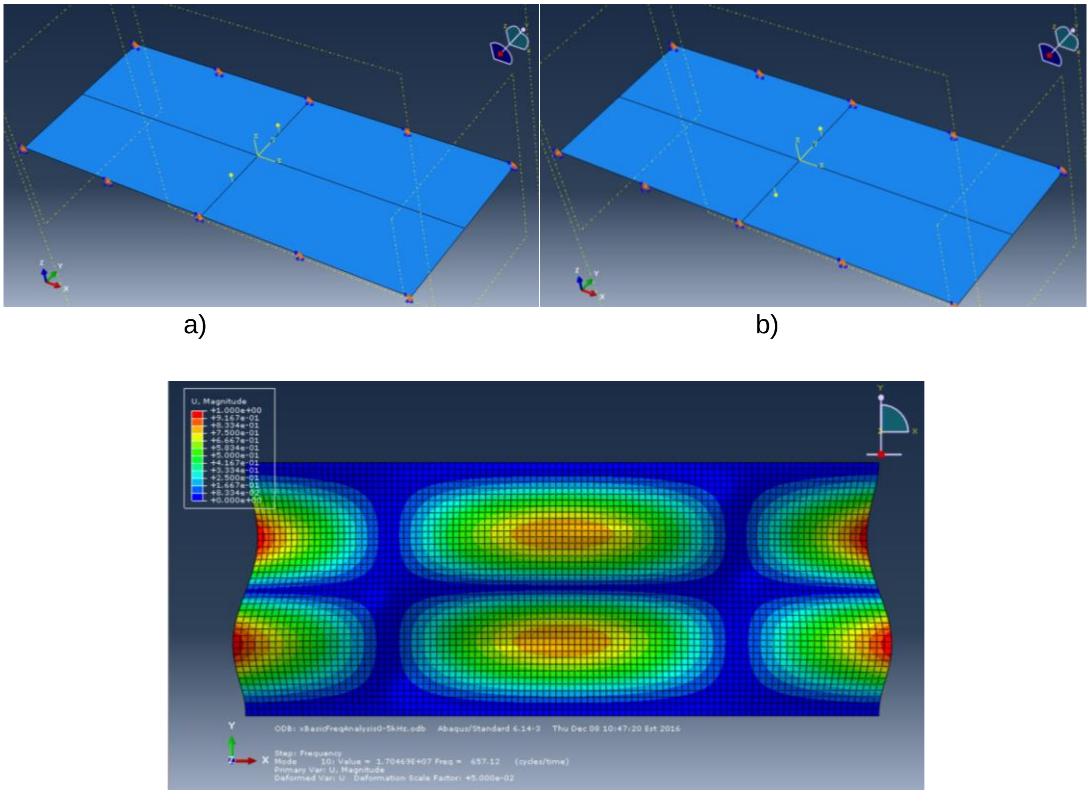
a) b)

c)

Figure 2.4:11 - Load application for load phasing simulations at 657 Hz (Mode 10)

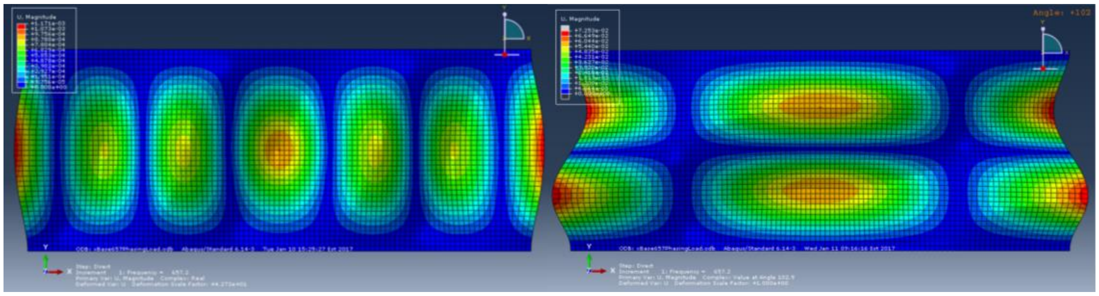

Figure 2.4:12 – Results of Mode 10 (657 Hz) excitation with direct-solution steady-state dynamic analysis A) phased loads B) counter phased loads

2.4.1.3 ACTUATOR POSITIONING FOR EXPERIMENTAL SETUP

Five Physic Instrumente P-876.A15 patches actuator were available at the laboratory. To define optimal actuator positioning for the actuators, a direct-solution steady-state dynamic numerical simulation analysis was performed from 0 to 25 000 Hz with a 1 N concentrated force applied at the center of the plate. Displacement at the center of the plate is presented at Figure 2.4:13. Displacement amplitudes diminished as frequency increases with modes resulting in the largest displacement being below 3 000 Hz. As the frequency increases, the power consumption of the actuators to activate the structure increases as well (see 8.2.6.3). For this reason, the first 15 modes were selected to define actuator positioning.

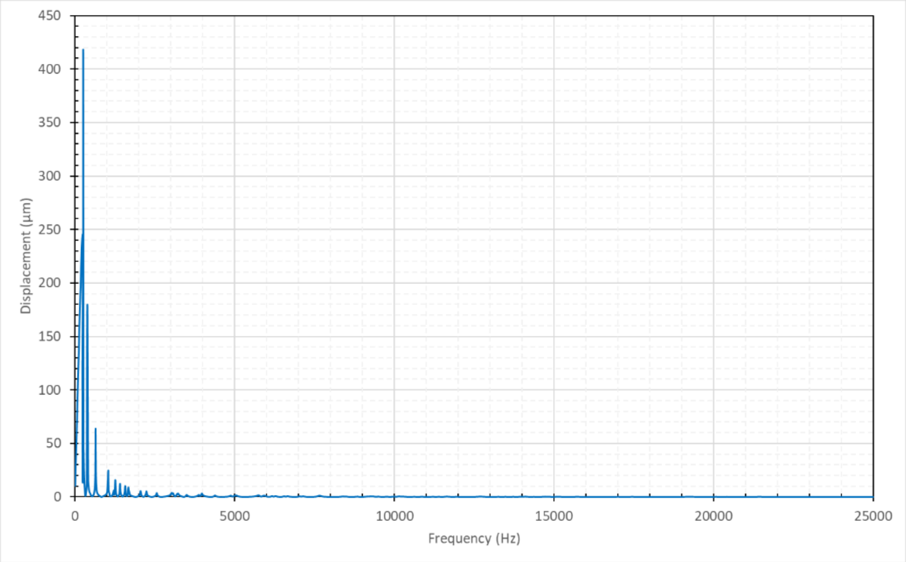

Figure 2.4:13 – Displacements at center of plate from 0 to 25 000 Hz with 1 N load applied at center of plate

Results from previous sections showed that optimal position for actuators was at center of anti-nodes. By looking at some of the first modes (Figure 2.4:14), it was possible to observe that positions for center of anti-nodes change between each mode.

Since most of the first 15 modes (9 out of 15) had only one line of anti-nodes, majority of center of anti-nodes positions were at the center of the plate in the width direction. Also, during de-icing tests, an ice layer was accumulated at mid-width on the plate, meaning that maximum displacements at that position were desired for optimal de-icing. The first decision was thus to place the actuators at the center of the plate in the width direction. By positioning the actuators there, deployment of modes with anti-nodes located under the ice layer were optimized. Higher displacements at that position show increase of the different stresses in the ice layer and ice/substrate interface (see section 8.2.2 for more information) which is what is required from the information gathered at Chapter 1.

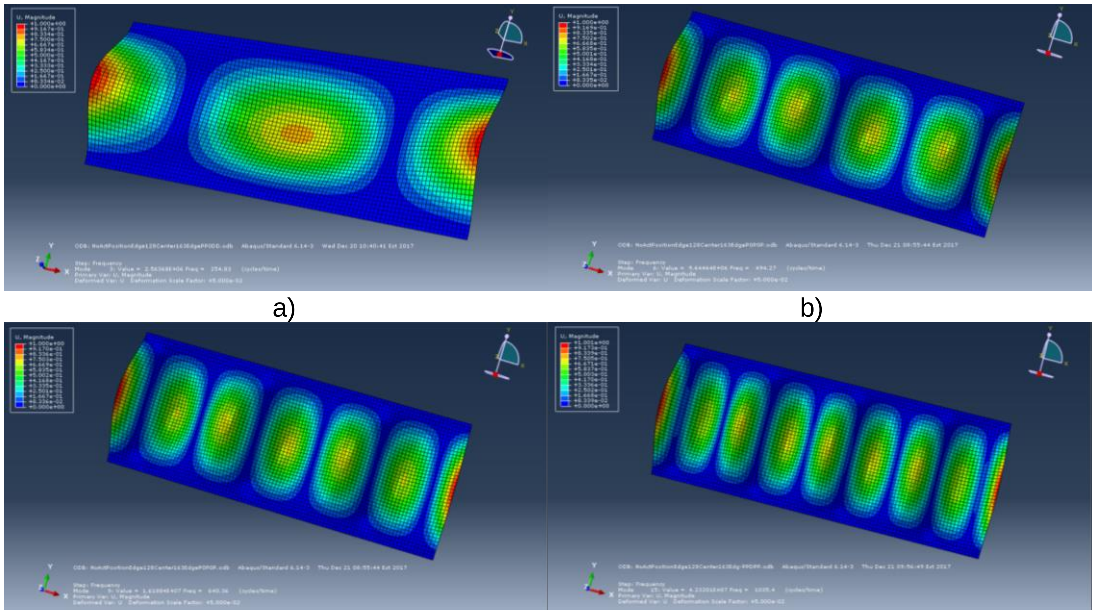

a) b)

c) d)

Figure 2.4:14 – Mode 3 (a), Mode 6 (b), Mode 9 (c) and Mode 15 (d)

To position the actuators lengthwise, positions of anti-nodes in the length direction were studied for the 9 modes of interest. The 6 modes with two lines of anti-nodes were neglected for the reasons explained at previous paragraph. Each of the 9 modes had a half anti-node located on each extremities of the plate, which was judged ideal to help in the activation of all the mode.

Every mode with an odd number of anti-nodes had an anti-node located at the center of the plate, meaning that an actuator placed there should contribute to the deployment of half of the modes.

By observing anti-nodes center on the plate for the various modes, it could be found that six nodes from the mesh have anti-nodes center for two different modes: Node 108 (60 mm from edge), Node 119 (115 mm from edge), Node 128 (160 mm from edge), Node 163 (160 mm from second edge), Node 172 (115 mm from second edge) and Node 183 (60 mm from second edge). Due to the symmetry, or anti-symmetry if there was an even number of anti-nodes, in this direction, each node from one side of the plate corresponded to a node on the other side. To define the best configuration for the actuators, direct-solution steady-state dynamic numerical simulation analysis were performed for the 9 modes considered, with the forces positioned at the settings described at Table 2.4:3. The 1 N force was divided by the number of loads for a force of 0.2 N at each position. The first 3 settings corresponded to both edges and center which were the positions with the more anti-nodes, matched with a pair of nodes that were symmetrically equivalent to each excite a different mode. The fourth setting replaced Nodes 108 and 183 with nodes 109 and 182. The fifth setting puts an asymmetrical loading to see if this could have lead to an optimization of more of the modes investigated.

Table 2.4:3 – Setting number for Node configuration of force position

Setting (#)	**Node (#)**
1	Edge1, 128, Center, 163, Edge2
2	Edge1, 119, Center, 172, Edge2
3	Edge1, 108, Center, 183, Edge2
4	Edge1, 109, Center, 182, Edge2
5	Edge1, 109, Center, 172 Edge2

Results from section 2.4.1.2 (Load Phasing) showed that phasing of the forces are key for mode deployment. For each force settings, different phasing were tested (Figure 2.4:15) to get optimal deployment for each of the mode investigated. The displacement at the edge, at one quarter and at the center of the plate were output. The results for setting #1 with the optimal phasing for each mode is plotted in function of the mode number for those three positions (Figure 2.4:16). The comparison between the five settings was limited to the first five modes to simplify analysis since no configuration can optimally satisfy all the modes between 0 and 1000 Hz.

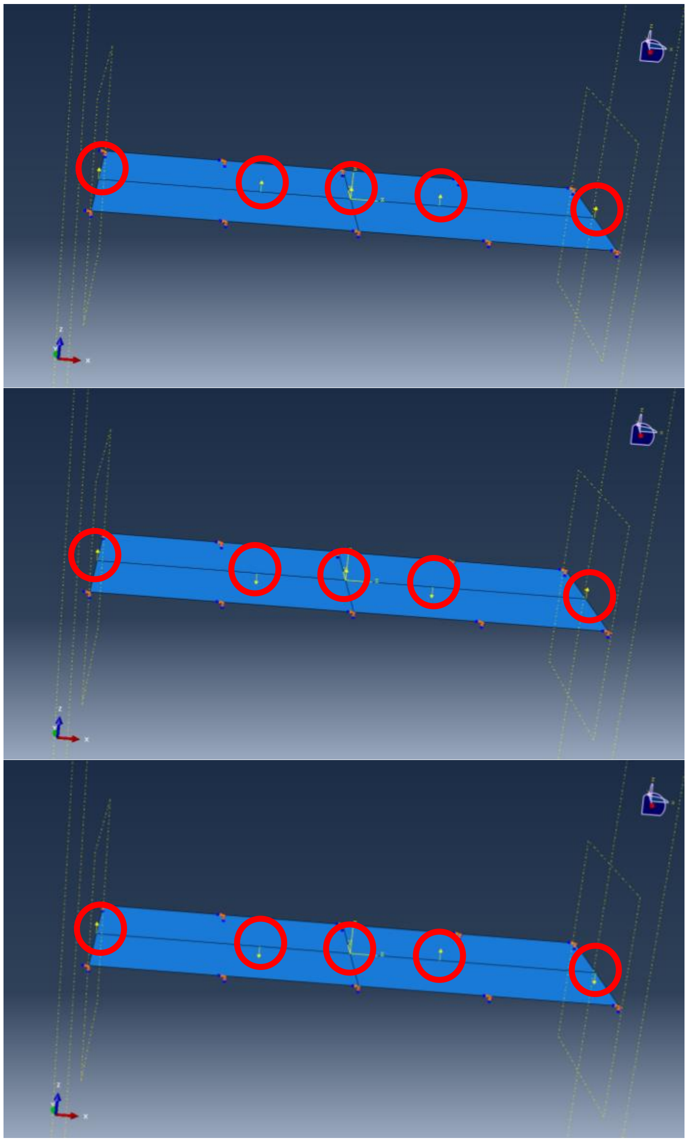

Figure 2.4:15 – Load position setting #1 with different phasing configuration (arrow directions)

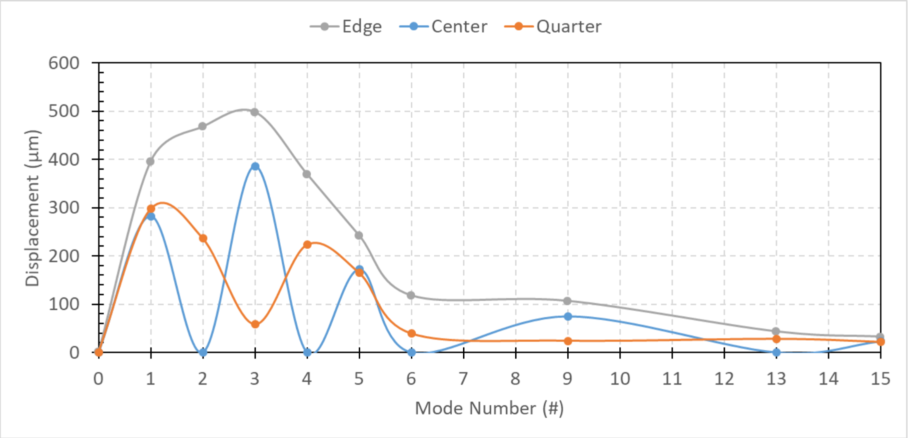

Figure 2.4:16 – Displacement for Setting #1 for 15 first modes

Maximum displacements obtained for each setting at the edge, one quarter and center of the plate are presented at Figure 2.4:17-A, B and C respectively. Setting #3 and setting #4 gave very similar results due to the close proximity of the forces. Setting #3 gave very slightly higher displacements in most of the modes so setting #4 was no longer considered. Setting #2 resulted in maximum displacement for none of the modes beside mode #5, which was the mode resulting in the smallest displacements. The results obtained with setting #5 were in the middle of the settings for all the mode. This setting did not give the highest displacements for any mode but was not the worst for any mode either. Setting #1 and #3 resulted in the highest displacements for three out of the five modes. Setting #1 created displacements 1.51 times and 1.11 greater than setting #3 for mode 4 and 5 respectively, while setting #3 created displacements 1.26 higher than setting #1 for mode 2. For these reasons, setting #1 was selected for actuator positioning (Figure 2.4:15).

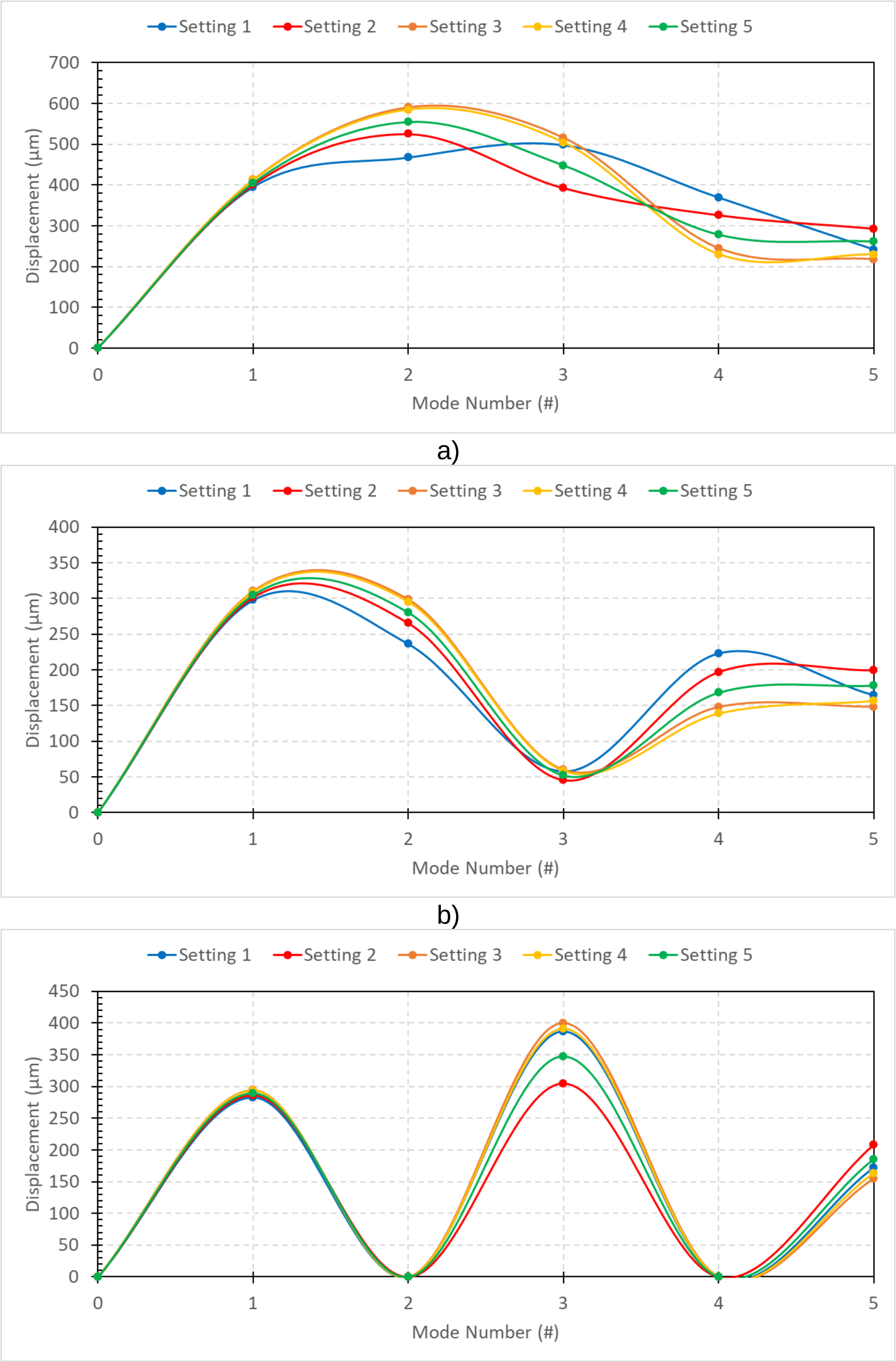

a)

b)

c)

Figure 2.4:17 – Maximum displacements for each force settings at a) Edge, b) One Quarter and c) Center of the plate

For the Physic Instrumente P-876.A15 patches actuator, the direction of the actuators needed to be defined as well as the position of the center of the actuator. To determine the optimal directions of the actuator, a solid deformable 3D part was created in ABAQUS to model the P-876.A15 patches. A solid homogenous section was assigned to the part with a custom material that represented the actuators. A pressure force was applied to both width face of the actuator. A total force of 1 N was equally distributed on the surfaces (Figure 2.4:18).

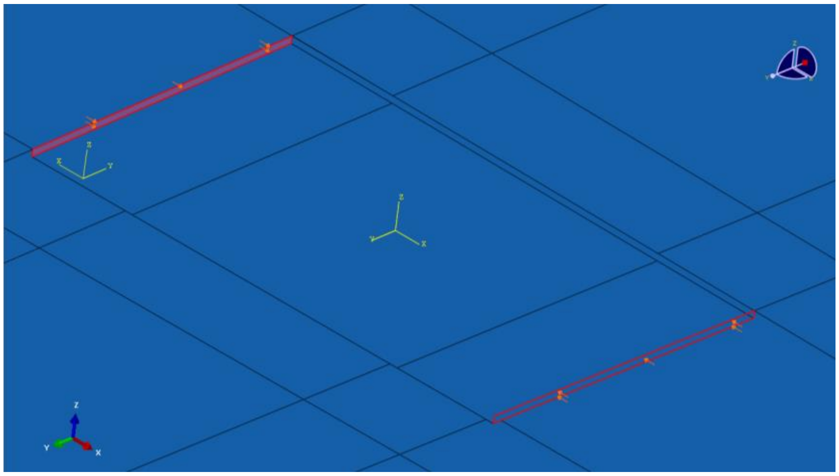

Figure 2.4:18 – Pressure load applied on actuator.

Direct-solution steady-state dynamic numerical simulations were performed with one patch placed at one of the edge of the plate, first positioned in the width direction then in the length direction. These simulations were repeated with the actuator positioned at the center of the plate instead of the edge (Figure 2.4:19). The results showed that the optimal direction of the actuator patch differed from a mode to another (Figure 2.4:20). Also, optimal direction was the same whether the patch was positioned at the edge or at the center of the plate. By observing the mode shape, it was possible to conclude that the optimal direction was when the longest dimension of the actuator was parallel to the shortest dimension of the anti-node (Figure 2.4:21). This meant that the optimal direction of all actuator patches was the same for a chosen mode since all the anti-nodes for a single mode have the same size besides the half anti-nodes on the edges of the plate.

Direct-solution steady-state dynamic numerical simulations were performed at the five first modes with five patch actuators positioned at the optimal position determined above (Setting #1). In these simulations, all actuators were in the same direction, either in the width or the length direction. For each mode, 0.2 N forces were distributed on the width surfaces of the five actuators as in Figure 2.4:18. The phasing of the forces applied on the actuators was set optimally for each mode as defined previously when deciding ideal positions of the actuators (Figure 2.4:15). Figure 2.4:22 presents the displacements for the first five mode when actuators were all placed in the width direction and when all place in the length direction with optimal phasing of the forces applied on each actuators. The results showed that the best direction for the patch actuators to maximize displacements generated at those resonant modes was when the actuators were in the width direction (Figure 2.4:19-a).

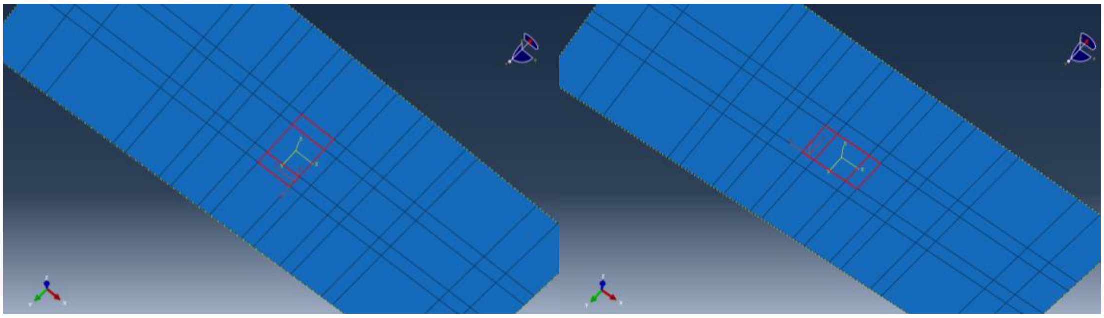
a) b)

Figure 2.4:19 – Patch Actuator positioned at center in the width direction (a) and length direction (b)

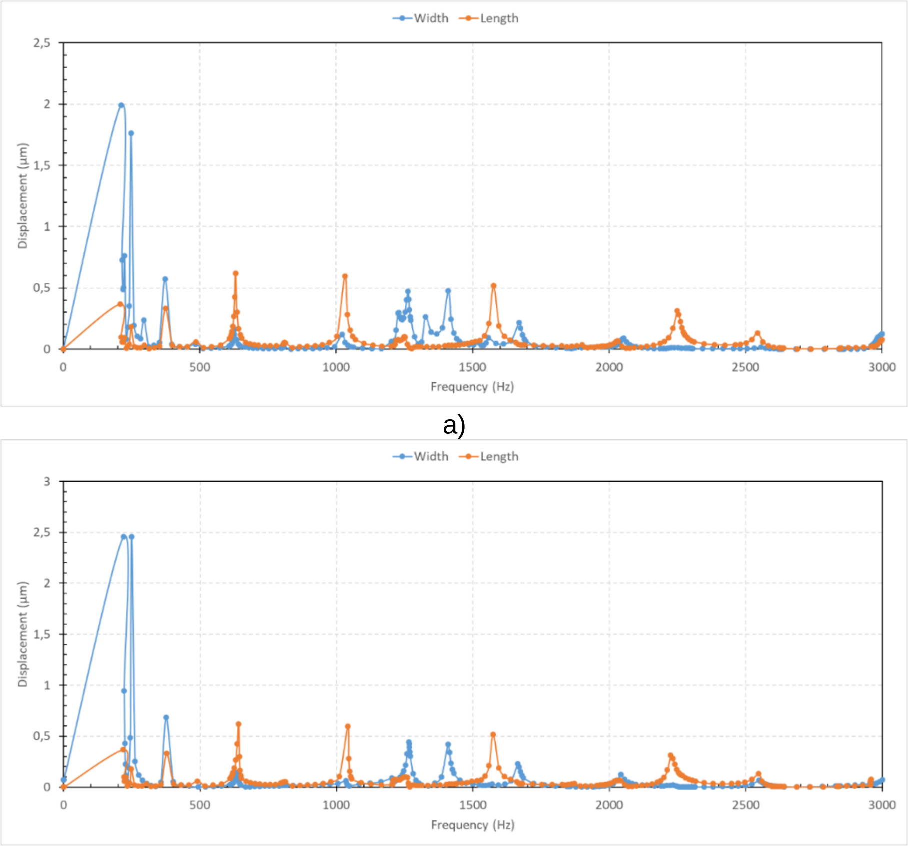

a)

b)

Figure 2.4:20 – Displacement at center of the plate for one patch actuator positioned at edge (A) and center (B) of the plate oriented in the width direction and in the length direction

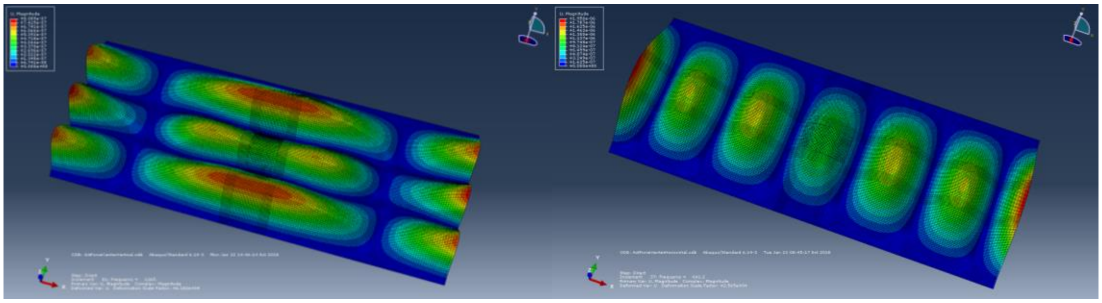
a) b)

Figure 2.4:21 – Example of mode for which (a) the width direction is optimal and (b) length direction is optimal

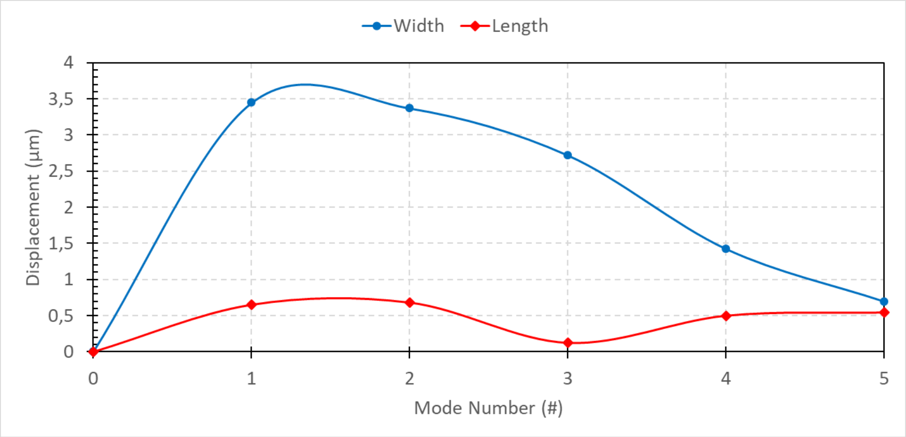

Figure 2.4:22 – Displacements at edge of the plate with five actuators optimally phased for each mode

2.5 SUMMARY

In this chapter a basic numerical model of a vibrating flat plate structure was developed. The model was then used to study different design criteria for the integration of piezoelectric actuators to the structure for efficient de-icing tests. Frequency analysis were used to compute resonant frequencies and modal shape of the resonant frequencies and Direct-Solution Steady-State Dynamic analysis were run to calculate vibration amplitudes. The results have shown that the optimal position for the actuators is at the center of the anti-nodes of vibration. Actuators positioned outside the anti-nodes will not excite the resonant modes. Actuators can be positioned at the center of any anti-nodes of a resonant mode for equivalent result and that the total fore generated by the actuators can even be split between multiple anti-nodes for the same vibration amplitude. This can provide a great degree of freedom when selecting number of and positions of actuators for a system. Results have also shown that, when multiple actuators are used, the relative phasing for each actuators is of paramount importance. Since each successive anti-node is vibrating in opposite direction, phasing of the actuators has to be set so that each actuator acts in phase with its anti-node. With those conclusions, the model was then used to integrate the piezoelectric actuators for optimal excitation of the plate during de-icing tests by defining the positions and orientations. The actuator setting obtained was then used to develop the more complex model at next section as well as the experimental setup.

CHAPTER 3

NUMERICAL MODEL OF FLAT PLATE EXPERIMENTAL SETUP WITH FORCED VIBRATION GENERATED BY PIEZOELECTRIC ACTUATOR PATCHES

In this chapter, the basic numerical model developed at chapter 2 is improved by integrating the piezoelectric actuator patches into the model and meshed with piezoelectric elements so that they can excite the structure by applying different electric boundary conditions. Then frequency analysis and direct-solution steady-state dynamic analysis are performed and will be used for experimental validation in following chapters.

3.1 NUMERICAL MODELING OF THE PIEZOELECTRIC ACTUATOR PATCHES

The experimental setup designed at previous section was created in ABAQUS with the actuator patches modeled with piezoelectric elements. Piezoelectric actuator patches modeled with piezoelectric material were added to the flat plate model. The actuators were modeled with a solid deformable 3D extruded part. The PIC255 material was created manually with the information provided by the manufacturer. The density was set to 7 800 kg/m³. As explained at section 1.4, three other material behaviors were input into the material properties. The elastic component was set to anisotropic and the values input are shown in this stiffness matrix:

$$\mathrm{c}^{E}=\begin{bmatrix}13.27 & 8.667 & 8.563 & 0 & 0 & 0\\ 8.667 & 13.27 & 8.563 & 0 & 0 & 0\\ 8.563 & 8.563 & 11.92 & 0 & 0 & 0\\ 0 & 0 & 0 & 2.128 & 0 & 0\\ 0 & 0 & 0 & 0 & 2.128 & 0\\ 0 & 0 & 0 & 0 & 0 & 2.299\end{bmatrix}*10^{10}\ \text{(N/m}^2\text{)}$$

The second behavior was the electrical permittivity (dielectric component), which is orthotropic, and the component matrix is:

$$\varepsilon^{S}=\begin{bmatrix}8.28 & 0 & 0\\ 0 & 8.28 & 0\\ 0 & 0 & 6.72\end{bmatrix}*10^{-9}\ \text{(F/m)}$$

The last behavior was the piezoelectric coefficient, an anisotropic constant, which can be described by the stress related coefficient or the strain related coefficient. The strain related coefficient matrix presented below was input into the material properties (Figure 3.1:1):

$$e=\begin{bmatrix}0 & 0 & 0 & 0 & 13.14 & 0\\ 0 & 0 & 0 & 13.14 & 0 & 0\\ -6.73 & -6.73 & 15.68 & 0 & 0 & 0\end{bmatrix}\ \text{(N/Vm)}$$

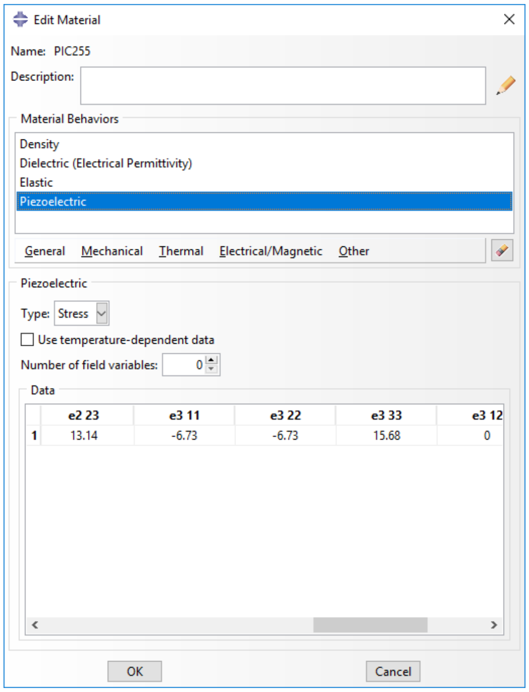

Name: PIC255

Description:

Material Behaviors

- Density
- Dielectric (Electrical Permittivity)
- Elastic
- Piezoelectric

Piezoelectric

Type: Stress

☐ Use temperature-dependent data

Number of field variables: 0

Data

	e2 23	e3 11	e3 22	e3 33	e3 12
1	13.14	-6.73	-6.73	15.68	0

Figure 3.1:1 – Piezoelectric material properties in ABAQUS model

With non-isotropic materials, an orientation must be defined into the model to assess the correct axis for the material properties direction. By observing the properties matrix, it was possible to see that the first and second directions were identical and the third direction was different from the other two. In our case, the third direction was the thickness of the actuators with a 3-1 piezoelectric effect. The orientation for the material is presented at Figure 3.1:2. The PIC255 custom material was then assigned to the piezoelectric actuators by applying a solid homogenous section to the 3D solid part. The actuators were meshed with one thousand Standard Linear C3D8E 8-node piezoelectric brick. These elements allowed the coupling between mechanical and electrical properties by including displacement and electrical potential degrees of freedom.

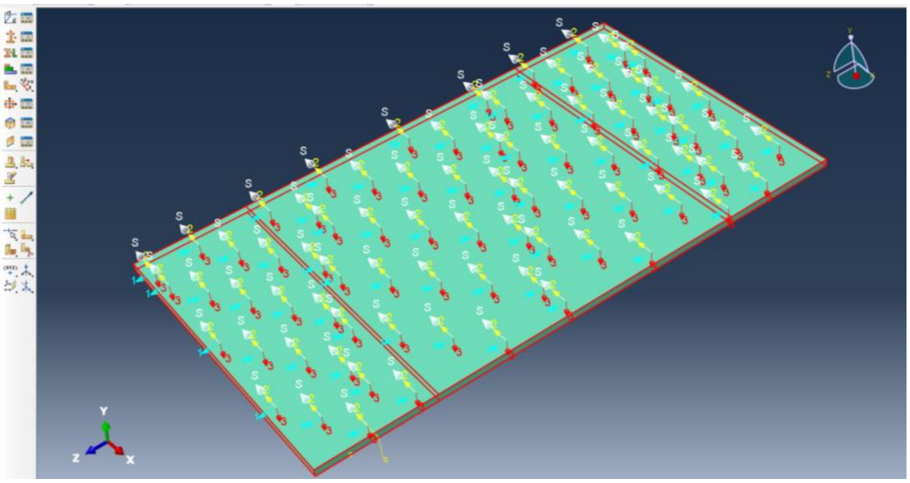

Figure 3.1:2 – Material orientation definition in ABAQUS for piezoelectric actuator patch

The actuators were tied to the surface which simulated a perfect bonding of the actuators on the flat plate, with the actuators' faces set as master surface and the plate as slave surface. Both a frequency analysis and a direct-solution steady-state dynamic numerical simulation analysis steps were defined from 0 to 1000 Hz. An electrical potential boundary condition was applied to the top and bottom face of the actuator to generate the deformation of the patch. On the bottom face, the electrical potential was set constant to zero and on the top face the potential was set to the value of the voltage applied during the different experiment testing (Figure 3.1:3). This simulated the two electrodes on the top and bottom of the actuator patch. During the direct-solution steady-state dynamic analysis, the voltage on the top face of the actuator varied sinusoidally with time at the different resonant frequencies investigated.

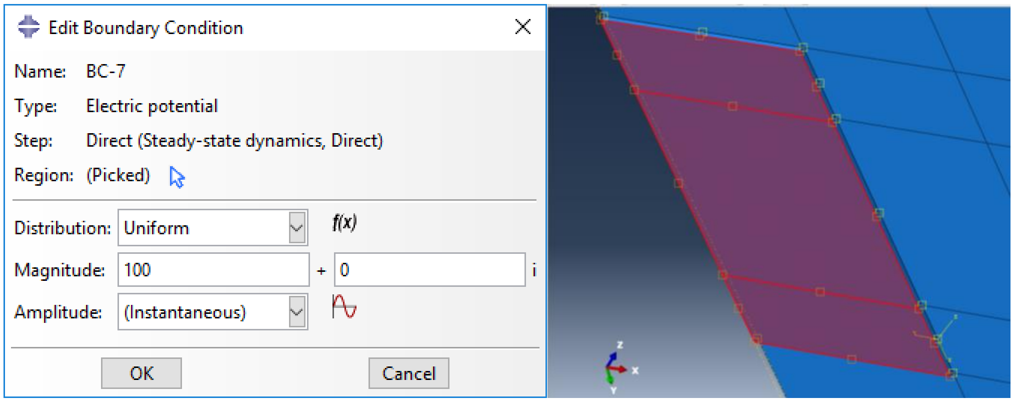

Edit Boundary Condition

Name: BC-7

Type: Electric potential

Step: Direct (Steady-state dynamics, Direct)

Region: (Picked)

Distribution: Uniform

Magnitude: 100 + 0 i

Amplitude: (Instantaneous)

Figure 3.1:3 – Electrical potential boundary condition on the actuator patch in ABAQUS

3.2 FREQUENCY ANALYSIS RESULTS

The five actuator patches when bonded to the flat plate slightly changed the stiffness of the flat plate, which had a small impact on the resonant frequency. Table 3.2:1 presents the resonant frequencies from 0 to 1 kHz for the flat plate with the five actuator patches bonded to it. Fifteen resonant modes were found for the frequency range.

Table 3.2:1 – Resonant Frequencies of the flat plate with the five actuators patches

Mode (#)	**Frequency (Hz)**
1	200
2	206
3	227
4	270
5	344
6	453
7	570
8	570
9	581
10	613
11	671
12	752
13	763
14	899
15	942

3.3 DIRECT-SOLUTION STEADY-STATE DYNAMIC ANALYSIS

In the direct-solution steady-state dynamic analysis, a voltage was applied at the top face of the actuators which varied sinusoidally at the different resonant frequencies investigated. This analysis predicted the displacement, velocities, accelerations, stresses and strains on the plate when excited by the actuators. Different voltage values could be applied to the actuators by setting the electric potential boundary conditions. An example of results obtained is presented at Figure 3.3:1. This analysis was used to generate numerical results for the experimental tests presented at section 5. Voltage, actuator activation and damping (see 5.2 for damping measurement) were set to match the conditions of each experimental test and the analysis was run. The results were then compared with experimental results for model validation.

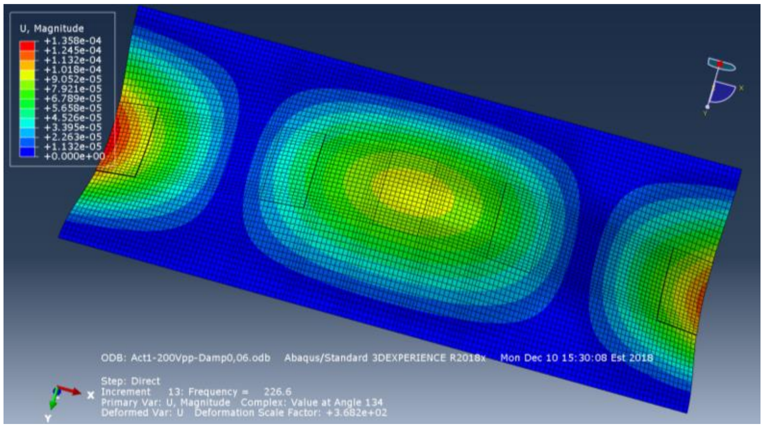

Figure 3.3:1 – Example of direct-solution steady-state dynamic analysis results, with a 100 V (200 Vpp) electrical potential boundary condition applied to piezoelectric actuator patch 1.

3.4 SUMMARY

The basic numerical model developed in chapter 2 was improved to integrate the piezoelectric actuator patches to the model and used them to excite resonance of the structure. Then the model was used to compute the resonant frequencies and modal shape with the added rigidity of the patches. Finally, the chapter also presents the details and parameters of the Direct-Solution Steady-State Dynamic analysis performed which were done for experimental validation. The results of those the analysis performed are presented in details at chapter 5.

CHAPTER 4

EXPERIMENTAL SETUP

This chapter presents the experimental setup built for numerical model validation as well as the different equipment used to drive the actuators and to measure the resulting vibration.

The setup consisted of a fixed 304 stainless steel flat plate, 1.6 mm thick with actuators bonded to it to activate its resonant frequencies. The plate was cut in a rectangle shape of 500 mm by 504.8 mm. The plate was divided in three part. Ten holes were drilled in each of the two part on the sides of the plate. Each of these parts of the plate were placed between two massive steel 44w 50.8 mm (2'') thick blocks. Ten screws and bolts were used on each side to tighten the plate with the blocks. The screws were tighten at 165 lb-in with a torque wrench. These sections were not modeled in the numerical simulations but were built to recreate the Clamped boundary conditions applied on the sides of the plate in the numerical model (Figure 4:1). This was necessary to reproduce the boundary conditions of the model as accurately as possible and maximize vibration of the plate. The middle section of the plate, which was 200 mm long, was free to vibrate and represented the plate in the numerical model.

Figure 4:1 – Flat plate experimental setup

4.1 PIEZOELECTRIC ACTUATORS PATCHES

Five Physik Instrumente (PI) P-876.A15 actuator patches (Figure 4.1:1) were installed on the lower surface of the plate. The patches were 61 mm in length by 35 mm wide with a total thickness of 0.8 mm. The patches were composed of a piezoceramic plate laminated with polymer materials and electrodes. The polymer coating served as a mechanical preload and an electrical insulation. The patches were bendable. The piezoceramic plate was made of PIC255 material. This material is a modified PZT material with high Curie temperature, high permittivity, high coupling factor and high charge constant. To bond the actuators to the surface, a process similar to the one used to install strain gages was used. First the surface was cleaned with a CSM-2 degreaser. Then, the surface was sandpapered at 45° in both direction (Figure 4.1:2) with a 400 grit. The surface was cleaned two more times, first with conditioner and then with neutralizer. The surface of each actuator was also clean with acetone.

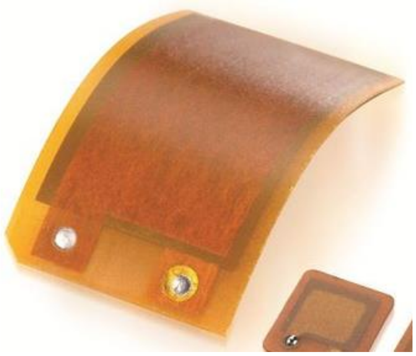

Figure 4.1:1 - Physik Instrumente (PI) P-876.A15 actuator patch [72]

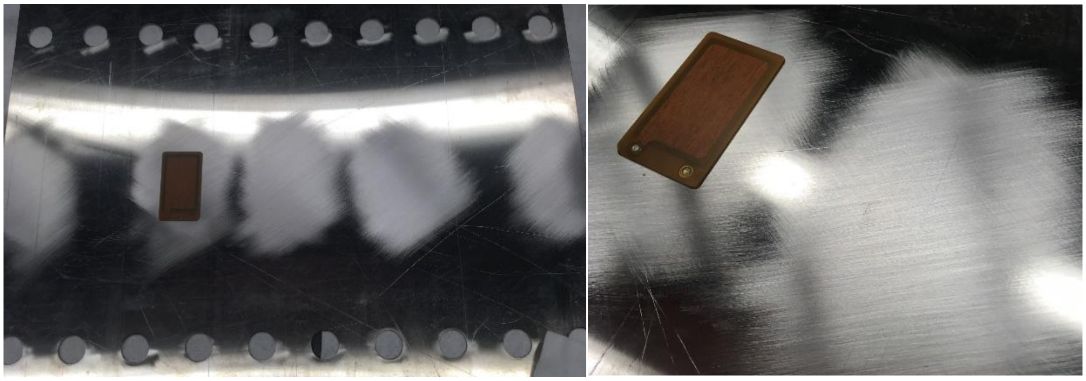

Figure 4.1:2 – Surface preparation for patch actuators installation

Epo-tek 353ND glue, as recommended by the piezoelectric actuators manufacturer, was applied both on the surface of the actuators and the plate. The actuators were carefully applied on the plate at the selected positions and pressure was applied on the actuators by depositing a heavy brick on each actuator for 72 hours. The position of the actuators was selected at section 2.4.1.3.

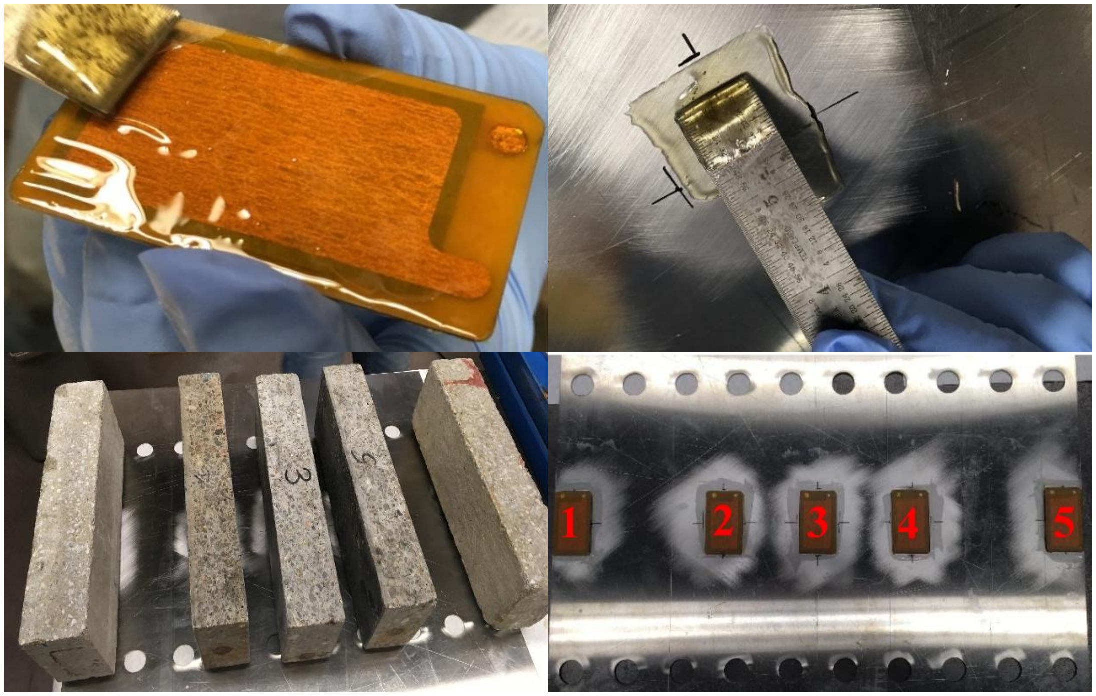

Figure 4.1:3 – Patch actuator installation on the flat plate

4.2 DRIVING UNIT

To drive and monitor the piezoelectric actuator system, an electrical system was required (Figure 4.2:1). This system used an Agilient 33500B waveform generator to generate and provide the electrical signal to the actuators. This device allowed for different signal generation like impulse, sine wave, square wave and sweep through different frequency range. It included two different channels that can each drive a separate set of actuators. Before reaching the actuators, the signal passed through an Amp-line AL-1000-HF-A amplifier, which amplified the voltage from low voltage (less than 10 V) to high voltage (50 to 1000 V) to generate higher vibration. Since the operational voltage of the actuators was -250 to 1000 V, an Amp-line AL-100DC power source was used to offset the voltage to allow testing close to the limit of the actuators. By offsetting the voltage to values around 400 or 500 V, an alternative voltage of 1000 to 1200 Vpp could be applied without compromising the integrity of the actuators. The voltage applied to the actuators was measured with a Fluke 105B oscilloscope. To monitor and record the signals from the accelerometers and piezofilms, a Gen2i-2 Bridge data acquisition system was used.

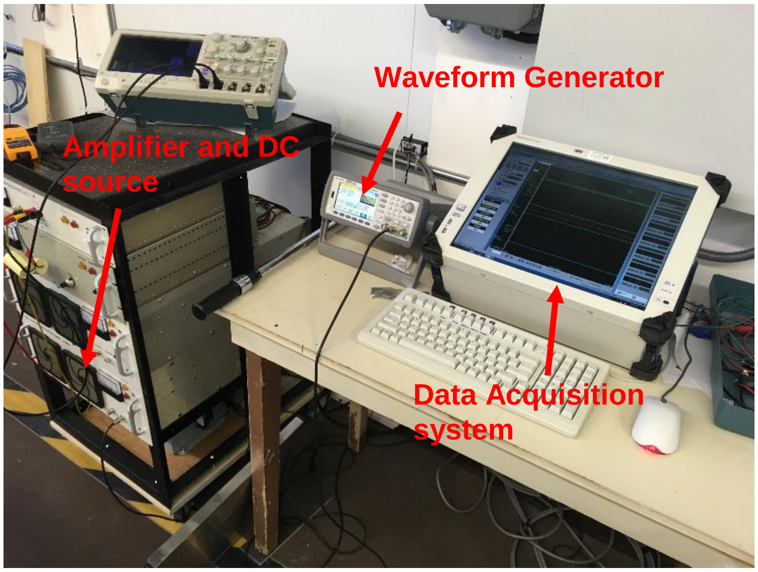

Figure 4.2:1 – Piezoelectric system driving unit

4.3 LASER SCANNING DOPPLER VIBROMETER

A PSV-200 Laser Scanning Doppler vibrometer (sensor head OFV 056) was available at the NRC in Ottawa (Figure 4.3:1). This device uses a laser to make optical vibration measurement. It was possible to record reliable and precise measures of vibration. Eigen modes and deflection shapes could be detected and measured at high frequency rate in a non-destructive and non-contact way. It can measure vibrational velocities from 0.01 µm/s to 30 m/s at frequencies from DC to 25 MHz. The flat plate setup when installed at the NRC to perform laser vibrometer measurements is presented at Figure 4.3:1. The laser was positioned immediately over the flat plate. A grid of measurement points was set on the computer software to define the location of the vibration measurements on the flat plate. When using the laser vibrometer, the electric signal was generated by the computer software instead of the Agilient 33500B waveform generator.

Figure 4.3:1 – Flat plate setup at NRC Ottawa for laser vibrometer measurements

4.4 ACCELEROMETERS

The laser vibrometer was only available at NRC in Ottawa, meaning it could not be used for measurement at AMIL and in cold room/wind tunnel for de-icing tests. This brought the necessity of using alternate measurement devices to perform data acquisition during de-icing tests. Accelerometers are electromechanical device used to measure acceleration forces. Miniature single axis piezoelectric accelerometers were selected since they have a high frequency range, small size and low weight. PCB Piezotronics model 352C22 were selected for their sensitivity of 10 mV/g. They have a measurement range of ±500 g peak for a frequency range of 1 to 10 000 Hz.

4.5 SUMMARY

In this chapter was found a detailed description of the experimental setup and how it was built for the experimental validation of the numerical model presented at next section. The piezoelectric actuator patches are also described as well as the driving unit used to excite the actuators. Finally, the different measurement tools were also described.

CHAPTER 5

EXPERIMENTAL VALIDATION OF THE NUMERICAL MODEL

This chapter presents the experimental validation of the numerical model. The experimental setup is tested and resulting vibration is measured with a Scanning Laser Vibrometer. Damping measurement of the plate is presented and the accuracy of the numerical model to piezoelectric actuator excitation is defined.

Experimental tests were performed with the flat plate to validate the numerical model. The displacement, velocities and accelerations of the plate were measured using the Polytec Scanning Laser Vibrometer PSV-300 (data acquisition board PCI-4452) at a sampling rate of 2.56 times the maximum frequency of interest. A grid of measurement points was defined over the surface of the flat plate in the software to set the measurement positions (Figure 5:1). The experimental tests were performed at fixed frequencies to obtain steady-state mode deployment and compare with the numerical analysis. The operating voltage of the piezoelectric actuator was set to 200 Vpp, both experimentally and in the numerical model. The laser was set to fastscan, where it scanned the whole surface at the positions defined at a fixed frequency. This created a dynamic steady-state vibration at each resonant modes and corresponded to the Direct Solution Steady-state Dynamic Analysis that was performed numerically. The actuator patches were referenced each by a different number. The numbering of the actuators is presented at Figure 5:2.

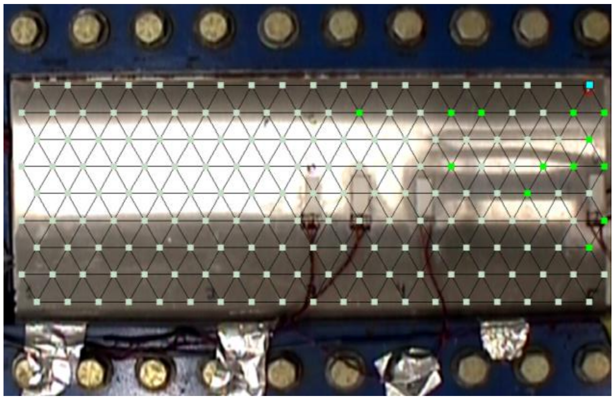

Figure 5:1 – Laser vibrometer measurement positions grid

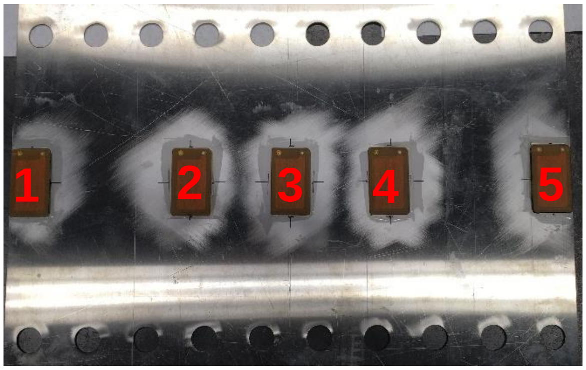

Figure 5:2 – Piezoelectric actuator patches reference number

5.1 FREQUENCY ANALYSIS VALIDATION

Table 5.1:1 presents the comparison between the resonant frequencies obtained numerically and experimentally. The frequencies were independent of which actuators were activated and at what voltage. Two modes, mode 10 and 13, could not be successfully activated or measured during the experimental testing for reasons explained in the next paragraph. For the other modes, the maximum difference between experimental and numerical results was 14%. Also, the predicted frequencies were all higher than the experimental frequencies which could be caused by the boundary conditions or due to the effect of damping.

Between 0 and 1000 Hz, it was possible to divide the resonant mode in two distinct groups: the modes with one line of anti-nodes (Figure 5.1:1) and the modes with two lines of anti-nodes (Figure 5.1:2). The modes with one line of anti-nodes are the modes in bold in Table 5.1:1. The actuators have been positioned to optimize displacement at the center of the plate. By doing so, the actuators were not in a favorable position to activate the modes with two lines of anti-nodes and the displacements generated were significantly lower than for the modes with one line of anti-nodes. The system has not been designed to excite those modes and the resonant modes were barely observable experimentally. This explains the higher difference between the numerical simulation and experimentation for those modes as well as the two missing modes. When excluding those modes (mode 7, 9, 10, 11, 13 and 14), the difference fell under 7% for all but the first mode. As with the numerical model, those modes were no longer investigated in this study since the system had been designed to maximize displacement and strain at the center of the width of the plate, thus optimizing the modes with one line of anti-nodes (see section 2.4.1.3).

Table 5.1:1 – Comparison of resonant frequencies between numerical model and experimental results

Natural Mode (#)	**Numerical Model (Hz)**	**Experimental Results (Hz)**	**Difference (%)**
1	***200***	***177***	***13***
2	***206***	***193***	***7***
3	***227***	***216***	***5***
4	***270***	***258***	***5***
5	***344***	***327***	***5***
6	***453***	***424***	***7***
7	570	501	14
8	***570***	***557***	***2***
9	581	527	10
10	613	-	-
11	671	604	11
12	***752***	***713***	***5***
13	763	-	-
14	899	799	13
15	***942***	***913***	***3***

Figure 5.1:1 and Figure 5.1:2 show that, in addition to predicting the resonant frequencies with great accuracy, the numerical model also correctly predicted the mode shapes and anti-node positions.

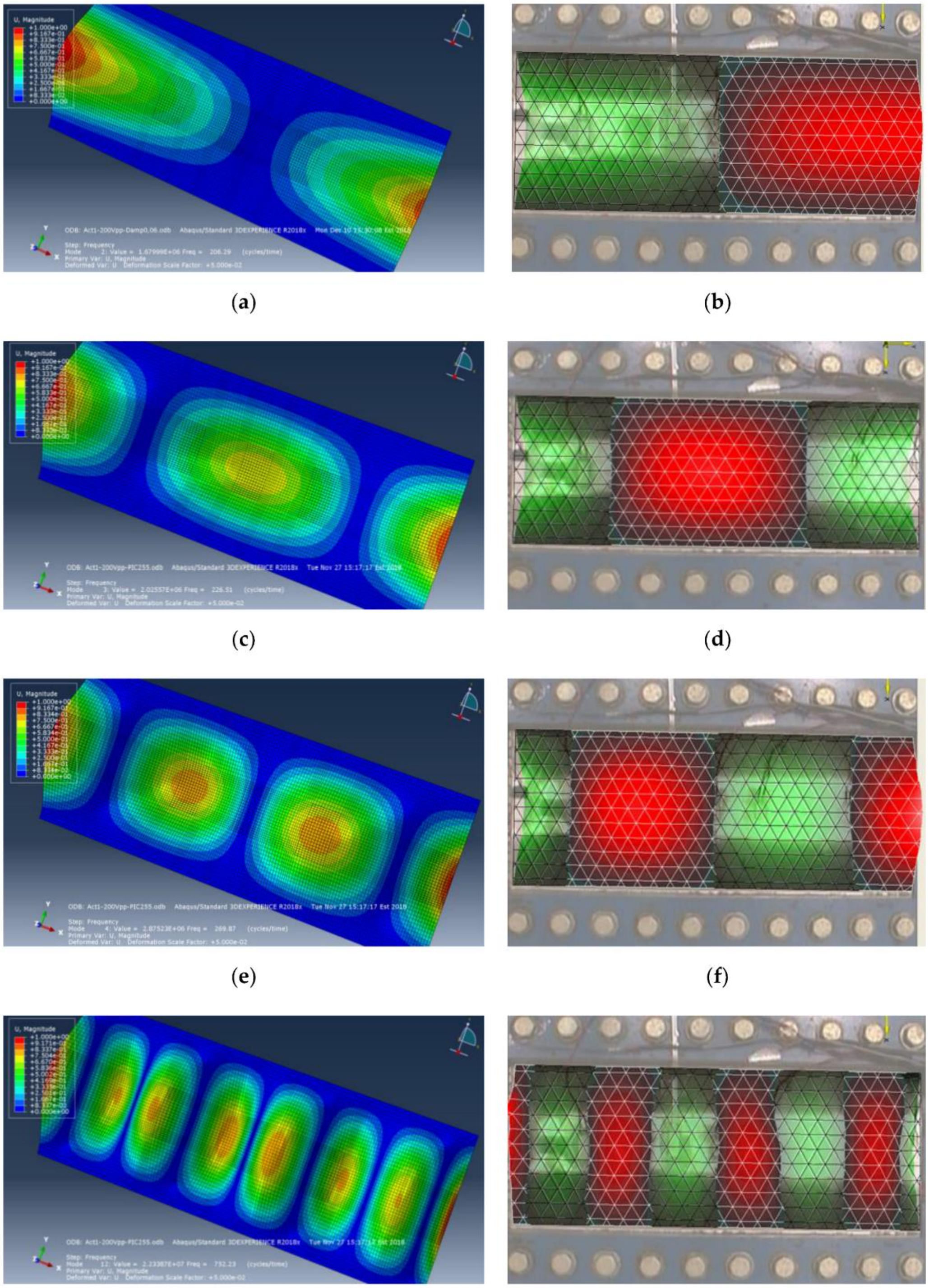

(a) (b)

(c) (d)

(e) (f)

(g) (h)

Figure 5.1:1 - Numerical result for mode 2 (a), mode 3(c), mode 4 (e) and mode 12 (g) and experimental result for mode 2 (b), mode 3 (d), mode 4 (f) and mode 12 (h)

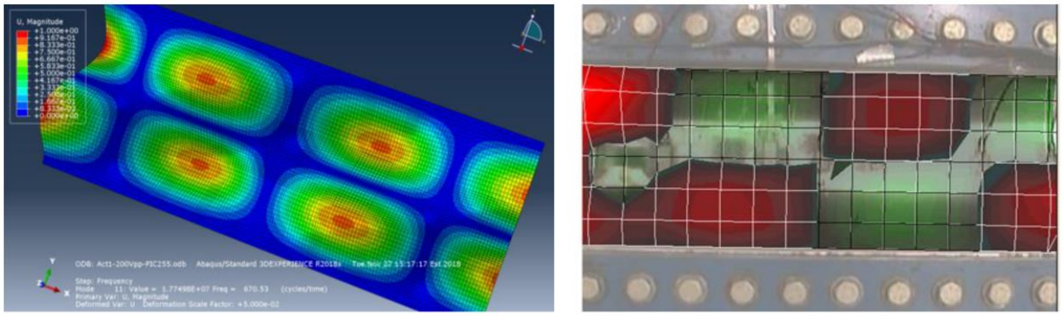
(a) (b)

Figure 5.1:2 – Numerical result (a) and experimental result (b) for mode 11

5.2 DAMPING MEASUREMENT

The damping is the dissipation of energy in a material or structure under cyclic solicitation. Theoretical damping values tend to be difficult to determine. A common practice for aluminum and steel materials in numerical simulations is to use the structural damping behavior with a value of 0.01. With the experimental setup, it was possible to determine experimentally the value of the damping for the structure. In order to do so, the half-power method, also called 3 dB method, was used. In a frequency response function, which was obtained with the laser vibrometer software, the damping is proportional to the width of the resonant peak of a resonant mode. The damping factor, or quality factor, could be calculated with the following equation:

$$Q = \frac{f_0}{f_2 - f_1} \tag{42}$$

with Q the damping factor, f_0 the resonant frequency, f_1 the frequency corresponding to -3dB before f_0 and f_2 the frequency corresponding to -3dB after f_0 (Figure 5.2:1).

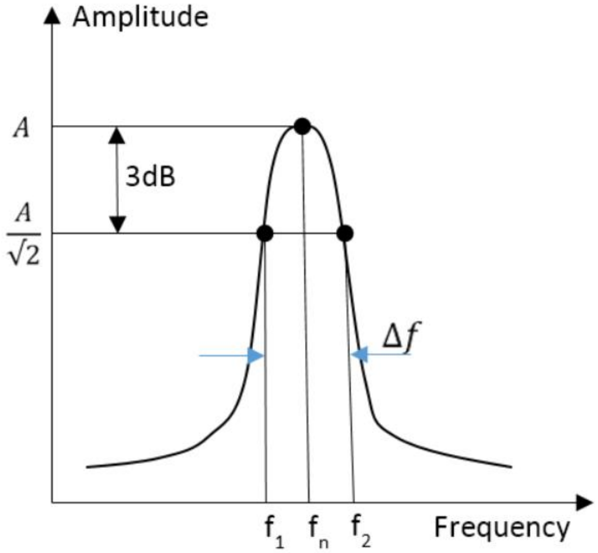

Figure 5.2:1 – Half power method (or 3dB method)

To obtain the damping experimentally, sweeping from 160 to 1000 Hz was performed with each actuator individually at 200 Vpp, except with actuator 1 because it got debonded from the plate during transportation of the test setup between AMIL and NRC laboratories. The frequency response function was obtained with the laser vibrometer and the software was used to compute the frequency difference for -3dB (Figure 5.2:2). The loss factor (η), which is the inverse of the damping factor (Q), was calculated at each resonant frequency for each actuator activation. Loss factor results are presented at Figure 5.2:3. Mode 15 was not considered for the calculation of the loss factor. When looking at the mode shape (Figure 5.2:4), it is possible to observe that it does not totally correspond to the mode shape obtained numerically. It seems to be the combination of two different modes, mode 15 and mode 16, which was predicted numerically at 1002 Hz. The combination of those two modes could explain the larger band in the frequency response function which resulted in a much higher loss factor than for the other modes.

For piezoelectric actuator 3, which was positioned at the middle of the plate, only modes with odd number of anti-nodes are activated correctly. The absence of anti-node at the center of the plate for the other modes resulted in very small displacements at those frequencies when the actuator 3 was driven (section 2.4.1.1). The loss factor obtained for all actuator activations were very similar. However, it slightly varied from mode to mode, with values ranging from 0.004 to 0.008. The average loss factor obtained from all actuators activation and all resonant modes was 0.006±0.002. This value was used for the direct-solution steady-state dynamic analysis.

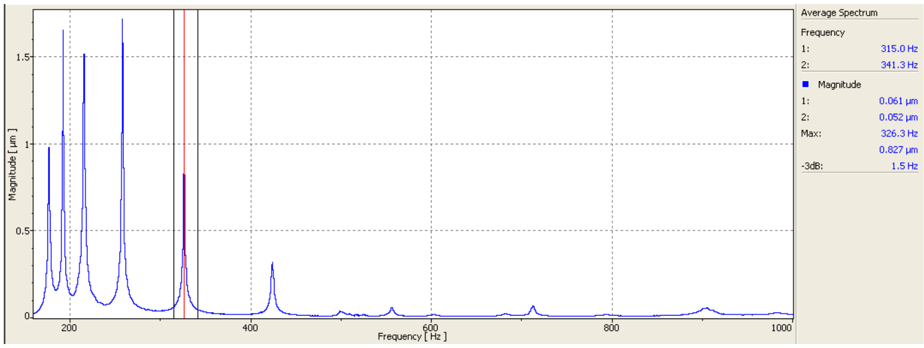

Average Spectrum

Frequency

1: 315.0 Hz

2: 341.3 Hz

Magnitude

1: 0.061 µm

2: 0.052 µm

Max: 326.3 Hz

0.827 µm

-3dB: 1.5 Hz

Figure 5.2:2 – Sweeping Frequency Response Function and -3dB analysis with piezoelectric actuator 2

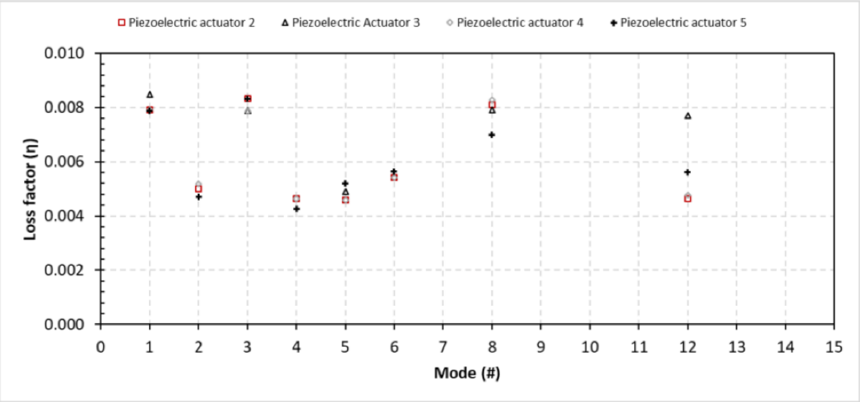

Figure 5.2:3 – Flat plate system Loss factor for each piezoelectric actuator activation

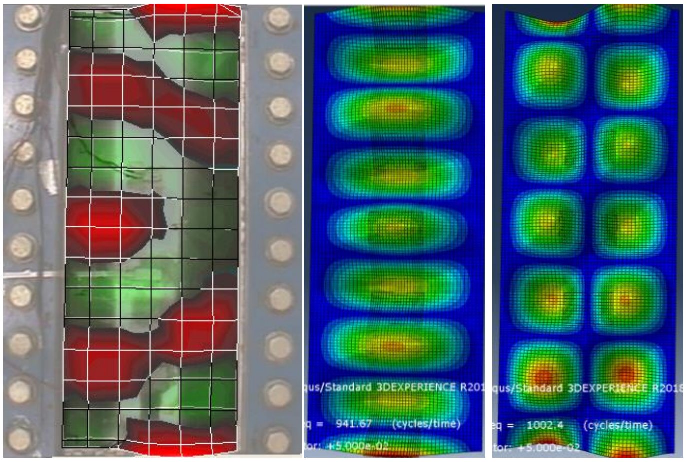

a) b) c)

Figure 5.2:4 – Experimental mode shape obtained at 93 Hz (a) compared to numerical mode shape for Mode 15 (b) and Mode 16 (c)

5.3 DIRECT-SOLUTION STEADY-STATE DYNAMIC ANALYSIS VALIDATION

The fastscan was performed at each of the nine resonant modes selected at section 5.1. The fastcan operation created a dynamic steady-state vibration at each resonant modes and corresponded to the Direct Solution Steady-state Dynamic Analysis that were performed numerically. The voltage was set to 200 Vpp and the damping of the numerical model was set to 0.006 as defined at section 5.2. The numerical and experimental displacements of the flat plate were compared to validate the model.

5.3.1 SINGLE PIEZOELECTRIC ACTUATOR EXCITATION

In this section, the fast-scan operation, which is based on a steady-state vibration excitation, were performed at each selected structural modal frequency that corresponded to the Direct Solution Steady-state Dynamic Analysis that were performed numerically. Fast-scans were performed with one actuator activated at a time at each structural resonant mode and for each actuator, except actuator 1. The displacements at the center in the width direction were compared between the experimental and numerical results for the entire length of the plate. In the numerical model, a path was created to extract the data at all the positions lengthwise (Figure 5.3:1). Due to the symmetry of the plate and position of actuator 1 and 5, numerical results were identical when activated by the first or the fifth actuator (Figure 5.3:2). This meant that experimental results obtained with actuator 1 and 5 should be identical and results obtained with actuator 5 were compared to the numerical results obtained with actuator 1. This symmetry also applied to actuator 2 and 4. Four test conditions were repeated twice and the repeatability of the experimental results was within an approximate range of 20%.

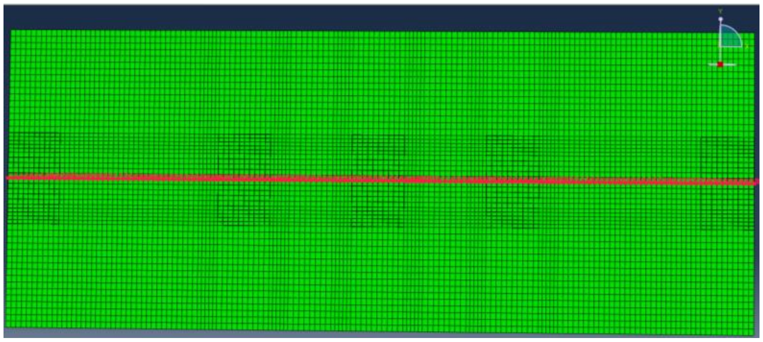

Figure 5.3:1 – Path at the center of the flat plate to extract numerical results

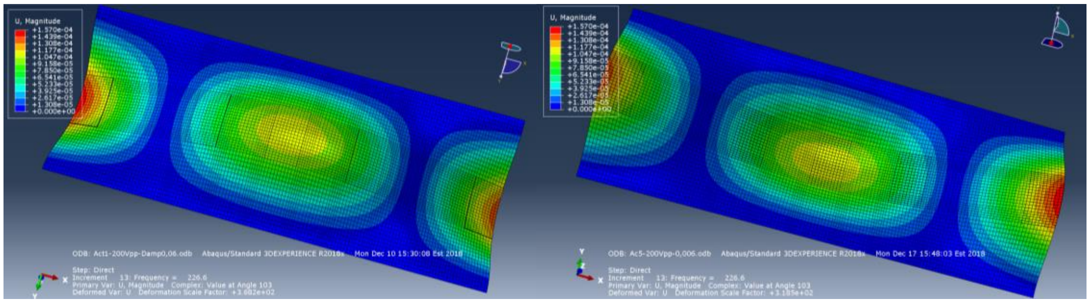
a) b)

Figure 5.3:2 – Numerical results of Mode 3 activated by actuator 1 (a) and actuator 5 (b)

Figure 5.3:3 to Figure 5.3:6 present some results of the displacements along the flat plate at the center of the width for the numerical model and experimental tests. For each test, a single actuator was activated. The figures show that the numerical results were very close to the experimental results for the entire length of the plate and matched the trends of the vibration modes.

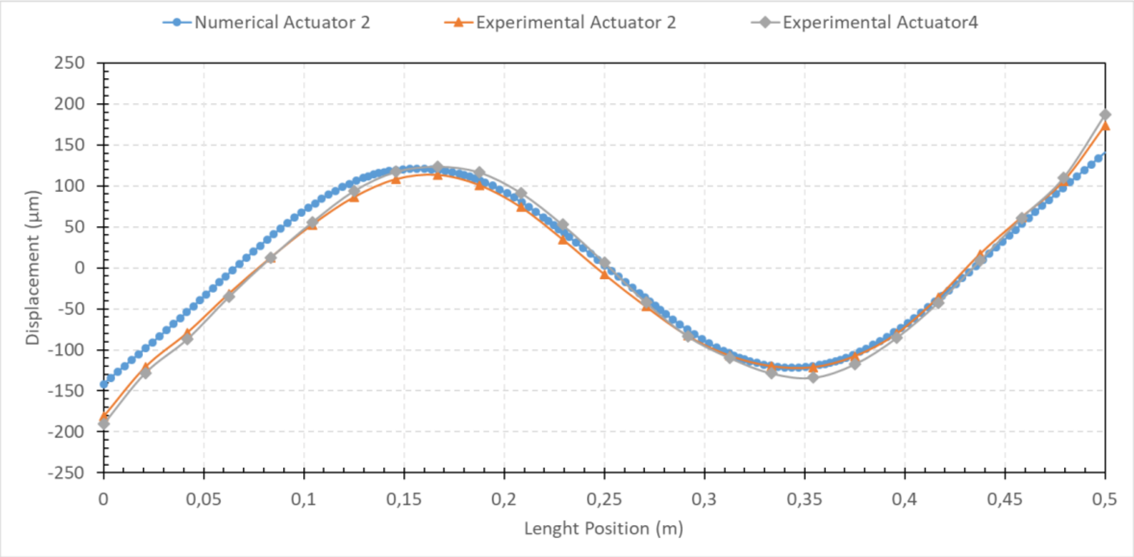

Figure 5.3:3 – Numerical and experimental results for Mode 4 with Piezoelectric Actuator 2 and 4

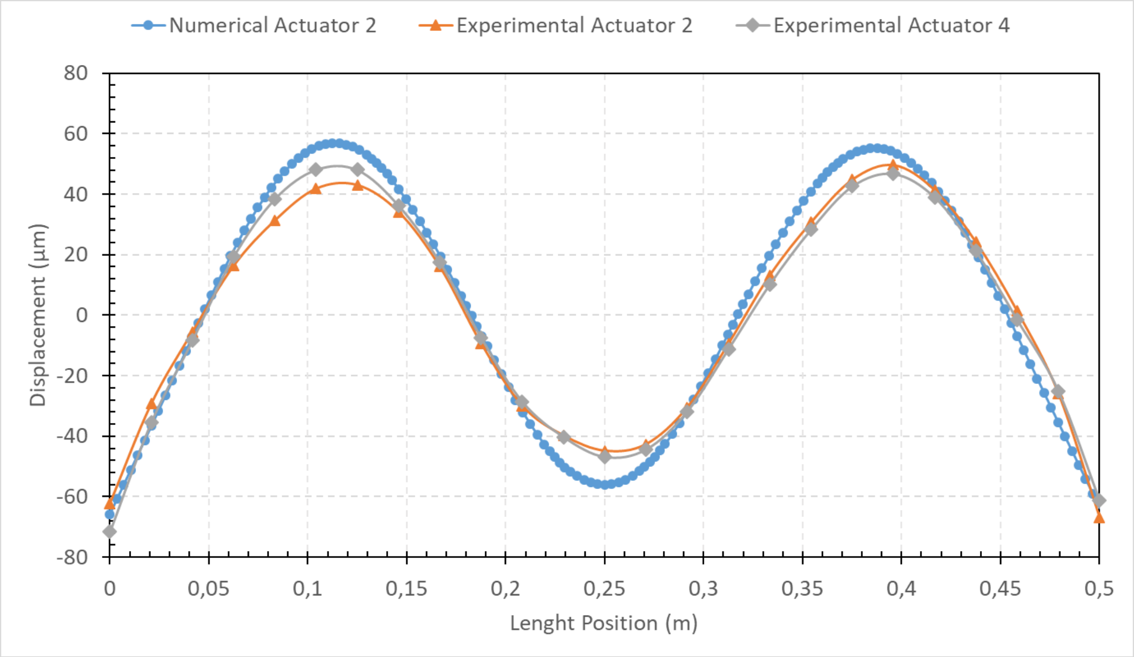

Figure 5.3:4 – Numerical and experimental results for Mode 5 with Piezoelectric Actuator 2 and 4

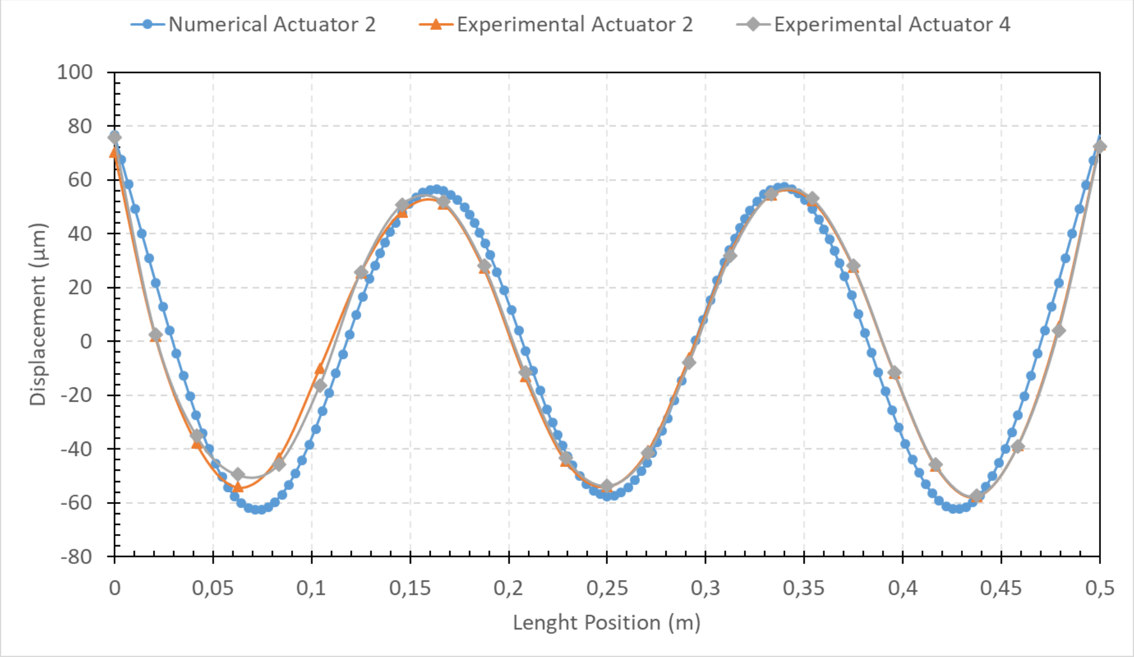

Figure 5.3:5 – Numerical and experimental results for Mode 8 with Piezoelectric Actuator 2 and 4

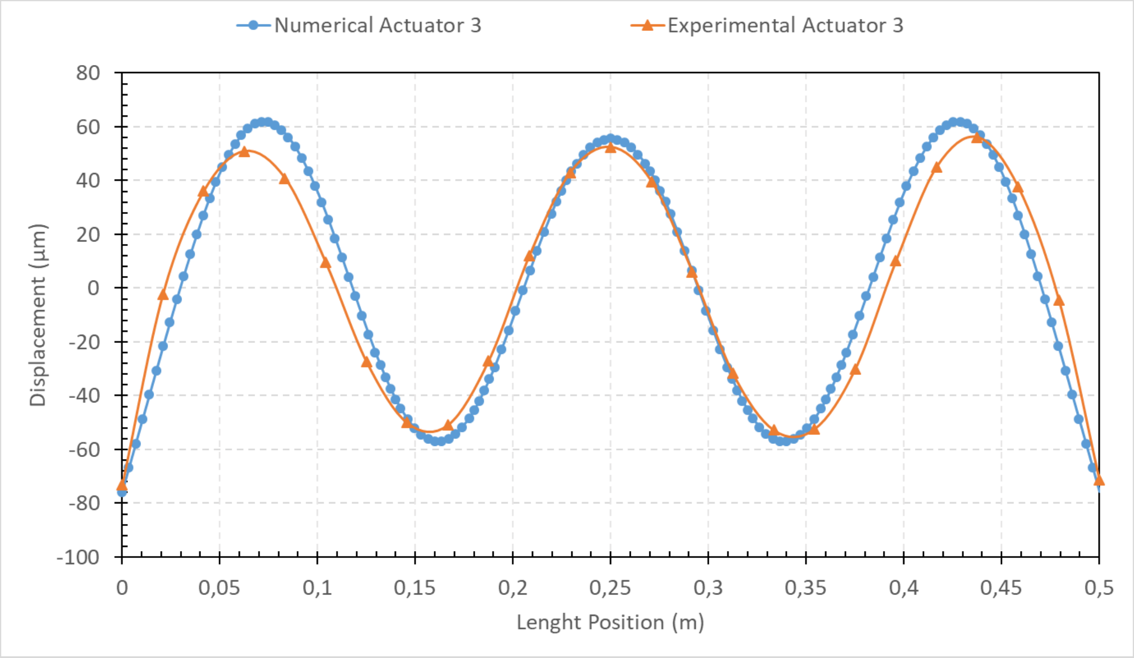

Figure 5.3:6 – Numerical and experimental results for Mode 8 with Piezoelectric Actuator 3

Table 5.3:1 and Table 5.3:2 present the numerical simulation and the experimental testing average displacements on the edges of the plate and at center of anti-nodes for each mode. The results obtained for excitations with the actuator 2 and 4 confirmed the symmetry of the vibration predicted by the numerical model. Except for mode 3, the experimental results obtained with these actuators were within the experimental repeatability of the test. For mode 3, the experimental results obtained with actuator 2 were abnormally different from the experimental results obtained with actuator 4, and also from the numerical results. This is looked at in more details at section 5.3.3.

Table 5.3:1 – Average displacements obtained at edge of plate for activation of a single actuator

Mode	Actuator 2		Actuator 3		Actuator 4		Actuator 5	
(#)	Num (µm)	Exp (µm)	Num (µm)	Exp (µm)	Num (µm)	Exp (µm)	Num (µm)	Exp (µm)
1	-	-	-	-	-	-	-	-
2	99	160	-	-	99	143	204	253
3	105	72	168	226	105	134	152	190
4	142	178	-	-	142	189	82	113
5	65	65	113	187	65	67	41	55
6	52	82	-	-	52	83	17	28
8	77	72	76	72	77	74	2.3	2.5
12	32	17	-	-	32	17	6.4	3.0
15	19	11	44	22	19	11	10.2	3.0

Table 5.3:2 – Average displacements obtained at anti-nodes for activation of a single actuator

Mode	Actuator 2		Actuator 3		Actuator 4		Actuator 5	
(#)	Num (μm)	Exp (μm)	Num (μm)	Exp (μm)	Num (μm)	Exp (μm)	Num (μm)	Exp (μm)
1	72	121	71	112	70	90	66	54
2	-	-	-	-	-	-	-	-
3	86	45	137	158	86	88	113	129
4	121	117	-	-	121	129	71	77
5	56	46	98	133	56	47	35	41
6	43	63	-	-	43	66	14	22
8	59	54	59	53	59	54	2	2
12	26	15	-	-	26	13	5	2
15	14	8	33	16	14	8	7	3

5.3.2 EXCITATION OF MULTIPLE PIEZOELECTRIC ACTUATORS

This section presents the results obtained when multiple actuators were driven at the same time. As observed during the preliminary simulations, the piezoelectric actuators must be driven with the proper phasing for optimal mode deployment. Each anti-node is out of phase with its neighboring anti-nodes, and actuators must be activated with the same phasing as the anti-node it is positioned onto. For these tests, piezoelectric actuator 1 was bonded in its place directly at NRC with instant glue in the best way possible so it had as few impacts on the results as possible. Table 5.3:3 and Table 5.3:4 present the average displacement at the edges of the plate and at anti-nodes for each mode for the different actuator activation tested. Actuators that were out of phase from the other actuators are separated by a backslash when marked in the table. For example, in activation 1-2/4-5, the actuators 1 and 2 were activated with a 200 Vpp loading and actuators 4 and 5 were activated out of phase with a −200 Vpp loading. During experimental testing, the connections of the actuators out of phase were inversed with the positive wires connected into the negative connectors and negative wires into the positive connectors. Only optimal activation was tested, in addition to three tests with actuators 1, 3, and 5 activated in phase.

Table 5.3:3 – Average displacements at edge of plate for activation of multiple actuators.

Mode	Actuator Activation	Displacement	
(#)	*Phase/Out of Phase*	Num (μm)	Exp (μm)
2	1-2/4-5	491	452
3	1-5/2-3-4	510	464
4	1-4/2-5	368	345
5	1-3-5	199	186
5	1-3-5/2-4	293	293
6	1-2/4-5	140	118
6	1-4/2-5	75	113
8	1-3-5/2-4	159	110
15	1-3-5	28	19
15	1-3-5/2-4	62	34

Table 5.3:4 – Average displacements at anti-nodes for activation of multiple actuators.

Mode	Actuator Activation	Displacement	
(#)	*Phase/Out of Phase*	Num (μm)	Exp (μm)
1	1-3-5	230	213
1	1-2-3-4-5	335	282
3	1-5/2-3-4	405	358
4	1-4/2-5	296	249
5	1-3-5	166	194
5	1-3-5/2-4	241	225
6	1-2/4-5	112	142
6	1-4/2-5	61	83
8	1-3-5/2-4	119	90
15	1-3-5	20	13
15	1-3-5/2-4	46	23

5.3.3 FLAT PLATE EXPERIMENTAL VALIDATION RESULTS ANALYSIS

Table 5.3:5 and Table 5.3:6 present the absolute value of the relative discrepancy in the predicted displacements obtained with the numerical model when compared to the experimental results at the edges of the plate and at the anti-nodes, respectively. The results predicted by the numerical model were within 40% of the results obtained experimentally for the first seven modes with an average of 20%, except for mode 3 when excited with the piezoelectric actuator 2. This deviation can be explained by the experimental repeatability of the test, as well as by the boundary conditions and the bonding of the actuators. In the numerical simulation, they were both considered ideal, which was not the case for the experimental setup despite all considerations taken to build the set-up. The material parameters input for the stainless steel were generic values for stainless steel obtained in literature, which could slightly influence the results. Also, PIC255 material values given by the manufacturer were general values for the actuator model and can slightly vary for each patch individually. For mode 3 with piezoelectric actuator 2, the measured displacement was unusual, with a difference of 91% at anti-nodes. When compared with actuator 4 for the same mode, the results were outside the experimental variability, which was also not in agreement with the symmetry predicted and observed for all other modes. For this reason, this result was deemed questionable and should be retested.

For modes 12 and 15, the results predicted by the numerical model were higher than those measured by the laser vibrometer. At those frequencies, the anti-nodes become much smaller compared to the size of the actuator patches. This creates a situation where the actuators act on the plate outside their anti-nodes, and for those modes, also act on neighboring anti-nodes. As was observed during the preliminary simulations, each anti-node is in counter-phase, which lead to a less ideal activation of the mode by the actuator due to their size (Figure 5.3:7). A slight loss of symmetry was also observed for those two modes that can result from the non-negligible stiffness added, which affect the modal shape. Figure 5.3:8 shows very narrow anti-nodes and even narrower half anti-nodes at edges. It also shows a big imperfection at one of the edges. This demonstrates that the size of the actuators is a very important criterion for design. When the dimensions of the actuator are equal or larger than half the wavelength of vibration of the structure, it is expected that (locally) the high order mode shapes and (globally) the behavior of the structure could be greatly affected. The vibration obtained experimentally was less symmetric and ideal for these reasons. These results are in accordance with the numerical predictions obtained by Tian et al. [73]. They concluded that the ideal length of an actuator patch is an odd integer multiple of the half wavelength of a mode, and an odd integer of one is optimal. The results in this thesis extrapolates those conclusions by demonstrating the negative effect of exceeding the size of half wavelength of the mode. The numerical model does not seem to completely account for this, which is why the numerical results were all overpredicted compared to the experimental results. The displacements were also much smaller compared to other modes, below 22 µm, and the macroscopic equation used by the numerical model could be less representative of the phenomenon at this scale. With those weak displacements, small differences also resulted in much higher error percentages. Finally, some coupling effect between mode 15 and mode 16 was observed for some of the tests, which could have impacted the comparison between numerical model and experimental results for this mode. The model gave less accurate prediction when the actuator positioning and activation was not optimal and the resulting vibration shape were slightly less symmetric than the shape of the resonant mode predicted by the frequency analysis, leading to overprediction of the numerical model. The displacement results were still satisfying for the numerical model, with a difference in the order of the micrometers between the model and experimental results for those two modes. Moreover, the numerical model was created to design optimal de-icing systems and was not intended to be used for those cases.

Table 5.3:5 – Absolute relative discrepancy of the numerical and experimental displacements at the edge of the plate for activation of a single actuator

Mode (#)	Actuator 2 (%)	Actuator 3 (%)	Actuator 4 (%)	Actuator 5 (%)
1	-	-	-	-
2	38	-	31	19
3	45	26	22	20
4	20	-	25	27
5	0	40	3	25
6	37	-	37	39
8	7	6	4	0
12	88	-	88	100
15	73	100	73	233

Table 5.3:6 – Absolute relative discrepancy of the numerical and experimental displacements at the center of anti-nodes for activation of a single actuator

Mode (#)	Actuator 2 (%)	Actuator 3 (%)	Actuator 4 (%)	Actuator 5 (%)
1	40	37	20	22
2	-	-	-	-
3	91	13	2	12
4	3	-	6	8
5	22	26	19	15
6	32	-	35	36
8	9	11	9	0
12	73	-	100	150
15	75	106	75	133

The absolute values of the discrepancy obtained between the numerical and experimental results when multiple actuators were activated (Table 5.3:7 and Table 5.3:8) were similar to the values when a single actuator was activated. Maximum difference for the first seven modes was 43% with an average difference of 17%. For modes 12 and 15, differences were also similar with the same phenomenon occurring. The maximum difference of the numerical model was established at 43% for modes efficiently activated with piezoelectric actuators properly positioned and with proper sizing.

The results obtained confirm the conclusions obtained at Chapter 3 on actuator optimal positioning at center of anti-nodes. It also allowed to determine that the ideal length of an actuator patch is an odd integer of one multiple of the half wavelength of a mode and demonstrated that exceeding the size of half wavelength of a mode has a significant negative impact on mode deployment.

Table 5.3:7 – Absolute relative discrepancy of the numerical and experimental displacements at the edge of the plate for activation of multiple actuators

Mode	**Actuator Activation**	**Discrepancy**
(#)	***Phase/Out of Phase***	**(%)**
2	1-2/4-5	9
3	1-5/2-3-4	10
4	1-4/2-5	7
5	1-3-5	7
5	1-3-5/2-4	0
6	1-2/4-5	19
6	1-4/2-5	34
8	1-3-5/2-4	43
15	1-3-5	47
15	1-3-5/2-4	82

Table 5.3:8 – Absolute relative discrepancy of the numerical and experimental displacements at the center of anti-nodes for activation of multiple actuators

Mode	**Actuator Activation**	**Discrepancy**
(#)	***Phase/Out of Phase***	**(%)**
1	1-3-5	8
1	1-2-3-4-5	19
3	1-5/2-3-4	13
4	1-4/2-5	19
5	1-3-5	14
5	1-3-5/2-4	7
6	1-2/4-5	21
6	1-4/2-5	27
8	1-3-5/2-4	32
15	1-3-5	54
15	1-3-5/2-4	100

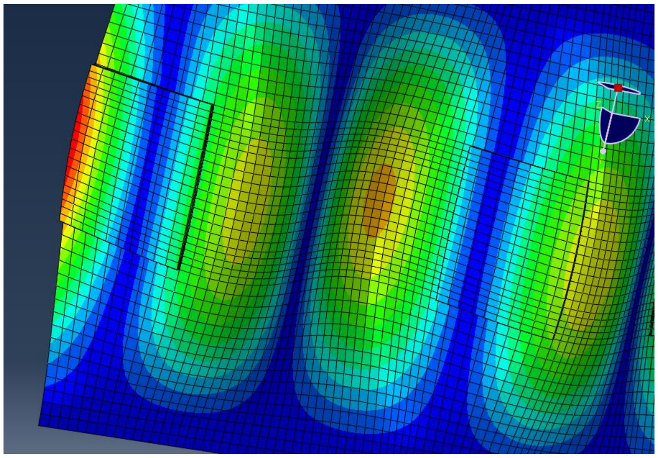

Figure 5.3:7 – Actuator positioned on two neighboring anti-nodes for mode 15

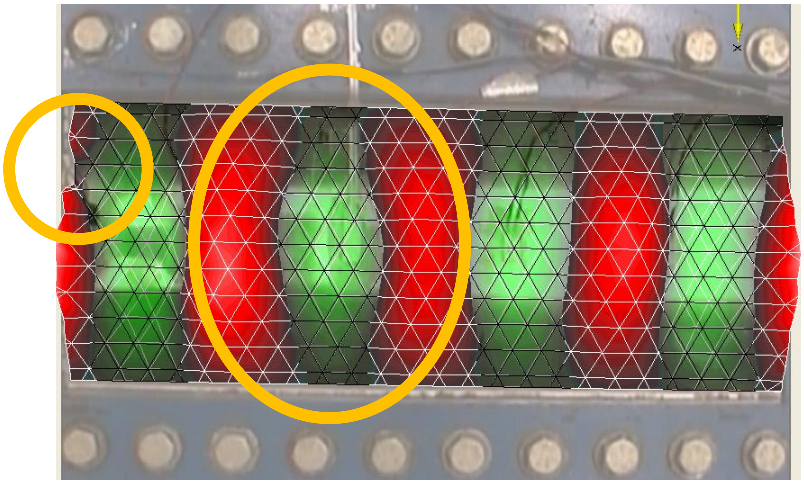

Figure 5.3:8 – Experimental results of mode 15 with piezoelectric actuator 4

5.3.4 PIEZOELECTRIC ACTUATOR EXCITATION EFFICIENCY

The actuators were positioned in order to activate optimally different modes. The actuators on both edges were always positioned on a half anti-node, which means they could activate all of the 9 resonant modes investigated (Figure 5.1:1). However, since it was a half anti-node, the center of the actuator never matched the position of maximum vibration like for the other anti-nodes. For modes 3 to 15, the displacements, both predicted numerically and obtained experimentally, were smaller than for the actuators that were positioned directly at the center of the anti-nodes (Table 5.3:1 and Table 5.3:2). Moreover, starting from mode 5, both the displacements predicted and measured diminishes greatly compared to the displacements obtained with the other actuators, even when actuators 2 and 4 were not positioned directly at the center of anti-nodes of a mode. As explained in the previous sections, the behavior of the structure could be greatly affected when the dimensions of the actuator are equal or larger than half the wavelength of vibration of the structure. The half anti-nodes on each side, corresponding to a quarter of the wavelength of vibration, was affected at even lower frequencies, which explained these smaller displacements for actuator 5 at those modes. For mode 1, the mode was composed of one anti-node over the complete length of the plate, which explained why the model predicted similar displacements for all actuators. For mode 2 (Figure 5.1:1-a and b), which consisted of only a half anti-node at each extremity of the plate, actuator 5 was positioned as close as possible to the most efficient position, which explains the highest numerical and experimental displacements for this mode.

For mode 3 (Figure 5.1:1-c andd), actuator 2 and 4 were not positioned optimally but could still activate the resonant mode. When activated on their own, the numerical prediction for the anti-node displacement was 86 µm compared to 137 µm for actuator 3 (Table 5.3:2). When the five actuators were activated with the optimal phasing (1-5/2-3-4), the prediction increased to 405 µm (Table 5.3:4). For five times the power, the displacement at anti-nodes was only increased by three times compared to actuator 3 only. For mode 4, the actuator 2 and 4 produced a maximum displacement of 121 µm with the numerical model. With activation of 1-4/2-5, this increased to 296 µm, 2.5 times higher for four times the injected power. The actuators were not all optimally positioned for these modes, which explains efficiency lost. An actuator that is positioned to activate a mode can also be used during other mode activation and help increase displacement, but with a loss of power efficiency depending on its position compared to anti-nodes center. This confirms that optimal positioning is at center of anti-nodes and that the actuators must be excited in phase with the direction of its anti-node.

5.4 SUMMARY

In this chapter, Scanning Laser Vibrometer was used to perform the experimental validation of the numerical model. The first analysis performed was a frequency analysis, where resonant frequencies and modal shapes are computed. Experimentally, all the resonant modes were excited but two. Resonant modes where two lines of anti-nodes are found were not optimally excited by the piezoelectric actuator patches positioning and configuration, explaining the two missing modes. When those modes were not considered, since they were not meant to be used in this study, the numerical model correctly predicted all the modal shapes and predicted the frequencies of resonance with a maximum discrepancy of 13%.

The second analysis performed was the Direct-Solution Steady-State Dynamic. Before performing the experimental validation for this analysis, the structural damping was measured with the laser and input into the numerical model with the half-power method. Then the experimental validation was first done by exciting a single actuator at the time. For the first seven modes investigated, a maximum discrepancy of 40% and an average discrepancy of 17% was obtained. This deviation was mainly explained first by the experimental variation of 20% and the boundary conditions that are no ideal with the experimental setup as opposed to the numerical model. For the other two modes, it was observed that the actuator patches were too large for the anti-node dimensions of the resonant modes, leading to suboptimal excitation of the plate experimentally, which explained the overprediction of the numerical model and higher discrepancy. This result has allowed to confirm that the ideal size for an actuator is half a wavelength of a resonant mode.

When multiple actuators were excited together, proper phasing of each patches was investigated for optimal excitation. Each actuator patch was phased relatively to the direction of its anti-node relatively with the other patches excited, as concluded in chapter 2. The maximum discrepancy obtained was 43% with an average of 17% for the mode where the actuators were properly sized. Those results confirmed the validity of the numerical model as well as the accurate positioning and phasing of the actuators as concluded in chapter 2.

CHAPTER 6

TRANSIENT VIBRATION AND FREQUENCY SWEEP EXCITATION

In this chapter, different type of excitation for the actuator are studied and transient phenomena are studied. In the previous phases of the project, de-icing or partial de-icing was obtained during sweeping tests in a cold chamber and in an icing wind tunnel [63]. Ice cracking and delamination was only achieved when sweeping through different frequency ranges was performed and never at a specific fixed frequency. The activation of the actuators with frequency sweeps during the de-icing tests performed during those phases were mostly based on trial and error. In order to understand the different transient vibration phenomenon and understand the reasons that de-icing only occurred during sweeping, different frequency sweep tests were performed with the flat plate setup. An accelerometer was positioned on one edge of the plate, on the side of actuator 5. This position was chosen due to the presence of a half anti-node on the plate's ends at every resonant modes studied in chapter 3.2. Frequency sweeps were then performed at 200 Vpp with a single piezoelectric actuator. The sweep range was set from 100 Hz to 2 500 Hz. Five different sweep durations were selected, 1, 2, 3, 5 and 10 seconds, to measure the effect of the speed of the frequency sweep on mode deployment. Figure 6:1 and Figure 6:2 show the acceleration measured with the accelerometer at the end of the plate when sweeping with actuator 4 and 5 respectively. Due to the position of the actuator 3, only odd resonant modes (with an odd number of anti-nodes) could be properly excited and for this reason it was not used for testing

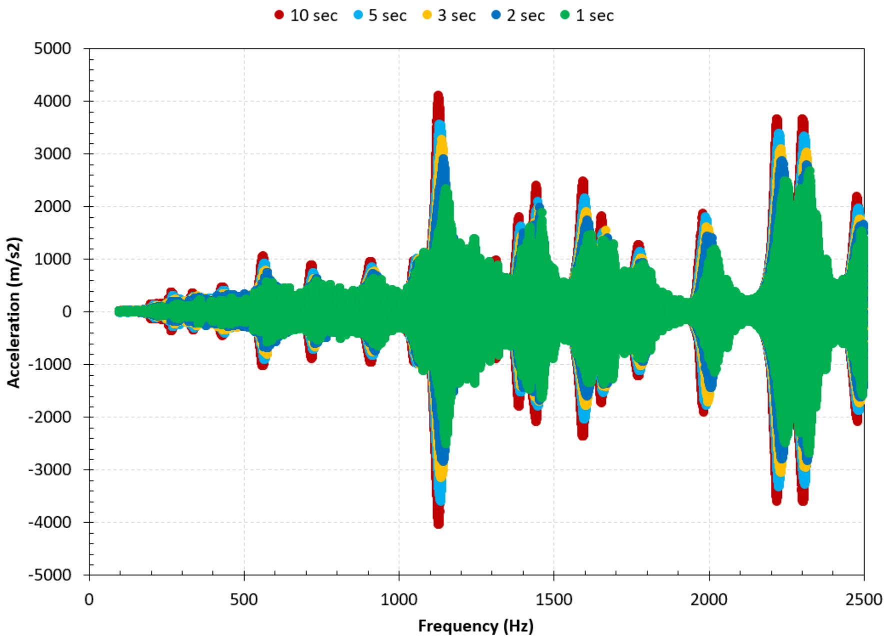

Figure 6:1 – Acceleration at plate’s end for a frequency sweep of 100 Hz to 2500 Hz for piezoelectric actuator 4 at 200 Vpp

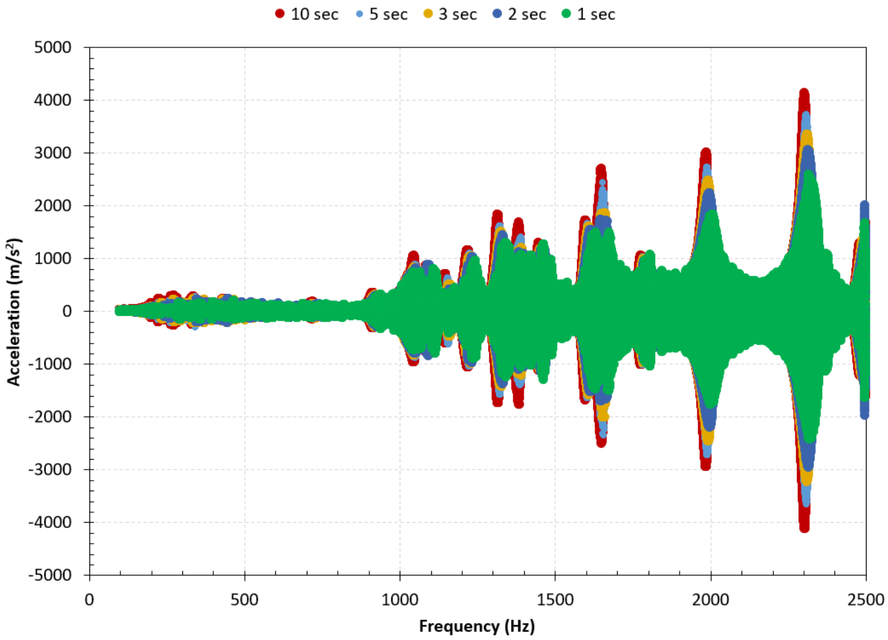

Figure 6:2 - Acceleration at plate’s end for a frequency sweep of 100 Hz to 2500 Hz for piezoelectric actuator 5 at 200 Vpp

Acceleration amplitudes for resonant modes generally show an increase with a frequency increase for a same input since acceleration amplitude is proportional to the square of the frequency of the displacement amplitude. This is why, even if larger displacements were obtained at the lower frequency modes investigated in chapter 5, the acceleration measured for those modes was small compared to other modes at higher frequencies. The resonant modes activated by the actuators were easily distinguishable by the distinct peaks in acceleration on the curve at their different frequencies. The two plots showed that the resonant modes were not all activated by each actuator, and some modes had a better deployment depending on the actuator activated, which is what was expected from the conclusions obtained in sections 2.4.1.1 and 2.4.1.3.

The two plots also show that the vibration pattern was the same for all the different sweep durations. The same modes were activated and their amplitude relative to the other modes was similar whether the frequency sweep was performed in 1 second or 10 seconds. The acceleration amplitude for each resonant mode increased with frequency sweep duration. For some modes, the amplitude was up to 1.8 times higher when the sweeping lasts 10 seconds compared to 1 second. These results indicated that when sweeping was performed at higher sweeping rates, complete mode deployment was not obtained and displacement and stress generation was not optimal for de-icing operations. The vibration pattern being the same for all duration, there did not seem to be any other transient effect, like mode superposition or residual effect from previous activated modes, at those sweeping speed.

More testing was performed to validate those conclusions by performing frequency sweeps of different frequency ranges and duration focused around a single resonant mode. The resonant mode at 1977 Hz was selected with its high acceleration amplitude. The different frequency ranges were performed to measure if residual modes deployed at other frequencies during a frequency sweep could have an effect on the acceleration obtained. A large frequency sweep, 100 Hz to 5000 Hz, was first performed for different durations, 1, 2, 3, 5 and 10 seconds, with piezoelectric actuator 5, to encompass a maximum of frequencies susceptible to affect the mode deployment of the selected mode (1977 Hz). More tests were performed with lower frequency ranges for the same durations, down to a frequency range of 1950 Hz to 2000 Hz, which completely isolated the frequency of 1977 Hz from any other resonant mode susceptible to interfere with its deployment. A last test was performed in steady-state mode at 1977 Hz to remove any effect that could be caused by sweeping and transient vibration. The maximum accelerations recorded are presented at Figure 6:3 and Figure 6:4 in function of the sweep rate in Hz/s. The sweep rate was defined as the rate of the variation of frequency during a sweep. For example, a sweep of 100 Hz to 5000 Hz in 1 second had a sweep rate of 4900 Hz/s, while a sweep of 1950 Hz to 2000 Hz in 10 seconds had a sweep rate of 5 Hz/s.

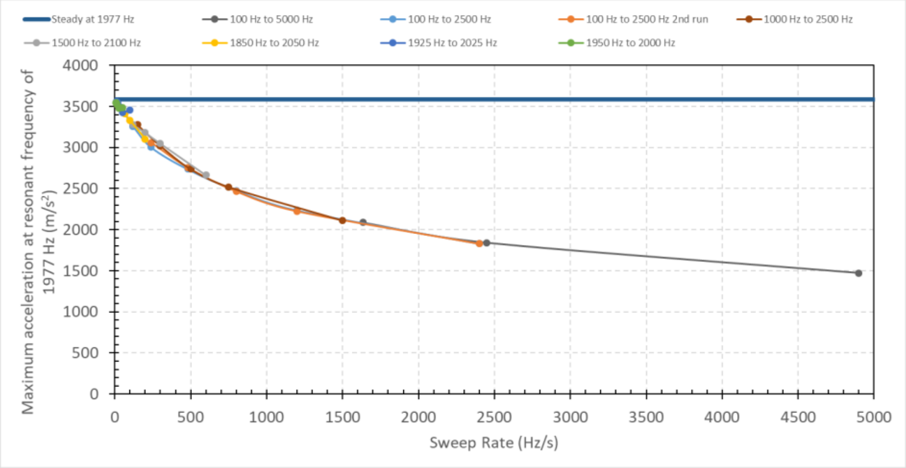

Figure 6:3 – Maximum acceleration at 1977 Hz on plate edge for frequency sweeps of different frequency ranges in function of sweep rate at 200 Vpp with piezoelectric actuator 5

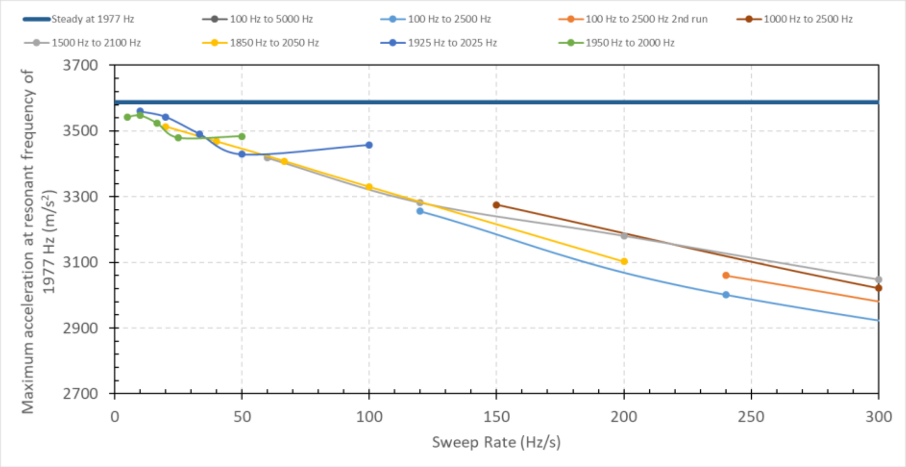

Figure 6:4 – Results of Figure 6:3, zoomed for sweep rates below 300 Hz/s

The results show that as the sweeping rate tends towards zero, acceleration tends toward the steady-state value, which means that there is no additional benefit in acceleration and displacement brought by transient effect during frequency sweeps. This means that maximum mode deployment is obtained at fixed frequency or when sweep rate tends towards zero. For this mode, at sweeping rates below 300 Hz/s, acceleration was around 85% and higher of the steady-state mode acceleration, and was above 90% at 120 Hz/s and below.

The results also indicated that the frequency range of the sweep has no impact on the maximum acceleration and mode deployment during resonance. The curves for the maximum acceleration in function of sweep rate of the different frequency range tested overlap each other and follow the same trend, which indicates that residual effects of other modes deployed during the same frequency sweep does not influence the mode deployment.

More sweep tests were performed around 192 Hz, 1310 Hz and 4669 Hz. The tests were done for different frequency ranges and different duration. Figure 6:5 a) b) and c) presents the results for the maximum acceleration obtained at those three frequencies during the different sweep tests. These curves again show that the frequency range of the frequency sweep had no impact on the maximum acceleration obtained at the resonant frequency. They also confirmed that the maximum acceleration increased when the sweep rate decreased and that as the sweep rate tended towards zero the maximum acceleration tended toward the steady-state value.

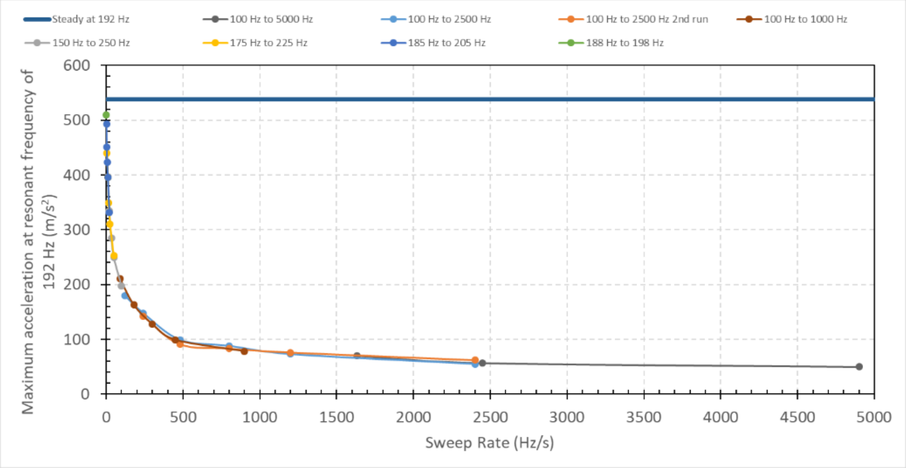

a)

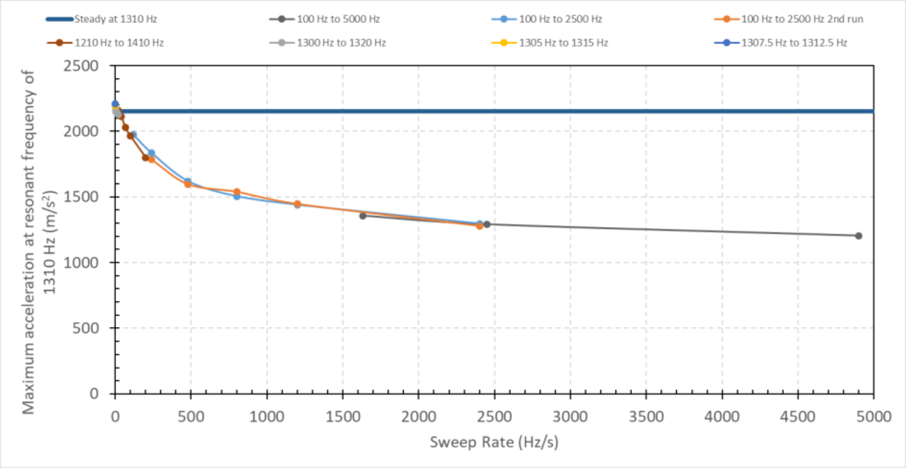

b)

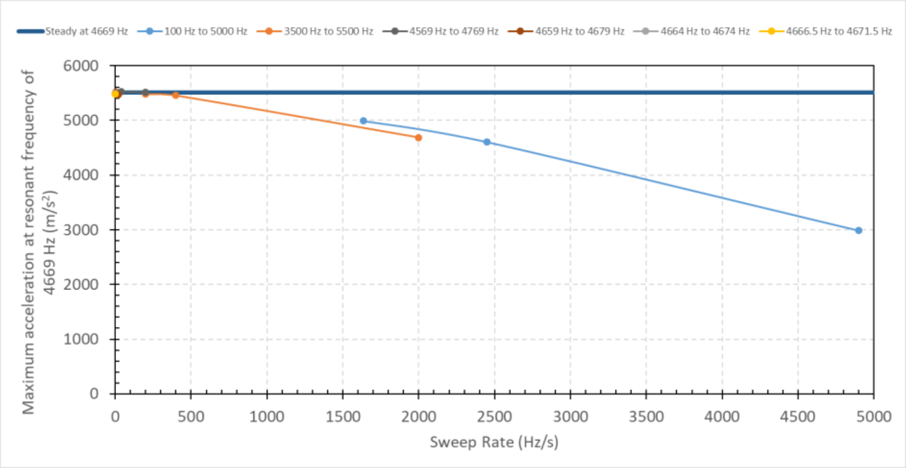

c)

Figure 6:5 – Maximum acceleration on plate edge for frequency sweeps of different frequency ranges in function of sweep rate at 200 Vpp with piezoelectric actuator 5 at a) 192 Hz b) 1310 Hz and c) 4669 Hz

It is also possible to observe from Figure 6:5 that at a lower frequency like 192 Hz, the maximum acceleration shows a very sharp increase at very low sweep rate while at a higher frequency like 4669 Hz, the maximum acceleration increases more steadily and reaches values close to the steady-state value at a much higher sweep rate. Figure 6:6 presents the ratio of the maximum acceleration measured during sweep tests compared to the steady-state value in function of sweep rate. It can be observed that lower sweep rates are required to obtain significant mode deployment at low frequencies. With higher frequencies, faster sweep can be performed to obtain similar maximum acceleration ratio, which mean that sweep rate during de-icing tests must take into account the frequency of the targeted modes to ensure sufficient mode deployment and strain generation. At a rate of 4900 Hz/s, the ratio of acceleration compared to steady-state mode was below 0.56 for all the frequencies. At 200 Hz/s the ratio was 0.28 for 192 Hz, 0.84 for 1310 Hz, 0.88 for 1977 Hz and 0.99 for 4669 Hz, while at 20 Hz/s the ratio was above 0.98 for all frequencies except 192 Hz where it was only 0.62.

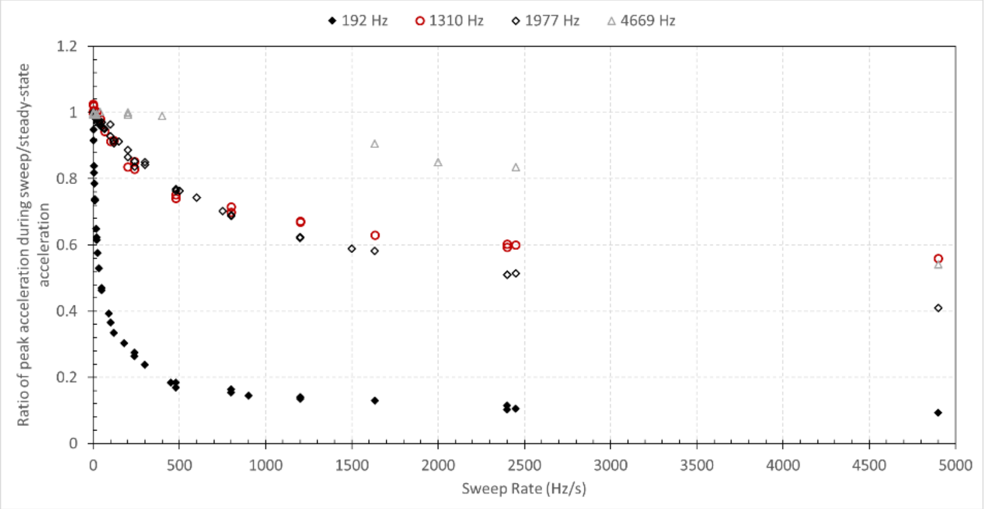

Figure 6:6 – Ratio of the maximum acceleration for sweep tests on the steady-state activation value

This was to be expected since higher frequency means shorter time period for a single vibration cycle, which means that the same number of cycles for a mode occurs in less time than at lower frequency. Figure 6:7 shows an example of mode deployment at 1977 Hz after voltage was applied to actuator 5. The time and number of cycles before 95% of the steady-state acceleration was reached after voltage was applied is compared in Table 6:1 for the four frequencies investigated. The number of cycles was in the same order of magnitude for all frequencies, ranging from 127 cycles to 297 cycles without a straight relationship to frequency value, while the time greatly diminished as the frequency increased, from 0.660 s to 0.046 s.

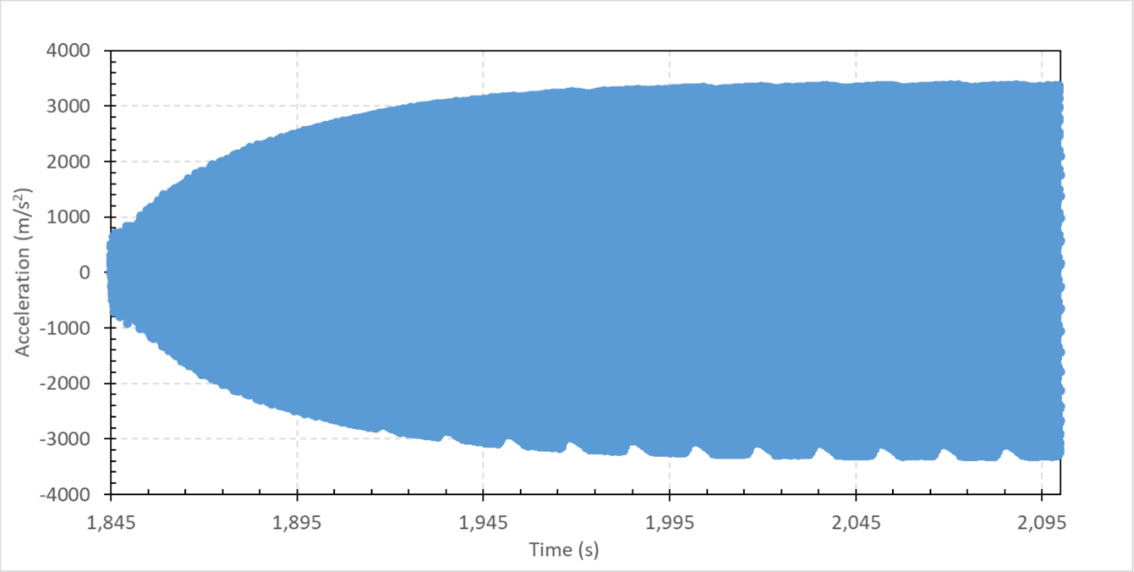

Figure 6:7 – Acceleration on edge of the plate after 200 Vpp at 1977 Hz is applied on piezoelectric actuator 5 in function of time

Table 6:1 – Number of cycle and time to reach 95% of steady-state acceleration after voltage application on actuator 5 at 200 Vpp

Frequency (Hz)	Nb of Cycles	Time (s)
192	127	0.660
1310	297	0.227
1977	230	0.116
4669	215	0.046

These results show that the transient effects occurring during frequency sweeps did not generate a different deployment of the resonant modes and could not provide increased acceleration value resulting in higher strain and stress generation on the plate. They also demonstrated that resonant modes require a minimum of vibration cycles before they reach steady-state regime. During sweeping, if the sweep rate is too high, not enough vibration cycles are generated, limiting mode deployment and maximum acceleration obtained. As the sweep rate tends towards zero, the acceleration of a resonant mode during the sweep will tend towards its steady-state value. Since a minimum of vibration cycles is required for complete mode deployment, this implies that at lower frequencies the time required to obtain full acceleration is higher. For this reason, lower sweep rate are required at lower frequencies. The frequency range of the sweep has no impact on the mode deployment and acceleration obtained for a resonant mode, meaning that no effect is transposed from mode to mode during the frequency sweeps performed. Those conclusions are in agreement with the theory on the response of a single degree of freedom system to harmonic excitation [74]. A system with distinct resonant modes like the one studied in this chapter can be simplified and study as a single degree of freedom system. The analytical solution of such systems is composed of two parts, the homogenous solution and the particular solution. The homogenous solution is transient and diminishes with time, while the particular solution is constant and will repeat itself continuously, resulting in the steady-state response of the system. This is in agreement with the results obtained, showing that as the modes gets more time to deploy, their vibration amplitude will tend towards the steady-state regime. The homogenous part, which describe the transient behavior of the system, is dependent on the magnitude of the natural frequency excited. This is also in agreement with the results obtained, explaining why higher frequencies will reach steady-state regime quicker than lower frequencies. If the frequency is low, the time for the homogenous solution to reach zero and stop impacting the vibration amplitude is longer, resulting in a longer time and slower sweep required to reach steady-state response.

These conclusions indicate that frequency sweeps do not help the de-icing process by generating higher acceleration or stress/strain on the plate and in an ice layer accumulated on the plate, and steady-state excitation of a resonant mode is the theoretical ideal case. However, they can help ensure that a resonant mode is excited by covering a defined frequency range. The exact frequency of a resonant mode will vary in function of the ice accumulation and other ambient condition effect impacting the mass and rigidity of the structure. By performing a frequency sweep, it is not required to target a very precise and specific frequency value that changes as the ice accumulates on the structure, which could be easier and more reliable for a de-icing system. The sweep rate of the sweep used must be studied correctly to allow for a sufficient mode deployment and strain/stress generation, while still permitting a rapid and efficient de-icing process. The conclusions obtained in this section do not explain the de-icing successes obtained with the frequency sweeps and unsuccessful results with steady-state frequencies in the previous phases of this project.

6.1 SUMMARY

In this chapter, frequency sweep and steady-state mode excitation of the actuators were studied and compared. Also, potential transient effect during frequency sweep excitation were also looked for. Results have shown no indication of transient effect during frequency sweep excitation and that the range of the frequency sweep had no effect also on vibration of a resonant mode. Also the results have shown that, as the sweep rate (velocity) of the frequency sweep decreased towards 0, the vibration amplitude tends towards the steady-state value, demonstrating that steady-state excitation is the optimal excitation. For mode at lower frequencies, more time and slower sweep rate are required to reach vibration levels close to the steady-state response during frequency sweeps as compared to mode at higher frequencies. Those results were in agreement with the theory on the vibration response of single degree of freedom systems to harmonic excitation.

CHAPTER 7

ICE ACCUMULATION ON THE FLAT PLATE STRUCTURE

Previous sections studied the vibration of the flat plate setup generated by the piezoelectric actuators, both numerically and experimentally. In this section, investigation was done on the flat plate setup when an ice layer is present to understand the vibration phenomenon as well as the mechanical phenomenon within the ice layer in order to create de-icing. The investigation was first performed experimentally. Ice was accumulated on the flat plate setup in a cold room and vibration and de-icing tests were performed. Then, ice was added to the flat plate numerical model and the results obtained experimentally were used to validate the model and explore and understand de-icing of the flat plate.

7.1 EXPERIMENTAL TESTING

7.1.1 ICE ACCUMULATION

The flat plate setup was installed in a refrigerated chamber that can maintain temperatures down to -30°C. The chamber was equipped with a hydraulic spraying system consisting of a pressurized refrigerator connected to a Spraying systems 650017 nozzle. The water pressure in the system was kept at 80 psi which generated droplets of 115 µm of Median Volumetric Diameter. The nozzle was installed on a translation track over the flat plate setup and was moved along this track at constant speed to evenly distribute water droplets over the length of the plate (Figure 7.1:1). Once the nozzle had made its movement back and forth along the track, the spraying was stopped for 10 seconds before a new spraying run was performed.

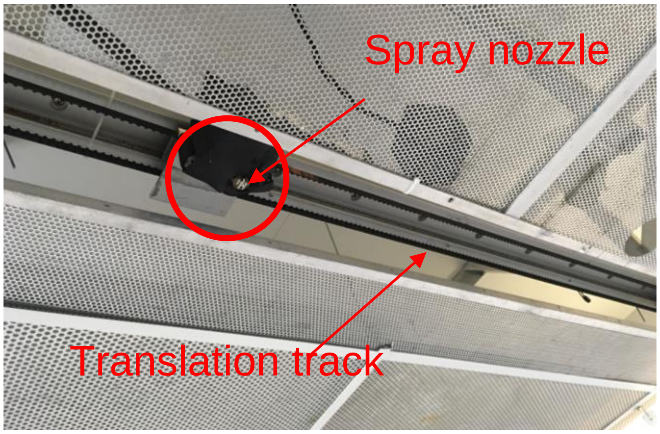

Figure 7.1:1 – Spray nozzle installed on translation track

Ice layer was accumulated on the plate before each tests at a temperature of -8°C. This temperature allowed for a glaze ice to be generated without liquid water flowing off the ice layer. An aluminum cover with a rectangular hole in the middle was installed on the flat plate setup before each ice accumulation. This allowed the accumulation of a 3 cm wide and 45 cm long ice layer, which was a good representation of ice accumulated on the leading edge portion of a complete profile. The accumulation was done in one hour at a precipitation of 2 mm/h, resulting in a 2 mm thick ice layer. An example of an accumulated ice layer is presented at Figure 7.1:3.

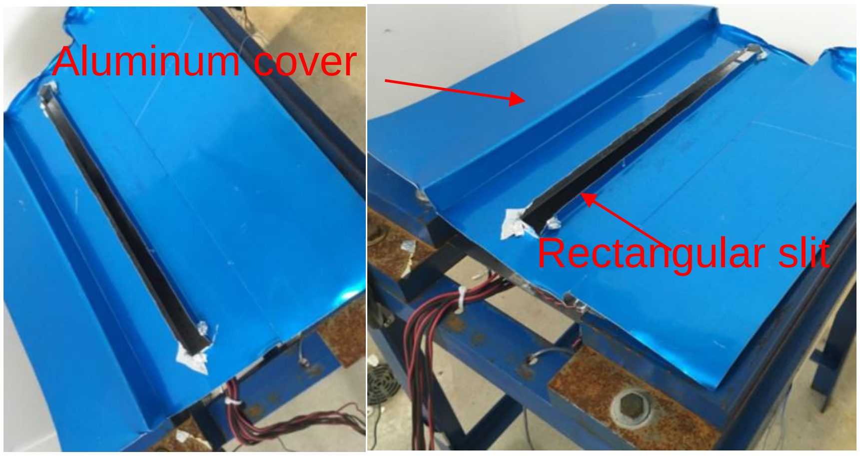

Figure 7.1:2 – Aluminum cover for ice accumulation

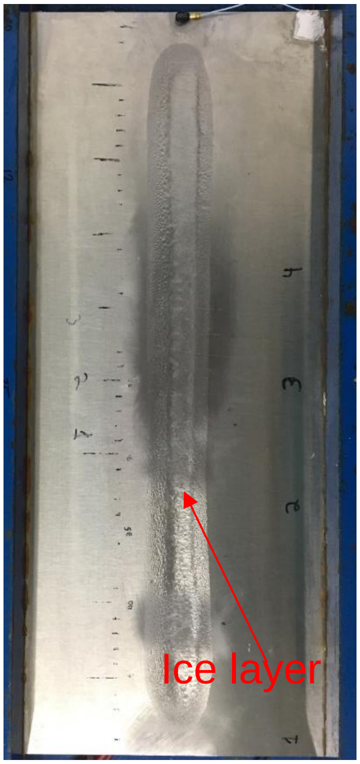

Figure 7.1:3 – Ice layer accumulated on the flat plate setup

7.1.2 FREQUENCY SWEEP DE-ICING TESTS WITH CAMERA

Results and conclusions obtained in section 6 showed that transient effect during sweeping tests should not provide any benefit in mode deployment and acceleration generation compared to steady-state mode. They demonstrated that acceleration tends toward steady-state value as the sweeping rate tends towards zero, meaning that steady-state vibration should be the ideal case for de-icing tests in term of stress and displacement generation. In previous phases, de-icing only occurred during frequency sweep tests and not for steady-state activations. Since steady-state is the optimal case, this means that the wrong resonant modes were used in steady-state activations or that the frequencies used to excited the modes were slightly off due to the impact of the ice layer on structure rigidity and mass. To verify this hypothesis, a Blaster ACA1300-200uc camera was installed in the cold room above the flat plate setup (Figure 7.1:4). The camera was used to take multiple pictures during de-icing tests to define the frequencies and resonant modes where cracking and delamination of the ice occur. The signal generator triggered the camera when the electrical signal was sent to the actuators to synchronize the pictures with the frequency sweep. The camera recorded pictures at a frame rate of 15 pictures/second and recorded the time at which the picture was taken. Equation 43 allowed to calculate the frequency corresponding to each picture taken:

$$f_{pic} = \frac{t_{pic}}{t_{sweep}}\left(f_f - f_i\right) + f_i \tag{43}$$

with f_{pic} the frequency of the picture, t_{pic} the time at which the picture was taken after the start of the sweep, t_{sweep} the duration of the sweep, f_i the initial frequency of the sweep and f_f the final frequency of the sweep.

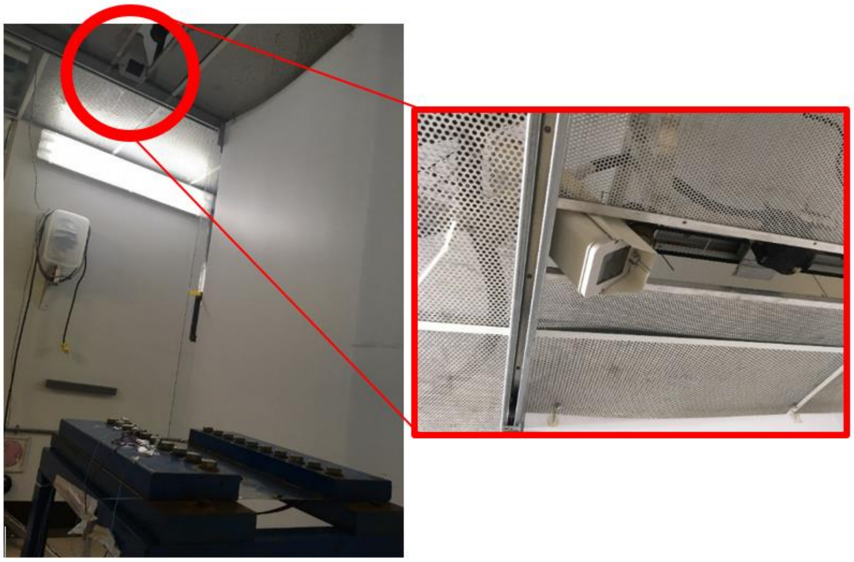

Figure 7.1:4 – Camera installed over flat plate setup

Four frequency sweep tests were performed with the five piezoelectric actuators activated in phase at 600 Vpp. This activation of all the actuators at a higher voltage favored fracture and delamination of the ice. The frequency sweeps were planned in the range studied in previous sections, from 160 Hz to 1000 Hz.

The first sweep was set at 160 Hz to 500 Hz. The sweep duration was set at 60 seconds to maximize precision of the calculated frequency values at which cracking and delamination occurred with the pictures obtained with the high-speed camera. It also allowed a sufficient mode deployment with a sweep rate lower than 10 Hz/s. The sweep was started at 160 Hz since the first resonant mode had been defined at 177 Hz at section 5.1. The pictures show that delamination of the ice layer from the flat plate was obtained on one half of the plate after 5.672 seconds (Figure 7.1:5). Delamination can be observed by the apparition of a white layer underneath the clear transparent ice accumulation, due to the presence of air between the substrate and the ice. Delamination on the other half of the plate was also observed after 6.614 seconds. With equation 43, this resulted in a frequency of 194 Hz.

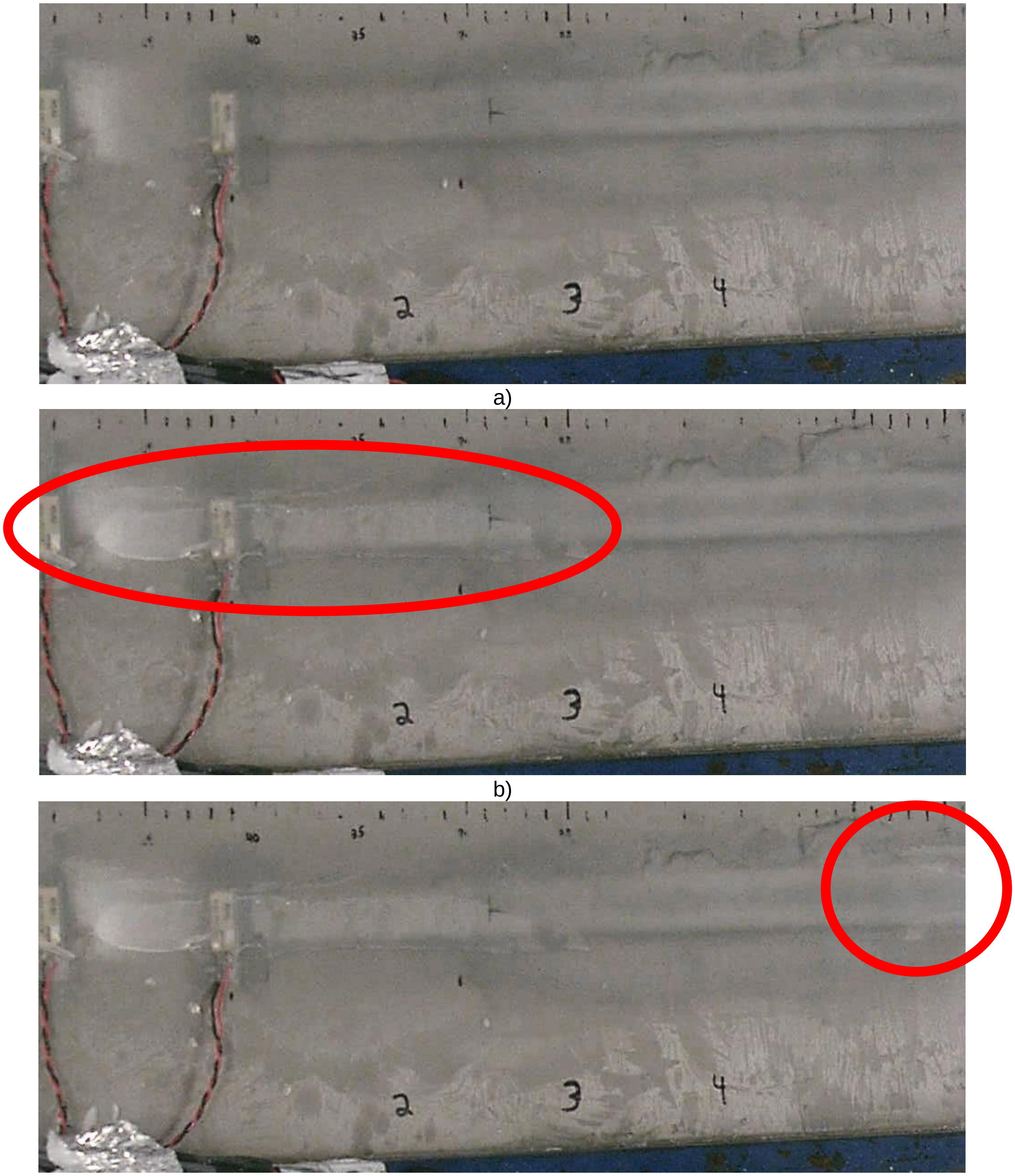

a)

b)

c)

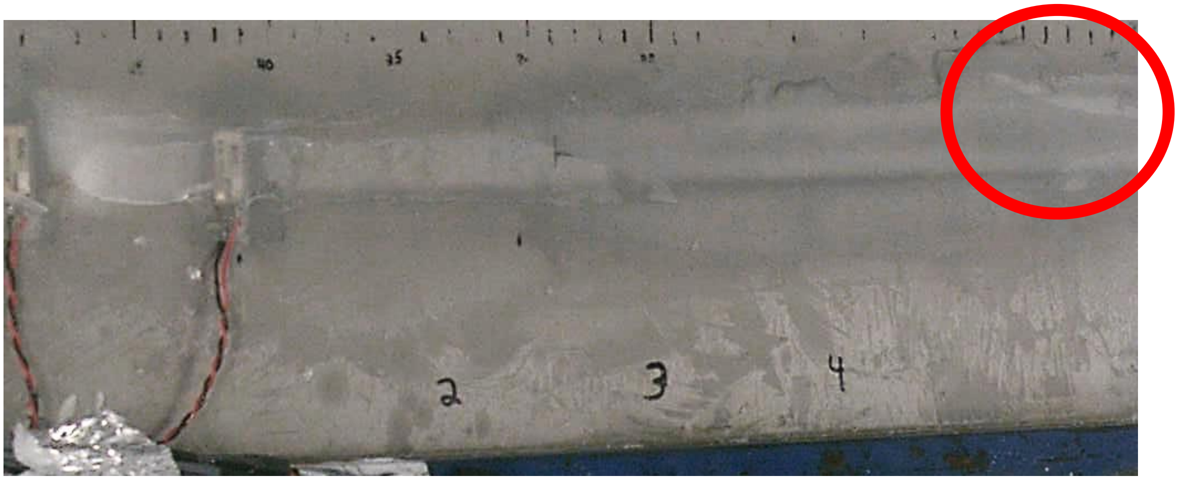

d)

Figure 7.1:5 - Pictures obtained during a frequency sweep of 160 to 500 Hz in 60 seconds with the five actuators activated in phase at 600 Vpp taken after a) 5.568, b) 5.672, c) 6.614 and d) 6.719 seconds respectively

In the previous sweep tests, only the frequency at which the first delamination occurred was investigated. After the delamination was obtained, the rigidity of the ice covered flat plate was different, which means that following cracking or delamination could be obtained due to higher vibration caused by a lower rigidity of the iced plate structure or that the frequency at which it occurs is different then for a clean uncracked ice layer due to this rigidity difference. This made these frequencies unreliable for the steady-state tests and was the reason why they were disregarded. In order to obtain more resonant modes which were susceptible to generate delamination and cracking of the ice, an additional test was performed in this frequency range starting at 250 Hz, passed the frequency obtained with the first test, up to 500 Hz, again in 60 seconds, for a sweep rate of 5 Hz/s. This test was performed on a newly accreted ice layer, without delamination or cracking. A single crack was observed during this second sweep at the center of the plate after 43.532 seconds (Figure 7.1:6) for a matching frequency of 431 Hz.

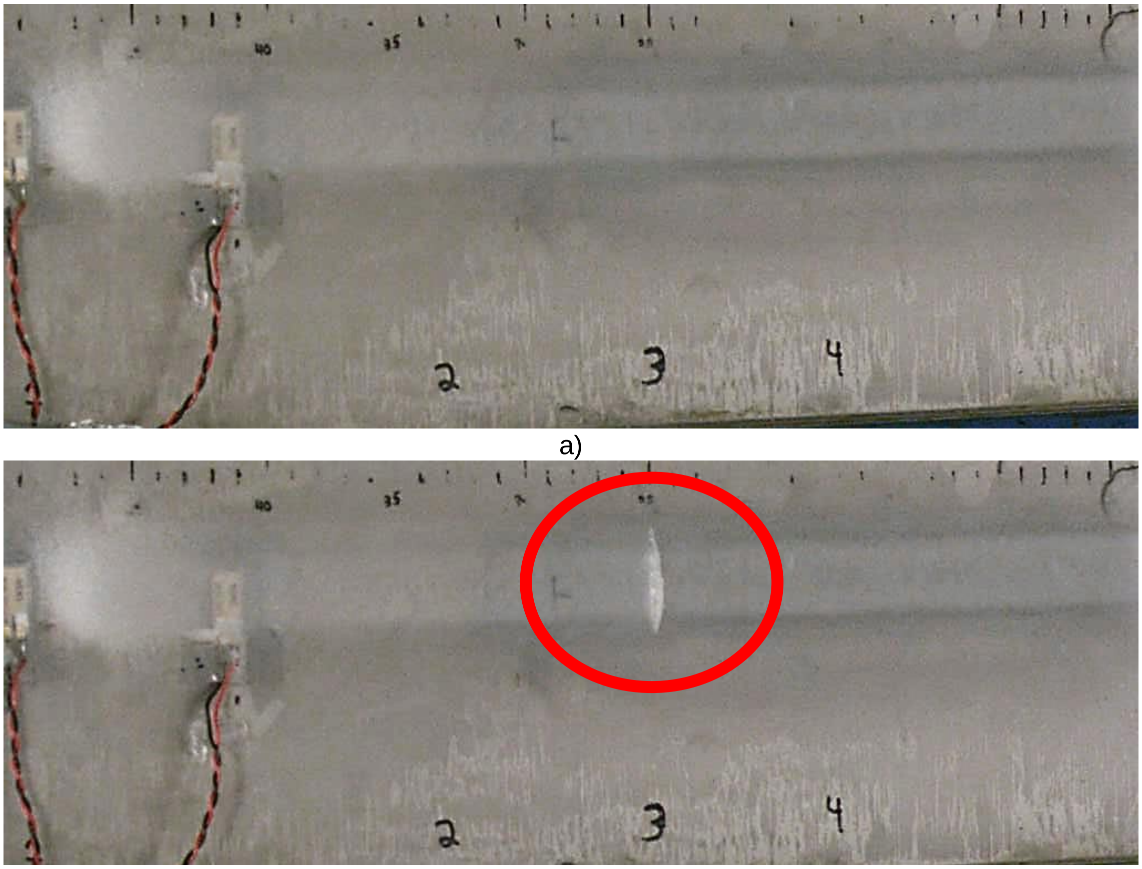

a)

b)

Figure 7.1:6 – Pictures obtained during a frequency sweep of 250 to 500 Hz in 60 seconds with the five actuators activated in phase at 600 Vpp taken after a) 43.465 and b) 43.532 seconds respectively

The third sweep test ranged from 500 to 1000 Hz, to study the other half of the frequency range investigated in the previous sections of this thesis. No cracking or delamination of the ice was obtained during this test. For this reason, the sweep range was extended to 1500 Hz. A fourth sweep was performed from 1000 Hz to 1500 Hz, again in 60 seconds. A very small delamination on one tip of the ice layer was observed after 13.265 seconds (Figure 7.1:7) with a more significant delamination and cracking in the longitudinal direction after 23.999 and 25.799 seconds. This lead to a frequency between 1111 and 1215 Hz. This broader frequency range was inspected more closely in the next sections of the project to define the frequency where acceleration and displacement was maximum and obtain the corresponding resonant mode.

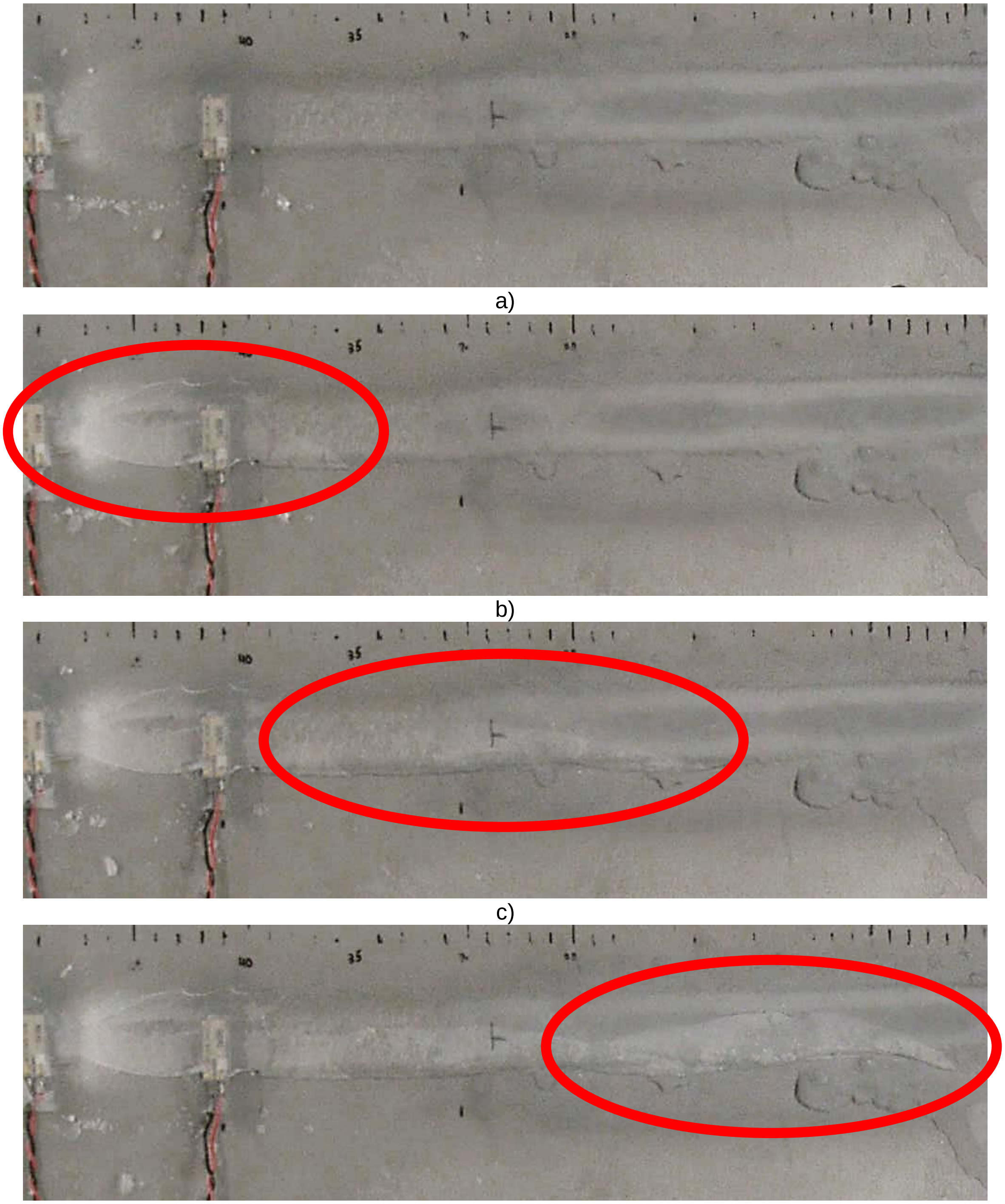

a)

b)

c)

d)

Figure 7.1:7 - Pictures obtained during a frequency sweep of 1000 to 1500 Hz in 60 seconds with the five actuators activated in phase at 600 Vpp taken after a) 13.265, b) 13.333, c) 23.999 and d) 25.799 seconds respectively

As for the tests below 500 Hz, an additional sweep test was performed on a newly accreted ice layer on the other half of the frequency range tested, from 1250 to 1500 Hz in 60 seconds. A single crack was first observed after 7.466 seconds. After 7.533 seconds, a second crack appeared on the second half of the plate as well as very small delamination zones next to the cracks (Figure 7.1:8). This corresponded to a frequency of 1281 Hz.

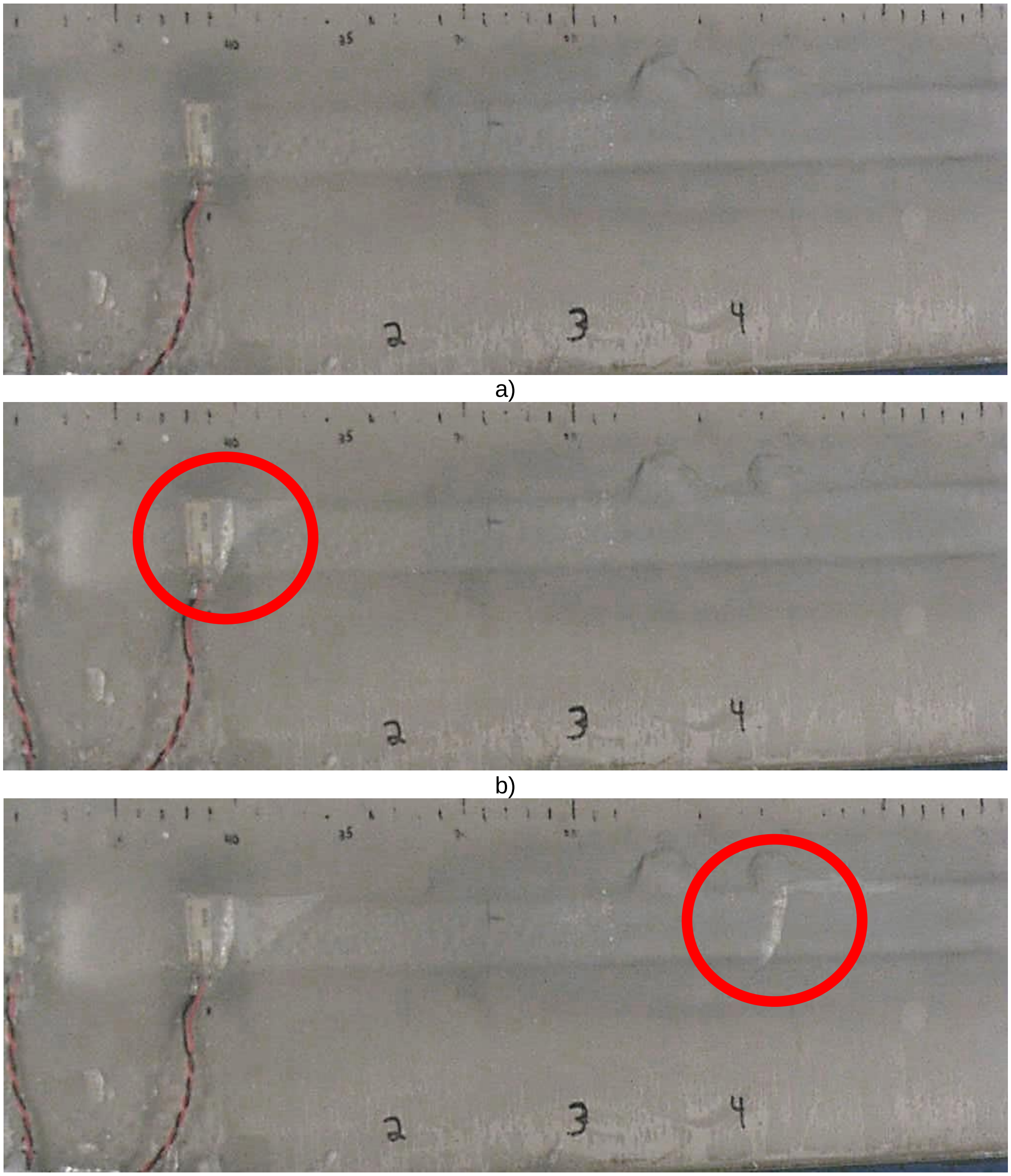

a)

b)

c)

Figure 7.1:8 – Pictures obtained during a frequency sweep of 1250 to 1500 Hz in 60 seconds with the five actuators activated in phase at 600 Vpp taken after a) 7.399, b) 7.466 and c) 7.533 seconds respectively

The use of the camera has allowed to locate two frequencies at which cracking occurred and two frequencies at which delamination occurred. In the third frequency sweep performed, from 500 to 1000 Hz, no cracking or delamination was obtained which is the reason why the frequency range studied was extended up to 1500 Hz. The frequencies and type of ice breaking obtained during those tests are presented at Table 7.1:1. The conclusions from section 6 indicated that no benefit in magnitude of vibration of the plate is obtained when sweeping is performed and that the optimal activation for mode deployment and vibration magnitude should be the steady-state mode. This means that cracking and delamination of the ice should also occur in steady-state activation at the four frequencies defined during the tests with the camera.

Table 7.1:1 – Frequencies and type of ice breaking obtained with camera frequency sweep tests

Frequency (Hz)	**Type of Ice Breaking**
194	Delamination
431	Crack
1111 to 1215	Delamination
1281	Crack

7.1.3 STEADY-STATE MODE DE-ICING TESTS

In previous phases of the project, de-icing or even cracking and delamination of the ice was not achieve by activating a single resonant mode in steady-state mode. However conclusions obtained at section 6 have shown that steady-state mode is the optimal case for mode deployment, acceleration and strain generation. With the new setup designed in this project and the help of an accelerometer and a camera, it has been possible to determine frequencies where cracking and delamination of the ice is obtained during sweeping tests. Four frequencies were found by performing frequency sweeps at low sweep rate, below 10 Hz/s and a summary of those frequencies and the type of ice breaking observed is presented at Table 7.1:1 in the previous section. In this section, those frequencies were submitted to tests in steady-state mode to confirm if they could create ice breaking and define if transient effect during sweeping did not help mode deployment and de-icing.

For these tests, ice was accumulated on the flat plate as per section 7.1.1 and the accelerometer on the plate was used to locate the frequency where acceleration was maximum around the frequencies of Table 7.1:1. The voltage during this procedure was kept below 100 Vpp to keep the integrity of the ice layer on the plate. Once the frequency was determined, voltage was slowly increased manually until cracking or delamination occurred or up to a maximum voltage of 700 Vpp, to prevent damaging of the actuators. The voltage could not be increased during data acquisition with the actual system due to interference in the signals. For this reason, data acquisition of the accelerometers was not done in this section. All actuators were activated in phase to repeat the activation done in the previous section.

The first frequency found with the camera was 194 Hz, where delamination of the ice was obtained. After ice was accumulated on the plate, a resonant frequency was found at 188 Hz. The voltage was slowly increased manually until delamination of the ice was obtained at one extremity of the ice layer at 550 Vpp (Figure 7.1:9). No change in frequency was done during the test, only voltage was increased. The delamination of the ice resulted in a change in rigidity of the structure which impacted its resonant frequency. After the delamination of the ice, a resonant frequency was now found at 185 Hz, by searching the frequency while the voltage was lower than 100 vpp. The voltage was then increased from this value until the delaminated zone increased to reach the middle of the plate, at 550 Vpp (Figure 7.1:10). This caused a new change in rigidity and the new resonant frequency was now obtained at 183 Hz. The voltage was increased from below 100 Vpp up to 575 Vpp, where the delamination zone increased until the other end of the ice layer (Figure 7.1:11). The final state of the ice layer after those three solicitation is shown at Figure 7.1:12.

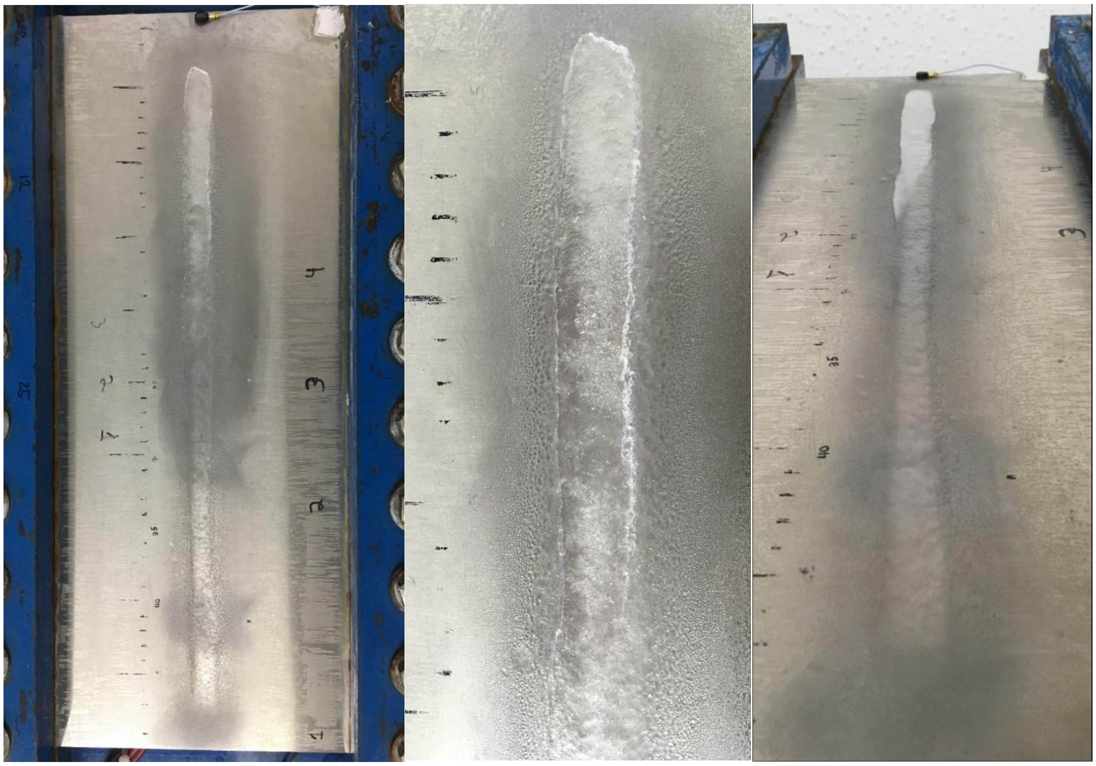

Figure 7.1:9 – Delamination of the ice at 550 Vpp in steady-state activation with all piezoelectric actuators activated in phase at 188 Hz

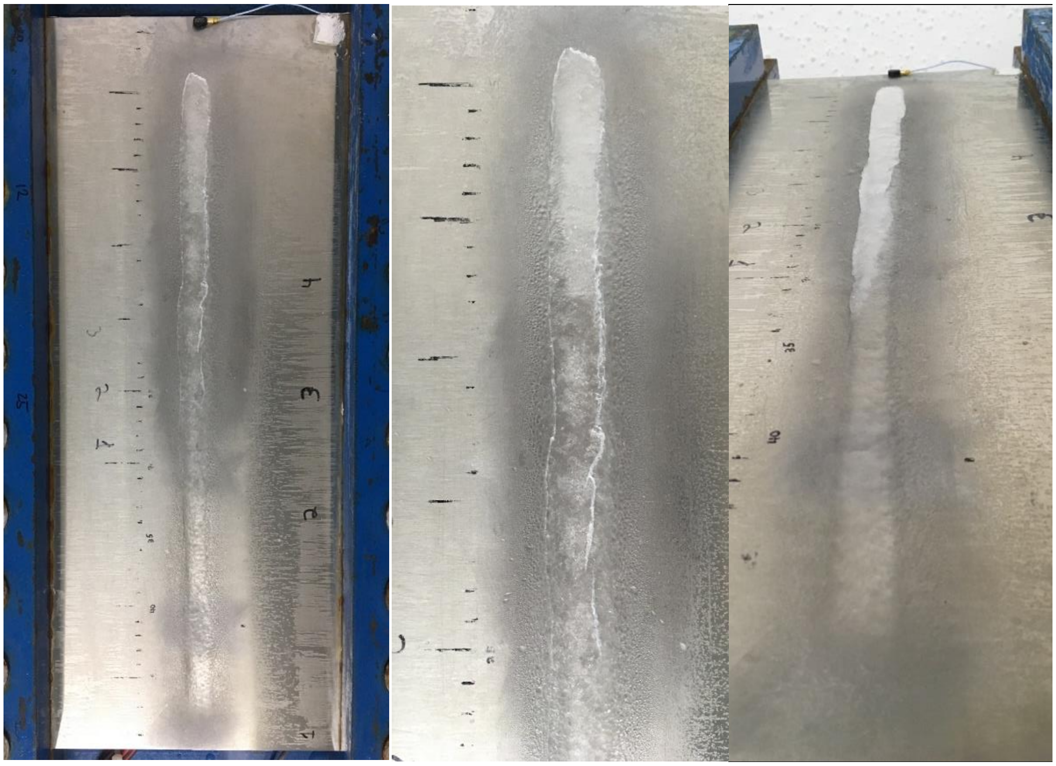

Figure 7.1:10 – Delamination of the ice at 550 Vpp in steady-state activation with all piezoelectric actuators activated in phase at 185 Hz

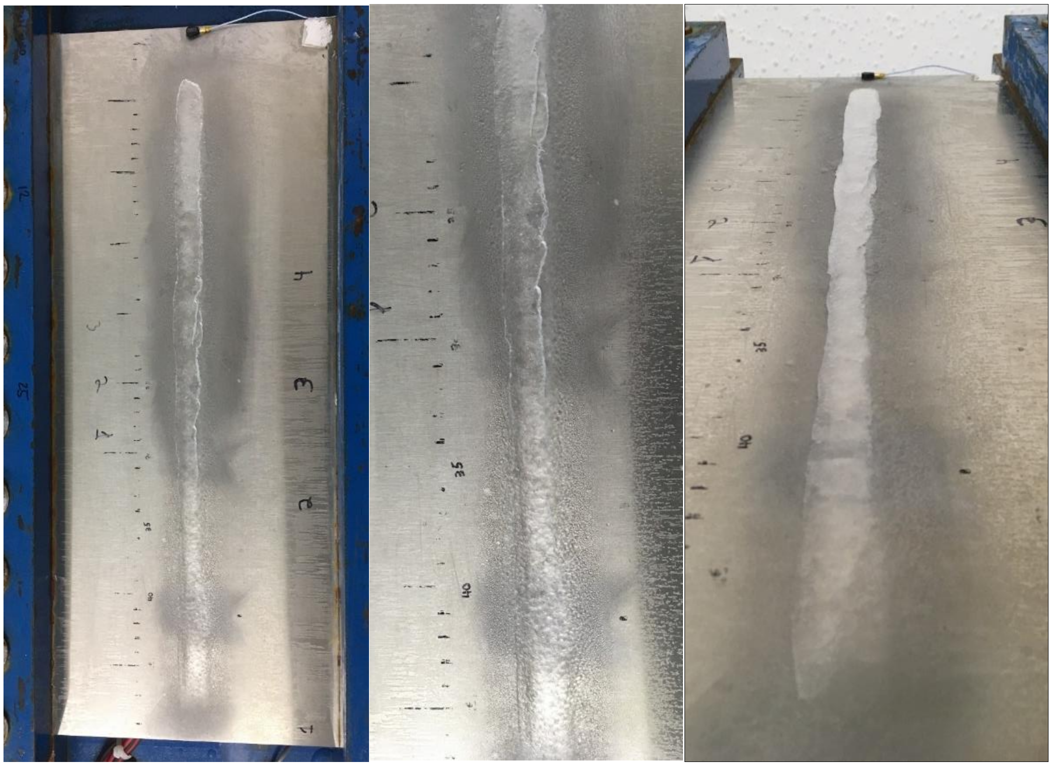

Figure 7.1:11 – Delamination of the ice at 575 Vpp in steady-state activation with all piezoelectric actuators activated in phase at 183 Hz

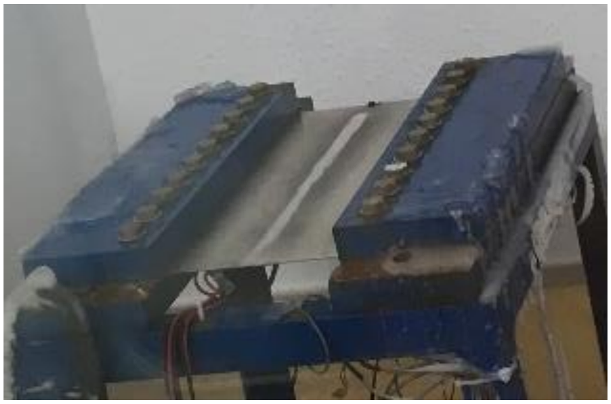

Figure 7.1:12 – Final state of the ice layer after steady-state tests at 188 Hz, 185 Hz and 183 Hz

The first frequency at which cracking of the ice was obtained was 431 Hz, with one crack in the center of the plate. After the ice accumulation, the resonant frequency was obtained with the accelerometer at 438 Hz. Voltage was increased until a single crack was obtained at 12 cm from the edge of the plate at 300 Vpp (Figure 7.1:13). The cracking of the ice layer resulted in a change of rigidity of the ice covered plate which changed the frequency of the resonant mode. The new frequency of the mode was found with the same method as for the first one and was now at 426 Hz. Tests at different voltage were performed in the same way and a new crack was obtained close to the center of the plate at 336 Vpp (Figure 7.1:13). This new crack once again resulted in a change of rigidity with a new resonant frequency of 418 Hz. A last crack was obtained on the other half of the plate (Figure 7.1:13) at 380 Vpp.

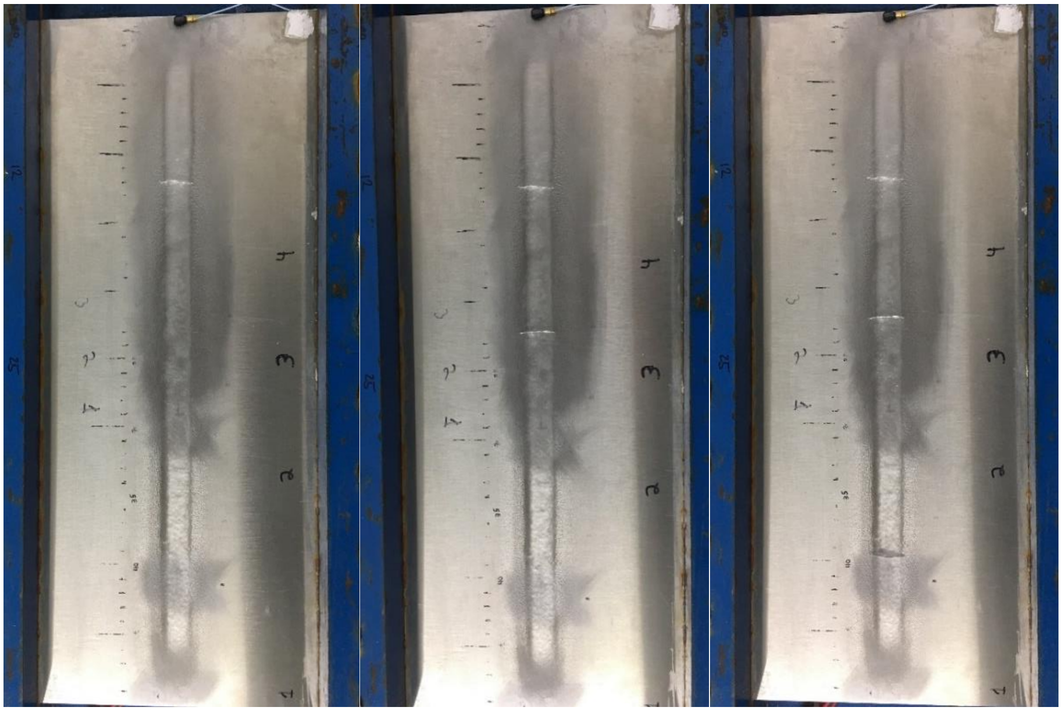

Figure 7.1:13 – Cracking of the ice layer in steady-state mode at 438 Hz and 300 Vpp (left), 426 Hz and 336 Vpp (middle) and 418 Hz and 380 Vpp (right)

Delamination and longitudinal cracking was observed between 1111 Hz and 1215 Hz. A resonant mode was found at 1138 Hz. The voltage was increased and delamination on both edge of the ice layer was obtained at 340 Vpp. Explanation for the broader range obtained in the previous section with the camera is given in the next section.

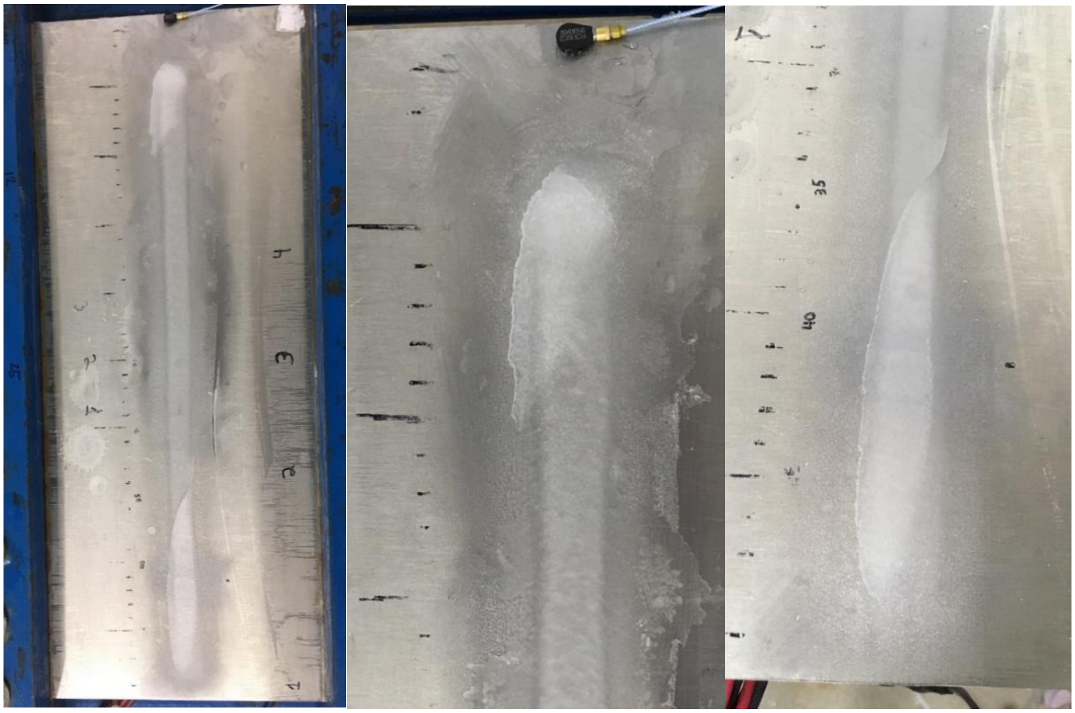

Figure 7.1:14 – Delamination of the ice layer in steady-state mode activation at 1138 Hz and 340 Vpp

The second mode found with the camera where cracking occured was at 1281 Hz. After the ice accumulation, the resonant frequency of the structure was found at 1338 Hz. The sinusoidal amplitude of excitation (voltage) was gradually increased to 320 Vpp, where a crack appeared at 11 mm from the edge (Figure 7.1:15).

Figure 7.1:15 - Cracking of the ice layer in steady-state mode at 1338 Hz and 320 Vpp

The tests performed in this section have proven that it is possible to create cracking and delamination of the ice layer on the flat plate in steady-state activation, without sweeping. This tended to confirm the conclusions obtained in section 6, in which maximum acceleration and mode deployment is obtained in steady-state mode and that surrounding modes during sweeping are not required to help cracking and delamination. They have also shown that it is mandatory to correctly determine which mode can lead to de-icing and the exact frequency of the resonant mode with the help of a sensor like an accelerometer to achieve de-icing. In previous studies de-icing in steady-state mode was tried by using frequencies selected arbitrarily from their mode shapes and accelerometers were not used to their full potential to find the actual frequency of the mode. Ice modifies the frequency of the resonant mode and repeatability of the ice layer accumulated can make the same mode varies in frequency from test to test. If the exact frequency is not used, acceleration and stress generation will be only a small fraction of those obtained at the exact frequency and de-icing will not occur. This explains the lack of success from previous studies: even if steady-state mode is the optimal activation, it is less practical and harder to achieve if the right tool are not used for these reasons.

The delamination obtained in those tests was due to an adhesive break. In a previous study [62], it was shown that two different delamination scenarios can be obtained during de-icing tests, an adhesive break and a cohesive break at the interface. The type of interface break is mainly defined by the atmospheric condition of accumulation of the ice as well as the surface parameters like roughness and thermal conductivity. Studies have been done on the subject where the impact of surface roughness structure was investigated on ice adhesion, from standard surface finish to specially engineered surface topography like hydrophobic and icephobic surfaces [75-77]. For an unpolished metal plate of standard mill finish similar to the one used in this study and at the selected accumulation conditions for the testing, Guerin has demonstrated that ice shows adhesive delamination [78], which is in consensus with the obtained results.

7.2 NUMERICAL MODEL OF THE FLAT PLATE WITH AN ICE LAYER

7.2.1 VALIDATION OF THE NUMERICAL MODEL WITH VERY LOW SWEEP RATE DE-ICING TESTS

In this section, sweep tests at very low sweep rate were performed around different resonant mode to measure the acceleration of the plate when cracking or delamination of the ice occurred. This information was then used to validate the accelerations predicted by the numerical model when an ice layer is added to the plate. Sweeps at very low sweep rate were used instead of steady-state regime for two reasons. First, the sweeping allowed damping calculation of the ice covered plate with the same method as for the clean plate without ice (see 5.2). The second reason was that in steady-state mode, cracking and delamination occurred immediately when the actuators were activated, which was most of the time not recorded by the accelerometers with the way the acquisition system worked. Section 6 has shown that at very low sweep rate, acceleration at resonant frequency tends towards the acceleration obtain in steady-state mode and the difference can be considered negligible. For this reason it was acceptable to use those values to validate the Direct-solution steady-state dynamic analysis validation.

7.2.1.1 ACCELEROMETER POSITIONING

Five accelerometers were installed on the flat plate for experimental validation of the numerical model with ice layer accumulation (Figure 7.2:1-a and b). A first accelerometer (accelerometer 1) was positioned at the edge on the top surface of the plate. Four additional accelerometers were installed underneath the plate to protect them from the ice accumulation. Positions of the accelerometers relative to the right edge of the plate are presented in Table 7.2:1. As a quality check measure, accelerometer 2 was installed underneath accelerometer 1. At this position, the signals of the two accelerometers were expected to be equal but in opposition of phase. Due to the system’s limitations, only the signal from three accelerometers could be recorded at the same time. The accelerometers were used to measure the frequency response functions of the plate and determine the natural frequencies to be used in the steady-state excitation. The accelerometer frequency response functions were also used to perform the numerical model validation of the set-up with an ice layer accumulation.

Table 7.2:1 – Accelerometer positions

Accelerometer (#)	Distance from right edge (cm)
1	0
2	0
3	12
4	25
5	30

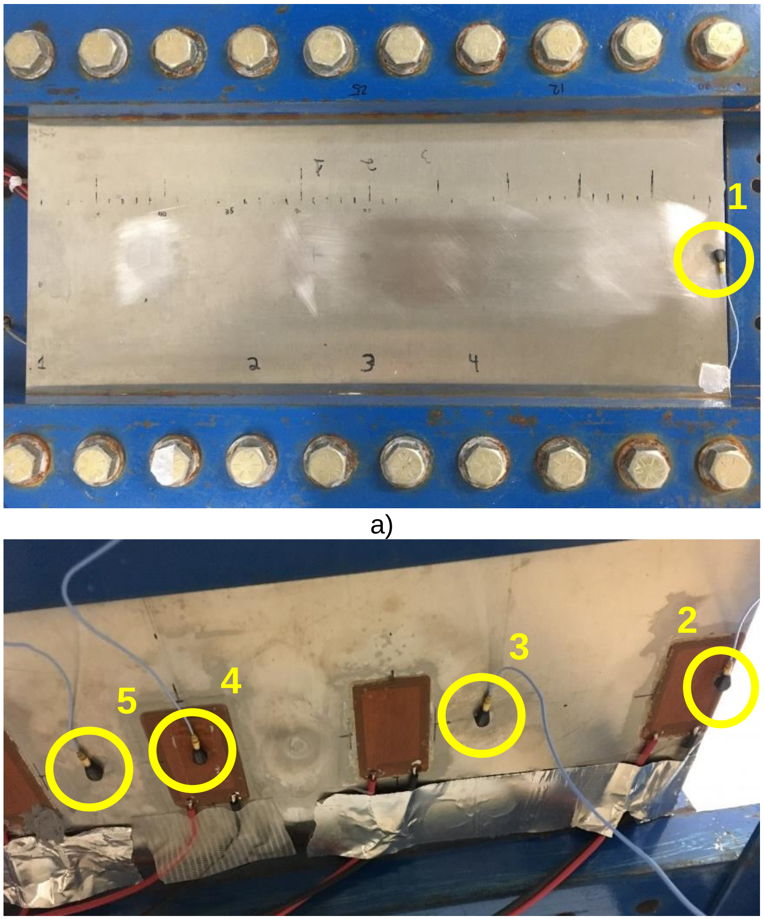

a)

b)

Figure 7.2:1 – Accelerometer positions on a) top of flat plate and b) under the flat plate

7.2.1.2 DAMPING CALCULATION

The ice layer on the flat plate modifies the rigidity of the structure as well as its damping. Damping in the numerical model must be adjusted to reflect the reality of the flat plate covered with the ice layer. The loss factor was used and input in the structural damping value in the numerical model. For the plate without ice, this value was obtained with the laser vibrometer software (see 5.2). With the laser being unavailable for this part of the project, the accelerometer signals were used to measure this value (Figure 7.2:2).

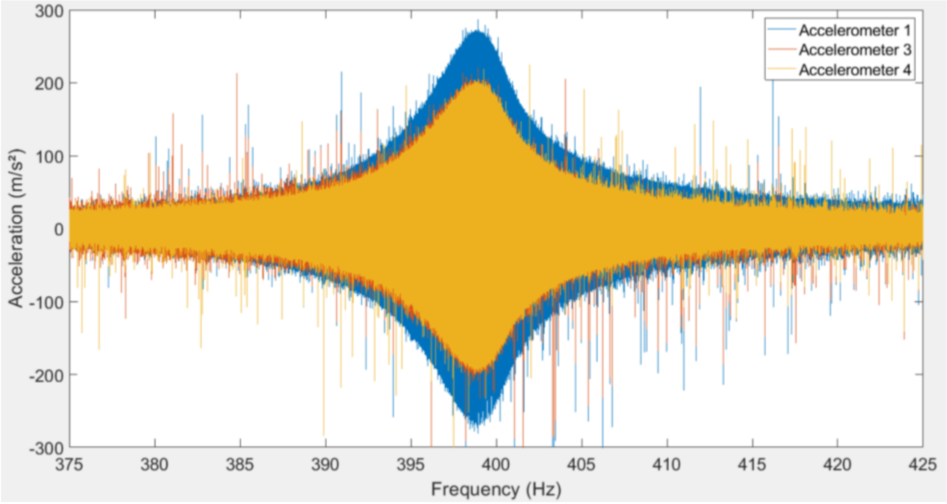

Figure 7.2:2 – Example of accelerometer signals obtained during a sweep with all the piezoelectric actuators activated in phase from 375 to 425 Hz in 10 s at 136 Vpp with accelerometers 1, 3 and 4

This signal was first converted from the time domain to the frequency domain with the help of a Fast Fourier Transform (FFT). This was previously done automatically by the laser vibrometer software. A homemade matlab code was used to convert the signal. A second matlab code, provided by the NRC, was then used to directly calculate the loss factor with the half power method from the matlab plot of the FFT. This was done with the signals obtained from the accelerometer during sweeps at low voltage before each de-icing tests to obtain the damping.

7.2.1.3 CRACKING OF THE ICE

Two modes have been found during the de-icing tests with the camera where cracking of the ice occurred. They were also successful in cracking the ice in steady-state activation. For each of those modes, ice accumulation was done on the flat plate with the same process as for previous sections and sweep tests at very low sweep rate were performed. Those sweeps were repeated and voltage was increased between each of them until cracking of the ice occurred. The acceleration and damping measured during those tests were used to validate the numerical model.

The first mode was found around 430 Hz during the camera tests and 438 Hz during the steady-state tests. Section 6 has shown that the sweep rate to reach at least 95% of the steady-state value depends on the mode frequency. The steady-state acceleration was obtained before the ice accumulation at 136 Vpp and compared to a sweep at 5 Hz/s, which was sufficient for 1310 Hz, but too high for 192 Hz. Figure 7.2:3 presents the accelerations in steady-state mode at 354 Hz while Figure 7.2:4 presents the acceleration during a sweep at 5 Hz/s around the same frequency. Acceleration for accelerometer 1 was 840 m/s² in steady-state mode while it was 810 m/s² at resonance during the sweep test, which corresponded to 96.5% of the steady-state value. For accelerometer 3 and 4, acceleration in steady-state mode was 650 m/s² while it reached 640 m/s² during the sweep at 5 Hz/s, which corresponded to 98% of the steady-state value. This confirmed that a sweep rate of 5 Hz/s was sufficiently low for this resonant mode, and as section 6 has concluded, for the other mode studied in this section.

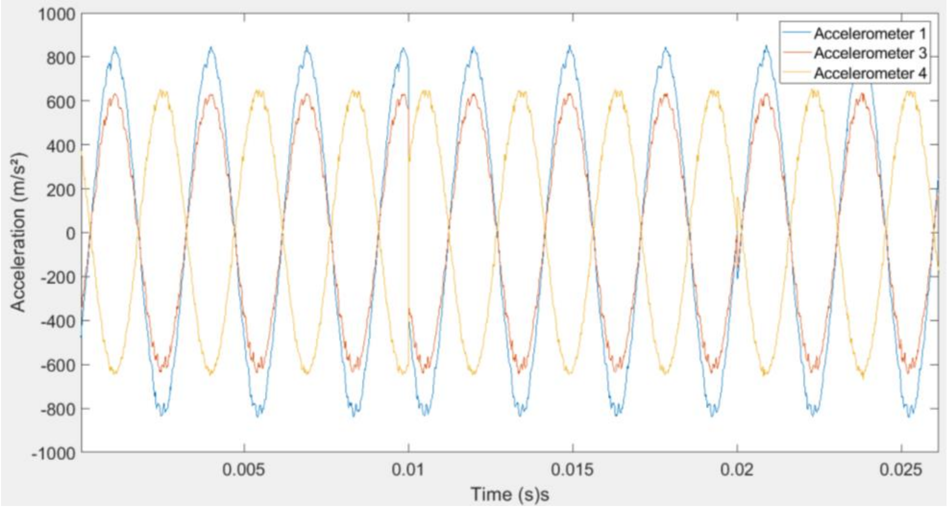

Figure 7.2:3 – Acceleration in steady-state mode at 354 Hz with all piezoelectric actuators activated in phase without ice

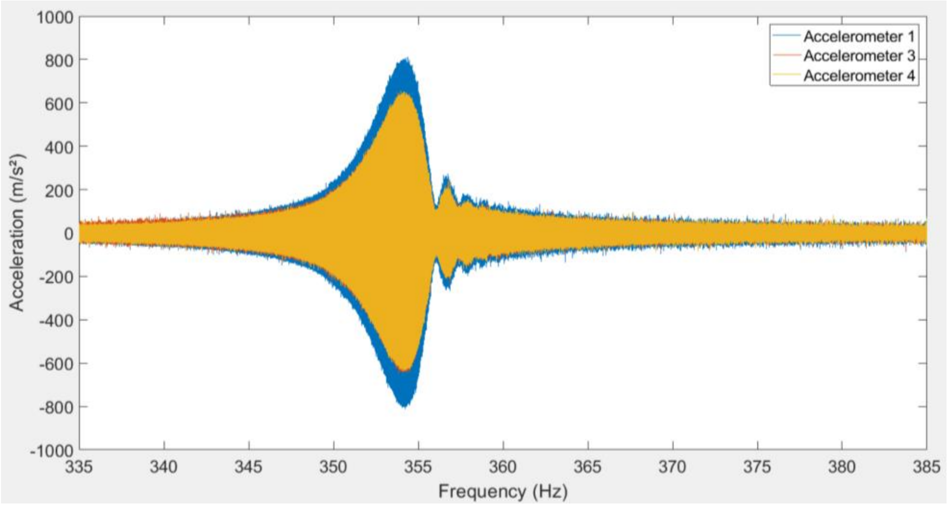

a)

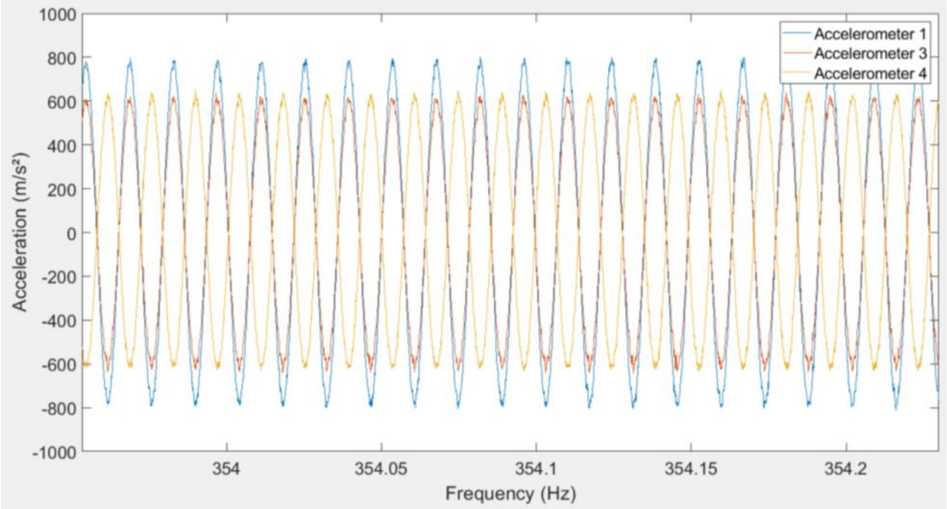

b)

Figure 7.2:4 – Acceleration during a sweep from 335 to 385 Hz in 10 s (5 Hz/s) with all piezoelectric actuators activated in phase without ice (a) and zoomed at resonance (b)

An ice accumulation was obtained on the plate, as per section 7.1.1, and a resonant mode was found at 400 Hz. Sweeping tests were performed from 375 Hz to 425 Hz in 10 seconds, for a sweep rate of 5 Hz/s, at a low voltage of 136 Vpp with accelerometers 1, 2 and 5 followed by a second sweep with accelerometers 1, 3 and 4. Figure 7.2:5 presents the acceleration measured during those sweeps. Accelerometers 1 was in phase with accelerometer 3, while accelerometers 2, 4 and 5 were in counter-phase. Accelerometers 1 and 2 were of equal force and in opposite direction as expected from their positions. Damping calculated from those sweeps was 0.9%.

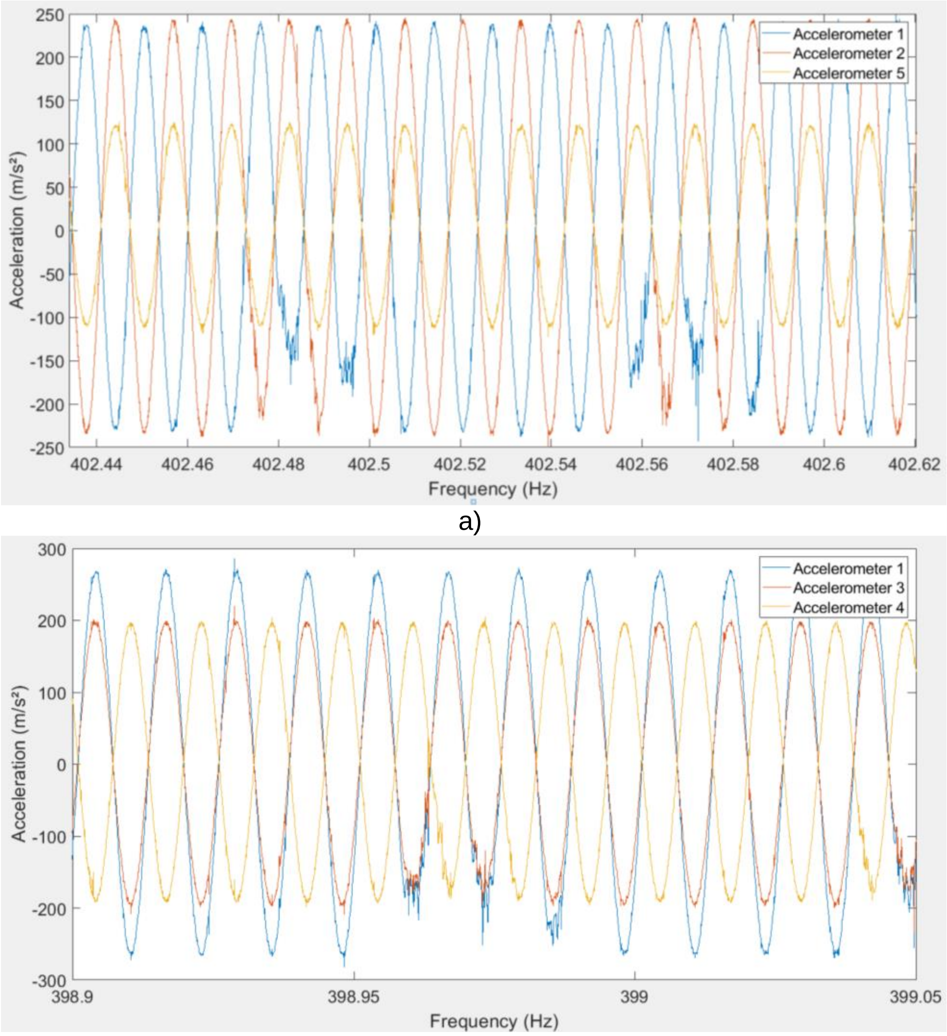

a)

b)

Figure 7.2:5 – Acceleration at resonance during sweep from 375 to 425 Hz in 10 s all actuators in phase at 136 Vpp for accelerometer 1, 2 and 5 (a) and 1, 3 and 4 (b)

The two modes closest to this frequency predicted by the frequency analysis were mode 5 and 6 at 350 Hz and 460 Hz respectively. Mode 6 has no anti-node at the center which would mean a very small amplitude for accelerometer 4, which was not what was obtained experimentally (Figure 7.2:6). Phasing of the accelerometers, as well as relative amplitudes, matched exactly the trends of mode 5. Accelerometers 3 and 4, both at anti-nodes, had an equal both opposite value, while accelerometers 1 and 2 had superior accelerations. It could be concluded that the experimental resonant mode was mode 5.

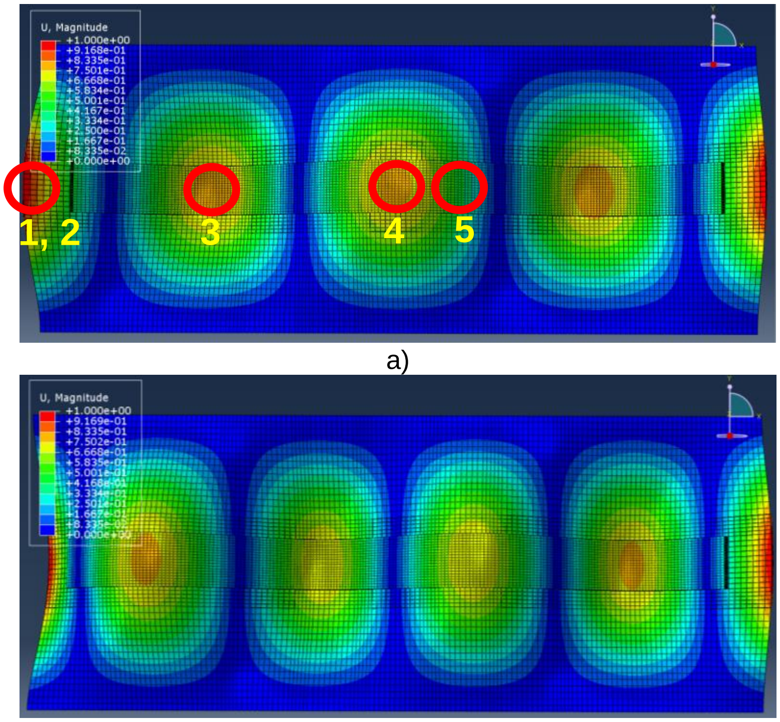

a)

b)

Figure 7.2:6 - Mode 5 (a) and 6 (b) predicted by the frequency analysis of the numerical model

The sweep from 375 to 425 Hz in 10 seconds was repeated at higher voltages until cracking occurred with accelerometers 1, 3 and 4. During sweep at 300 Vpp a crack was observed in the ice at 10 mm from the edge of the plate (Figure 7.2:7), which was in accordance with the anti-node at 11 mm in the mode shape predicted by the numerical model. Accelerations measured during this sweep were presented at Figure 7.2:8. A value of 610 m/s^2 was obtained for accelerometer 1 and 450 m/s^2 for accelerometers 3 and 4. The Direct-solution steady-state dynamic analysis predicted 425 m/s^2 at the edge of the plate and 325 m/s^2 at the anti-nodes.

Figure 7.2:7 - Crack at 300 Vpp for a sweep test with all piezoelectric actuators activated in phase from 375 Hz to 425 Hz in 10 seconds

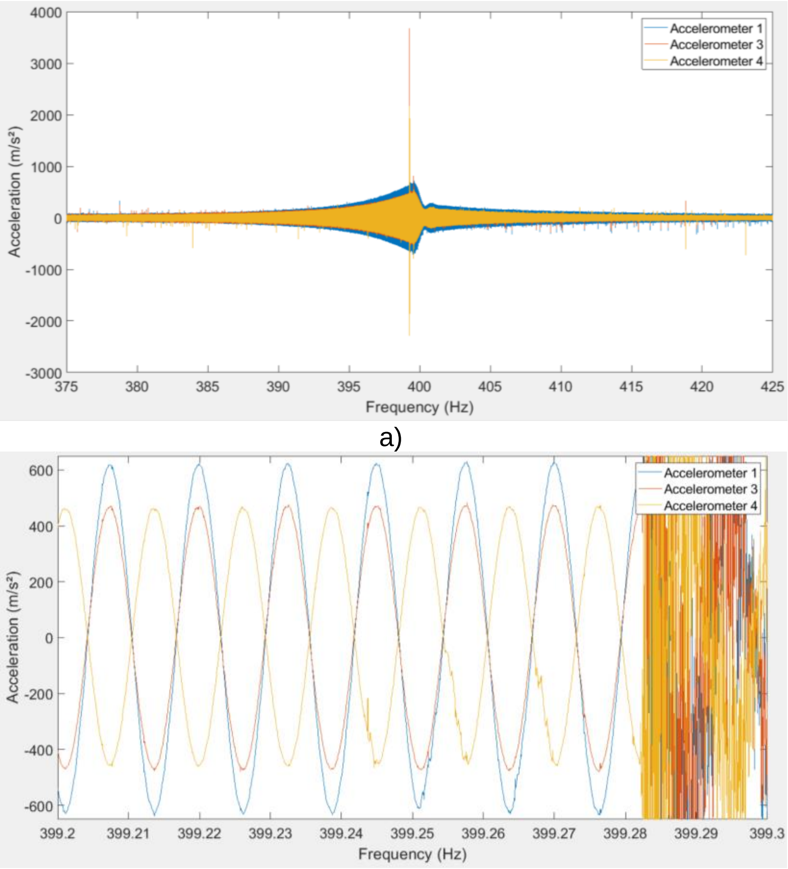

a)

b)

Figure 7.2:8 – Acceleration from accelerometers 1, 3 and 4 at 300 Vpp for a sweep test with all piezoelectric actuators activated in phase from 375 Hz to 425 Hz in 10 seconds (a) and zoomed plot at cracking (b)

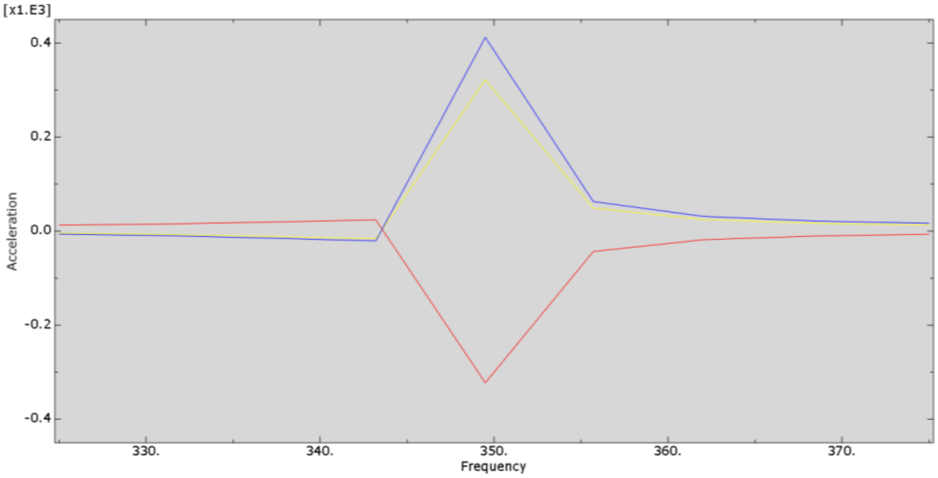

Figure 7.2:9 – Acceleration predicted by the numerical model for mode 5 with all actuators in phase and damping of 0.9 at edge of the plate (blue curve), at 11 mm (red curve) and center of the plate (yellow curve)

To measure repeatability, the test was repeated three additional times. For each of those repetitions, the same process was performed to accumulate the ice, find the frequency and obtain the damping value. The resonant frequency and damping obtained was 425 Hz and 1.3% for the second repetition, 400 Hz and 1.0% for the third repetition and 390 Hz and 0.9% for the last repetition. Cracks appeared at 370 Vpp, 304 Vpp and 360 Vpp respectively for each repetition and each time between 10 and 11 mm from the edge of the plate (Figure 7.2:10). This was the same distance but from the other end of the plate than for the first test, which should encounter the same stresses due to symmetry of the resonant modes. Results for all repetitions, including original test (repetition 1) are presented at Table 7.2:2, while Figure 7.2:11 shows the experimental accelerations for repetition 2 and Figure 7.2:12 the predicted accelerations by the numerical model.

Table 7.2:2 – Results of test repetitions for mode 5

Repetition (#)	Frequency (Hz)	Damping (%)	Vpp (V)	Acc. at edge (m/s^2)		Acc. at anti-nodes (m/s^2)	
				Exp.	Num.	Exp.	Num.
1	400	0.9	300	610	425	450	325
2	425	1.3	370	460	375	340	300
3	400	1.0	300	510	390	380	300
4	390	0.9	360	660	500	520	390
5*	400	1.0	216	850	1050	675	800

*performed with optimal phasing of actuators

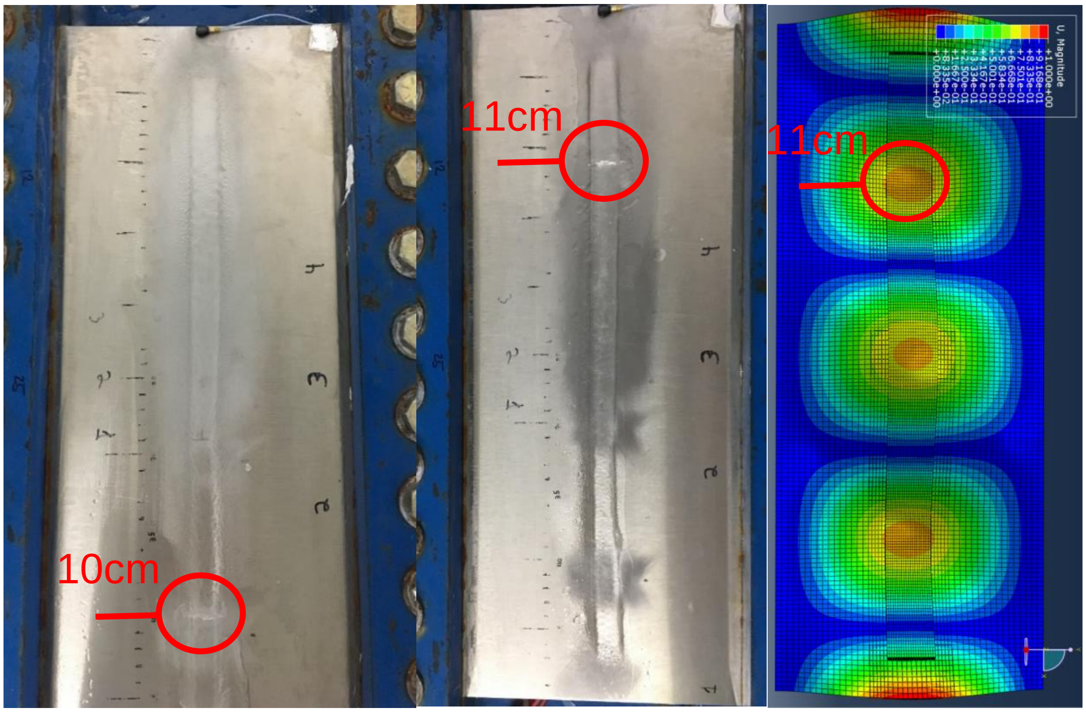

a) b) c)

Figure 7.2:10 – Crack at 300 Vpp at 10 cm from edge for repetition 1 (a) and at 370 Vpp at 11 cm from edge for repetition 2 (b) and modal shape predicted numerically (c)

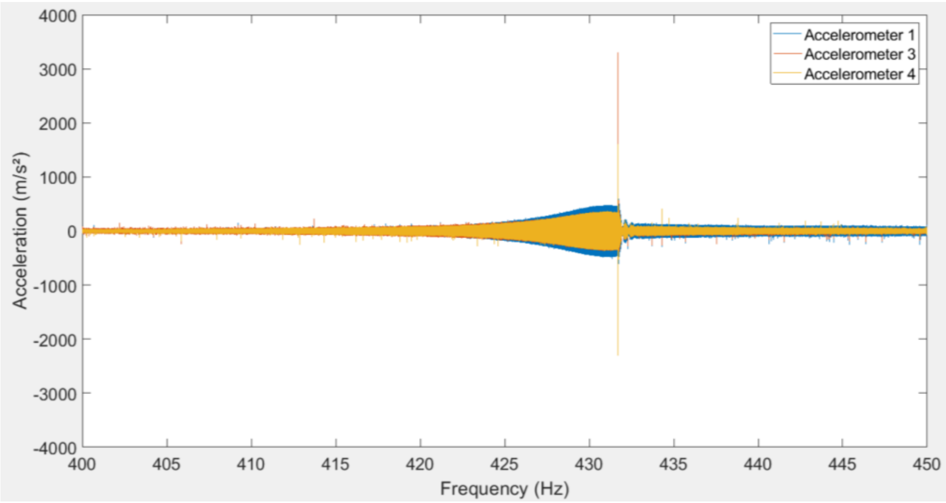

a)

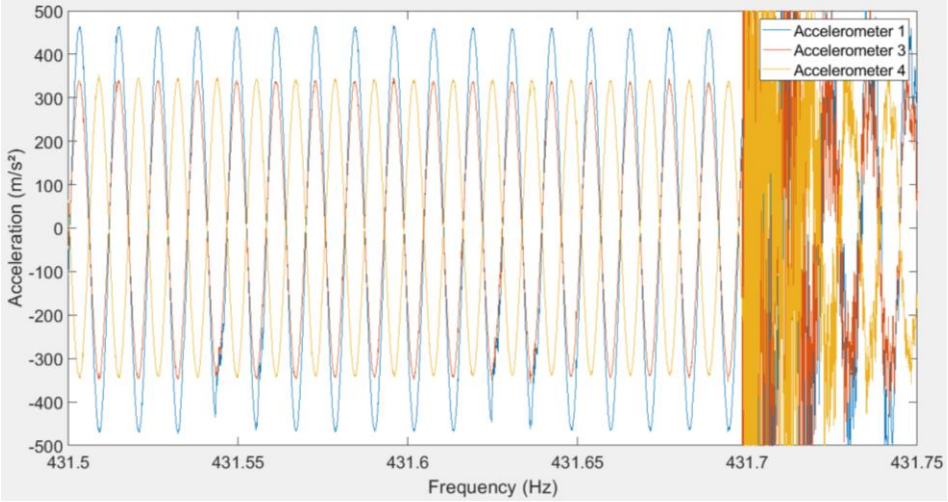

b)

Figure 7.2:11 – Acceleration from accelerometers 1, 3 and 4 at 370 Vpp for repetition 2 (a) and zoomed plot at cracking (b)

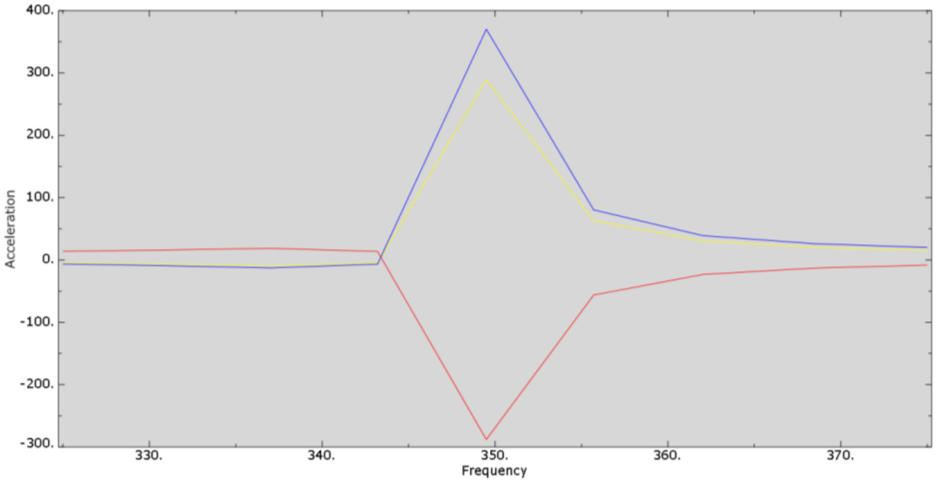

Figure 7.2:12 – Acceleration (m/s²) predicted by the numerical model for mode 5 (frequency in Hz) with damping of repetition 2 at edge of the plate (blue curve), at 11 cm (red curve) and center of the plate (yellow curve)

One last repetition was done for mode 5 with the same piezoelectric actuator excitation. For this test the frequency was found at very low voltage, below 60 Vpp, and the sweep test was performed directly at 370 Vpp, the highest voltage obtained during previous repetitions. This was done to validate that no damaging or weakening of the ice occurred during the sweep at lower voltages for the other repetitions before cracking was obtained. Since the frequency sweep was performed only once at 370 Vpp, it ensured that only this sweep was responsible for cracking of the ice and confirmed the results obtained with previous repetitions and validity of the method. The frequency was found around 400 Hz and the sweep was performed directly at 370 Vpp from 375 to 425 Hz in 10 s. A crack was obtained at 403 Hz at 12 mm from the edge of the plate (Figure 7.2:13) and acceleration during the test is presented at Figure 7.2:14. This confirmed that there was no effect of weakening or damaging of the ice during sweeps where no cracking occurred and that the method and results obtained can be used to determine acceleration at cracking to compare with numerical model stress predictions.

Figure 7.2:13 – Crack obtained after a sweep from 375 to 425 Hz in 10 s with all piezoelectric actuators activated in phase performed at 370 Vpp without any other sweeps performed

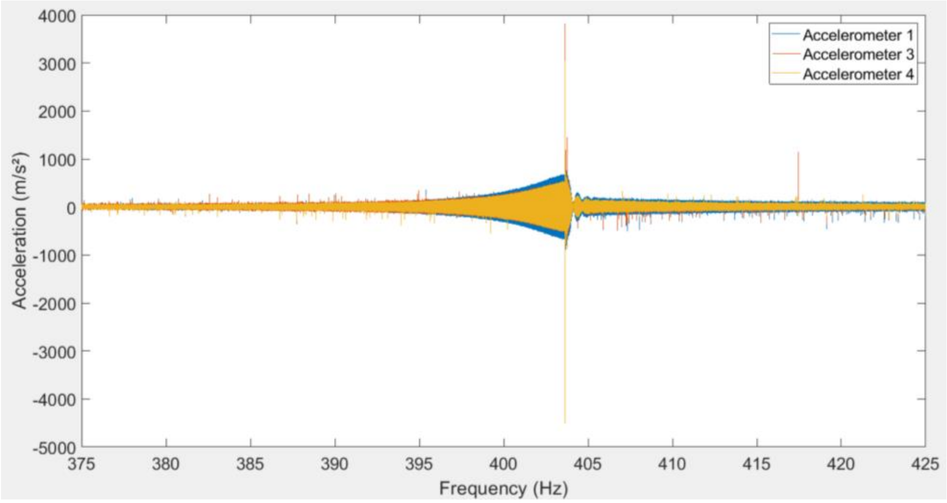

a)

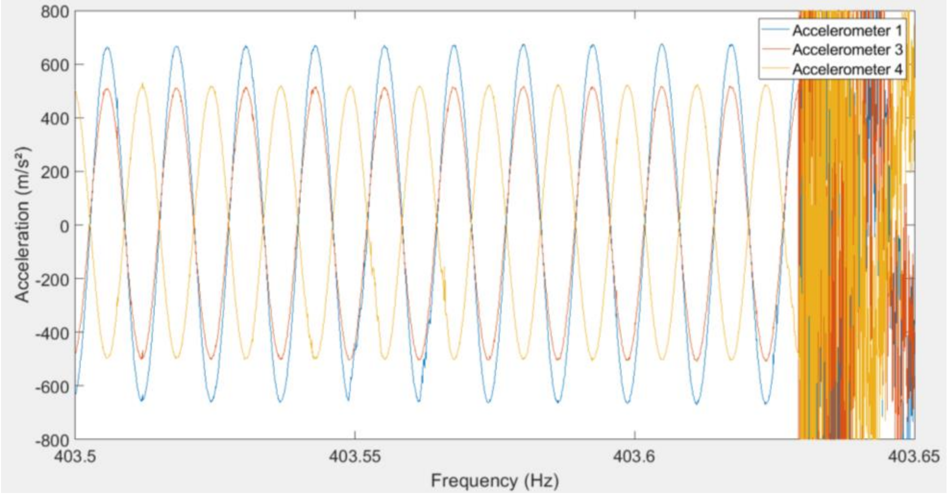

b)

Figure 7.2:14 – Acceleration from accelerometers 1, 3 and 4 at 370 Vpp for a sweep test with all piezoelectric actuators activated in phase from 375 Hz to 425 Hz in 10 seconds and no other tests performed on the ice layer (a) and zoomed plot at cracking (b)

Section 2.4.1.2 studied the optimal excitation of the piezoelectric actuators in function of the mode shape. By using the conclusions obtained in this section, it could be observed from Figure 7.2:6 that activating all the actuators in phase was not the optimal activation. Piezoelectric actuators 2 and 4 should be activated out of phase from the 3 other actuators. A second test with the optimal activation was done. After the ice layer was accumulated on the flat plate, the resonant frequency was found again at 400 Hz. The same sweep was then selected, from 375 Hz to 425 Hz in 10 seconds, but with piezoelectric actuators 2 and 4 out of phase from the other actuators. Damping was measured once again with sweeps at very low voltage and a value of 1.0% was obtained, very close to the values obtained previously. A crack was obtained during the sweep at 216 Vpp at 11 mm from the edge, as for the previous tests (Figure 7.2:15). The acceleration measured for accelerometer 1 was 850 m/s², for accelerometer 3 and 4 was 675 m/s² (Figure 7.2:16). The optimal activation has lowered the voltage required for cracking from an average of 333 Vpp to 216 Vpp (Table 7.2:2). After setting the voltage and damping in the numerical model, predictions for the accelerations were 1050 m/s² at the edge, and 800 m/s² at anti-node positions.

Figure 7.2:15 - Crack at 216 Vpp for a sweep test with piezoelectric actuators 2 and 4 out of phase with the 3 other piezoelectric actuators from 375 Hz to 425 Hz in 10 seconds

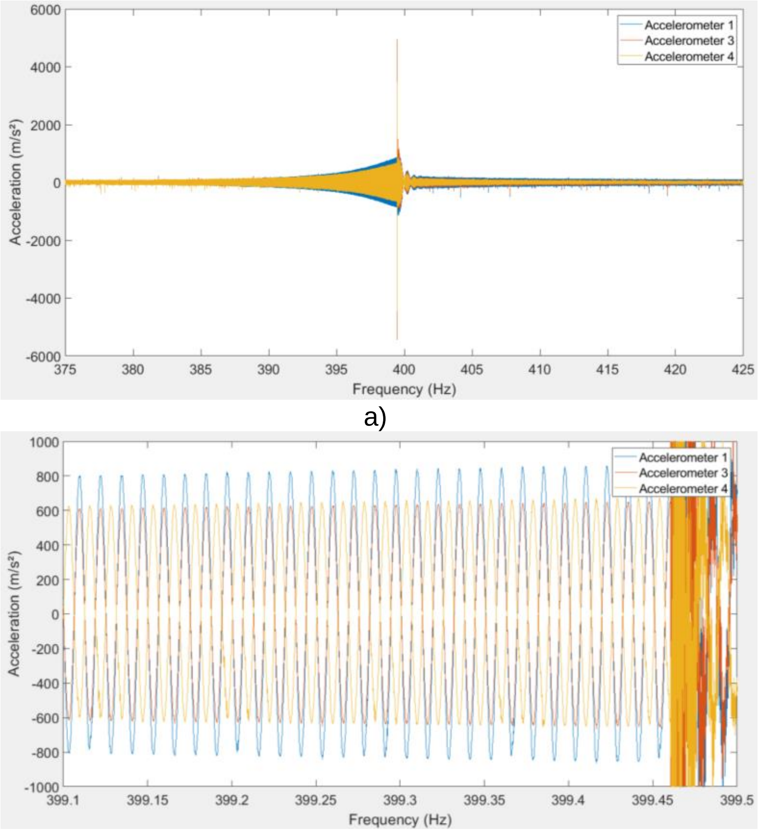

a)

b)

Figure 7.2:16 - Acceleration from accelerometers 1, 3 and 4 at 216 Vpp for a sweep test with piezoelectric actuators 2 and 4 out of phase with the 3 other piezoelectric actuators from 375 Hz to 425 Hz in 10 seconds (a) and zoomed plot at cracking (b)

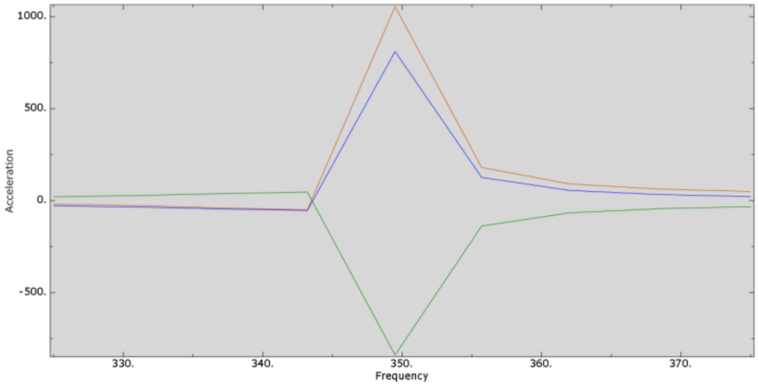

Figure 7.2:17 – Acceleration predicted by the numerical model for mode 5 with piezoelectric actuators 2 and 4 out of phase with the 3 other piezoelectric actuators and damping of 1.0 at edge of the plate (red curve), at 11 mm from edge (green curve) and center of the plate (blue curve)

The second mode was obtained around 1281 Hz. After the ice accumulation on the flat plate the resonant frequency was found at 1325 Hz. Sweep tests were performed from 1300 to 1350 Hz in 10 seconds for a sweep rate of 5 Hz/s at low voltage (136 Vpp) with accelerometers 1, 2 and 5 and with accelerometer 1, 3 and 4. Results, at Figure 7.2:18, show that accelerometers 1 and 3 were in phase while accelerometer 2, 4 and 5 were all in counter phase with 1 and 3. Accelerometers 1 and 2 were of equal force and in opposite direction as expected from their positions. Damping calculated with these sweeps was 1.1%.

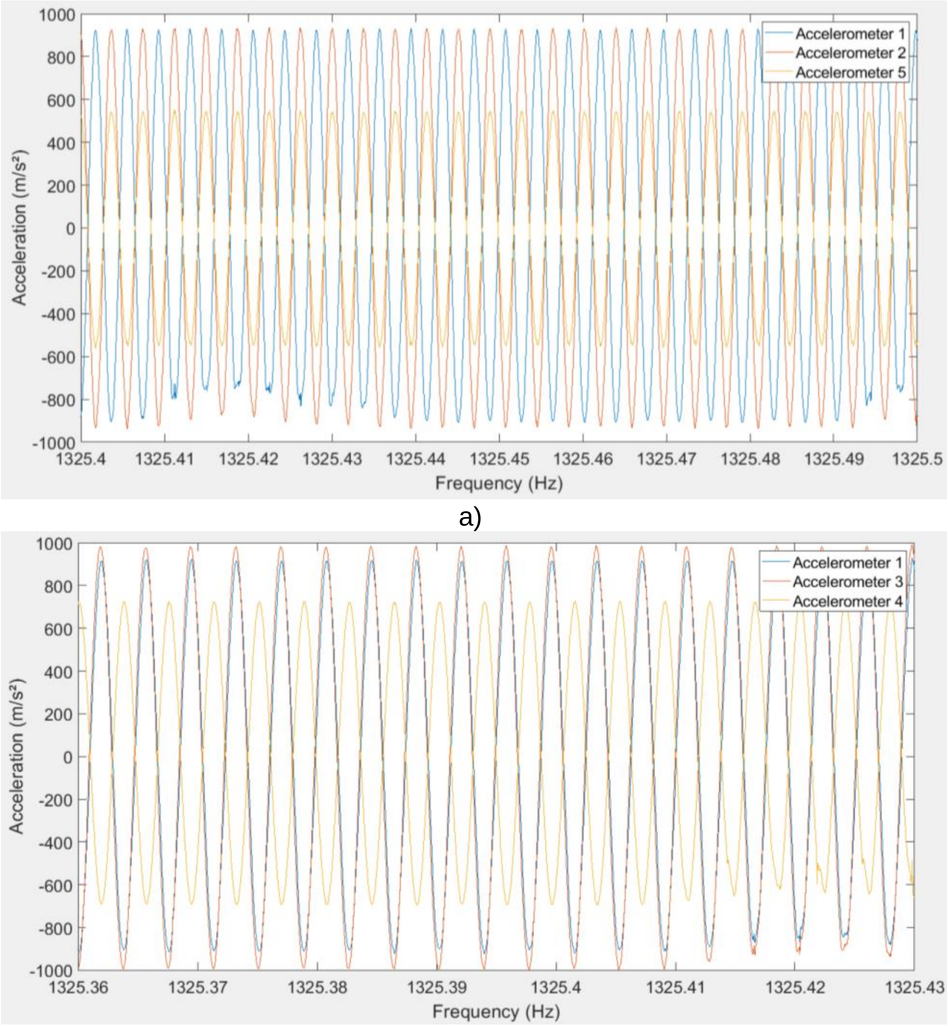

a)

b)

Figure 7.2:18 – Acceleration at resonance during sweep from 1300 to 1350 Hz in 10 s all actuators in phase at 136 Vpp for accelerometer 1, 2 and 5 (a) and 1, 3 and 4 (b)

The frequency analysis of the numerical model predicts three modes within ±75 Hz of 1325 Hz: one at 1263 Hz (mode 22), one at 1338 Hz (mode 23) and one at 1371 Hz (mode 24). Those three modes are presented at Figure 7.2:19. Since mode 22 does not have vibration at the center of the plate and accelerometer 4 was not null this indicated that this was not the right mode. Mode 24 has only anti-nodes on the top and bottom halves of the plate, which indicated that it was not the correct mode either. For mode 23, an anti-node is located on the center of the plate and is in the same phase as the half anti-node on the edge, which was in agreement with phasing of accelerometer 1, 2 and 4. The position of accelerometer 5 on the plate was in agreement with shape of mode 23, being in the same phase as 2 and 4, while having a lower acceleration than accelerometer 4. Position of the anti-node between the center anti-node and half anti-node at the edge is 12 mm, which corresponded exactly to the position of accelerometer 3. This anti-node is in counter phase with the center and half anti-node which was in agreement with the signal obtain from accelerometer 3 and also the magnitude of the acceleration which was on par with accelerometers 1 and 2. It could be concluded that the resonant mode obtained at 1325 Hz was mode 23 predicted by the frequency analysis at 1338 Hz.

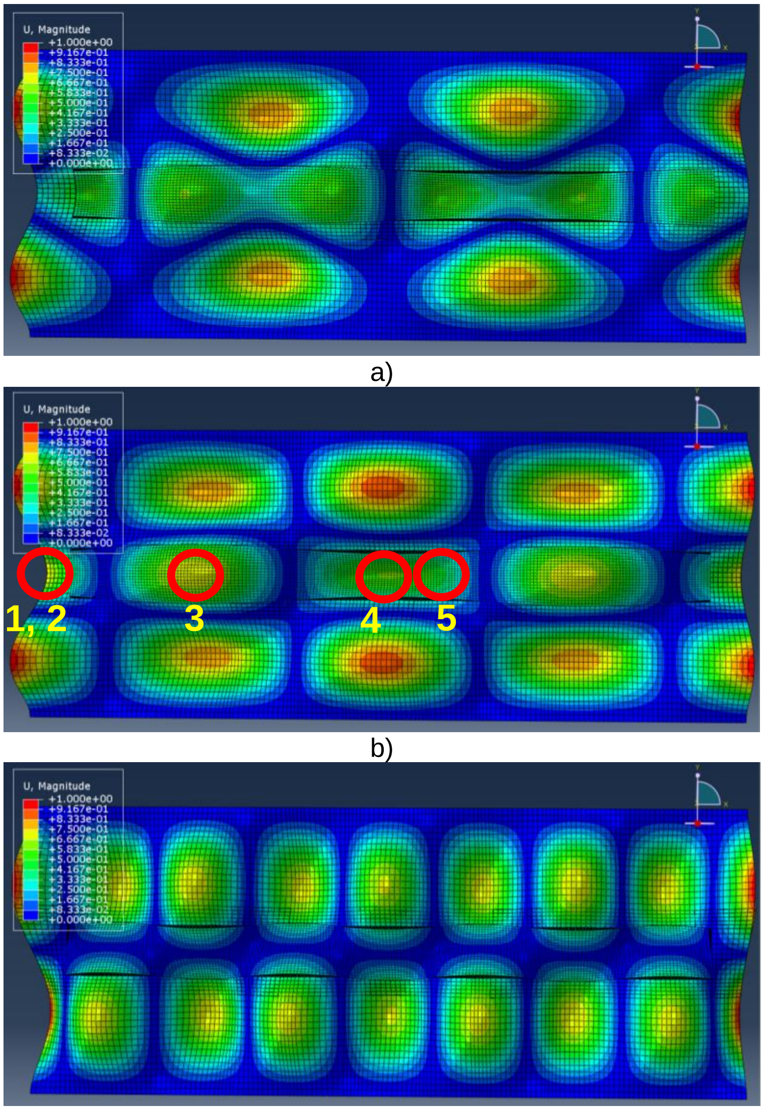

a)

b)

c)

Figure 7.2:19– Mode 22 (a), 23 (b) and 24 (c) predicted by the frequency analysis of the numerical model

The same sweep was performed at higher voltages with accelerometer 1, 3 and 4 and cracking of the ice was observed at 360 Vpp. Crack was observed between 11 and 12 cm from the edge of the plate which corresponded to the position of accelerometer 3 and the center of an anti-node on mode 23. A small delaminated zone was also observed with its center at 11 cm from the edge on the other half of the plate. Acceleration measured by the accelerometers is shown at Figure 7.2:21. A value of 2100 m/s² for accelerometer 1, 2600 m/s² for accelerometer 3 and 1700 m/s² for accelerometer 4 was obtained. The numerical model predicted 1700 m/s² at the edge of the plate, 1550 m/s² at 12 mm (accelerometer 3) and 1300 m/s² at the center of the plate (Figure 7.2:22).

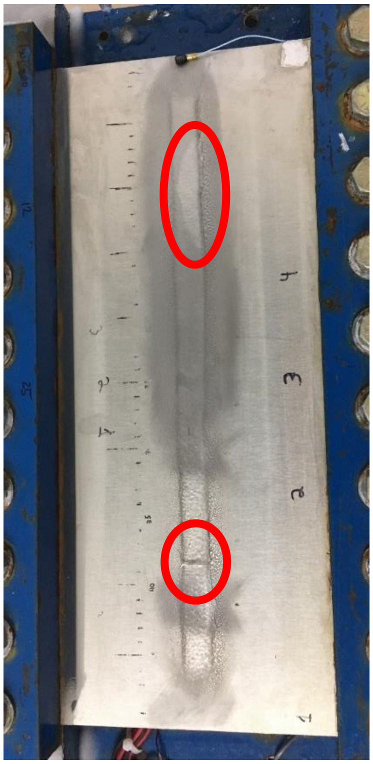

Figure 7.2:20 – Crack and delaminated zone at 360 Vpp for a sweep test with all piezoelectric actuators activated in phase from 1300 Hz to 1350 Hz in 10 seconds

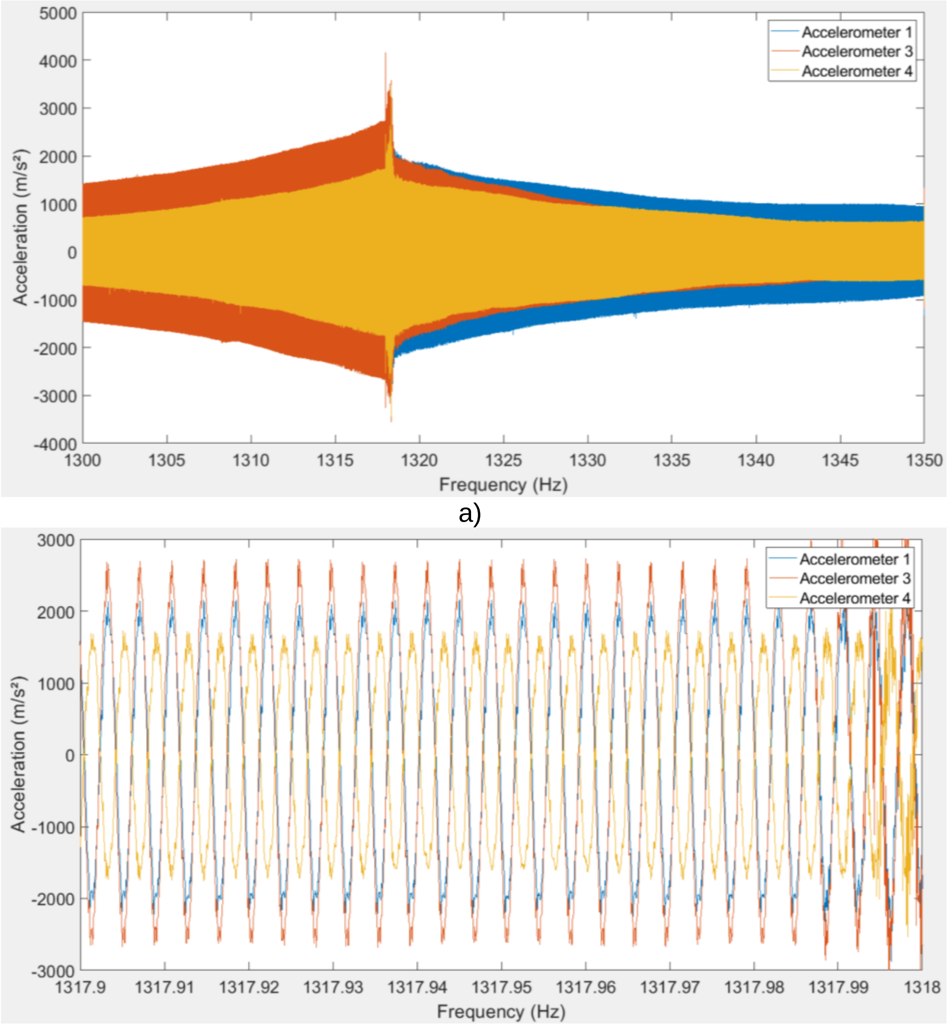

a)

b)

Figure 7.2:21 – Acceleration from accelerometers 1, 3 and 4 at 360 Vpp for a sweep test with all piezoelectric actuators activated in phase from 1300 Hz to 1350 Hz in 10 seconds (a) and zoomed plot at cracking (b)

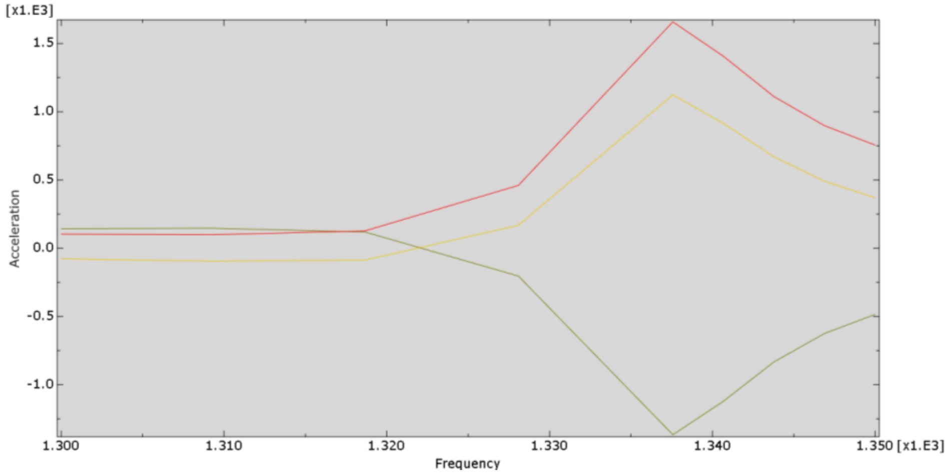

Figure 7.2:22 – Acceleration predicted by the numerical model for mode 23 with all actuators in phase and damping of 1.1 at edge of the plate (red curve), at 12 mm (brown curve) and center of the plate (yellow curve)

Repeatability, which was tested for mode 5, was tested again for this mode. This strengthened the value obtained previously by adding more results and a repeatability for a second mode. The test with all piezoelectric actuators in phase was repeated twice, with the same procedure as for the first test. The resonant frequency and damping obtained was 1320 Hz and 1.2% for the second repetition and 1335 Hz and 1.3% for the third repetition. Cracks appeared at 400 Vpp and 380 Vpp respectively and both times at 12 cm from the edge of the plate (Figure 7.2:23). Table 7.2:3 presents the results for all repetition, including original test (repetition 1)

Table 7.2:3 – Results of test repetitions for mode 23

Repetition (#)	**Frequency (Hz)**	**Damping (%)**	**Vpp (V)**	**Acc. at edge (m/s²)**		**Acc. at accelerometer 3 (m/s²)**		**Acc. at Center (m/s²)**	
				Exp.	**Num.**	**Exp.**	**Num.**	**Exp.**	**Num.**
1	1325	1.1	360	2100	1700	2600	1550	1700	1300
2	1320	1.2	400	1900	1700	2400	1550	1900	1300
3	1335	1.3	380	1300	1500	2100	1375	1450	1150
4*	1330	1.5	240	2300	2350	2800	2250	2200	1800

*performed with optimal phasing of actuators

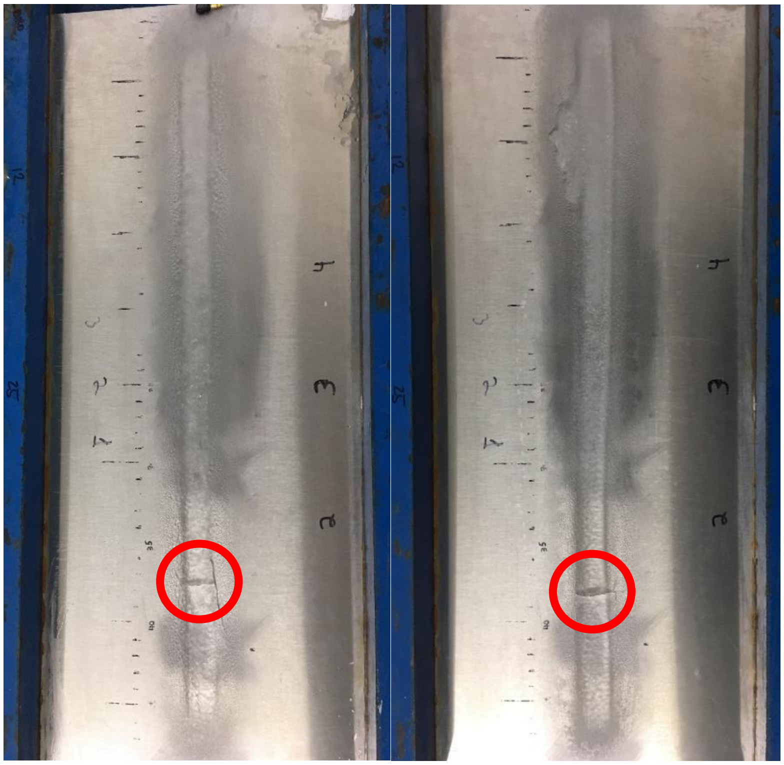

Figure 7.2:23 – Cracks during test repetitions for mode 23, a) second test repetition and b) third test repetition

As for mode 5, a last repetition was done to validate that no damaging or weakening of the ice was responsible for cracking at the voltage obtained previously. The frequency was found at 1325 Hz and a sweep from 1300 to 1350 Hz in 10 s was performed directly at 400 Vpp which corresponded to the highest voltage obtained in the previous tests for this mode and activation. Two cracks were obtained during this sweep, one where a small delaminated zone could even be observed on both sides of the crack. Both cracks were located between 11 and 12 cm from each edge of the plate (Figure 7.2:24).

Figure 7.2:24 – Crack obtained after a sweep from 1300 to 1350 Hz in 10 s with all piezoelectric actuators activated in phase performed at 400 Vpp without any other sweeps performed before

The conclusions of section 2.4.1.2 indicated that the phasing used for the sweeps was not the ideal phasing for this mode. Piezoelectric actuators 2 and 4 should be activated out of phase from the 3 other actuators (see Figure 7.2:19-b). A new ice layer was accumulated on the flat plate and the resonant frequency was found at 1330 Hz. The sweep selected was from 1305 Hz to 1355 Hz in 10 seconds, but with piezoelectric actuators 2 and 4 out of phase from the other actuators. Damping was measured once again with sweeps at very low voltage and a value of 1.5 was obtained, higher than the values obtained previously. Sweep tests were performed with increased voltage and a crack was obtained at 240 Vpp between 11 and 12 mm from the edge of the plate (Figure 7.2:25), where was located the crack obtained with all the actuators in phase. The acceleration measured was 2300 m/s² for accelerometer 1, 2800 m/s² for accelerometer 3 and 2200 m/s² for accelerometer 4. The optimal activation has lower the voltage required for cracking from 360 Vpp to 240 Vpp. The numerical model predicted for these parameters an acceleration of 2350 m/s² at the edge, and 2250 m/s² at position of accelerometer 3 and 1800 m/s² at the center (Table 7.2:3).

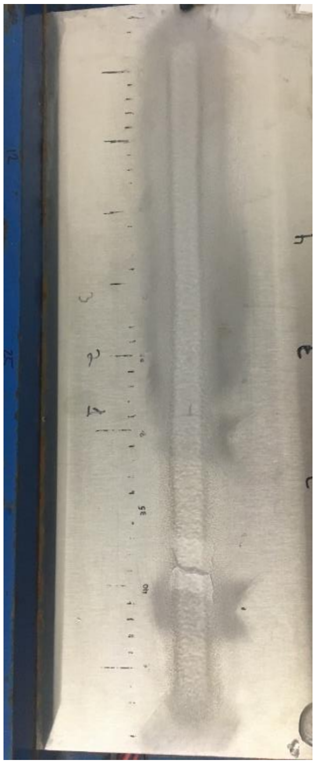

Figure 7.2:25 - Crack at 240 Vpp for a sweep test with piezoelectric actuators 2 and 4 out of phase with the 3 other piezoelectric actuators from 1305 Hz to 1355 Hz in 10 seconds

7.2.1.4 DELAMINATION OF THE ICE

Two modes have been found during the de-icing tests with the camera where delamination of the ice occurred. They were also successful in delamination of the ice layer during the steady-state tests. As for the cracking of the ice, new icing tests were performed with sweeps at very low sweep rate and the acceleration measured during those tests were used to calculate damping and validate the numerical model.

The first mode was found around 194 Hz during the high speed camera tests and at 188 Hz during the steady-state de-icing mode. After ice was accumulated on the flat plate, the highest acceleration around 194 Hz was found at 192 Hz. Sweep tests were performed from 187 Hz to 197 Hz in 10 seconds, for a sweep rate of 1 Hz/s. Figure 6:6 has shown that for this frequency a sweep rate of 1 Hz/s was required to reach 95% of the steady-state value. The sweep was performed at a low voltage of 136 Vpp with accelerometers 1, 2 and 5 followed by a second sweep with accelerometers 1, 3 and 4. Acceleration measured during those sweeps are presented at Figure 7.2:26. Accelerometers 1 was out of phase with all the other accelerometers. Accelerations of accelerometers 1 and 2 were of equal force and in opposite direction as expected from their positions, and higher than all the other accelerometers. Damping obtained for this mode was 2.2%.

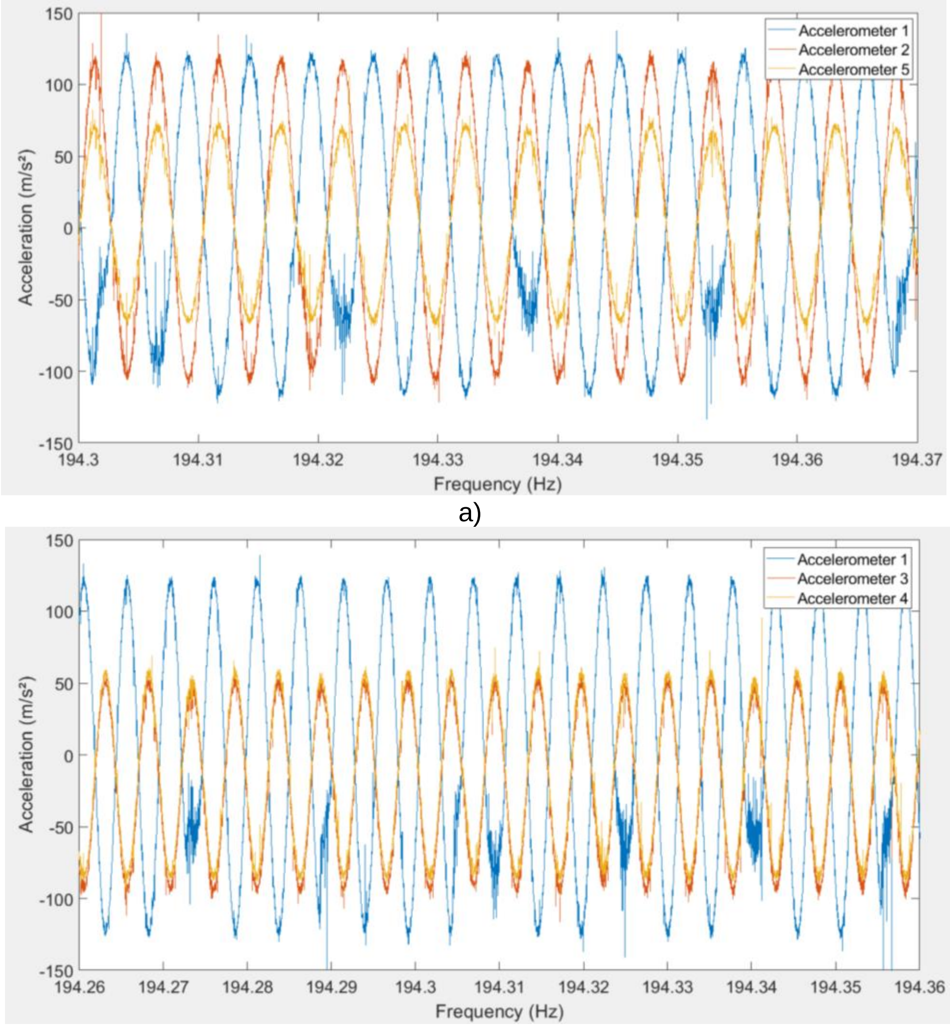

a)

b)

Figure 7.2:26 – Acceleration at resonance during sweep from 187 to 197 Hz in 10 s all actuators in phase at 136 Vpp for accelerometer 1, 2 and 5 (a) and 1, 3 and 4 (b)

The first mode predicted by the frequency analysis was at 203 Hz. Figure 7.2:27 presents mode 1 at 203 Hz, mode 2 at 208 Hz and mode 3 at 229 Hz. From the mode shape, it appeared that only in mode 1 accelerometers 2, 3, 4 and 5 would be in the same phase, which means that mode 1 was the mode obtained experimentally.

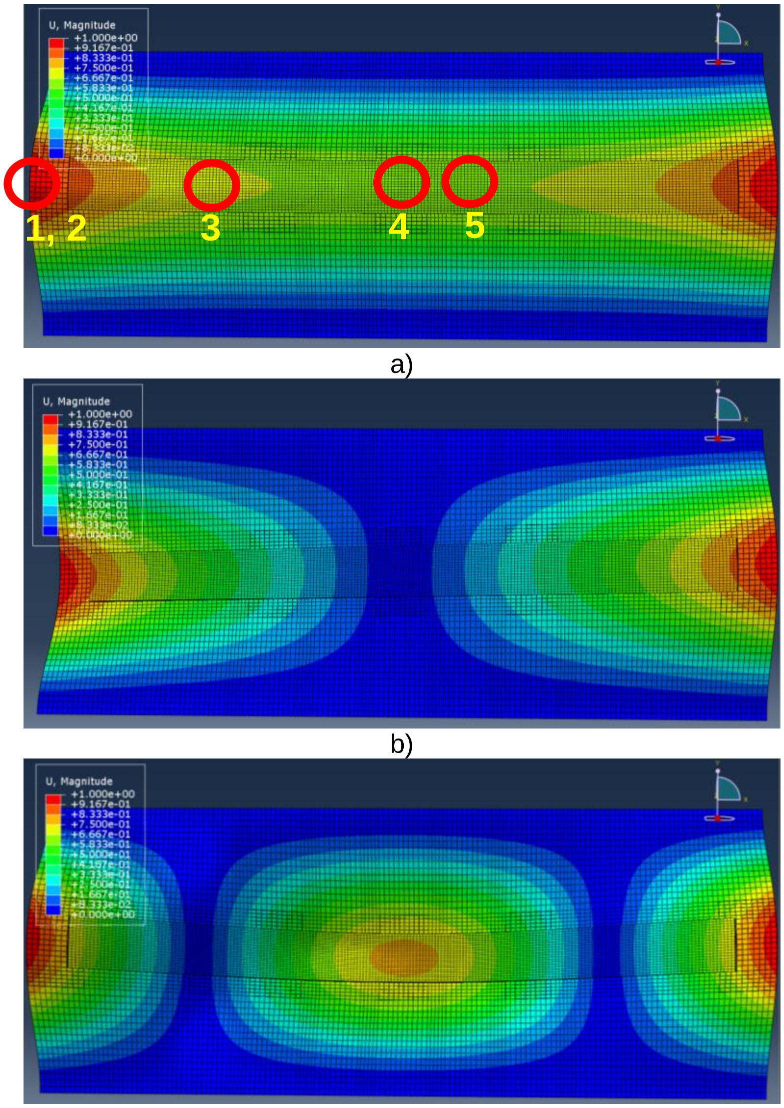

a)

b)

c)

Figure 7.2:27 - Mode 1 (a), mode 2 (b) and mode 3 (c) predicted by the frequency analysis of the numerical model

The sweep from 187 to 197 Hz in 10 seconds was repeated with accelerometers 1, 3 and 4 at higher voltages until delamination occurred. During sweep at 560 Vpp, delamination of a zone of approximately 9 cm long was observed at one side of the ice layer (Figure 7.2:28). An acceleration of 725 m/s² was obtained for accelerometer 1, 400 m/s² for accelerometer 3 and 425 m/s² for accelerometer 4. The Direct-solution steady-state dynamic analysis predicted an acceleration of 675 m/s² at the edge of the plate and 460 m/s² and 440 m/s² at positions of accelerometer 3 and 4 respectively (Figure 7.2:30). All actuators in phase was already the optimal activation for this mode so no other test was performed at that frequency.

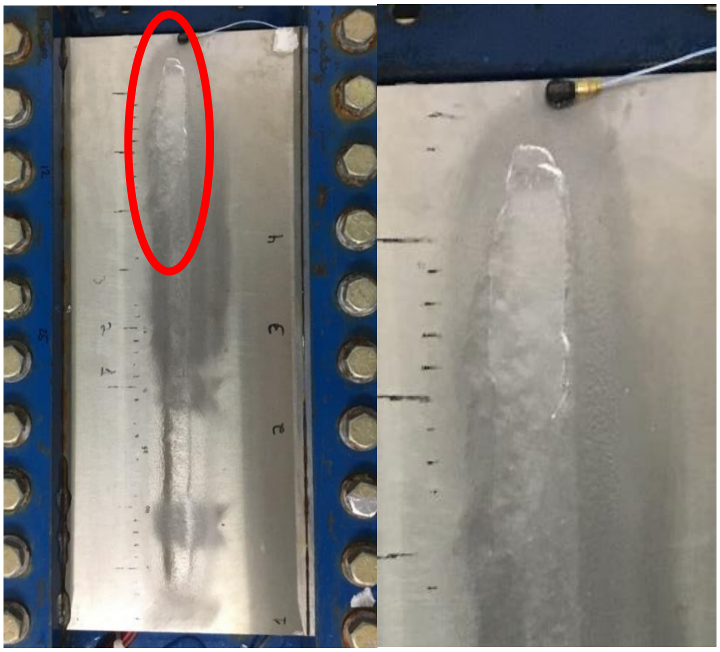

a) b)

Figure 7.2:28 – a) Delamination at 560 Vpp for a sweep test with all piezoelectric actuators activated in phase from 187 Hz to 197 Hz in 10 seconds b) Zoomed picture of delamination

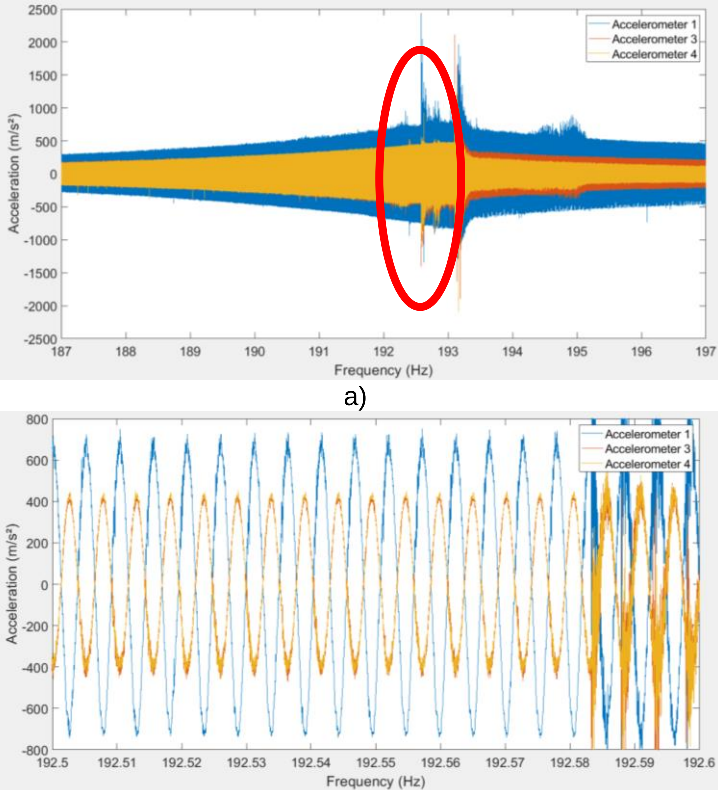

a)

b)

Figure 7.2:29 – Acceleration from accelerometers 1, 3 and 4 at 560 Vpp for a sweep test with all piezoelectric actuators activated in phase from 187 Hz to 197 Hz in 10 seconds (a) and zoomed plot at delamination (b)

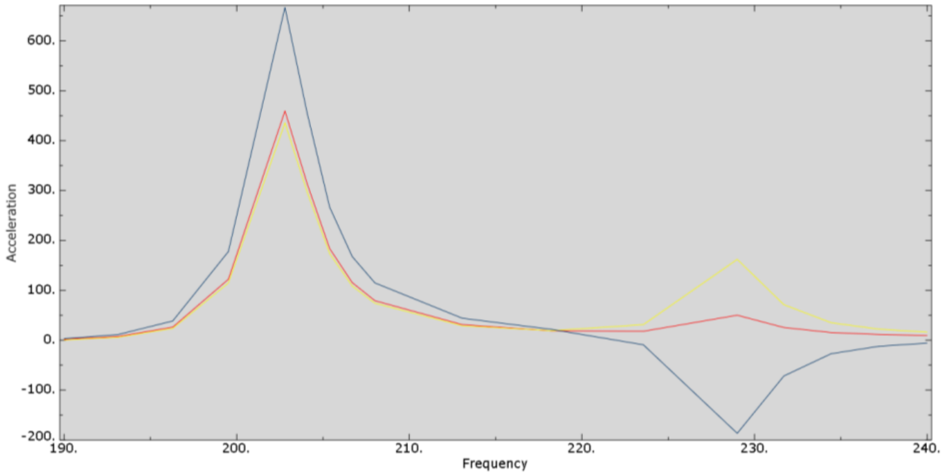

Figure 7.2:30 – Acceleration predicted by the numerical model for mode 1 with all actuators in phase and damping of 2.2 at edge of the plate (blue curve), at 12 mm (red curve) and center of the plate (yellow curve)

The second mode resulting in delamination that was found with the camera was obtained between 1111 and 1215 Hz, with a longitudinal crack also observed in the ice. For this mode it was difficult to clearly identified the frequency where delamination happened and it appeared to be more over a frequency range than at a single frequency. During steady-state tests, delamination was successfully achieve at 1138 Hz. After the ice accumulation, research of the maximal amplitude was done between 1100 and 1250 Hz. In this frequency range, a resonant frequency was found at 1155 Hz. A frequency sweep was performed at 136 Vpp from 1130 to 1180 Hz in 10 seconds with accelerometers 1, 2 and 5 and then 1, 3 and 4 (Figure 7.2:31). Damping obtained for these sweeps was 1.3%.

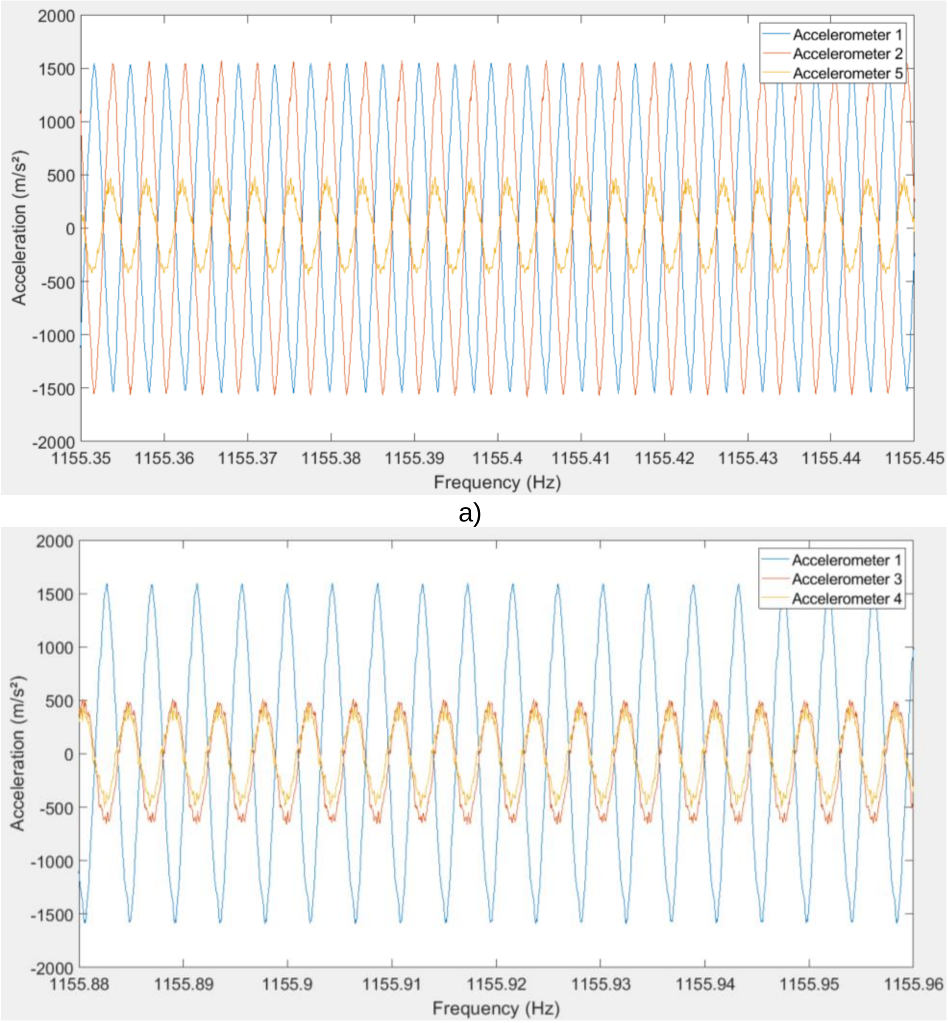

a)

b)

Figure 7.2:31 – Acceleration at resonance during sweep from 1130 to 1180 Hz in 10 s with all actuators in phase at 136 Vpp for accelerometer 1, 2 and 5 (a) and 1, 3 and 4 (b)

Five modes were found within this frequency range with the frequency analysis, mode 17 at 1158 Hz, mode 18 at 1164 Hz, mode 19 at 1177 Hz, mode 20 at 1198 Hz and mode 21 at 1209 Hz (Figure 7.2:32). Mode 19 has not anti-node on the centerline of the plate and mode 18, 20 and 21 did not matched the accelerometer phasing obtained with the accelerometers. The phasing of the accelerometers corresponded to the mode shape of mode 17. However three modes were very close to one another, within 40 Hz and even within 6 Hz for mode 17 and 18. This explained why multiple delamination was observed in this range with the camera test. These modes, while less excited due to the piezoelectric actuator activation favoring mode 17, were still activated and created small delamination and cracking in the ice layer.

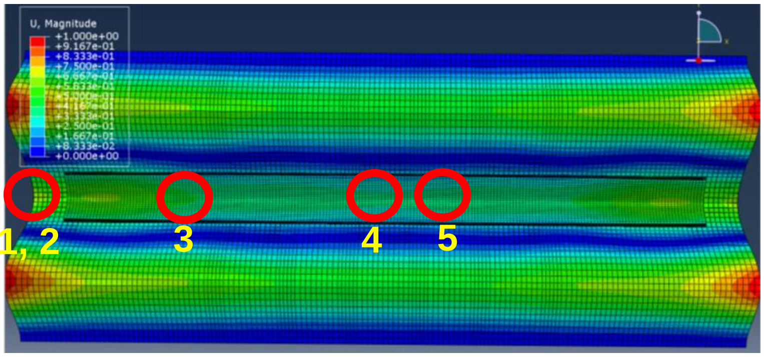
U, Magnitude
+1.000e+00
+9.167e-01
+8.333e-01
+7.500e-01
+6.667e-01
+5.833e-01
+5.000e-01
+4.167e-01
+3.333e-01
+2.500e-01
+1.667e-01
+8.333e-02
+0.000e+00
1, 2
3
4
5

a)

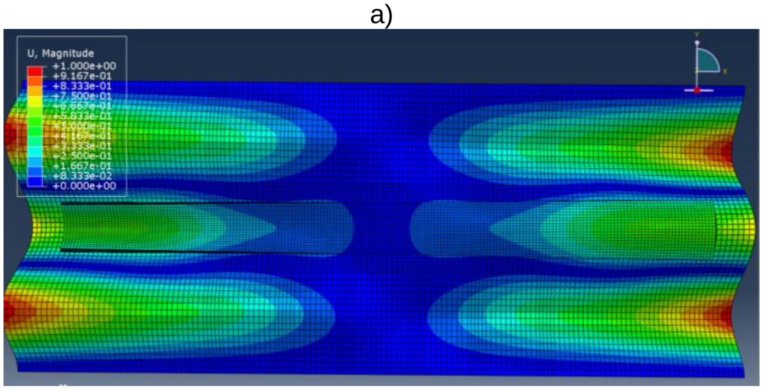
U, Magnitude
+1.000e+00
+9.167e-01
+8.333e-01
+7.500e-01
+6.667e-01
+5.833e-01
+5.000e-01
+4.167e-01
+3.333e-01
+2.500e-01
+1.667e-01
+8.333e-02
+0.000e+00

b)

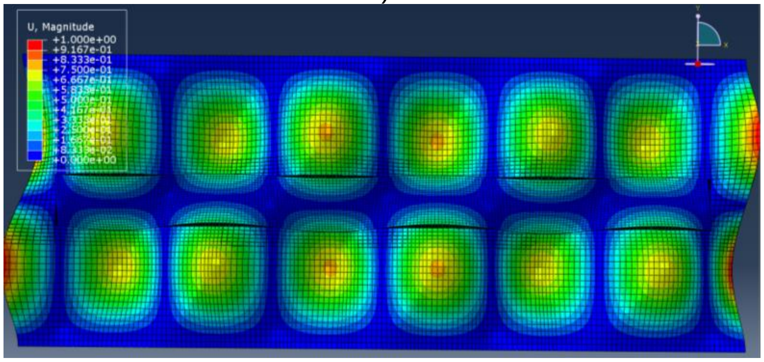
U, Magnitude
+1.000e+00
+9.167e-01
+8.333e-01
+7.500e-01
+6.667e-01
+5.833e-01
+5.000e-01
+4.167e-01
+3.333e-01
+2.500e-01
+1.667e-01
+8.333e-02
+0.000e+00

c)

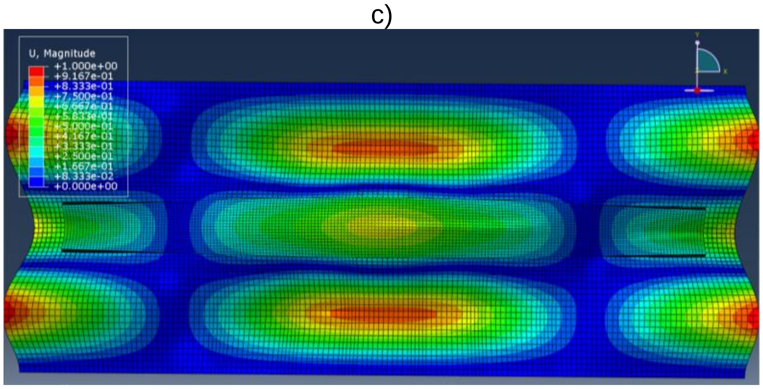
U, Magnitude
+1.000e+00
+9.167e-01
+8.333e-01
+7.500e-01
+6.667e-01
+5.833e-01
+5.000e-01
+4.167e-01
+3.333e-01
+2.500e-01
+1.667e-01
+8.333e-02
+0.000e+00

d)

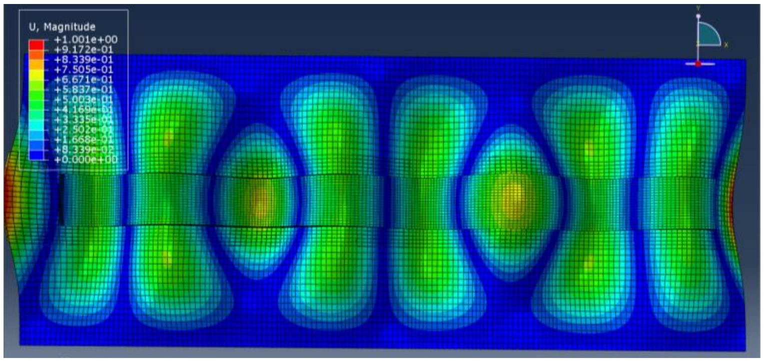

e)

Figure 7.2:32 - Mode 17 (a), mode 18 (b), mode 19 (c), mode 20 (d) and mode 21 (e) predicted by the frequency analysis of the numerical model

Same sweep was performed with accelerometer 1, 3 and 4 and voltage was increased until delamination was obtained at 192 Vpp (Figure 7.2:33). Acceleration measured at edge of the plate was 2100 m/s² and for accelerometer 3 and 4 was 825 m/s² and 725 m/s² respectively (Figure 7.2:34). The numerical model predicted at those positions 1750 m/s², 1125 m/s² and 1025 m/s² (Figure 7.2:35).

Figure 7.2:33 – Delamination at 192 Vpp for a sweep test with all piezoelectric actuators activated in phase from 1130 Hz to 1180 Hz in 10 seconds

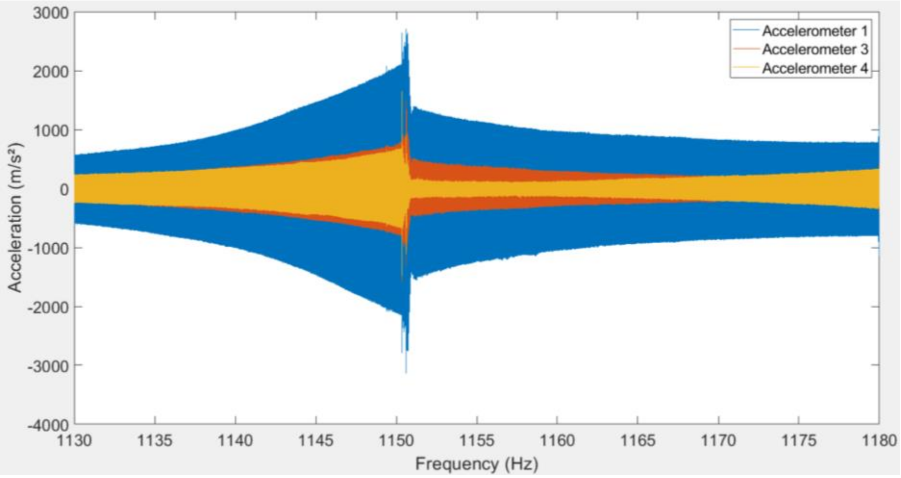

a)

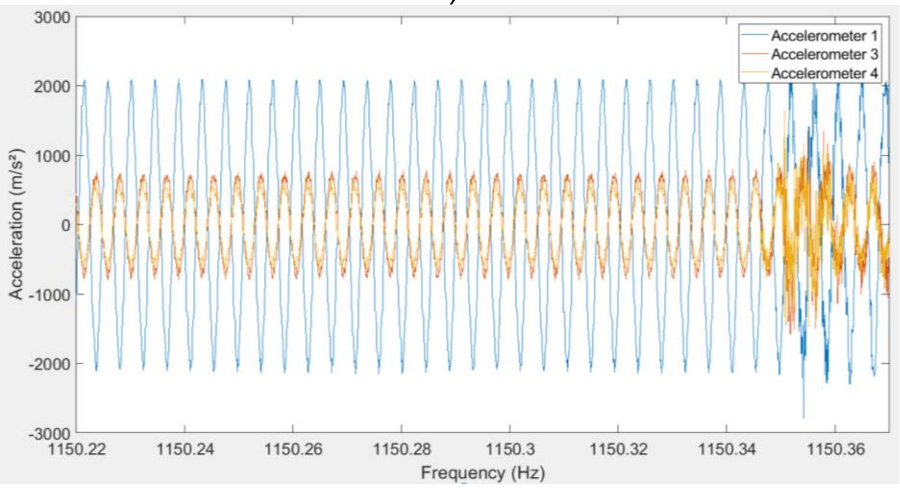

b)

Figure 7.2:34 – Acceleration from accelerometers 1, 3 and 4 at 192 Vpp for a sweep test with all piezoelectric actuators activated in phase from 1130 Hz to 1180 Hz in 10 seconds (a) and zoomed plot at delamination (b)

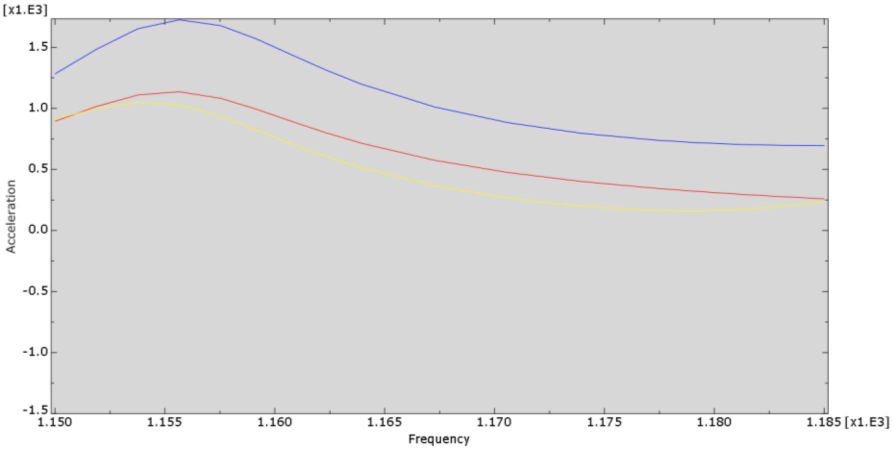

Figure 7.2:35 – Acceleration predicted by the numerical model for mode 17 with all actuators in phase and damping of 1.3 at edge of the plate (blue curve), at 12 mm (red curve) and center of the plate (yellow curve)

All piezoelectric actuators activated in phase was the optimal phasing for mode 17. With the camera tests, delamination was obtained in a larger band meaning that more modes were susceptible of having generated delamination. Mode 18 and 20, from their mode shapes, were the two modes that could have caused this additional delamination. For mode 18, the optimal phasing was actuator 1 and 2 in counterphase with actuator 4 and 5 and no power to actuator 3. After the ice accumulation, the maximum acceleration was obtained at 1160 Hz. A sweep from 1135 to 1185 Hz in 10 seconds was performed at low voltage (136 Vpp) with accelerometers 1, 2 and 5 and repeated with accelerometers 1, 3 and 4. The phasing and relative magnitude of the accelerations presented at Figure 7.2:36 show that mode 18 was activated and the resulting damping was 1.6%. However, the results seem to show that another closely spaced mode, probably mode 17, was also excited to a certain extent. It did not seem to impact the validity of the results obtained during de-icing tests (Figure 7.2:38) and a MAC or COMAC type of analysis could confirm this.

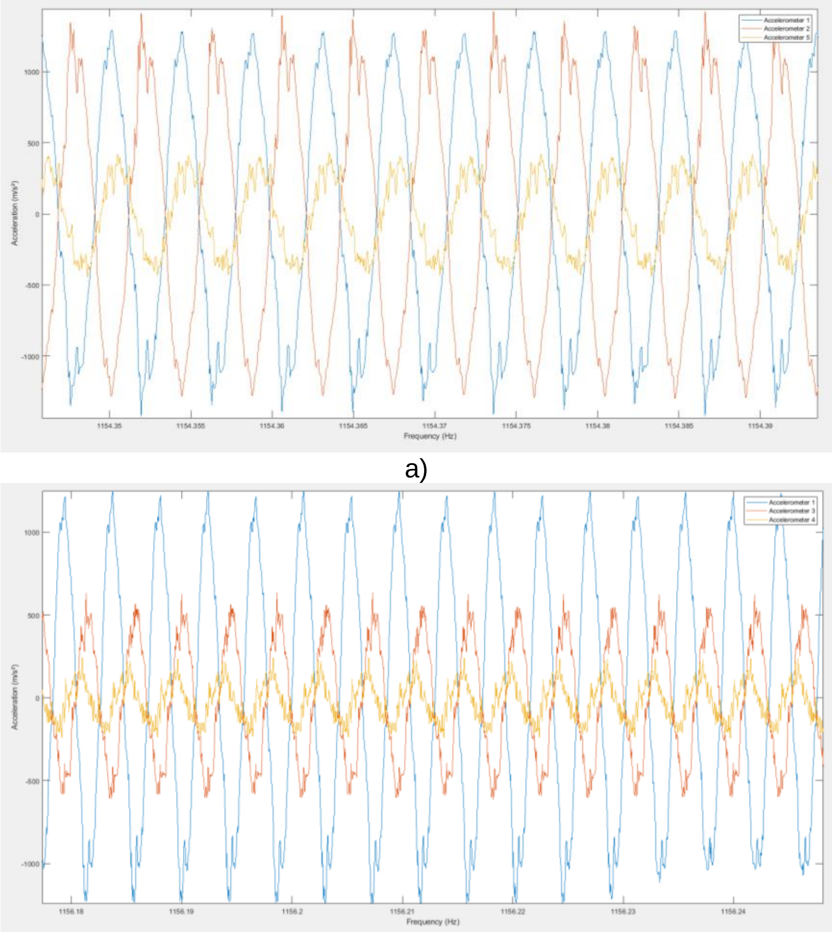

a)

b)

Figure 7.2:36 - Acceleration at resonance during sweep from 1135 to 1185 Hz in 10 s with actuators 1 and 2 out of phase with actuators 4 and 5 at 136 Vpp for accelerometer 1, 2 and 5 (a) and 1, 3 and 4 (b)

The sweep was repeated at higher voltages and two small delamination were observed on each side of the ice layer at 216 Vpp (Figure 7.2:37). An acceleration of 2200 m/s² was obtained for accelerometer 1, 1000 m/s² for accelerometer 3 and 400 m/s² for accelerometer 4 (Figure 7.2:38). An acceleration of 1825 m/s² at the edge of the plate and 950 m/s² at positions of accelerometer 3 were predicted by the numerical model (Figure 7.2:39).

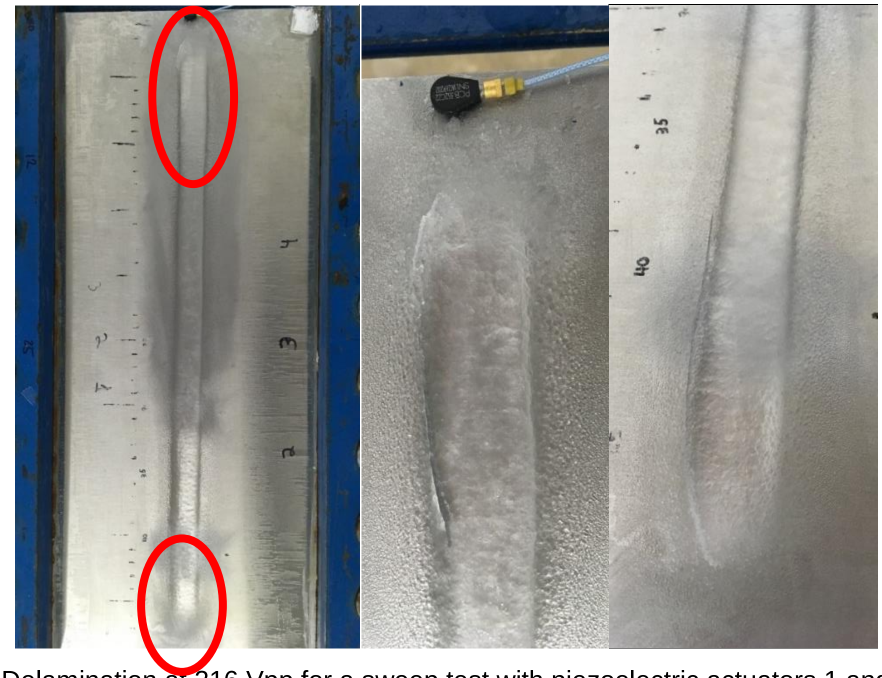

Figure 7.2:37 - Delamination at 216 Vpp for a sweep test with piezoelectric actuators 1 and 2 activated out of phase with piezoelectric actuators 4 and 5 from 1135 Hz to 1185 Hz in 10 seconds

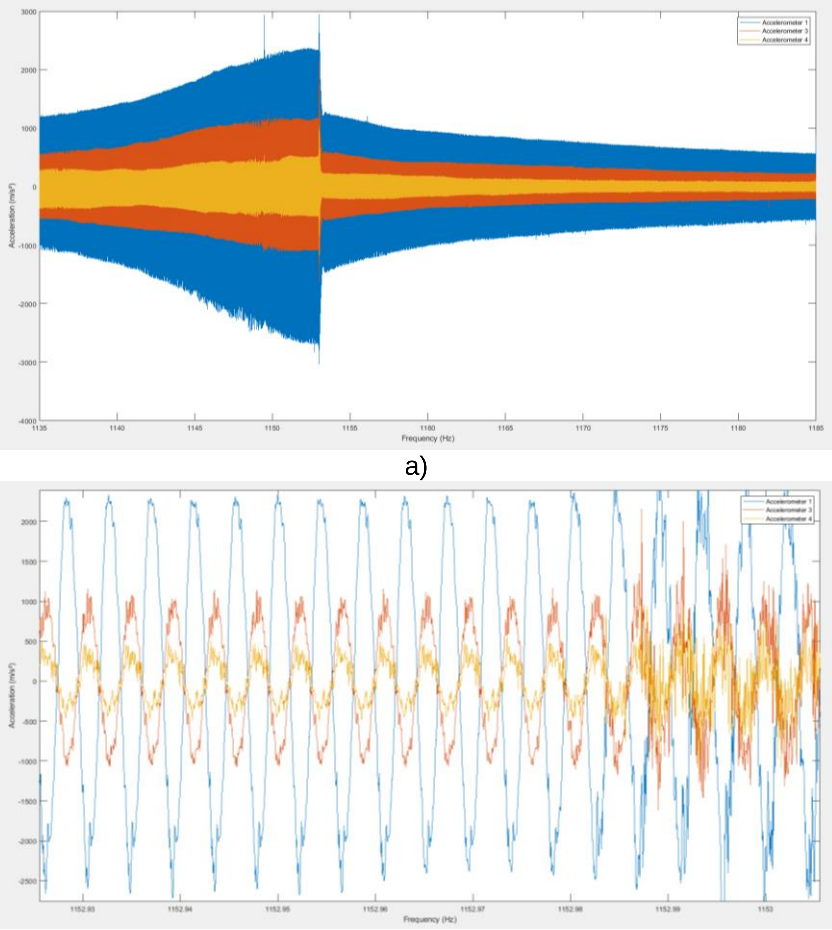

a)

b)

Figure 7.2:38 – Acceleration from accelerometers 1, 3 and 4 at 216 Vpp for a sweep test with piezoelectric actuators 1 and 2 activated out of phase with piezoelectric actuators 4 and 5 from 1135 Hz to 1185 Hz in 10 seconds (a) and zoomed plot at delamination (b)

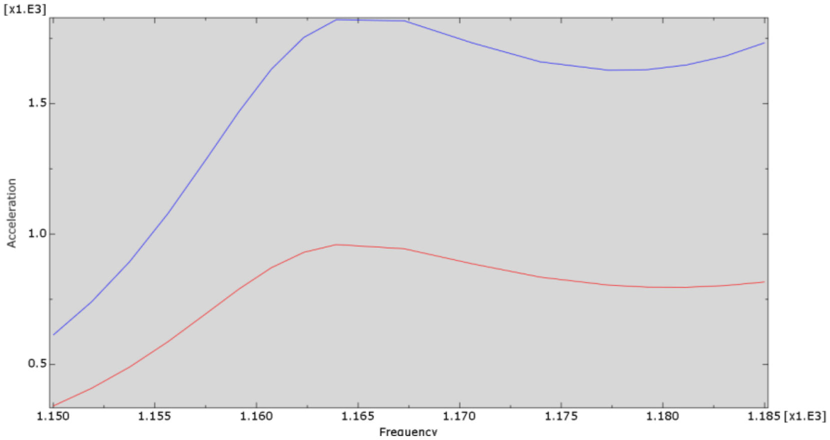

Figure 7.2:39 – Acceleration predicted by the numerical model for mode 18 with actuators 1 and 2 out of phase with 4 and 5 and damping of 1.6% at edge of the plate (blue curve), and at 12 mm (red curve)

For mode 20, the optimal activation was piezoelectric actuators 1 and 5 out of phase with piezoelectric actuators 2, 3 and 4. The frequency at maximum acceleration after the ice accumulation was 1195 Hz. A sweep from 1170 to 1220 Hz was performed twice at 136 Vpp, first with accelerometers 1, 2 and 5 and then with accelerometers 1, 3 and 4. The damping obtained was 1.9% and phasing and amplitudes matched the mode shape predicted by the frequency analysis.

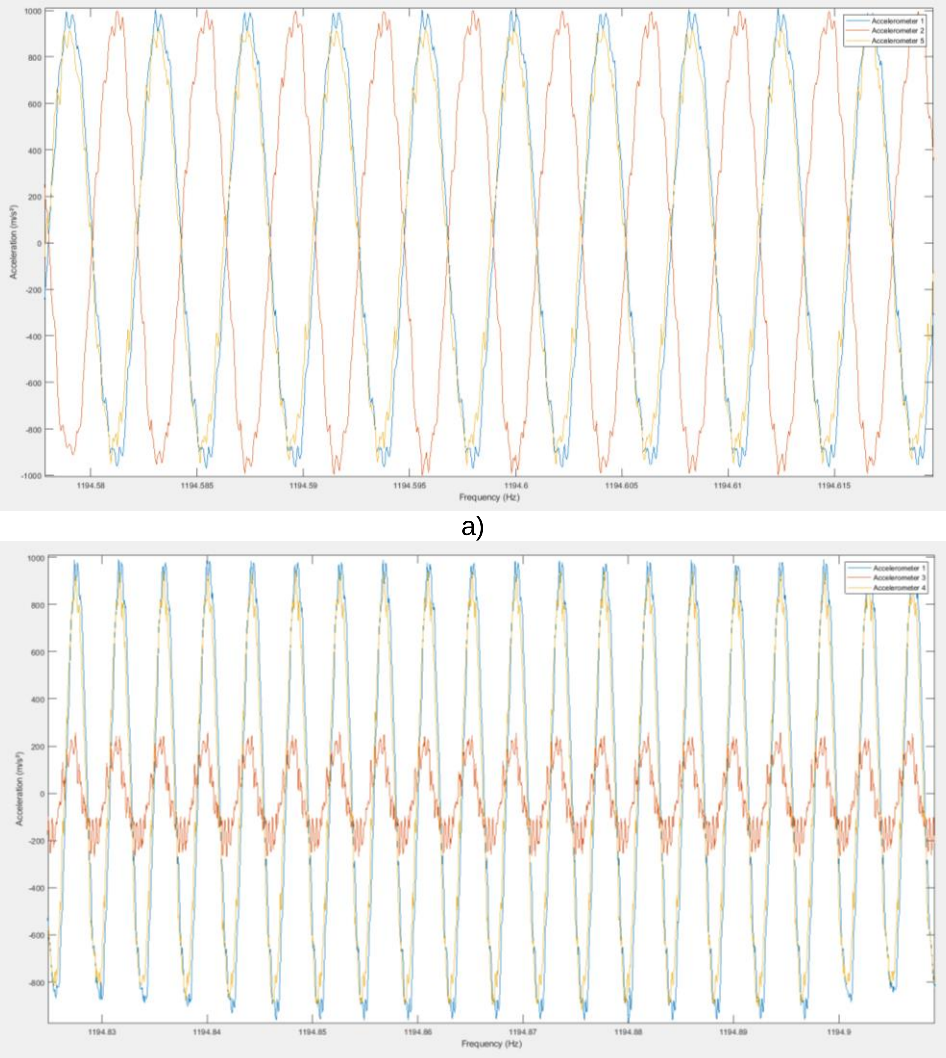

a)

b)

Figure 7.2:40 – Acceleration at resonance during sweep from 1170 to 1220 Hz in 10 s with actuators 1 and 5 out of phase with actuators 2, 3 and 4 at 136 Vpp for accelerometer 1, 2 and 5 (a) and 1, 3 and 4 (b)

The sweep test was repeated at increased voltage and delamination was obtained in the middle of the plate at 240 Vpp. Acceleration obtained at the edge and center of the plate was 1800 m/s² and at accelerometer 3 was 600 m/s² (Figure 7.2:42). Figure 7.2:43 presents the prediction of the numerical model for the same case. At edge and center of the plate the model predicted 2000 m/s² while it predicted 600 m/s² at position of accelerometer 3. The results of the four modes investigated are presented at Table 7.2:4.

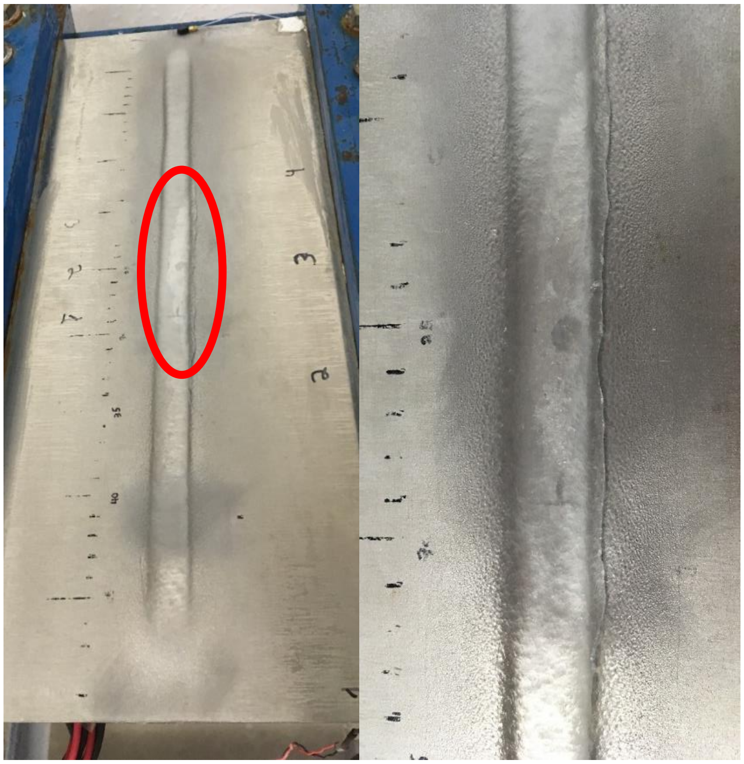

Figure 7.2:41 – Delamination at 240 Vpp for a sweep test with piezoelectric actuators 1 and 5 activated out of phase with piezoelectric actuators 2, 3 and 4 from 1170 Hz to 1220 Hz in 10 seconds

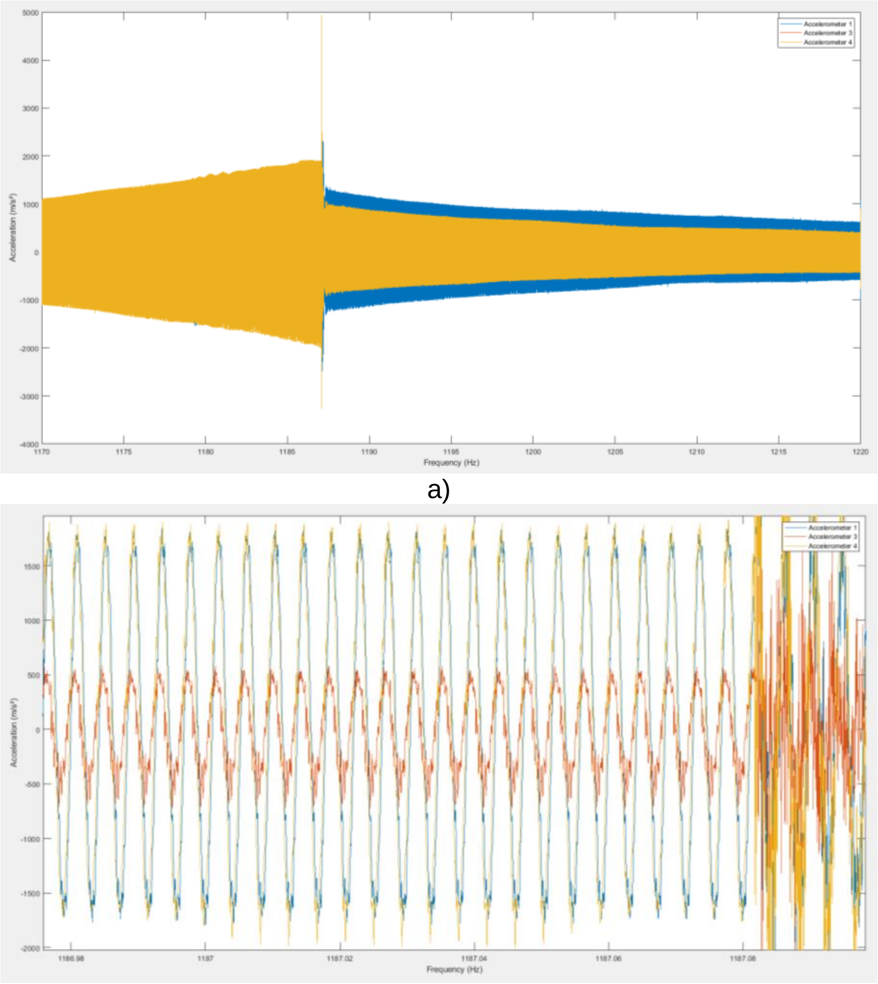

a)

b)

Figure 7.2:42 – Acceleration from accelerometers 1, 3 and 4 at 240 Vpp for a sweep test with piezoelectric actuators 1 and 5 activated out of phase with piezoelectric actuators 2, 3 and 4 from 1170 Hz to 1220 Hz in 10 seconds (a) and zoomed plot at delamination (b)

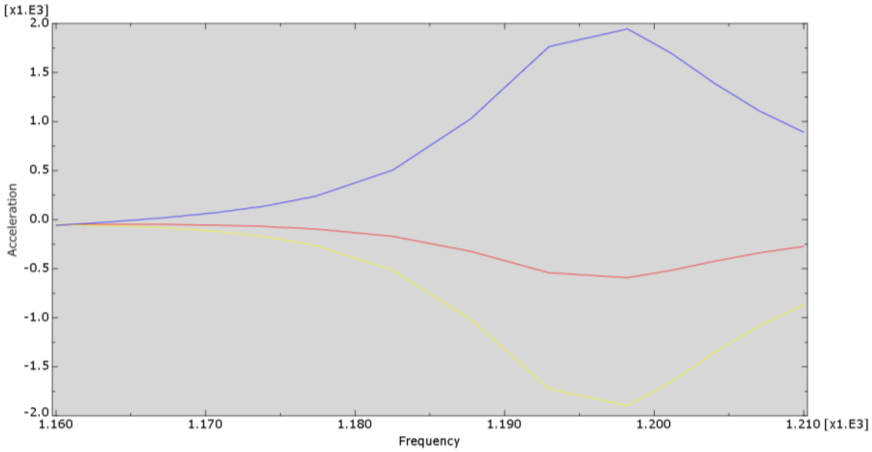

Figure 7.2:43 – Acceleration predicted by the numerical model for mode 20 with actuators 1 and 5 out of phase with 2, 3 and 4 and damping of 1.9% at edge of the plate (blue curve), at 12 mm (red curve) and at center of plate (yellow curve)

Table 7.2:4 – Results obtained for delamination tests

Mode (#)	**Frequency** (Hz)	**Damping** (%)	**Vpp** (V)	**Acc. at edge** (m/s^2)		**Acc. at accelerometer 3** (m/s^2)		**Acc. at Center** (m/s^2)	
				Exp.	**Num.**	**Exp.**	**Num.**	**Exp.**	**Num.**
1	192	2.2	560	725	675	400	460	425	440
17	1138	1.3	192	2100	1750	825	1125	725	1025
18	1160	1.6	216	2200	1825	1000	950	-	-
20	1195	1.9	240	1800	2000	600	600	1800	2000

7.2.1.5 RESULTS ANALYSIS

7.2.1.5.1 EXPERIMENTAL TEST REPEATABILITY

The repeatability of the experimental results were studied by repeating the ice accumulation and sweep tests for two modes. For the first mode, mode 5, the test was repeated four times and results were presented at Table 7.2:2. The resonant frequency obtained during these tests was 404 ± 21 Hz and voltage at cracking was 333 ± 38 Vpp. The acceleration measured was 558 ± 103 m/s^2 for accelerometer 1 and 423 ± 98 m/s^2 for accelerometer 3 and 4. The damping measured was 1.0 ± 0.3 %.

For mode 23, the test was repeated three times. The resonant frequency obtained was 1327 ± 8 Hz, while the voltage at cracking was 380 ± 20 Vpp. The accelerations were 1767 ± 467 m/s^2 for accelerometer 1, 2367 ± 267 m/s^2 for accelerometer 3 and 1683 ± 233 m/s^2 for accelerometer 4. The damping was measured at 1.2 ± 0.1 %.

The resulting percentages of variation are presented at Table 7.2:5. The results show that the variation of the test can be considered ± 26%. Damping variation, which was at ± 26 % for mode 5, reflects the variation in the ice accumulation for each test. This shows that a significant part of the variation could be attributed to the ice accumulation on the plate, which was expected. Since the specific damping was input in the numerical for each test, some of this variation had a lesser impact on the accuracy of the numerical model.

Table 7.2:5 – Percentage of variation for test repetitions for mode 5 and 23

Mode	Frequency	Damping	Vpp	Acc. at edge	Acc. at accelerometer 3	Acc. at Center
5	5%	26%	11%	18%	23%	23%
23	<1%	8%	5%	26%	11%	14%

7.2.1.5.2 ACCURACY OF THE NUMERICAL MODEL (NUMERICAL MODEL VALIDATION)

The numerical model predicted the resonant frequency and shape for each mode with the frequency analysis, and predicted the acceleration, displacement, stress, strain, etc. with the direct-solution steady-state dynamic analysis. Table 7.2:6 presents the comparison between the predicted frequencies and the frequencies obtained during the experimental testing. The model was able to accurately predict the resonant frequencies of each of the modes investigated, with a difference of 13% or less. As the frequency increased above 1000 Hz, the model had an accuracy of 98% or higher for all of the modes investigated.

Table 7.2:6 – Comparison of experimental and numerical frequencies for the resonant modes

Mode (#)	Experimental Frequency (Hz)	Numerical Frequency (Hz)	Discrepancy (%)
1	192	203	6
5	404	350	13
17	1138	1158	2
18	1160	1164	<1
20	1195	1198	<1
23	1327	1338	<1

Table 7.2:7 and Table 7.2:8 present the difference of the acceleration amplitudes predicted by the direct-solution steady-state dynamic analysis with regard to the accelerations measured experimentally. The damping loss factor used in the numerical model was obtained using the half power method for frequency sweep excitation at 136 Vpp for all resonant modes. The damping coefficient associated to each mode was assumed to be constant irrespective of the voltage range of excitation within the voltage ranges of interest. This was confirmed through testing at different voltages of excitation for mode 1 and 5 and no significant difference in the damping coefficient was observed for each mode irrespective of the voltage range of excitation. Furthermore, since for most cases, the voltage of excitation at each modal frequency of interest

resulting in ice breaking was very close to the voltage used to measure the damping coefficient, this assumption was considered acceptable for the numerical simulations. Table 7.2:7 shows the comparison for modes where cracking was obtained for all test repetitions, identified by their repetition number in brackets, as well as the tests with the optimal phasing, identified by a "(p)" in the table. Table 7.2:8 presents the comparison for modes where delamination of the ice layer was obtained. The average difference was 20%, while the maximum difference obtained was 41%. The error of the numerical model can be defined at ±41%. This value was considered acceptable considering the test repeatability of ±26%. This difference could be explained by different factors. First, the ice layer was modeled as a perfect rectangular prism while the ice layer accumulated on the plate had rounded edges and was not perfectly rectangular. The thickness of the layer varied to a certain extent along its length, which was not reflected in the numerical model. The density and elastic modulus of the ice were not measured but taken from literature values. The data was recorded with accelerometers, while still small, could have been slightly intrusive. Also, in some cases, the anti-nodes of the resonant modes obtained experimentally could have been offset by a very small distance compared to the position predicted by the numerical model due to a little asymmetry and position of the ice layer accumulated. The model's accuracy was deemed acceptable for the model's purpose, which was to predict if and at which voltage and phasing a piezoelectric system can crack and delaminate an ice layer from a structure as well as to assist in the design of an optimal system.

Table 7.2:7 – Difference of the numerical model prediction with experimental results for modes with cracking of the ice

Mode (#)	Difference at edge of plate (%)	Difference at accelerometer 3 (%)	Difference at center (%)
5 (1)	-29	-28	-28
5 (2)	-18	-12	-12
5 (3)	-24	-21	-21
5 (4)	-24	-25	-25
5 (p*)	+24	+19	+19
23 (1)	-19	-40	-24
23 (2)	-11	-35	-32
23 (3)	+15	-35	-21
23 (p*)	+2	-20	-18

*performed with optimal phasing of actuators

Table 7.2:8 – Difference of the numerical model prediction with experimental results for modes with delamination of the ice

Mode (#)	Difference at edge of plate (%)	Difference at accelerometer 3 (%)	Difference at center (%)
1	-7	+15	+4
17	-17	+36	+41
18	-17	-5	-
20	+11	0	+11

7.2.2 NUMERICAL MODEL STRESS PREDICTIONS

7.2.2.1 STRESS AT CRACKING OF THE ICE

The numerical model was used to define the stress obtained in the ice layer at cracking and delamination. For modes where cracking occurred, the vibration of the plate created bending in the ice layer at the anti-nodes position, which was responsible for the stress generation. From beam theory, it could be concluded that the crack generation was caused by tensile stress normal to the crack. The normal stress S11, normal to the crack direction, was investigated for the two modes where cracking was obtained.

For mode 5, four test repetitions with all actuators in phase were conducted for the model validation, as well as a fifth test with the optimal phasing of the actuators. The normal stress S11 calculated by the numerical model for each case was investigated. Figure 7.2:44 presents the S11 stress in the ice layer for the first test performed with all actuators in phase for mode 5. The figure confirmed that the maximum stress was obtained at anti-nodes positions where cracks were obtained during the experimental tests (see Figure 7.2:44). It could also be observed that, as predicted by beam theory, maximum stress was generated at the top of the ice layer. Table 7.2:9 presents the maximum normal stress obtained at anti-nodes, where cracking occurred, for all the repetitions. The average normal stress predicted by the numerical model was 1.01 MPa. The results were very close, within 20%, for the four tests with the same phasing. The stress obtained with the optimal phasing was about twice as large as the results obtained during the other four tests. This great difference could be attributed to the fact that the vibration amplitude of the four repetitions was under evaluated by the numerical model while it was over evaluated for the test with the optimal phasing. The normal stress for ice cracking can be adjusted by simply increasing or decreasing the value predicted by the model for the error difference with the experimental results. This is done by imposing the vibration amplitudes obtained experimentally in the numerical model. After adjustment, the stress at cracking varies from an average of 1.01 to 1.13 MPa, and a range of 0.71 MPa – 1.90 MPa to a range of 0.8 MPa – 1.60 MPa.

Table 7.2:9 – Normal stress S11 and adjusted normal stress S11 calculated by the numerical model for all repetitions performed experimentally for mode 5

Repetition	**1**	**2**	**3**	**4**	**5 (o.p.*)**	**Average**
Normal stress S11 (MPa)	0.78	0.71	0.73	0.93	1.90	1.01
Adjusted Normal stress S11 (MPa)	1.08	0.80	0.92	1.24	1.60	1.13

*performed with optimal phasing of actuators

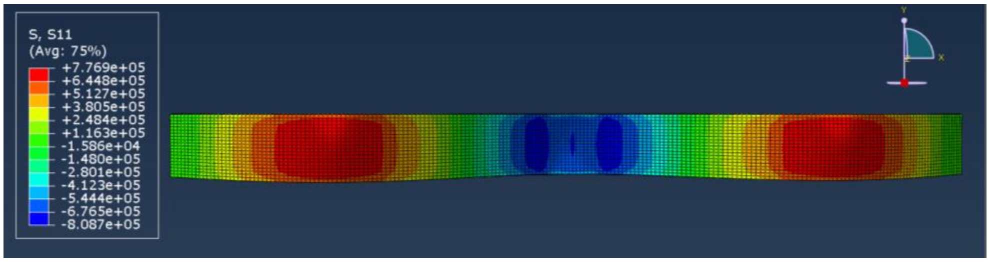

a)

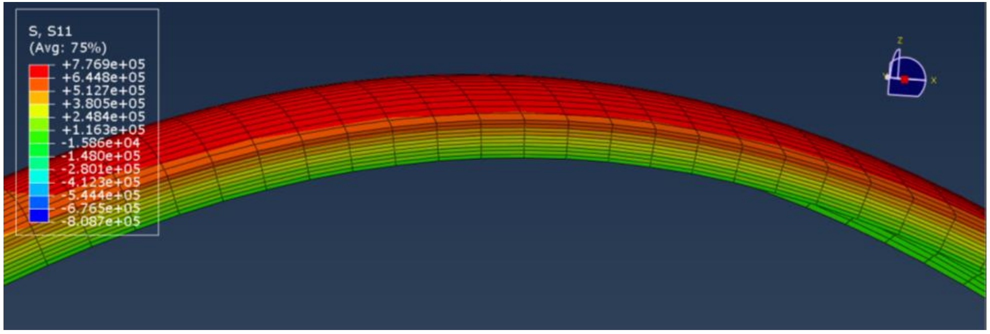

b)

Figure 7.2:44 – Normal stress S11 in the ice layer for first test with al actuators in phase for mode 5, top view (a) and side view (b)

A similar numerical investigation was conducted with the four tests performed experimentally for the mode 23. As expected, the maximum stress was calculated at the anti-node positions where cracking occurred. The average stress was 0.63 MPa, with a stress range from 0.51 MPa to 0.87 MPa. If the normal stress is adjusted as done for mode 5, the average stress increases to 0.93 MPa, with stresses ranging from 0.82 MPa to 1.08 MPa (Table 7.2:10).

Once the error in the vibration magnitude for the numerical model was taken into account, adjusted averages of 1.13 MPa and 0.93 MPa were obtained for the two modes (mode 5 and 23), which was within 20% difference, meaning that the two modes predicted a similar stress for ice failure. When including all tests performed for the two modes, an average of 1.04 MPa was obtained, which is in accordance with literature values [11]. The stress predicted by the numerical model responsible for ice cracking ranged from 0.80 MPa to 1.60 MPa. With the stochastic nature of the ice, as well as difference in the ice structure, ice formation and ice shape from test to test due to test variation, this value compared favorably with the range of 0.70 to 3.10 MPa obtained in the literature [11]. When the numerical model was used to predict ice cracking, the accuracy of the model needed to be taken into account in the stress range. When the 41% error of the numerical model was applied, the stress range that the numerical model which should create cracking was 0.47 MPa to 2.26 MPa.

Table 7.2:10 – Normal stress S11 and adjusted normal stress S11 calculated by the numerical model for all repetitions performed experimentally for mode 23

Repetition	1	2	3	4 (o.p.*)	Average
Normal stress S11 (MPa)	0.51	0.61	0.54	0.87	0.63
Adjusted Normal stress S11 (MPa)	0.86	0.94	0.82	1.08	0.93

*performed with optimal phasing of actuators

7.2.2.2 STRESS AT DELAMINATION OF THE ICE

In a previous study [62], it was shown that two different delamination scenarios can be obtained during de-icing tests, an adhesive break and a cohesive break at the interface. At higher temperatures, the break is adhesive and a delamination occurs between the ice layer and the steel plate. At lower temperatures, the break starts to become cohesive and the break occurs in the ice layer itself instead of at the interface. The results obtained in this testing has shown adhesive breaks, which was in agreement with the results obtained at similar temperatures during the previous phases. Moreover, Guerin has demonstrated that at -8°C, ice shows adhesive delamination [78]. For the stresses responsible for adhesive delamination of the ice layer, the beam theory for composite beams in flexion predicts that the strain created in the plate during flexion will create shearing at the bottom of the ice layer. Since the ice layer has a much lower young modulus, the difference in strain of the two materials should be responsible for shear stresses at the interface.

The anti-nodes generated by the vibration of the plate created flexion in both the length (x-direction) and width (y direction), which created shearing stresses in those two directions. Figure 7.2:45 a) and b) show the distribution of stress S13 and S23 in the ice layer for mode 17. Stress in both directions are maximal at the bottom of the ice layer and around the edges of the ice layer. Stress S13 is higher on the edge corresponding to the width of the ice layer while S23 is higher along its length. Table 7.2:11 shows that S23 is significantly higher, about four times, than S13, with an average of 0.42 MPa compared to 0.11 MPa. The values range from 0.09 to 0.12 MPa for S13 and from 0.33 to 0.60 MPa for S23. When the values were adjusted to take into account the inaccuracy of the model for each mode, S13 ranges from 0.10 to 0.14 MPa with an average of 0.12 MPa and from 0.33 to 0.65 MPa with an average of 0.46 MPa for S23. The shear stress distribution followed the same pattern for all modes investigated. As presented in Figure 7.2:45 for mode 17, shearing was concentrated around the edges at the bottom of the ice layer. The shear stress tended towards zero at the middle of the ice layer and increased rapidly close to the edges. It could be concluded that delamination of the ice was initiated at the edges and propagated towards the center as the layer delaminated. This conclusion was in agreement with the shear model developed and finite element results obtained by Tian and al. [73]. In their study, the 2D shear model along the length of an ice patch on a plate in vibration developed showed the same type of distribution. They concluded that the maximum shear stress was found to be concentrated on the edges of the ice and that as a result, the delamination starts off from edges of the ice. The maximum shear stress emerges on the new edges until the shedding off of the entire ice patch or layer.

Numerical prediction of the stresses at the bottom layer of the ice shows that the stresses in other direction are negligible, except for S33. S33 is a normal stress caused by the up and down movement of the plate pushing and pulling the ice layer. S33 is larger than the shear stresses with values ranging from 0.53 to 0.84 MPa and an average of 0.63 MPa (Table 7.2:11). When adjusted with the numerical error for each mode, values for S33 ranges from 0.50 to 0.90 MPa with an average of 0.69 MPa. Figure 7.2:45 c) shows that S33 follows a similar distribution on the ice surface than S23.

Table 7.2:11 – Stress S13, S23 and S33 for delamination modes

Mode	1	17	18	20	Average
Shear stress S13 (MPa)	0.09	0.12	0.12	0.11	0.11
Adjusted shear stress S13 (MPa)	0.10	0.14	0.14	0.10	0.12
Shear stress S23 (MPa)	0.60	0.38	0.33	0.37	0.42
Adjusted shear stress S23 (MPa)	0.65	0.46	0.40	0.33	0.46
Normal stress S33 (MPa)	0.84	0.58	0.53	0.56	0.63
Adjusted normal stress S33 (MPa)	0.90	0.70	0.64	0.50	0.69

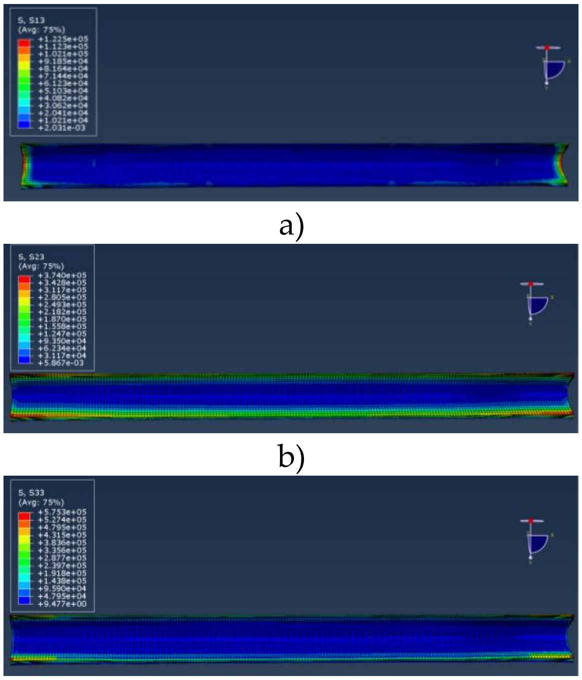

c)

Figure 7.2:45 – Stress S13 (a), S23 (b) and S33 (c) at bottom of ice layer for mode 17

S23 and S13 are two stresses which act on the adhesion by shearing the ice layer at the interface. S23 is significantly higher than S13 and acts on a different edge of the ice layer. This means that S23 is considered the principal stress in shearing and S13 is considered negligible. The adjusted average value of S23 (0.46 MPa) is in the range of values found in the literature. Hardesty [79], from his literature study, established that the adhesion strength on steel due to shearing at -8°C ranges from 0.20 to 0.90 MPa, with the large majority of the results being between 0.30 and 0.60 MPa. A shear stress of 0.61 MPa was obtained with

Centrifuge Adhesion Tests performed at the laboratory on steel beams [80]. The numerical model predicts a shearing of 0.33 to 0.65 MPa at ice delamination, which is again in the range obtained in the literature. When including the 41% error of the numerical model, the range of shear stress within which the numerical model predicts ice delamination becomes 0.20 to 0.92 MPa.

S33 is a tensile/compressive stress that acts on the adhesion in the normal direction. The model predicts adjusted stresses of 0.50 to 0.90 MPa, and when including the 41% error, this becomes 0.30 to 1.27 MPa. With an adjusted average of 0.69 MPa, this stress is 1.5 times higher than S23. This stress could be responsible for a tensile adhesive break of the ice, instead of an adhesive break due to shearing stress S23. No literature values for tensile adhesive break on steel were found, making comparison with other results impossible. However, Jellinek [36] has determined that the adhesive breaks for tensile tests was at minimum 15 times larger than for shearing tests, which is 10 times more than the 1.5 times for S33 obtained numerically. This, and the fact that S23 falls within the values found in literature, indicates that S23 is responsible for the delamination of the ice layer. More investigation could be done to validate Jellinek's results on steel.

7.2.2.3 STRESS PREDICTION SUMMARY

A summary of the minimum and maximum stress limits calculated by the numerical model, with and without the numerical error taken into account is presented in Table 7.2:12.

Table 7.2:12 – Summary of the stress limit criteria calculated by the numerical model with and without numerical error

Stress	**Average**	**Min.**	**Max.**	**Min. with 41% numerical error**	**Max. with 41% numerical error**
S11	1.04	0.80	1.60	0.47	2.26
S23	0.46	0.33	0.65	0.20	0.92
S33	0.69	0.50	0.90	0.30	1.27

7.2.3 PREDICTION OF ICE BREAKING WITH THE NUMERICAL MODEL

The numerical model has been validated experimentally with accelerometers and the stresses at breaking predicted by the numerical model have been analyzed and validated by the literature. As a proof of concept, the numerical model was used to find modes where ice breaking occurs and predict voltages at which it will occur. This was done both to predict cracking and delamination of the ice.

7.2.3.1 PREDICTION OF CRACKING OF THE ICE LAYER

The frequency analysis was used to find modes where cracking of the ice was susceptible to occur. Two modes were targeted, mode 27 at 1577 Hz and mode 35 at 1940 Hz (Figure 7.2:46). Those modes were selected due to their mode shapes similar to shape of mode 23 where cracking was successful.

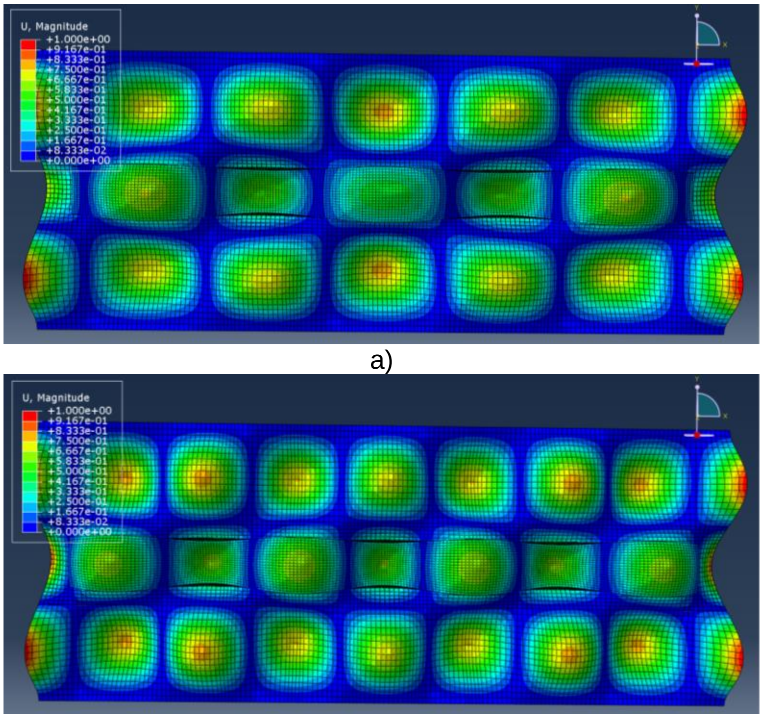

a)

b)

Figure 7.2:46 – Mode 27 (a) and mode 35 (b)

Ice accumulation was repeated on the flat plate and the resonant modes around 1577 Hz were searched with acceleration signals from the accelerometers. A resonant frequency was obtained at 1600 Hz. Sweep tests were performed from 1575 to 1625 Hz in 10 seconds at a low voltage (136 Vpp) with all the piezoelectric actuators in phase once with accelerometers 1, 2 and 5 and once with accelerometer 1, 3 and 4. The results, presented at Figure 7.2:47, show that accelerometers 1 and 4 were in phase and accelerometer 2 was dephased of 180°. Accelerometers 3 and 5 had very low accelerations, which meant that they were located in node locations. For mode 27, Figure 7.2:48 shows that acceleration at the edge, corresponding to accelerometers 1 and 2, was in counter-phase with the acceleration at the center of the plate, which corresponds to accelerometer 4. At 12 and 30 mm, positions of accelerometer 3 and 5, a null acceleration was obtained. This matched the accelerations measured by the accelerometer, meaning that mode 27 was found at 1600 Hz.

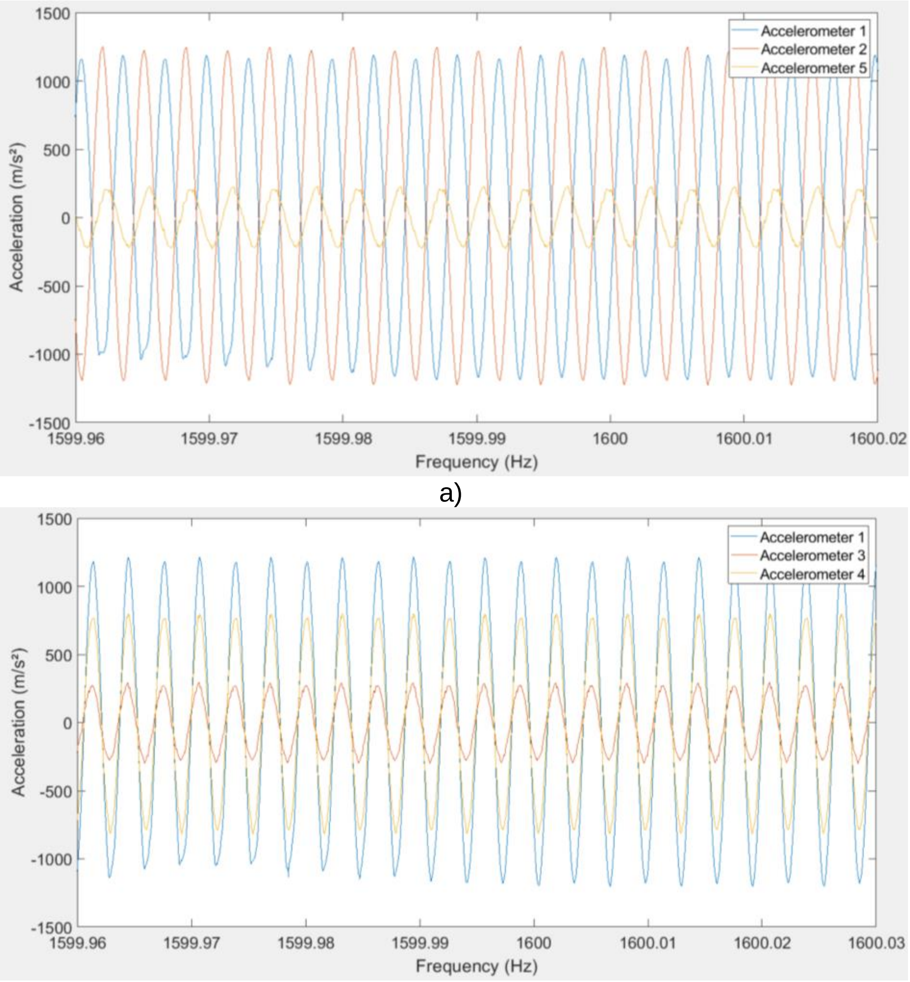

a)

b)

Figure 7.2:47 – Acceleration at resonance during sweep from 1575 to 1625 Hz in 10 s all actuators in phase at 136 Vpp for accelerometer 1, 2 and 5 (a) and 1, 3 and 4 (b)

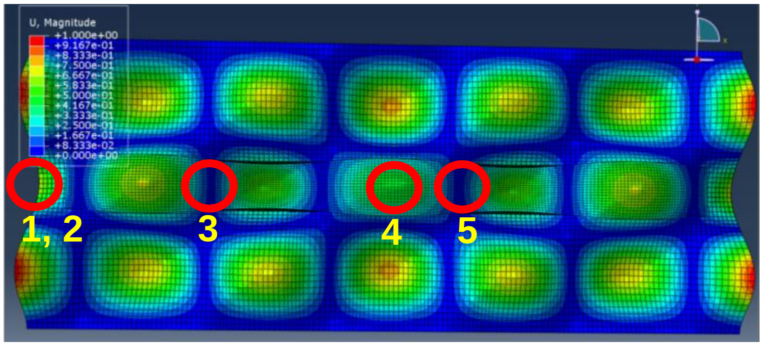

Figure 7.2:48 – Mode 27 predicted by the frequency analysis of the numerical model

The damping calculated from the signals obtained with the accelerometers was 1.1%. With this value, the numerical model predicted a voltage of 190 Vpp to obtain 0.8 MPa and 380 Vpp to obtain 1.6 MPa in stress S11 in the ice layer. Those stresses correspond to the range of stress defined previously where cracking is susceptible to occur. By taking into account the error of the numerical model, this meant that the numerical model predicted cracking of the ice between 112 Vpp and 535 Vpp (0.47 MPa to 2.26 MPa, section 7.2.2.3).

The sweep test was then performed with accelerometers 1, 3 and 4 at higher voltages and a crack was formed during the sweep at 335 Vpp (Figure 7.2:49). The stress calculated with the numerical model for this voltage was 1.4 MPa (Figure 7.2:50). Acceleration measured by the accelerometers is shown at Figure 7.2:51, with a value of 3200 m/s² for accelerometer 1, 500 m/s² for accelerometer 3 and 2500 m/s² for accelerometer 4. The numerical model predicted 2850 m/s² at the edge of the plate and 2000 m/s² at the center of the plate (Figure 7.2:52). This resulted in an average error of 15% for the numerical model, meaning that the adjusted value for stress S11 was 1.64 MPa.

Figure 7.2:49 – Crack at 335 Vpp for a sweep test with all piezoelectric actuators activated in phase from 1575 Hz to 1625 Hz in 10 seconds

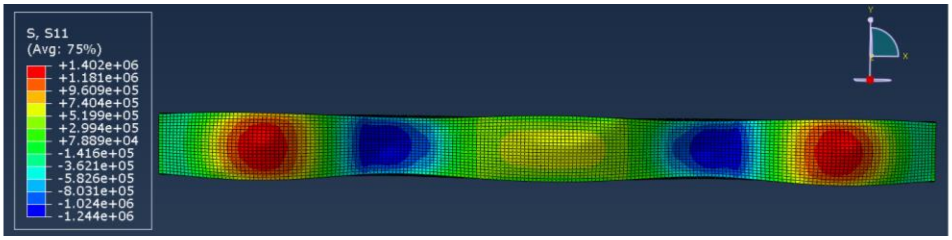

Figure 7.2:50 – Stress S11 for mode 27 at 335 Vpp with all actuators activated in phase

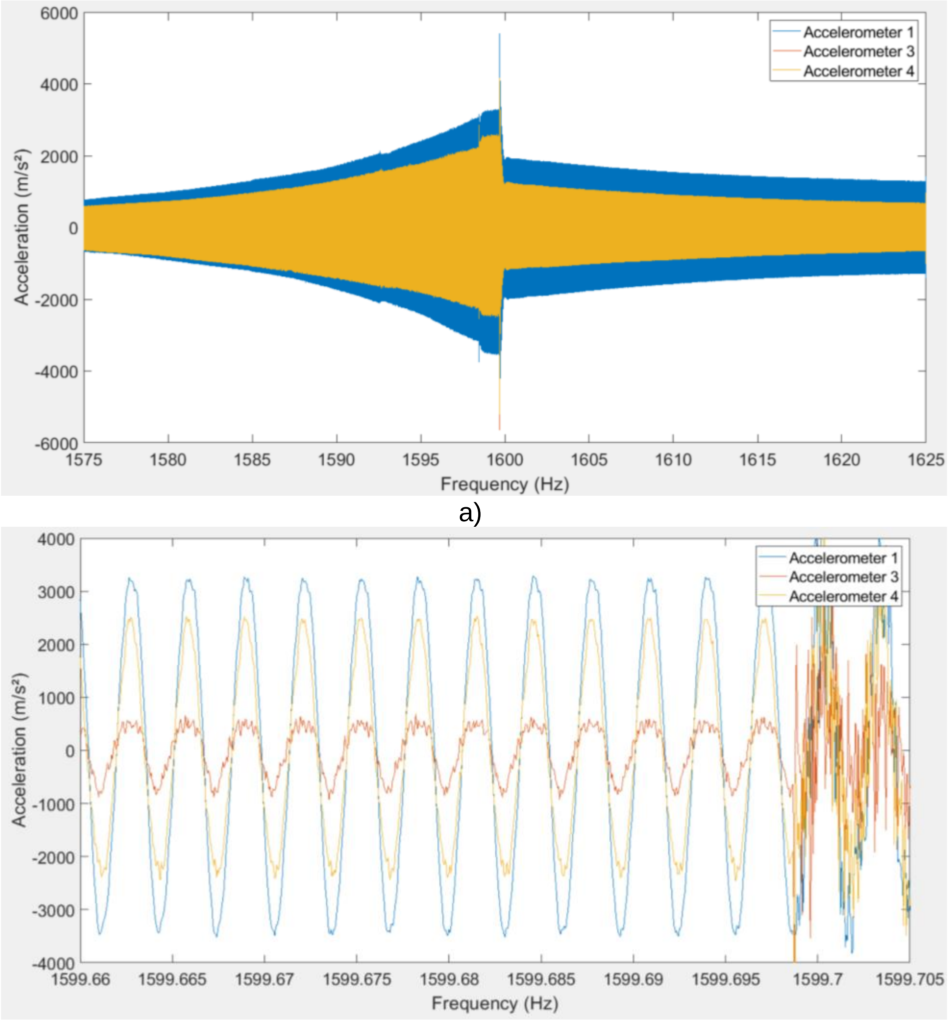

a)

b)

Figure 7.2:51 – Acceleration from accelerometers 1, 3 and 4 at 335 Vpp for a sweep test with all piezoelectric actuators activated in phase from 1575 Hz to 1625 Hz in 10 seconds (a) and zoomed plot at cracking (b)

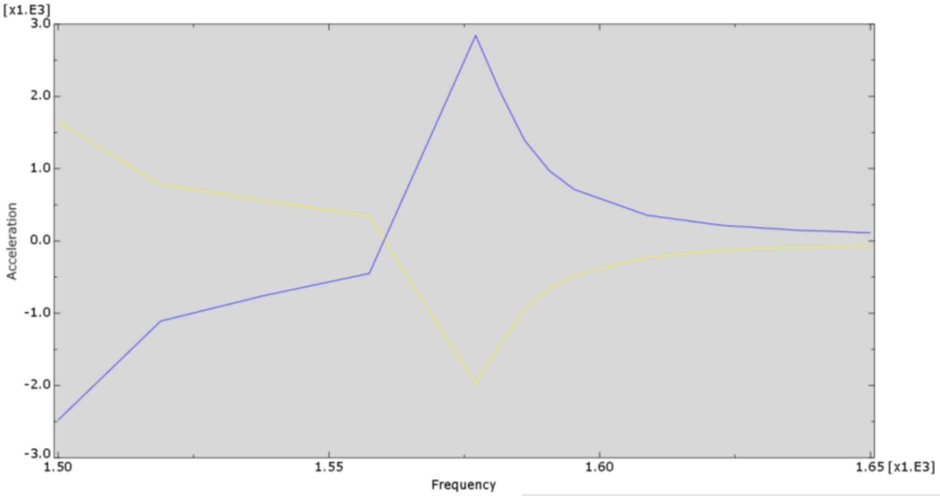

Figure 7.2:52 – Acceleration predicted by the numerical model for mode 27 with all actuators in phase and damping of 1.1% at edge of the plate (blue curve) and center of the plate (yellow curve)

From the conclusions obtained at section 2.4.1.2, it could be observed that activating all the actuators in phase was not the optimal phasing for this mode. Piezoelectric actuator 3 located in the center of the plate should be activated out of phase from the 4 other actuators (see Figure 7.2:48 top). A new ice accumulation was done on the flat plate and the resonant frequency was found at 1591 Hz. The sweep selected was the same as for the previous accumulation, from 1575 Hz to 1625 Hz in 10 seconds, but with piezoelectric actuator 3 out of phase from the other actuators. Damping was measured once again with sweeps at low voltage and a value of 1.0% was obtained. For this damping, the model predicted 0.8 MPa for stress S11 at 120 Vpp and 1.6 MPa at 240 Vpp. With the numerical error taken into account, the model predicted cracking between 70 Vpp and 340 Vpp.

Sweep tests were performed with increased voltage and a crack was obtained at 170 Vpp at the center of the plate. At this voltage, the model predicted a stress S11 of 1.15 MPa (Figure 7.2:54). The accelerations measured were 3200 m/s² for accelerometer 1, 450 m/s² for accelerometer 3 and 2400 m/s² for accelerometer 4 (Figure 7.2:55). The results of the simulation for mode 27 with actuator 3 out of phase and a damping of 1.0% at 170 Vpp, presented at Figure 7.2:56, predicted an acceleration of 2900 m/s² and 2000 m/s² at position of accelerometer 1 and 4 respectively. The numerical error was 13% and the adjusted stress S11 was 1.32 MPa.

Figure 7.2:53 - Crack at 170 Vpp for a sweep test with piezoelectric actuator 3 out of phase with the 4 other piezoelectric actuators from 1575 Hz to 1625 Hz in 10 seconds

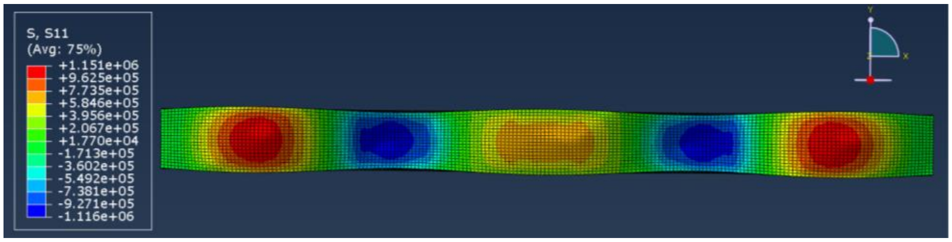

Figure 7.2:54 – Stress S11 for mode 27 at 170 Vpp with actuator 3 out of phase from all other actuators

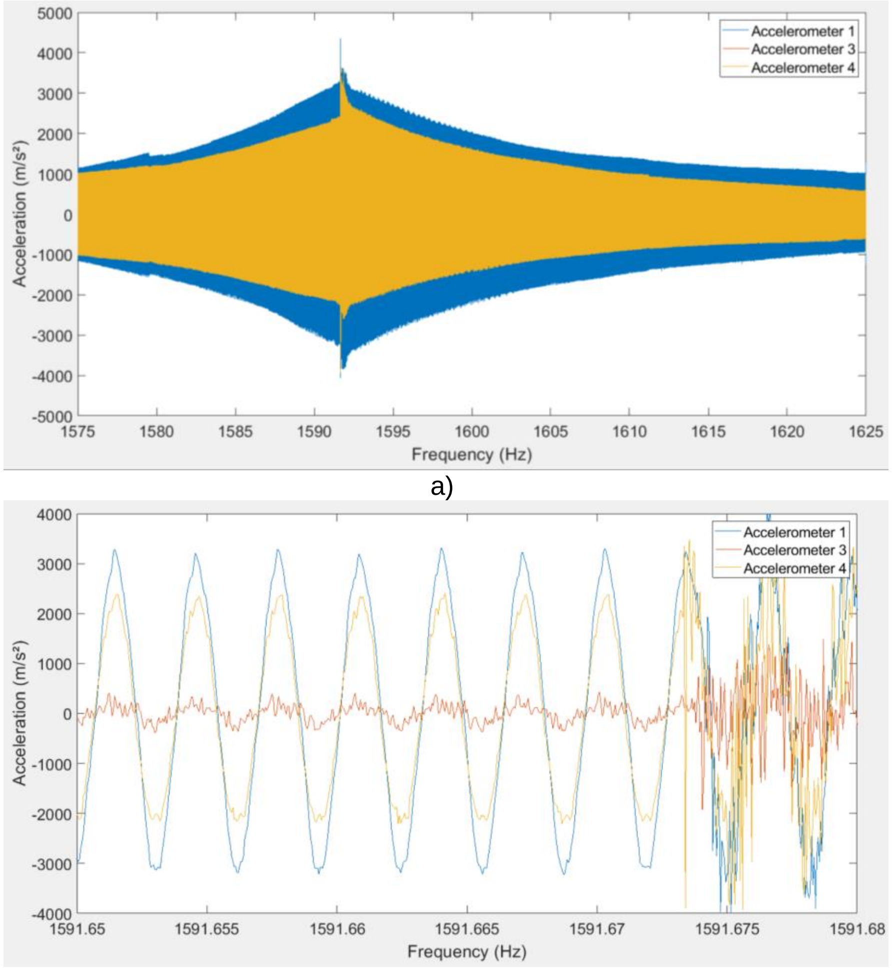

a)

b)

Figure 7.2:55 - Acceleration from accelerometers 1, 3 and 4 at 170 Vpp for a sweep test with piezoelectric actuator 3 out of phase with the 4 other piezoelectric actuators from 1575 Hz to 1625 Hz in 10 seconds (a) and zoomed plot at cracking (b)

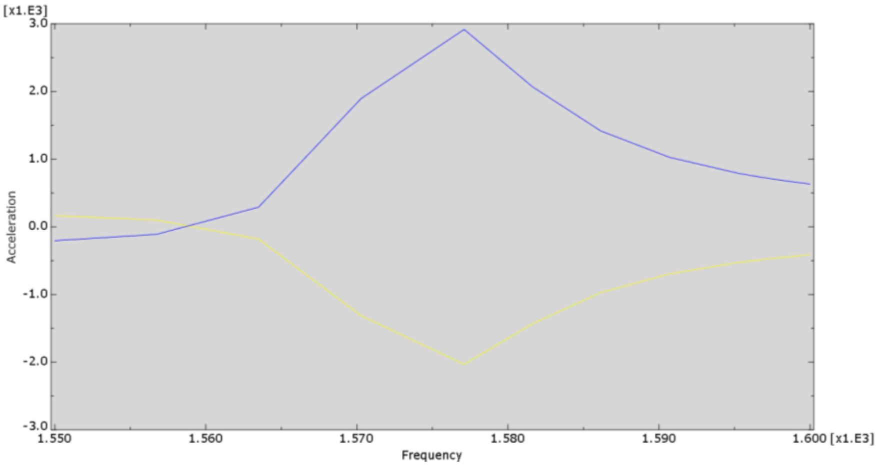

Figure 7.2:56 – Acceleration predicted by the numerical model for mode 27 with piezoelectric actuator 3 out of phase with the 4 other piezoelectric actuators and damping of 1.0 at edge of the plate (blue curve) and center of the plate (yellow curve)

For mode 35, resonant frequencies were searched around 1940 Hz and a frequency was found at 2010 Hz. Sweep tests were performed from 1985 to 2035 Hz in 10 seconds at a low voltage (136 Vpp) with accelerometers 1, 2 and 5 and with accelerometer 1, 3 and 4 respectively (Figure 7.2:57). Accelerometers 1 and 5 were in phase and accelerometer 2, 3 and 4 were dephased 180° from 1 and 5. In mode 35, anti-nodes corresponding to accelerometers 2, 3 and 4 were in phase, while anti-node at accelerometer 5 was in counter-phase, which corresponded to what was obtained experimentally. Also, amplitude of accelerometer 5 was lower than the other accelerometers, which was in accordance with the mode shape of mode 35 since its position on the plate did not correspond to the center of the anti-node (Figure 7.2:58). This confirms that mode 35 was found at 2010 Hz.

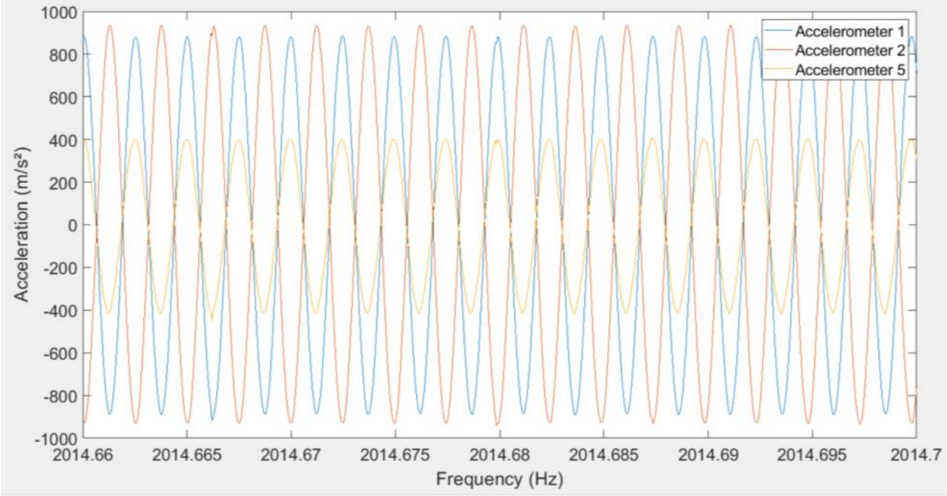

a)

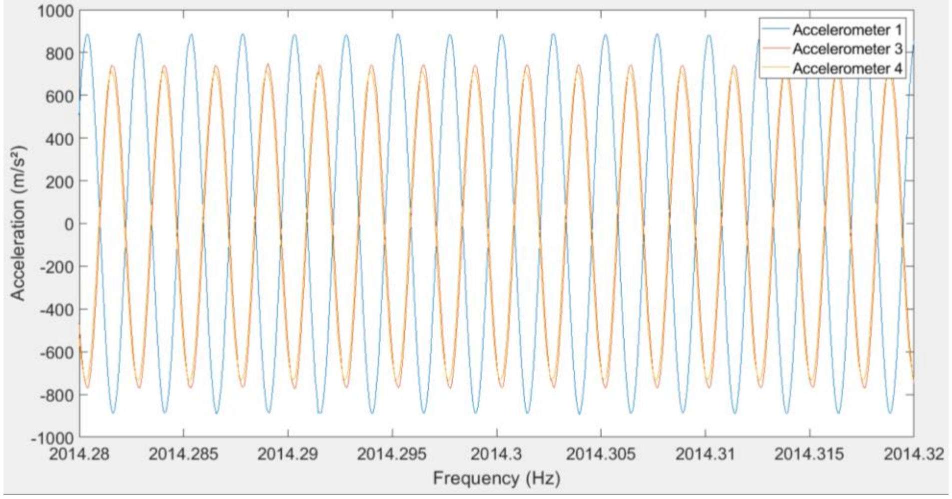

b)

Figure 7.2:57 – Acceleration at resonance during sweep from 1985 to 2035 Hz in 10 s all actuators in phase at 136 Vpp for accelerometer 1, 2 and 5 (a) and 1, 3 and 4 (b)

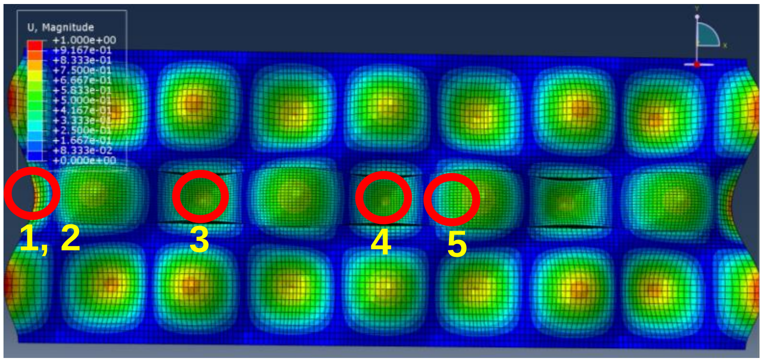

Figure 7.2:58 – Mode 35 predicted by the frequency analysis of the numerical model

The damping calculated from the signals obtained with the accelerometers was 1.0%. The numerical model predicted a stress S11 between 0.8 to 1.6 MPa for voltages of 442 to 884 Vpp. With the potential maximum numerical error, this meant that the model predicted cracking between 265 Vpp and 1245 Vpp. With the operating range of the piezoelectric actuators, from -250 to 1000 V, this corresponded to the maximum Vpp achievable by the actuators. The same sweep test was performed with accelerometers 1, 3 and 4 at higher voltages and a crack was formed at 265 Vpp (Figure 7.2:59), which corresponded to a stress of 0.47 MPa in the numerical model. The acceleration measured by the accelerometers with a value of 1850 m/s² for accelerometer 1, 1700 m/s² for accelerometer 3 and 1675 m/s² for accelerometer 4. The prediction of the numerical model at the edge of the plate was 1600 m/s², at position of accelerometer 3 was 1060 m/s² and at center of the plate was 1110 m/s². With the numerical model error, the adjusted shear stress S11 was 0.76 MPa.

Figure 7.2:59 – Crack at 265 Vpp for a sweep test with all piezoelectric actuators activated in phase from 1985 Hz to 2035 Hz in 10 seconds

The optimal phasing for this mode is piezoelectric actuator 2 and 4 activated out of phase from the 3 other actuators (see Figure 7.2:58). After a new ice accumulation was done on the flat plate, the resonant frequency was found at 2015 Hz. The new sweep selected was from 1990 Hz to 2040 Hz in 10 seconds with piezoelectric actuator 2 and 4 out of phase from the other actuators. Damping was measured with sweeps at low voltage and a value of 1.4% was obtained. The numerical model predicted stresses S11 between 0.8 MPa and 1.6 MPa for voltages of 310 Vpp to 620 Vpp. With the numerical error, the voltage ranges where cracking should occur was 183 Vpp to 875 Vpp. Sweep tests were performed and voltage was increased until a crack was obtained at 200 Vpp. At this voltage the numerical model predicted 0,52 MPa. The acceleration measured was 1600 m/s² for accelerometer 1 and 3 and 1450 m/s² for accelerometer 4. The results of the numerical simulation run for mode 35 with the actuators 2 and 4 out of phase and a damping of 1.4 at 200 Vpp resulted in an acceleration at the edge of the plate of 1800 m/s² and of 1100 m/s² at position of accelerometer 3 and 4. With the numerical error, the adjusted shear stress was 0.71 MPa.

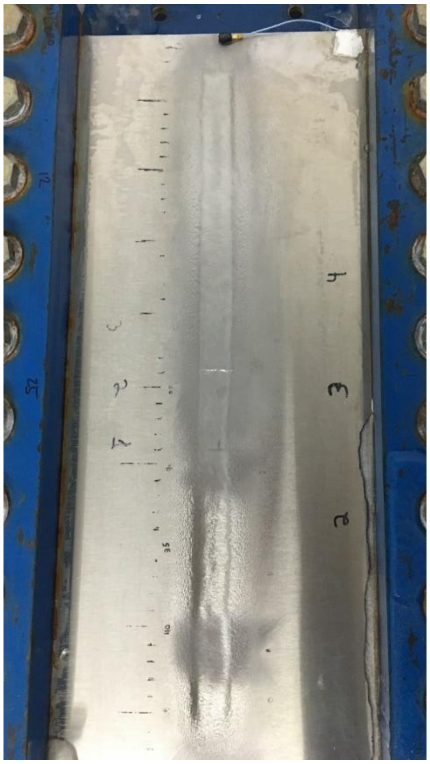

Figure 7.2:60 - Crack at 200 Vpp for a sweep test with piezoelectric actuator 2 and 4 out of phase with the 3 other piezoelectric actuators from 1990 Hz to 2040 Hz in 10 seconds

7.2.3.2 PREDICTION OF DELAMINATION OF THE ICE LAYER

The same process was repeated for predicting delamination of the ice layer. The results from the frequency analysis has allowed to target two modes from their mode shapes, Mode 2 (208 Hz) and 3 (229 Hz). Those modes, as shown in Figure 7.2:61, are similar to modes 18 and 20 for which delamination was proven possible. The frequencies of those modes were very close to mode 1, which is similar in shape to mode 17, showing the same pattern between modes 1, 2 and 3 and modes 17, 18 and 20. Since those two modes are very low in frequencies, a first study was performed for mode 2 to assess if 5 Hz/s sweep rate was appropriate. The frequency was found at 198 Hz without an ice layer and acceleration was measured in steady-state mode and for a sweep from 175 to 225 Hz in 10 seconds at 136 Vpp with actuators 1 and 2 out of phase from actuators 4 and 5. The results showed that with amplitudes of 600 m/s², 200 m/s² and 60 m/s² for accelerometers 1, 3 and 4 respectively in steady-state mode and 575 m/s², 200 m/s² and 60 m/s² during the sweep, a sweep rate of 5 Hz/s was adequate for mode 2 by reaching 96%, 100% and 100% of the acceleration during the sweep.

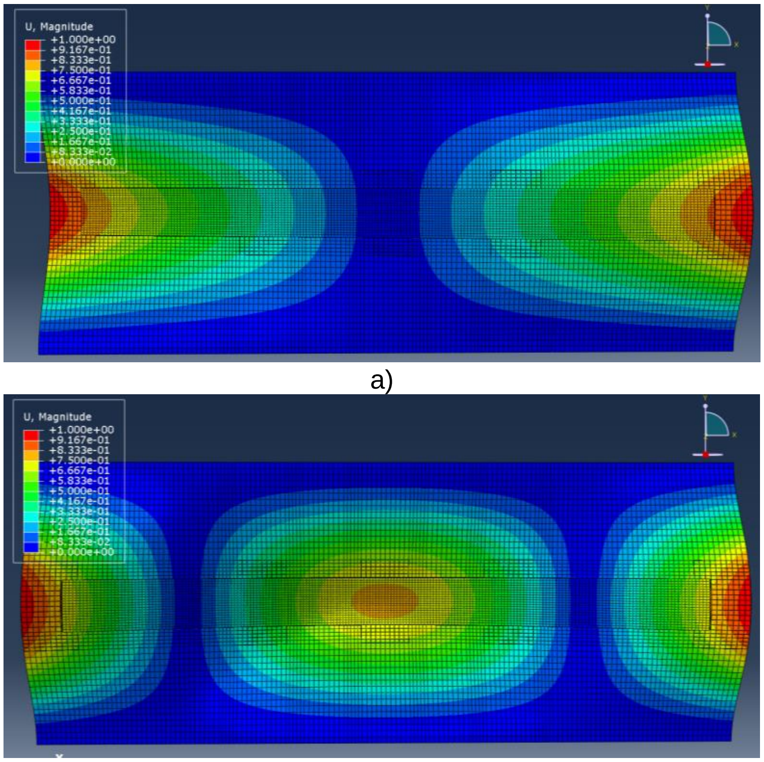

a)

b)

Figure 7.2:61 – Relative displacement for a) Mode 2 (208 Hz) and b) mode 3 (229 Hz)

Ice accumulation was repeated on the flat plate and resonant mode 2 was searched around 208 Hz with piezoelectric actuators 1 and 2 out of phase with actuators 4 and 5, which was the optimal activation for this mode. Only the optimal activation was used for the same reasons as for mode 18 and 20. Mode 2 was found at 205 Hz and sweep tests were performed from 180 to 230 Hz in 10 seconds at low voltage (136 Vpp) with the optimal phasing. Accelerations presented at Figure 7.2:62 confirmed that mode 2 was excited.

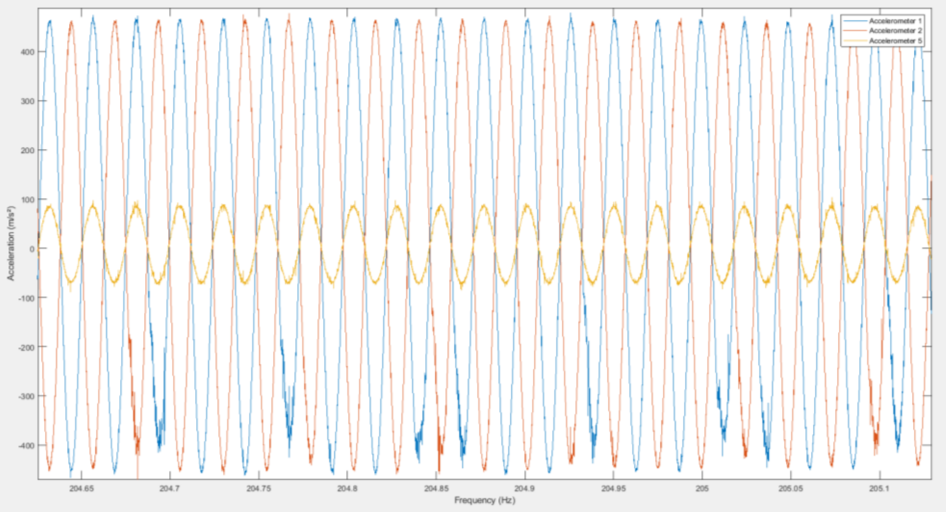

a)

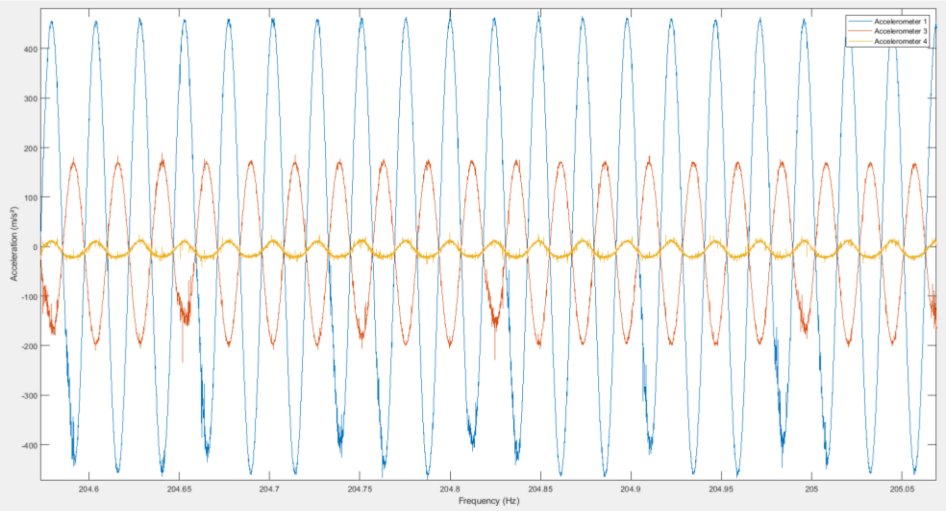

b)

Figure 7.2:62 – Acceleration at resonance during sweep from 180 to 230 Hz in 10 s with actuators 1 and 2 out of phase with 4 and 5 at 136 Vpp for accelerometer 1, 2 and 5 (a) and 1, 3 and 4 (b)

The damping calculated from the sweep tests was 0.7%. To obtain a shear stress S23 between 0.33 and 0.65 MPa the numerical model predicted 105 Vpp to 207 Vpp, and to obtain a normal stress S33 of 0.5 to 0.9 MPa, the numerical model predicted 108 Vpp to 195 Vpp. With the error of the model, delamination should occur between 62 Vpp and 292 Vpp.

Sweep tests were performed with accelerometers 1, 3 and 4 at higher voltages and delamination was obtained during the sweep at 216 Vpp (Figure 7.2:63). The shear stress S23 calculated with the numerical model at this voltage was 0.68 MPa, while normal stress S33 was 1.00 MPa. Acceleration of 820 m/s² for accelerometer 1 and 360 m/s² for accelerometer 3 was obtained. The numerical model predicted 820 m/s² at the edge of the plate and 380 m/s² at position of accelerometer 3. From these results, the adjusted values for S23 and S33 were 0.66 MPa and 0.97 MPa.

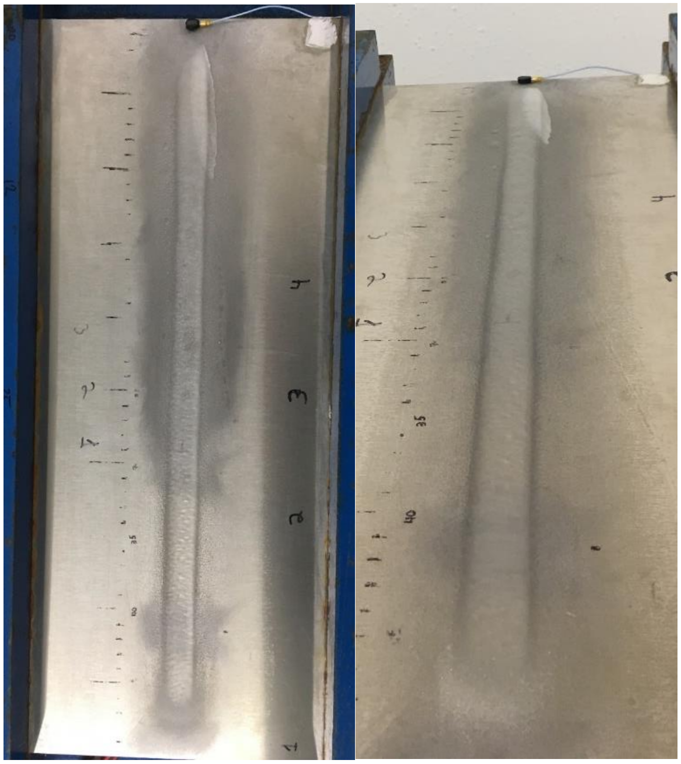
a) b)

Figure 7.2:63 – Delamination at 216 Vpp for a sweep test with piezoelectric actuators 1 and 2 activated out of phase with 4 and 5 from 1575 Hz to 1625 Hz in 10 seconds a) top view b) side view

For mode 3, a resonant frequencies was found at 237 Hz. Sweep tests were performed from 210 to 260 Hz in 10 seconds at a low voltage (136 Vpp) with accelerometers 1, 2 and 5 and with accelerometer 1, 3 and 4 respectively. The sweeps were performed with the optimal phasing for this mode, same as for mode 20, with actuators 1 and 5 out of phase with 2, 3 and 4. The accelerations obtained during those sweeps confirmed that mode 3 was excited.

The damping calculated from the signals obtained with the accelerometers was 0.8%. With this value, voltages of 115 Vpp to 226 Vpp were predicted to obtain S23 between 0.33 and 0.65 MPa and voltages of 108 Vpp to 194 Vpp for a stress S33 between 0.5 to 0.9 MPa. With the numerical model error, this meant that delamination was predicted between 64 Vpp and 320 Vpp.

Sweep tests were performed with accelerometers 1, 3 and 4 at higher voltages and delamination was obtained at both extremities of the ice layer during the sweep at 250 Vpp (Figure 7.2:64). The shear stress S23 calculated with the numerical model at this voltage was 0.72 MPa, while normal stress S33 was 1.15

MPa. Acceleration measured by the accelerometers was 1050 m/s² for accelerometer 1 and 750 m/s² for accelerometer 4. The numerical model predicted 1120 m/s² at the edge of the plate and 870 m/s² at position of accelerometer 4. With this difference, the adjusted values for S23 and S33 were 0.65 MPa and 1.03 MPa.

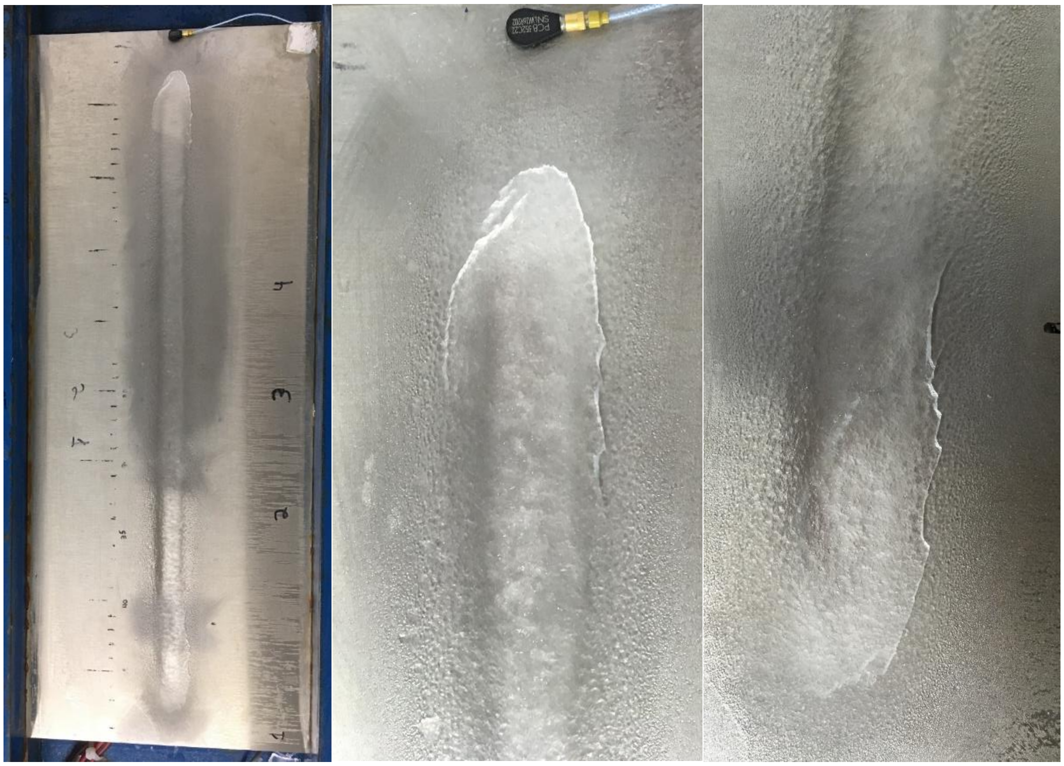
a) b) c)

Figure 7.2:64 – a) Delamination at 250 Vpp for a sweep test with piezoelectric actuators 1 and 5 activated out of phase with 2, 3 and 4 from 210 Hz to 260 Hz in 10 seconds b) Zoomed on top delamination c) Zoomed on bottom delamination

7.2.3.3 RESULTS ANALYSIS OF NUMERICAL MODEL ICE BREAKING PREDICTIONS

The numerical model has been used to find two modes where cracking should occur, two modes where delamination should occur and predicted the voltage range within which the breaking should happen. Mode 27 and 35 has been identified for cracking of the ice and mode 2 and 3 for delamination of the ice layer. Table 7.2:13 presents a summary of the experimental and numerical results obtained for those four modes.

Table 7.2:13 – Summary of results obtained for mode 2, 3, 27 and 35

Mode (Opt. Phasing)	Frequency (Hz)	Damping (%)	Vpp (V)	Acc. at edge (m/s^2)		Acc. at accelerometer 3 (m/s^2)		Acc. at Center (m/s^2)	
				Exp.	Num.	Exp.	Num.	Exp.	Num.
27	1600	1.1	335	3200	2850	-	-	2500	2000
27 (p*)	1591	1.0	170	3200	2900	-	-	2400	2000
35	2010	1.0	265	1850	1600	1700	1060	1675	1110
35 (p*)	2015	1.4	200	1600	1800	1600	1100	1450	1100
2	205	0.7	216	820	820	360	380	-	-
3	237	0.8	250	1050	1120	-	-	750	870

*performed with optimal phasing of actuators

Table 7.2:14 presents a comparison between the experimental and numerical results for those four modes. The maximum difference obtained between the numerical model and the experimental results was 38%, which was in the 41% range established for the numerical model error in a previous section. The average error obtained for all the results was 17%, which was similar to the 20% obtained for the other modes tested previously.

Table 7.2:14 – Comparison of the accelerations between the experimental tests and numerical model predictions for modes 2, 3, 27 and 35

Mode (#)	Exp. Acc. #1 (m/s^2)	Num Acc. #1 (m/s^2)	Diff. (%)	Exp. Acc. #3 (m/s^2)	Num Acc. #3 (m/s^2)	Diff. (%)	Exp. Acc. #4 (m/s^2)	Num Acc. #4 (m/s^2)	Diff. (%)
27	3200	2850	**-11**	-	-	**-**	2500	2000	**-20**
27 (p*)	3200	2900	**-9**	-	-	**-**	2400	2000	**-17**
35	1850	1600	**-14**	1700	1060	**-38**	1675	1110	**-34**
35 (p*)	1600	1800	**+13**	1600	1100	**-31**	1450	1100	**-24**
2	820	820	**0**	360	380	**+6**	-	-	**-**
3	1050	1120	**+7**	-	-	**-14**	750	870	**+16**

*performed with optimal phasing of actuators

Table 7.2:15 compares the voltage obtained experimentally at cracking with the voltages predicted by the numerical model. The first voltage range, for stress S11 between 0.8 MPa and 1.6 MPa, represents the voltage predicted to obtain a stress where the model predicted cracking. The second voltage range, for stress S11 between 0.47 MPa to 2.26 MPa, was the voltage range when the 41% numerical error was taken into account. It also presents the stress at cracking calculated by the model for the voltage obtained experimentally and the value adjusted with the numerical model error. When taking into account the maximum numerical model error obtained previously of 41%, all results obtained experimentally falls within the voltage range predicted by the numerical model.

The stress calculated at cracking, when adjusted for the numerical error of each mode, ranged from 0.71 MPa to 1.64 MPa with an average of 1.11 MPa. The average stress was similar to the values obtained with the previous mode tested of 1.04 MPa, with only a 6% difference. The stress range where cracking occurs, once adjusted with the numerical error, was defined between 0.80 and 1.60 MPa. The range of 0.71 MPa to 1.64 MPa obtained with the four tests was slightly outside this range. This meant that, even if the numerical model accurately predicted the voltage range within which cracking occurred, the range of stress S11 had to be slightly widened to 0.70 MPa to 1.65 MPa.

Table 7.2:15 – Stress S11 and voltage prediction by the numerical model compared to experimental results for cracking modes

Mode (opt. phas.)	**Damping (%)**	**Vpp (V)**	**Voltage Vpp predicted for S11 (V)**				**Stress S11 at cracking (MPa)**	
			=0.80 MPa	**=1.60 MPa**	**=0.47 MPa.**	**=2.26 MPa.**	**Num.**	**Adj.**
27	1.1	335	190	380	112	535	1.40	1.64
27 (p*)	1.0	170	120	240	70	340	1.15	1.32
35	1.0	265	442	884	265	1245	0.47	0.76
35 (p*)	1.4	200	310	620	183	875	0.52	0.71

*performed with optimal phasing of actuators

Table 7.2:16 and Table 7.2:17 presents the equivalent of Table 7.2:15 but for delamination tests. The first table is for stress S23 and the second for S33. As for the cracking tests, voltage at delamination fell within the voltage range predicted by both stresses, when the maximal numerical error was calculated. The stress obtained at delamination when adjusted was 0.66 and 0.65 MPa for S23 and 0.97 and 1.03 MPa for S33. For S23, stress for mode 2 was very slightly out of the range of 0.33 to 0.65 MPa predicted previously for delamination of the ice, while for mode 3 the value was on the upper limit of the range. For S33, the values were both higher than the range predicted of up to 15% for mode 3.

Table 7.2:16 – Stress S23 and voltage prediction by the numerical model compared to experimental results for delamination modes

Mode (#)	**Damping** (%)	**Vpp** (V)	**Voltage Vpp predicted for S23** (V)				**Stress S23 at delamination** (MPa)	
			=0.33 MPa	**=0.65 MPa**	**=0.20 MPa.**	**=0.92 MPa.**	**Num.**	**Adj.**
2	0.7	216	105	207	62	292	0.68	0.66
3	0.8	250	115	226	68	320	0.72	0.65

Table 7.2:17 – Stress S33 and voltage prediction by the numerical model compared to experimental results for delamination modes

Mode (#)	**Damping** (%)	**Vpp** (V)	**Voltage Vpp predicted for S33** (V)				**Stress S33 at delamination** (MPa)	
			=0.50 MPa	**=0.90 MPa**	**=0.30 MPa.**	**=1.27 MPa.**	**Num.**	**Adj.**
2	0.7	216	108	195	64	275	1.00	0.97
3	0.8	250	108	194	64	274	1.15	1.03

All results obtained experimentally fell within the voltage range predicted by the numerical model. The stress calculated at cracking, when adjusted for the numerical error of each mode, ranged from 0.71 MPa to 1.64 MPa with an average of 1.11 MPa. The average stress was similar to the values obtained with the previous modes tested of 1.04 MPa, with only a 6% difference. The stress range where cracking occurs, once adjusted with the numerical error, was defined between 0.80 and 1.60 MPa. The range of 0.71 MPa to 1.64 MPa obtained with the four tests was slightly outside this range. This meant that, even if the numerical model accurately predicted the voltage range within which cracking occurred, the range of stress S11 had to be slightly widened to 0.70 MPa to 1.65 MPa. The stress obtained at delamination when adjusted was 0.66 MPa and 0.65 MPa for S23 and 0.97 MPa and 1.03 MPa for S33. For S23, the stress for mode 2 was very slightly out of the range of 0.33 to 0.65 MPa predicted previously for delamination of the ice, while for mode 3 the value was on the upper limit of the range. For S33, the values were both higher than the range predicted of up to 15% for mode 3, but this was explained by the fact that it was unlikely that this stress was the limiting stress.

The numerical model has been able to predict the voltage range within which cracking and delamination occurs, but some of the adjusted stress results obtained during those tests fell outside the range criteria established. For cracking tests, the range of 0.80 MPa to 1.60 MPa needed to be slightly modified to 0.70 to 1.65 MPa. For shearing stress S23, one mode was within the range and the other one was 0.01 MPa above. The range was modified accordingly to 0.33 to 0.66 MPa. Even with those small increases in range for those stresses, the resulting ranges were still well inside the limit found in the literature and still confirmed the viability of the method and the ability of the numerical model to be used to predict ice breaking and to assist in the design of a piezoelectric system. For S33, the change in range was a little bit more significant, from 0.50 to 1.03 MPa, but it was unlikely that it was a limiting stress.

7.3 SUMMARY

In this chapter, conclusions obtained in the previous chapter are validated with de-icing tests in a cold room. An ice layer is accumulated on the plate and different breaking of the ice layers accumulated are generated with frequency sweeps. A camera installed above the setup has allowed to obtain the frequencies at which those breaking occurred. With this information and the help of an accelerometer, the resonant modes around those frequencies are found an breaking of the ice layer is then obtained at fixed frequencies in steady-state mode for the first time at the laboratory confirming the results obtained at the previous chapter.

An ice layer is then added to the numerical model replicating the ice accumulation obtained in the cold room. The improved model is then validated with experimental tests by comparison acceleration obtained numerically and experimentally by adding more accelerometers on the flat plate. The numerical model correctly predicted the modal shape and resonant frequencies with an accuracy of 87% or more with the frequency analysis. The model also predicted vibration amplitudes with a maximum discrepancy of 41% and an average of 20%. The discrepancy was mainly attributed to the boundary conditions, imperfection of the ice layer and ice material properties. The model was deemed more than satisfactory considering the 26% experimental variability obtained during testing.

The validated model was then used to study the different stresses involved in the ice breakings. Two types of ice breaking were obtained, cracking and delamination. For cases of cracking of the ice layer, stress S11 was found responsible, while for delamination S23 was judged the cause of the break. In both cases, the stress calculated by the model matched the values found in the literature, confirming the validity of the results. As a proof-of-concept, the numerical model was then used to find frequencies susceptible of generating the two types of breaking. In each case, the numerical model successfully predicted the voltage range within which breaking occurred experimentally, demonstrating the validity of the method.

CHAPTER 8

INTEGRATION OF THE PIEZOELECTRIC ACTUATOR DE-ICING SYSTEM TO THE BLADE STRUCTURE

Following the comprehensive investigation of the different phenomena involved in the piezoelectric vibration based de-icing system applied to a flat plate, the conclusions obtained were used to perform a preliminary analysis for a small blade setup, both fixed and in rotation. In order to do that, new experimental setups were designed and fabricated. With the limited time left in the project, as well as the pandemic situation, only a partial preliminary study and validation could be performed. Also, the complexity of the rotating setup only allowed very limited measurement on the blade, which also greatly limited vibration characterization of the blade structure. However, multiple experiments were successfully performed, complete de-icing was obtained and preliminary study of the application of a piezoelectric de-icing system to a rotating blade structure was performed.

8.1 EXPERIMENTAL SETUP

8.1.1 ICING WIND TUNNEL

AMIL's Icing Wind Tunnel (IWT), shown in Figure 8.1:1, is a closed-loop low speed refrigerated wind tunnel able to operate at subzero temperatures at sea level pressure. The refrigeration system capacity is able to vary the total air temperature between -40°C and 22°C by circulating the air through a heat exchanger of 1.6 m by 1.6 m (Figure 8.1:2), which is powered by a compressor and a glycol pump (Figure 8.1:2).

Figure 8.1:1 – Icing Wind Tunnel

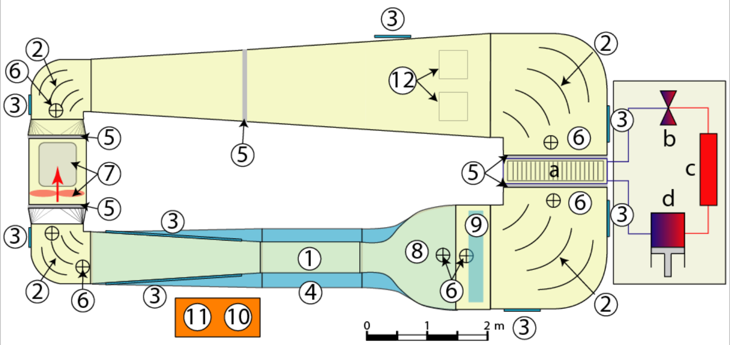

1	Test section	9	Spray nozzles
2	Corner vanes	10	Motor control panel
3	Access doors	11	Control console
4	Access panels	12	Traps
5	Thermal expansion joints	a	Evaporator
6	Drains	b	Expansion valve
7	Fan and Motor	c	Condenser
8	Contraction cone 9.4:1	d	Compressor

Figure 8.1:2 – Icing Wind Tunnel Schematic

The IWT has two test sections. The smaller test section is 0.5 m wide by 0.6 m high and the tests can be run at air speeds up to 110 m/s at room temperature. The larger test section is 0.91 m wide by 0.76 m high and tests can be run at air speeds up to 50 m/s at room temperature. The larger IWT test section, used for these tests, meets the conditions [81] of the SAE Aerospace Recommended Practice for icing wind tunnel ARP5905 [82] and Aerospace Information Report for droplet sizing AIR4906 [83].

The IWT test section air speed is controlled by computer via a control program and data acquisition card. The computer sends out a frequency of rotation to the drive generating the desired air speed in the test section . At the same time, the pressure differential is measured between the convergent entry (8) and the test section (1) (see Figure 8.1:2), the information is returned to the control program via the acquisition data card. The test section air speed is calculated with the Bernoulli equation. The speed in the test section is given by Equation 44.

$$U_{TestSection} = \sqrt{2\left(1-\frac{A^2_{TestSection}}{A^2_{RampSection}}\right)^{-1}\frac{p_{RampSection}-p_{TestSection}}{\rho_{air}}} \tag{44}$$

The IWT air temperature is controlled by a computer controller. The controller sends out an opening or a closing signal to the solenoid valve which controls the refrigerated liquid flow in the heat exchanger. At the same time, the air temperature is measured in the test section (1), and the information is returned to the controller. The error between the desired and measured air temperatures is calculated and the controller corrects the output signal accordingly. The IWT static pressure is measured in the test section as well as the room barometric pressure.

A water spray system, composed of a spray ramp of nine nozzles (Figure 8.1:3) with nine rotameters controlling the flow rate, pressure regulators and pressure gages control the air pressure. A cooling unit controls the water temperature used to produce a cloud of supercooled water droplets with median volumetric diameters (MVD) ranging from 20 to 60 µm and liquid water contents (LWC) ranging from 0.1 to 3.0 g/m³.

The water is filtered and cleaned to obtain osmotic de-mineralized distilled water. The spray system is located upstream of the center of the test section in the straight section (9) before the convergent (8), and oscillates up and down to cover, when necessary, the entire test section height (1), Figure 8.1:3.

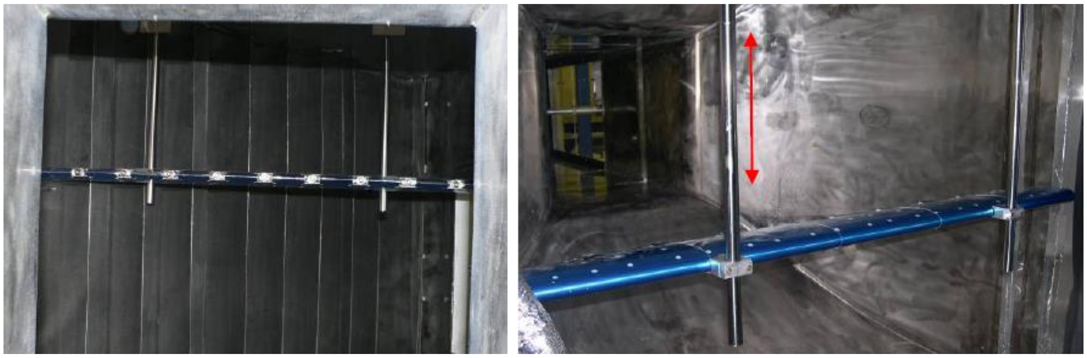

Figure 8.1:3 – Sprinkler Ramp

The super-cooled droplets simulating a freezing fog or cloud impinge on the scale model in the center of the test section. During a test, the water flows continually, the air pressure is open when the test begins and the simulated cloud is formed in the IWT test section.

To generate the cloud, air atomizing nozzles composed of pneumatic sprinklers are used. The water line is under pressure and a rotameter controls the flow rate to meet the desired liquid water content, the water droplet diameter is controlled by the air pressure injected into the nozzle.

8.1.2 STATIC SMALL BLADE SETUP

A blade experimental setup was designed to test the conclusions obtained with the flat plate on a curved airfoil blade structure. The setup was based on a Bell 206 tail rotor blade with a NACA 0012 airfoil shape and a 13.1 cm (5.25 inches) chord. The span was limited to 22.9 cm (9 inches) to prevent excessive imbalances in rotation as well as to fit in the wind tunnel test section used for testing. An aluminum foil of 0.8 mm thick, same thickness as for the tail rotor blade hollow leading edge, was curved to recreate the first 4.5 cm (1.8 inch) of a NACA0012 airfoil shape (Figure 8.1:4). Six piezoelectric actuator patches PI876.A15, same actuators used on the flat plate setup, were installed on the curved aluminum foil. The patches were installed along their length direction due to size limitation in the profile (Figure 8.1:4). This configuration was chosen to allow installation of the patches while limiting the hollow part in the profile (Figure 8.1:4). For a real Bell 206 tail rotor, the hollow part behind the leading edge is around 1 cm which is the reason the test setup hollow dimension is kept as close to this value as possible. Three patches were installed on each the upper and lower surface. The patches were installed as close as possible to the leading edge in the chord direction, limited by the curvature of the profile, which gave a distance of 1.3 cm (0.50 inch) from the leading edge. Spanwise, an actuator was installed centered with the profile on both the top and bottom surface. On each side of those actuators, the other actuators were centered in the remaining available space, at 1.14 cm (0.45 inch) from the edges of the profile (Figure 8.1:5). The actuators were bonded using the same method as for the flat plate setup. Only one accelerometer could be installed in the profile due to the limitation of the slip ring. The accelerometer, same model as used for the flat plate setup, was installed on the actuator at the center of the top surface of the blade as shown in Figure 8.1:5. This limitation greatly diminished the capability for the numerical validation.

Figure 8.1:4 – Leading edge part of the blade setup with piezoelectric actuator patches installed

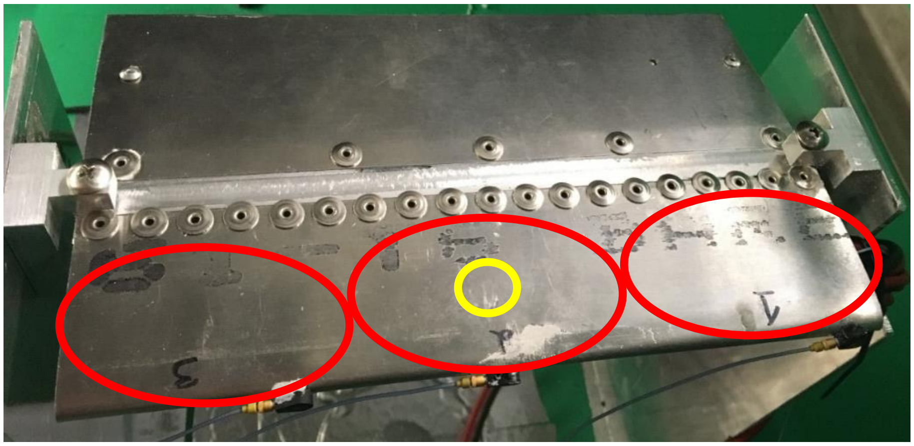

Figure 8.1:5 – Blade profile with actuator positions circled in red and accelerometer position in yellow

Two other aluminum foils, of same thickness, were used to build the back of the profile. They were shaped to correspond to the back of the NACA 0012 profile shape. The leading edge and back of the profile were assembled using an H spar (Figure 8.1:6). Rivets were used to fix the parts on the H spar. The maximum number of rivets was used for the leading edge part to recreate as closely as possible a fully clamped boundary condition (Figure 8.1:7). However this configuration was not as representative of a fully clamped boundary condition as the configuration used for the flat plate, which was not possible to recreate in rotation. Only the leading edge part was subjected to vibration. The blade structure was held in place in the wind tunnel with two fixations plate on each side of the profile as shown in Figure 8.1:7. To operate the piezoelectric actuators, the same electrical system used for the flat plate setup was employed. With this configuration, for dephasing of an actuator, the positive wire was plugged in the negative output. However, this meant that when an actuator was dephased a maximum voltage of 500 Vpp could be applied to the actuators due to their voltage limit of -250 V to 1000 V.

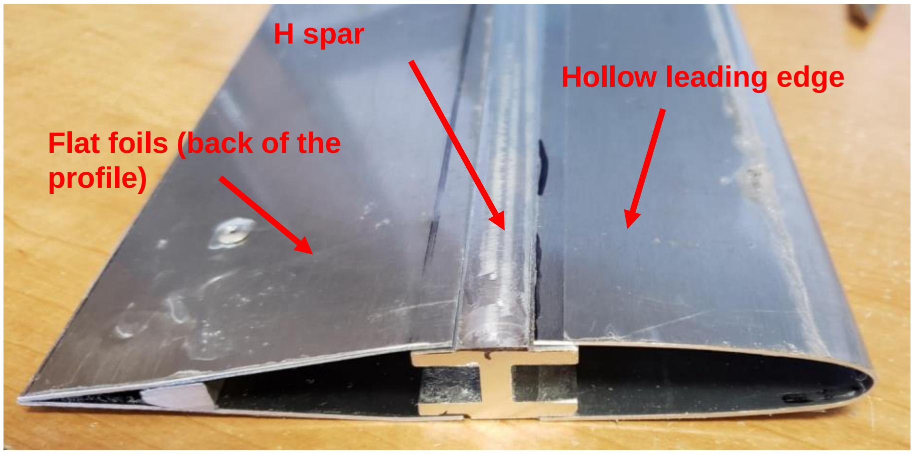

Figure 8.1:6 – Assembled profile with leading edge, H spar and back of the profile

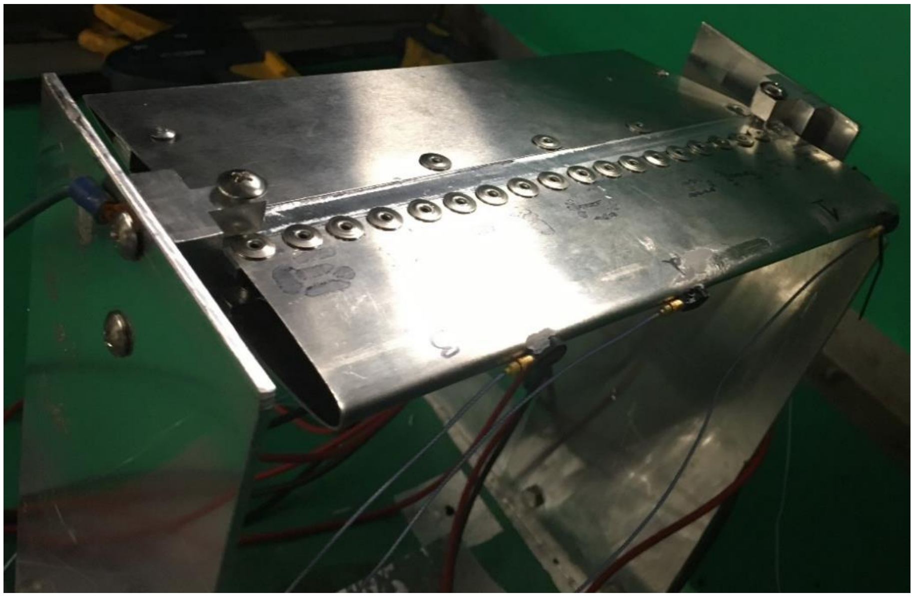

Figure 8.1:7 – Blade profile with rivets and fixation for static tests in wind tunnel

8.1.3 ROTATING SMALL BLADE SETUP

In order to rotate the blade setup, an existing laboratory setup e.g. the Spinning Rotor Blade (SRB) system, was modified. In more details, the SRB setup is a horizontal spinning model and is composed of a motor, a power shaft transmission, a hub and two blades. The hub is connected to a 3 600 RPM 10 hp motor by a 1 inch diameter power steel shaft connected to a 10 hp drive. To safely operate the SRB in the icing wind tunnel (IWT), the test section windows are made of polycarbonate thermoplastic resin (Lexan) which has a high impact resistance. The motor generator is computer-controlled and set at a constant rotor speed feedback system that maintains a constant RPM throughout an icing encounter. The spinning rotor blade angular speed is measured by an optical encoder. The hub is a homemade conception with a diameter of 200 mm, as shown at Figure 8.1:8. The hub allows for two angle of attack for testing, 0° and 6° (Figure 8.1:9).

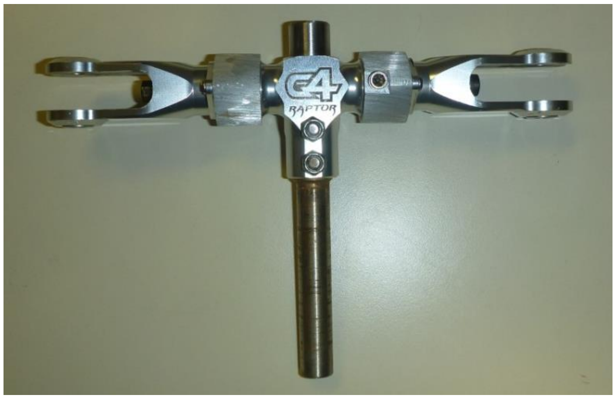

Figure 8.1:8 – Spinning Rotor Blade Hub for 0°

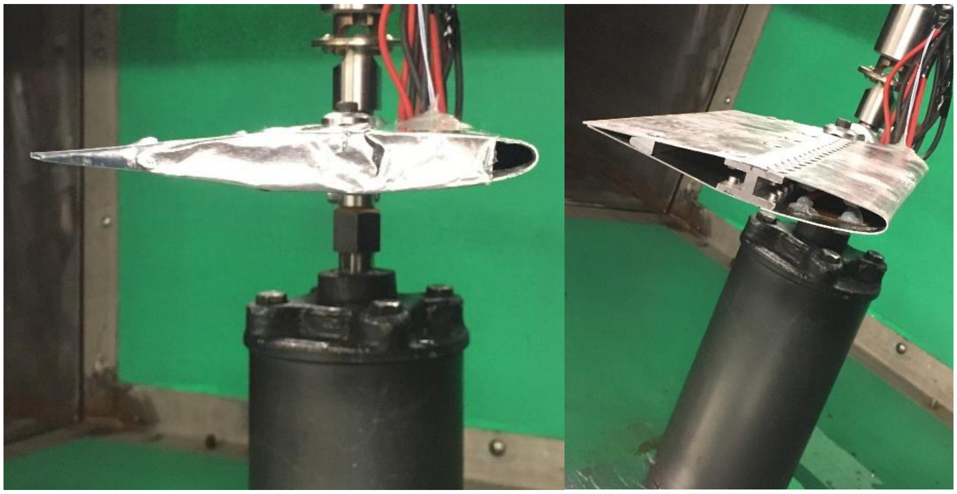

a) b)

Figure 8.1:9 – Blade profile at a) 0° AOA and b) 6° AOA

This setup was modified to accommodate the blade prototype. An IEC corporation FMA-2-UHF-2FT-SH slip ring was added to the setup to bring the power to the rotating blade to excite the actuators. The slip ring voltage range was -500 to 500 V which limited the voltage of operation for the actuators. The slip ring had 10 channels which allowed the connection of the six actuators and one accelerometer, while style allowing to test the different actuator phasing required. A test dummy of cylindrical shape was built and installed on the second attach of the hub. The test dummy was fabricated with the same weight as the blade profile in order to minimize unbalance during rotation. The rotation speed was limited to 600 RPM to ensure safe operation of the system and limit excessive vibration during rotation. The final setup is shown at Figure 8.1:10.

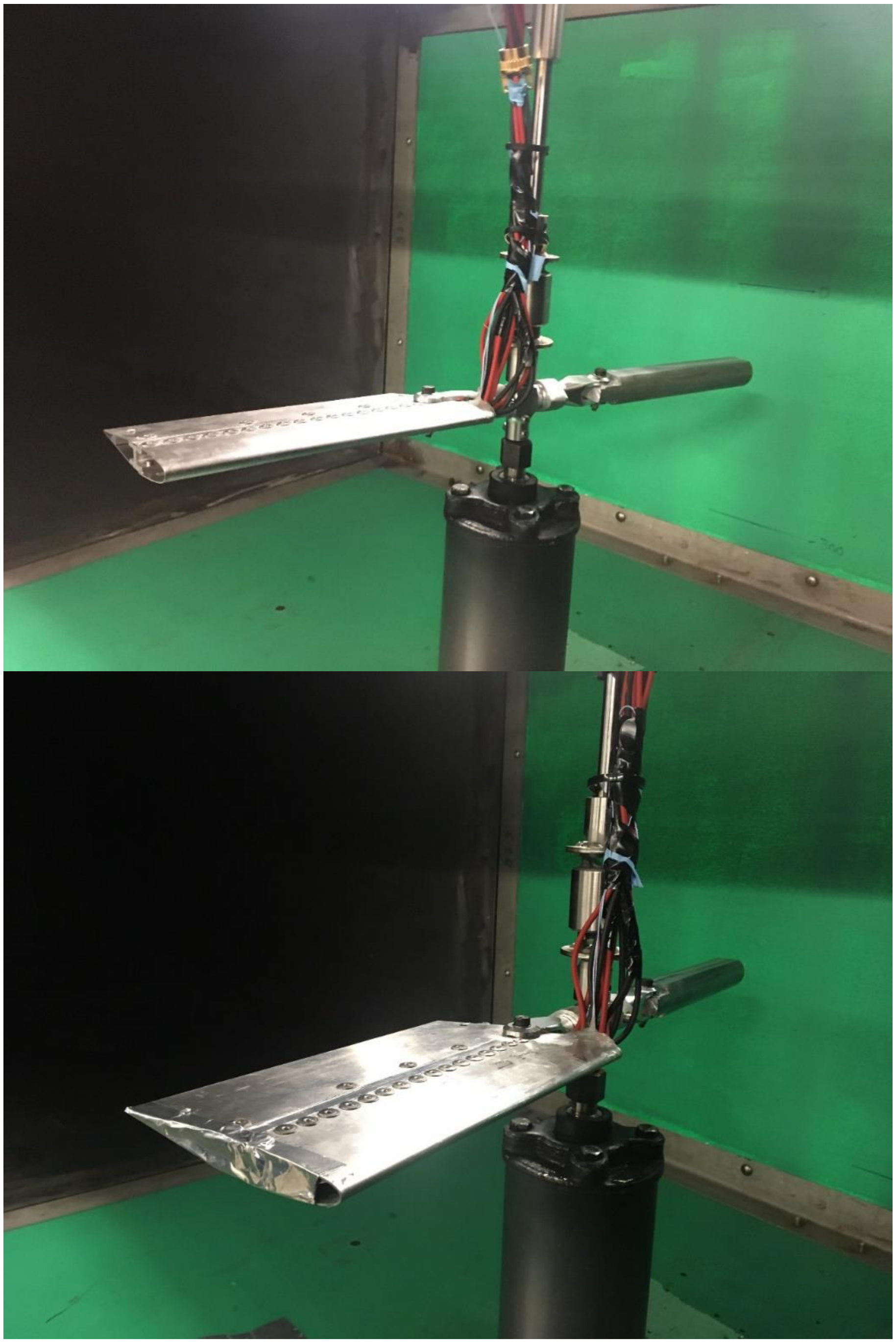

Figure 8.1:10 – Rotating blade setup in wind tunnel

8.1.4 TEST CONDITIONS

The test conditions for the static and rotating wind tunnel tests are presented at Table 8.1:1. Those conditions were selected to simulate in-flight icing conditions within the limitations of the tunnel while staying close to the cold room test conditions. The air temperature was the same than for the cold room tests. Those conditions were selected in order to obtain a glaze type of ice, similar to the one obtained on the flat plate. This resulted in a transparent ice of higher density, usually close to 900 kg/m³.

Table 8.1:1 – Experimental conditions for static and rotating wind tunnel tests

Test	**Wind Speed (m/s)**	**Air temperature (°C)**	**LWC (g/m³)**	**MVD (μm)**	**Rotation Speed (RPM)**
Static	20	-7	0.8	26	0
Rotating	20	-7	0.8	26	600

8.2 NUMERICAL MODEL

8.2.1 SMALL BLADE SETUP DESIGN

The numerical model was designed to replicate as accurately as possible to the experimental setup. An extruded shell part was created using NACA 0012 coordinates to create the profile with a chord of 13.3 cm (5.25 in). The NACA profile was cut to 4.5 cm which corresponded to the part free to vibrate of the experimental setup (Figure 8.2:1-a). The resulting profile was extruded to a span of 22.9 cm (9 in) (Figure 8.2:1-b). The thickness of the shell was set to 0.8 mm. Aluminum 2024-T4 material was defined with a mass density of 2780 kg/m³, a Young's modulus of 73 GPa and a Poisson's ratio of 0.33.

The six actuator patches were modeled similarly to the flat plate setup case (section 3), but curved to fit the profile as per the experimental setup (Figure 8.2:2). The patches were positioned on the blade part to correspond to their actual position in the physical setup.

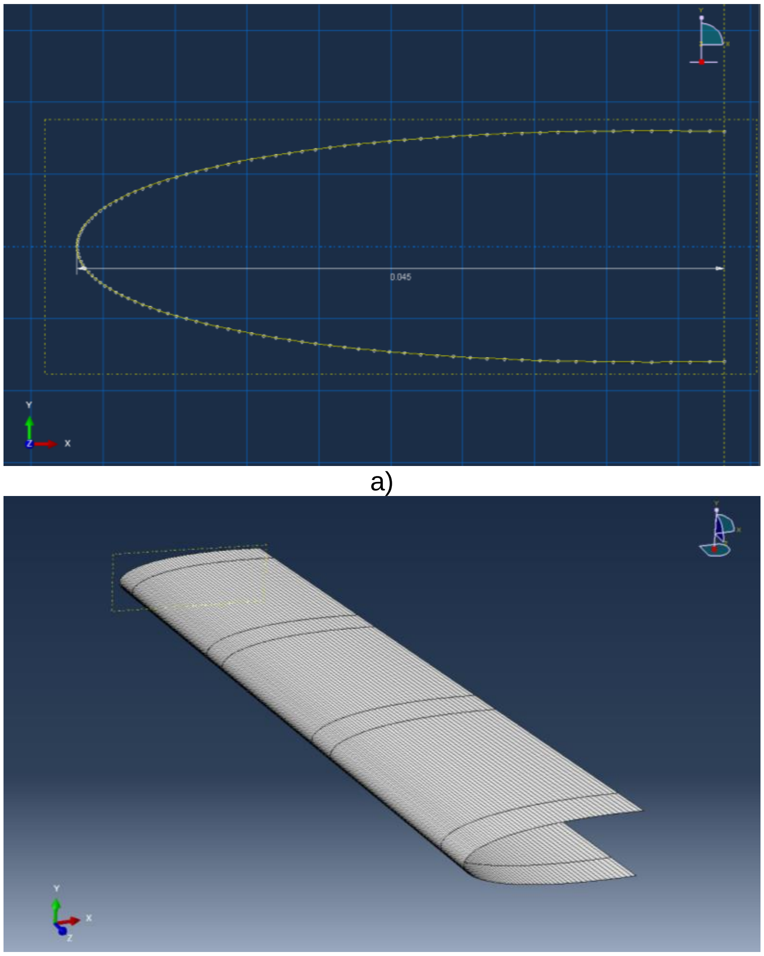

a)

b)

Figure 8.2:1 – Model of the NACA profile used in the simulation: a) Sketch of the numerical aerodynamic profile and b) extruded part

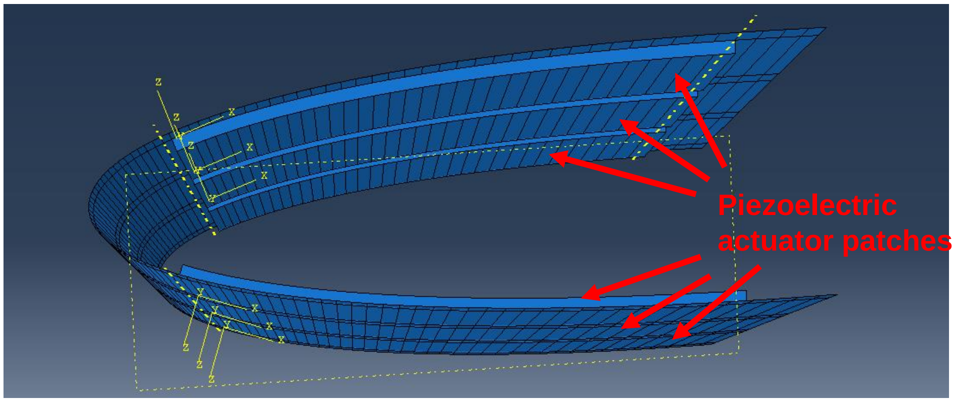

Figure 8.2:2 – Piezoelectric actuator patches tied to curved blade shell

The ice layer was created as a 3D homogenous deformable extruded part in the numerical model. The thickness was set to 6.35 mm (1/4th of an inch) as it is the maximum allowed thickness on the rotorcraft blade has agreed with the industrial partner. Ice material properties were kept the same as for the flat plate model due to the similarity in accumulation conditions. The shape of the ice was based on the NACA 0012 airfoil profile as the ice tends to preserve the shape of the leading edge at this accumulation regime (Figure 8.2:3-a). The ice and the piezoelectric actuator patches were tied to the blade shell structure with Tie constraints. A fully constrained clamped boundary condition was applied to the back of the profile along the span direction. Frequency and Direct Steady-state dynamic analysis were run similarly to those of the flat plate with electric potential boundary conditions applied to the actuators for the dynamic analysis.

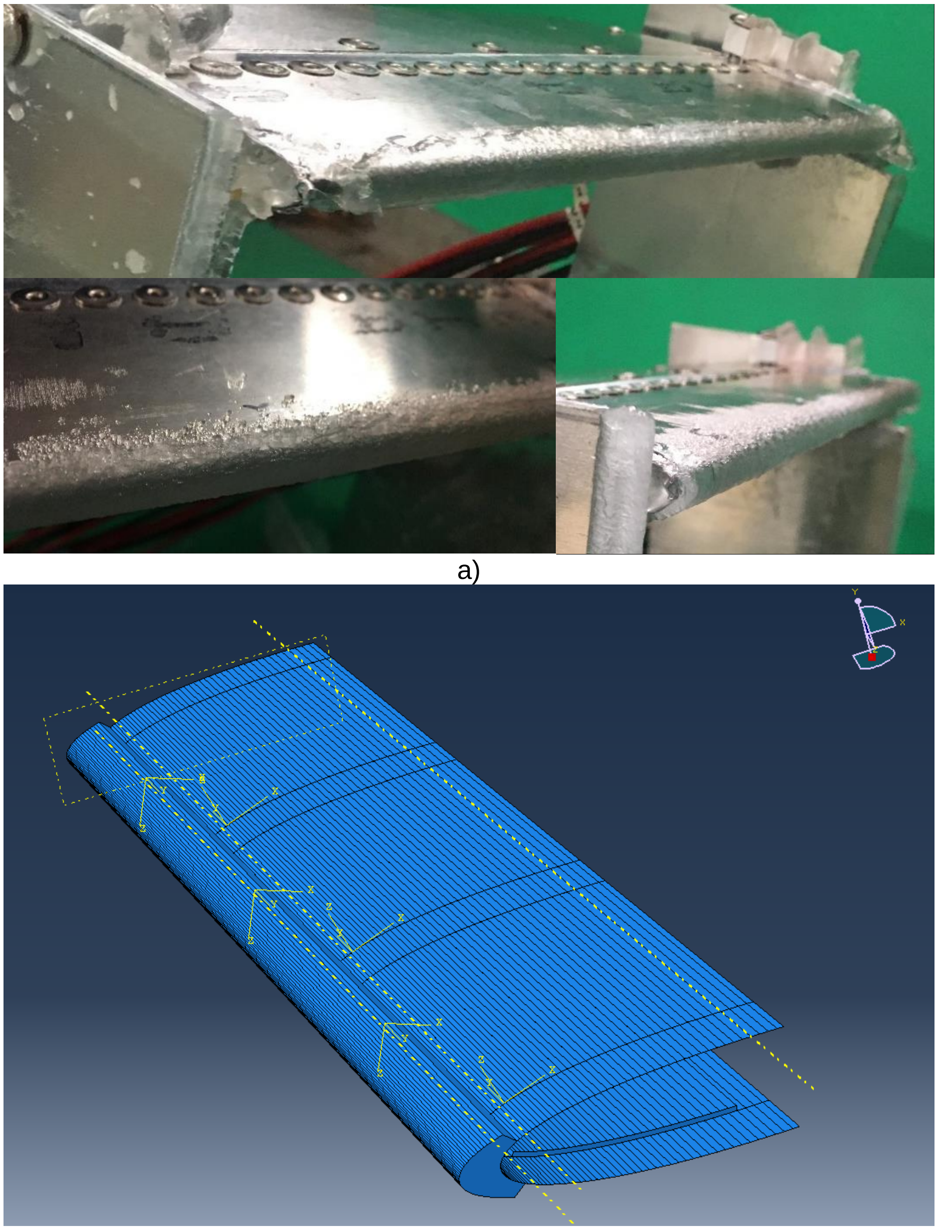

a)

b)

Figure 8.2:3 – a) Experimental ice accumulation and b) numerical model with ice layer

Ice accumulation can be altered due to the rotation of the profile, which is something to consider for the numerical model of the rotating blade. With the increase in tangential velocity along the radius, usually more ice will accumulate at the tip of the blade than at the root. However, experimentation showed that for the low rotation speed and small radius of the rotating blade setup, the rotation had a negligible effect on the ice accumulation and ice shape was similar to the one obtained during fixed tests (Figure 8.2:4). For this reason, the ice part was not modified for numerical analysis of the rotating setup. To add the effect of rotation, a pressure force load was applied to the tip of the ice layer, in an additional general static step, determining the base state for the frequency and direct steady-state dynamic step. The force was calculated from the ice mass of 11 g, rotation speed of 600 RPM and average radius of 16 cm for a total force of 7 N.

Figure 8.2:4 – Ice accumulated at 600 RPM rotation speed

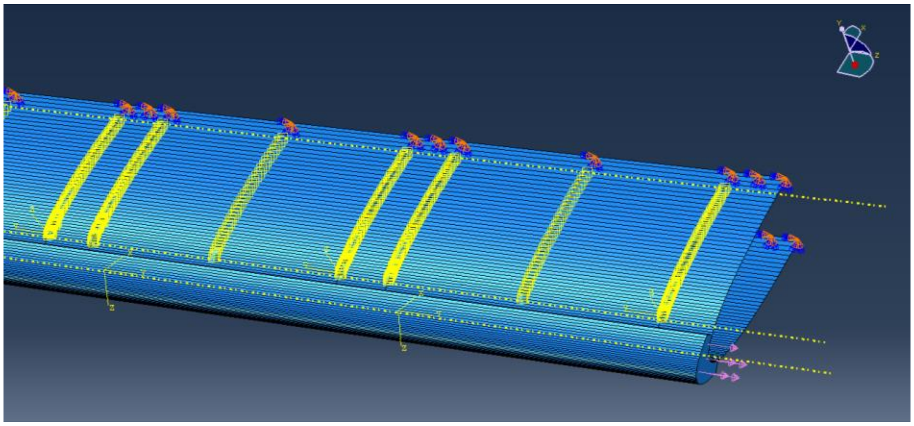

Figure 8.2:5 – Force load applied to the ice layer to simulate centrifugal force

8.2.2 MESH AND CONVERGENCE STUDY

The same element types were used for the blade numerical model than for the flat plate numerical model. Linear S4R shell elements were used to mesh the plate, C3D8E 8-node linear piezoelectric brick elements for the piezoelectric actuators and C3D8R 8-node linear brick elements for the ice layer. A convergence study was performed to validate the proper element number and size for the model. Three configurations for the number of elements were tested with the same voltage applied, 400 Vpp to all piezoelectric actuators, and same damping of 0.1%. Those configurations are presented at Table 8.2:1. Frequency modal analysis and direct steady-state dynamic analysis were performed with the different number of elements for the first six modes. The results of each analysis are presented at Table 8.2:2 and Table 8.2:3. The calculation of the resonant frequencies varied by less than 0.3% for configuration 1 and 2 when compared to configuration 3. For the maximum acceleration prediction, configuration 1 varied by 18% for the first two modes and by 4% or less for the other modes investigated with configuration 3. For configuration 2, the variation was 12% and 10% for the first two modes and 2% for the other modes investigated with configuration 3. Meshing configuration of scenario 2 was selected to obtain significant saving on computation times as well as a good precision of the results.

Table 8.2:1 –Number of elements for convergence study

Configuration (#)	Number of elements for profile	Number of elements for ice layer
1	4332	13200
2	8664	26400
3	26448	79200

Table 8.2:2 – Resonant frequency prediction for different mesh configurations

Mode (#)	Frequency for configuration 1 (Hz)	Frequency for configuration 2 (Hz)	Frequency for configuration 3 (Hz)	Discrepancy of Configuration 1 with Configuration 3 (%)	Discrepancy of Configuration 2 with Configuration 3 (%)
1	559.3	559.2	559.3	<0.1	<0.1
2	1134.8	1135.5	1136.0	<0.1	<0.1
3	1827.5	1828.1	1828.3	<0.1	<0.1
4	1864.1	1864.8	1865.3	<0.1	<0.1
5	2036.9	2038.0	2042.0	0.3	0.2
6	2148.8	2149.4	2152.9	0.2	0.2

Table 8.2:3 – Maximum acceleration prediction for different mesh configurations

Mode (#)	Max. Acceleration for configuration 1 (m/s²)	Max. Acceleration for configuration 2 (m/s²)	Max. Acceleration for configuration 3 (m/s²)	Discrepancy of Configuration 1 with Configuration 3 (%)	Discrepancy of Configuration 2 with Configuration 3 (%)
1	20	19	17	18	12
2	80	75	68	18	10
3	397	411	408	4	<1
4	403	407	400	1	2
5	1106	1115	1143	4	2
6	1028	1015	996	3	2

8.2.3 FREQUENCY ANALYSIS

The frequency analysis was performed from 0 to 5 kHz. The modal shapes of the first six predicted modes are presented in Figure 8.2:6. For higher resonant modes, the anti-nodes were smaller than the actuator patches (Figure 8.2:7). As seen in section 5.3.3, the flat plate was not optimally excited and resulting vibration was weak for such modes. Moreover, in those cases, the numerical model was less accurate for reasons detailed under that section. Finally, as detailed in section 8.2.6.3, the power consumption increases with an increase in frequency of excitation. For these reasons, only the first six resonant modes were studied for breaking of the ice layer.

Preliminary icing tests were performed with an ice layer accumulation to locate the different resonant modes and their corresponding frequencies. Table 8.2:4 compares the experimental and numerical frequencies for the profile with an ice layer accumulation. With only an accelerometer on one of the actuator located in the center, it was not possible to locate modes 2 and 4. Also, it was not possible to locate mode 3 for reasons detailed in the next section.

Table 8.2:4 – Experimental and numerical frequencies of blade resonant modes with the ice layer

Mode (#)	**Numerical Frequency (Hz)**	**Experimental Frequency (Hz)**
1	559	800
2	1136	N/A
3	1828	N/A
4	1865	N/A
5	2038	2019
6	2149	1918

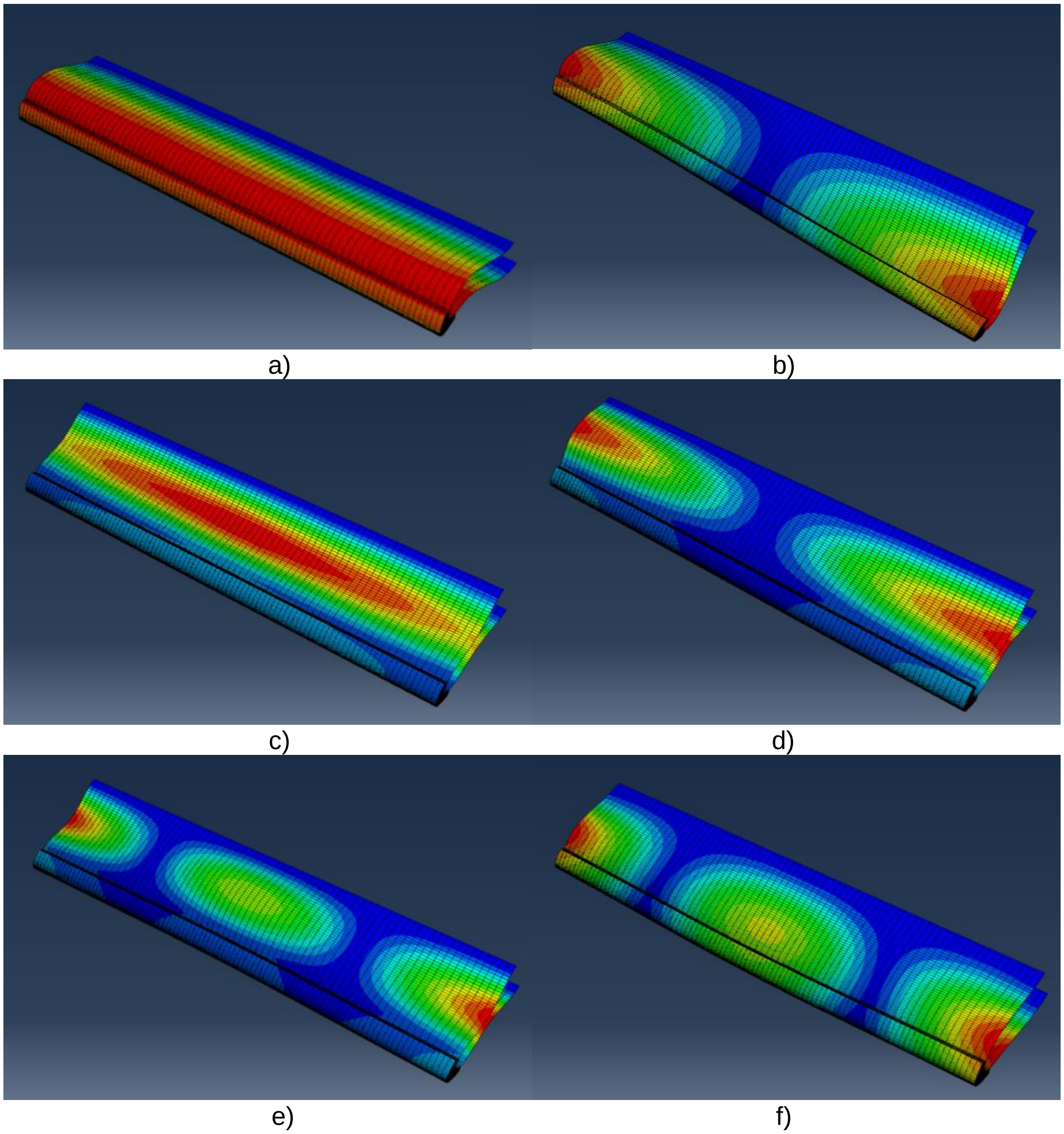
a) b) c) d) e) f)

Figure 8.2:6 – First sixth resonant mode for the blade structure: a) mode 1 at 559 Hz b) mode 2 at 1136 Hz c) mode 3 at 1828 Hz d) mode 4 at 1865 Hz e) mode 5 at 2038 Hz f) mode 6 at 2149 Hz

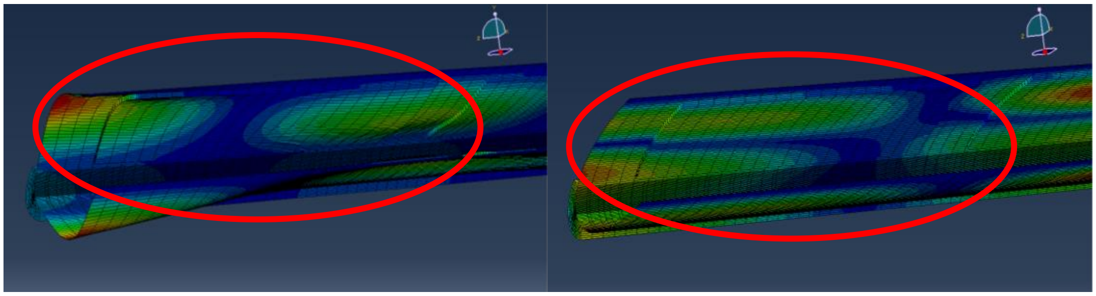
a) b)

Figure 8.2:7 – Resonant mode: a) mode 7 at 2487 Hz and b) mode 12 at 3340 Hz

8.2.4 STATIC DIRECT STEADY-STATE DYNAMIC ANALYSIS

Direct steady-state dynamic analysis was performed for the frequencies selected in the previous section on the iced blade structure. Experimental icing tests were also performed with the blade with an ice layer accumulation for each of those mode where ice breaking was predicted numerically to perform a partial validation of the numerical model.

For the first mode (Figure 8.2:6-a), the optimal excitation was defined by the three upper actuators, 1, 2 and 3, out of phase with the three lower actuators, 4, 5 and 6. Damping obtained for this mode with ice accumulation in the wind tunnel is 12%, which is considered very high damping. To obtain stresses susceptible of generating ice breaking as per section 7.2.2.3, the model predicted minimum possible voltages higher than 800 Vpp, which was not achievable with the actuators without compromising their integrity. As predicted by the model, no ice breaking was obtained for this mode with voltages up to 500 Vpp, which was the maximum operation voltage with this phasing (see 8.1.2).

For the second mode (Figure 8.2:6-b), optimal actuator activation was defined by the actuators 1 and 6 out of phase with actuators 3 and 4. Actuators 2 and 5 were not excited for this mode due to the absence of anti-nodes in the center of the profile. Damping was not obtained for this mode with only an accelerometer at the center of the blade in the span direction. The numerical model predicted minimum voltage for ice breaking of 700 Vpp for a damping similar to mode 1. Frequency sweeps at low sweep rate around the frequency of interest were conducted and, as predicted, no ice breaking occurred with voltages up to 500 Vpp.

For the third mode, optimal actuator excitation was defined by all actuators in phase (Figure 8.2:6-c). With this activation, the numerical model showed that the piezoelectric actuators did not excite properly the structure. The mode deployment only partially corresponded to the third resonant mode, mixed with the mode shape of the fifth resonant mode (Figure 8.2:8). This meant that this frequency of excitation tended to generate a vibration pattern as predicted for mode 3, while the piezoelectric actuator patches deformation favored deployment of mode 5. This was explained by the direction of the patches. The d_{31} effect, as explained at section 1.4 and shown at Figure 8.2:9, created the deformation of the actuators in both direction. With the greater deformation generated in the length direction, actuators at center created more of an anti-node corresponding to that of the middle anti-node of mode 5. If the actuators were positioned in the perpendicular direction, their deformation should favor bending mostly in the direction proper to mode 3 generation. However, due to size restriction, it was not possible to position them in that direction to excite this mode. This showed that experimentally, mode 5 would be excited and not mode 3. This is what was obtained experimentally, no distinct resonant mode was obtained around those frequencies and acceleration kept increasing until mode 5, as shown later in this section.

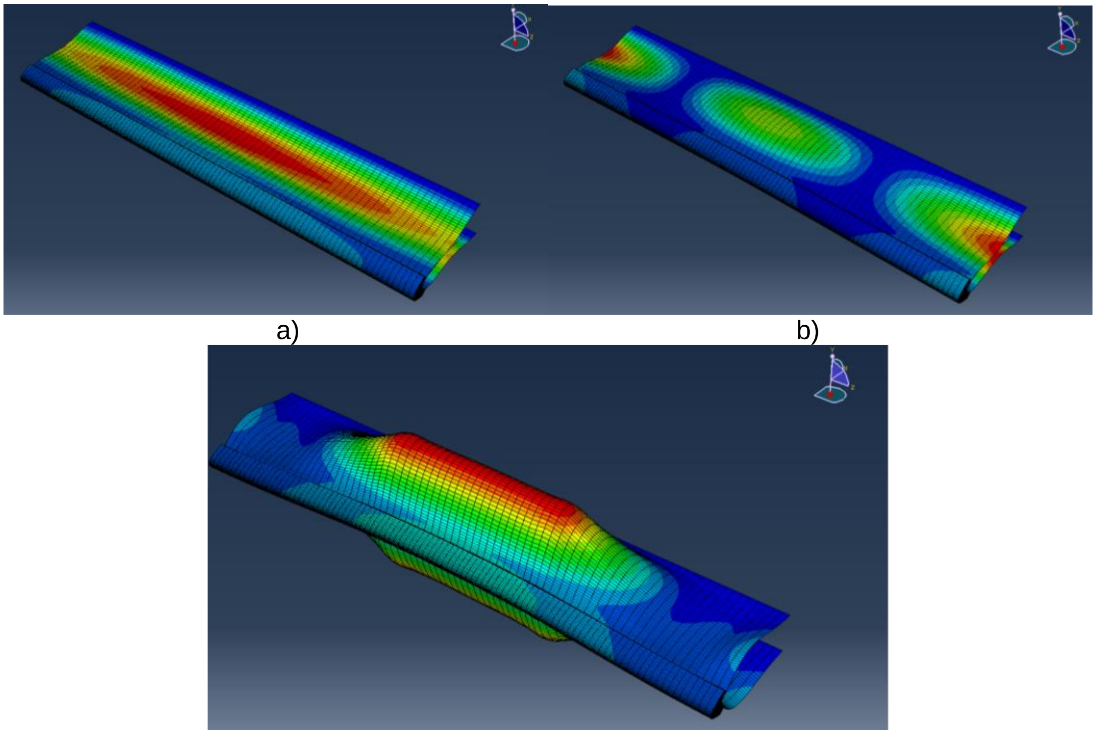
a) b)

c)

Figure 8.2:8 – Frequency analysis of a) mode 3 and b) mode 5 and c) direct steady-state dynamics analysis for mode 3

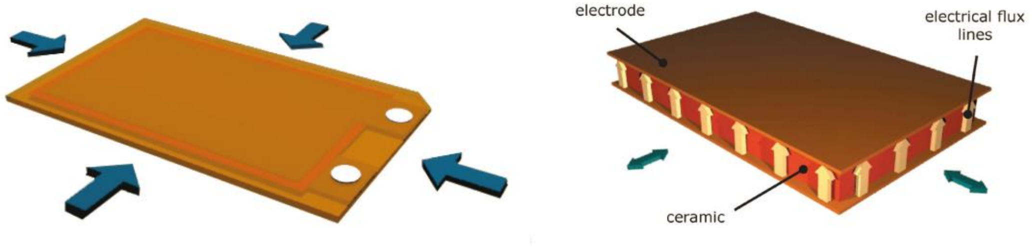

Figure 8.2:9 – Lateral contraction and d_{31} effect [72]

For mode 4, optimal excitation was obtained by actuators 1 and 4 out of phase with actuators 3 and 6 (Figure 8.2:6-d). Actuators 2 and 5 were not excited. As for mode 2, no damping could be measured for this mode with only an accelerometer in the middle of the blade. Ice delamination was predicted somewhere between 425 Vpp and 1950 Vpp by the numerical model with a damping similar to mode 1. Frequency sweeps up to 500 Vpp were performed around the predicted frequency and yielded no breaking of the ice layer.

For mode 5, optimal excitation was obtained by exciting actuators 1, 3, 4 and 6 out of phase with actuators 2 and 5 ((Figure 8.2:6-e). The resonant frequency was found experimentally at 2160 Hz and a damping of 14% was obtained with the ice accumulation in wind tunnel. Using this damping coefficient, the numerical model predicted a delamination between 250 Vpp and 1100 Vpp. During experimentation, delamination was obtained at the center of the profile (Figure 8.2:10) at 336 Vpp during a sweep from 2000 to 2200 Hz in 10 seconds. Delamination occurred at the very start of the sweep and was not captured by the accelerometers. A second test repetition was done and the resonant frequency was obtained at 1870 Hz with a damping coefficient of 15%, similar to the value measured in the first test. Delamination was obtained at 352 Vpp and numerical and experimental accelerations are presented in Figure 8.2:11.

Figure 8.2:10 – Delamination of the ice layer for mode 5 during first repetition

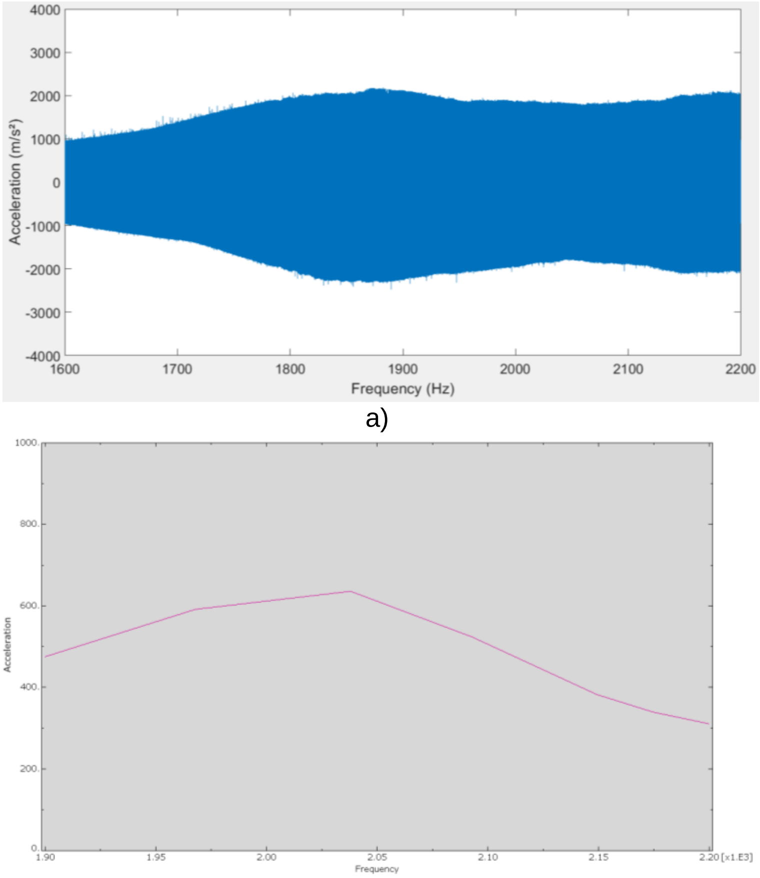

a)

b)

Figure 8.2:11 – a) Experimental and b) numerical acceleration for mode 5 with actuators 1, 3, 4 and 6 out of phase with actuators 2 and 5 second repetition

Investigation of mode 3 showed that with all the piezoelectric actuators excited in phase, mode 5 should be excited due to the geometry and bending properties of the actuator patches. Two additional icing tests were performed with this excitation. The resonant frequency was obtained at 1974 Hz and 2105 Hz with damping coefficients of 13% and 9% respectively. The numerical model predicted ice breaking between 200 Vpp and 900 Vpp. For the first test, ice breaking was obtained at 350 Vpp for a frequency sweep between 1800 and 1900 Hz in 10 seconds. Breaking was obtained at the very beginning of the sweep and was not captured by the accelerometer. For the second test, ice delamination was obtained at 352 Vpp during a frequency sweep from 1600 to 2200 Hz in 10 seconds (Figure 8.2:12). Experimental and numerical acceleration are presented at Figure 8.2:13.

Figure 8.2:12 – Delamination at 352 Vpp for mode 5 repetition 2 with all piezoelectric actuators excited in phase

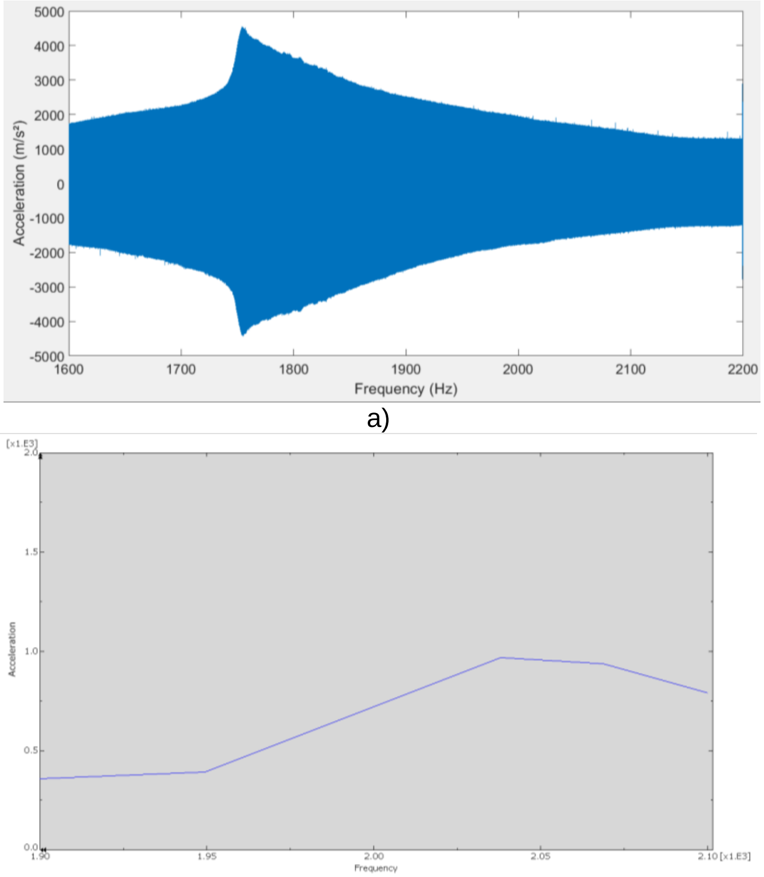

a)

b)

Figure 8.2:13 – a) Experimental and b) numerical acceleration for mode 5 with all piezoelectric actuators second repetition

For the sixth mode, the optimal excitation was obtained using actuators 1, 3 and 5 out of phase with actuators 2, 4 and 6 (Figure 8.2:6-f). The resonant frequency was obtained at 1974 Hz and the damping with the ice accumulation was 22%. For those conditions, the numerical model predicted delamination between 540 and 2500 Vpp. Delamination was obtained at 385 Vpp during a frequency sweep from 1600 to 2200 Hz in 10 seconds, below the numerical model prediction (Figure 8.2:14). A second and third tests were performed for repeatability. The resonant frequency was observed at 1880 Hz with a damping coefficient of 20% for the second test. Frequency sweeps from 1700 to 1900 Hz in 10 seconds rate were performed and delamination was obtained at 400 Vpp. For the third repetition, the measured resonant mode was obtained at 1900 Hz with a damping coefficient of 14% and delamination was obtained at 385 Vpp (Figure 8.2:15). As for mode 5, the geometry and bending of the actuators should excite mode 6 with actuators 1, 2 and 3 out of phase with actuators 4, 5 and 6. An additional experimental test was performed with this excitation configuration. A frequency of 1952 Hz was obtained with a damping coefficient of 14%. The numerical model predicted ice breaking between 450 and 2100 Vpp. Frequency sweeps from 1950 to 2050 Hz were performed and delamination was obtained at 450 Vpp. A summary of the results is presented at Table 8.2:5.

Figure 8.2:14 – Delamination during frequency sweep from 1600 to 2200 Hz in 10 seconds at 385 Vpp with piezoelectric actuators 1, 3 and 5 out of phase with 2, 4 and 6

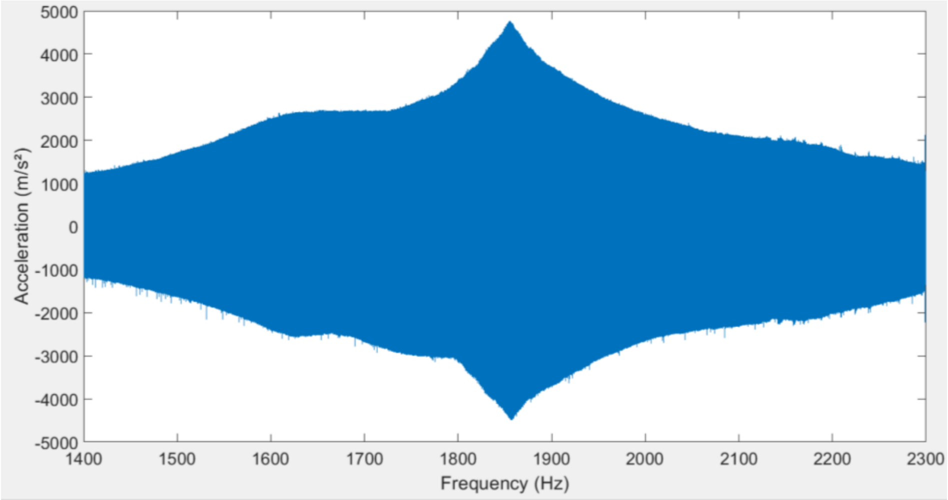

a)

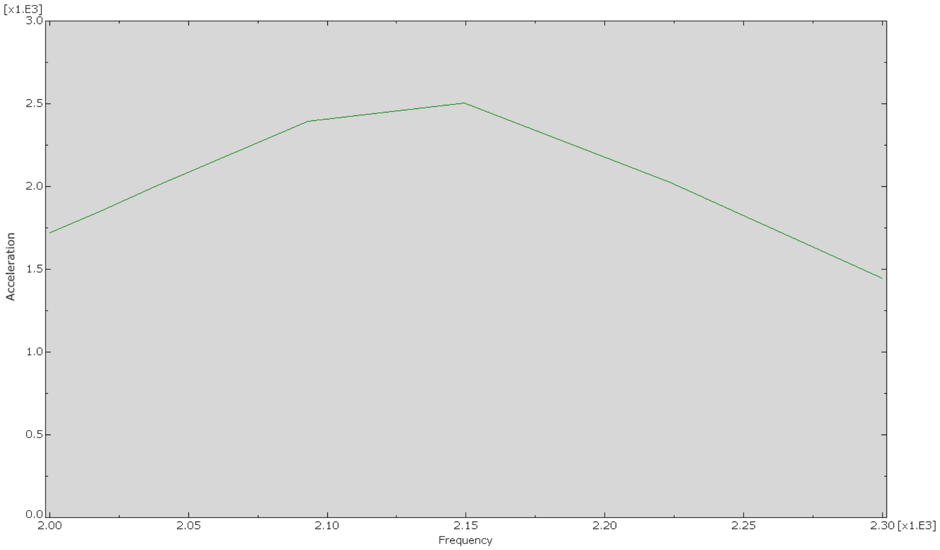

b)

Figure 8.2:15 – a) Experimental and b) numerical acceleration for mode 6 with piezoelectric actuators 1, 3 and 5 out of phase with 2, 4 and 6 third repetition

Table 8.2:5 – Summary of numerical and experimental results for static short blade setup (repetition number (#) and optimal phasing *p*)

Mode	**Frequency**	**Damping**	**Vpp**	**Acceleration**	
(Repetition)	**(Hz)**	**(%)**	**(V)**	**(m/s^2)**	
				Exp.	**Num.**
5 p* (1)	2160	14	336	N/A	600
5 p* (2)	1870	15	352	2100	680
5 (1)	2105	13	370	N/A	800
5 (2)	1975	9	352	2900	1125
6 p* (1)	1974	22	385	3800	1700
6 p* (2)	1880	20	400	3700	1950
6 p* (3)	1900	14	385	4650	2550
6 (1)	1952	14	450	3300	2100

*with optimal phasing of the actuators

8.2.5 ROTATING BLADE NUMERICAL ANALYSIS

As explained under section 8.2.1, a pressure force was applied to the ice layer to simulate the centrifugal force during rotation of the blade. For the experimentation, tests were performed at the conditions described under section 8.1.4, for an angle of attack of 0° and 6°. The small difference in angle of attack resulted in a very similar ice accumulation at the leading edge (Figure 8.2:16). The only difference was observed underneath the profile were a very thin layer of brittle ice was accumulated (see Figure 8.2:20).

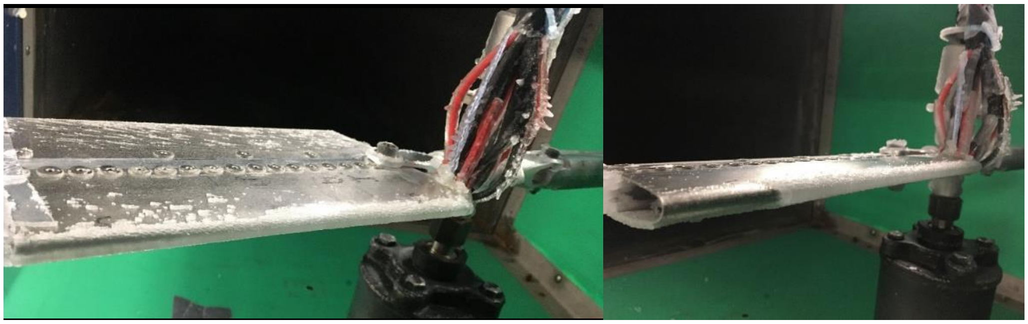

Figure 8.2:16 – Ice layer at a) 0° AOA and b) 6° AOA

Delamination was obtained only for two modes during static tests. In rotation, frequency sweeps at low sweep rate (below 70 Hz/s) up to 4000 Hz were first performed to assess if and at what frequency complete de-icing of the ice layer could occur. Due to the voltage offsetting, explained under section 8.1.2, voltage was limited to 500 Vpp for all actuator phasing tested except with all actuators in a single phase. The voltage phasing configurations tested in rotation were the same as for the static tests (see 8.2.4). For the phasing configurations where voltage was limited to 500 Vpp, no de-icing was obtained. The very low rotation speed and small radius of the setup did not generated sufficient force to help vibration de-icing the profile. When all piezoelectric actuators were activated in phase, voltage could be increased up to 750 Vpp, from -250 V to 500 V, by offsetting the voltage to 125 V. With lack of other measurements over the surface of the profile, it was assumed that the de-icing occurred for the same resonant mode where a delamination zone was obtained for the static profile. Ice breaking was not observed for other modes investigated, as predicted by the numerical model.

De-icing tests were repeated four times at 6° of angle of attack (AOA). At 0°, during the third test a connection to the actuator was broken and tests were stopped. Table 8.2:6 presents the experimental and numerical results. Acceleration measured using the accelerometer was not fully symmetrical around the acceleration axis and the resonant mode was not as well defined as for the flat plate (Figure 8.2:17). This can be caused by the vibration of the blade in rotation, the different boundary conditions (weak clamping of the shell structure) and the signal passing through the slip ring. An average of the positive and negative acceleration was used as the acceleration magnitude. The results were similar at 0° and 6° angle of attack (AOA), which could be expected due to the similarity in ice accumulation.

Table 8.2:6 – Experimental and numerical results for rotating setup

AOA	Frequency	Damping	Vpp	Acceleration	
(Repetition)	**(Hz)**	**(%)**	**(V)**	**(m/s²)**	
				Exp.	**Num.**
0 (1)	2375	N/A	660	N/A	N/A
0 (2)	2550	7	650	8100	2900
6 (1)	2675	9	680	8500	2275
6 (2)	2750	10	680	8000	2045
6 (3)	2575	9	660	8800	2275
6 (4)	2425	12	680	8500	1800

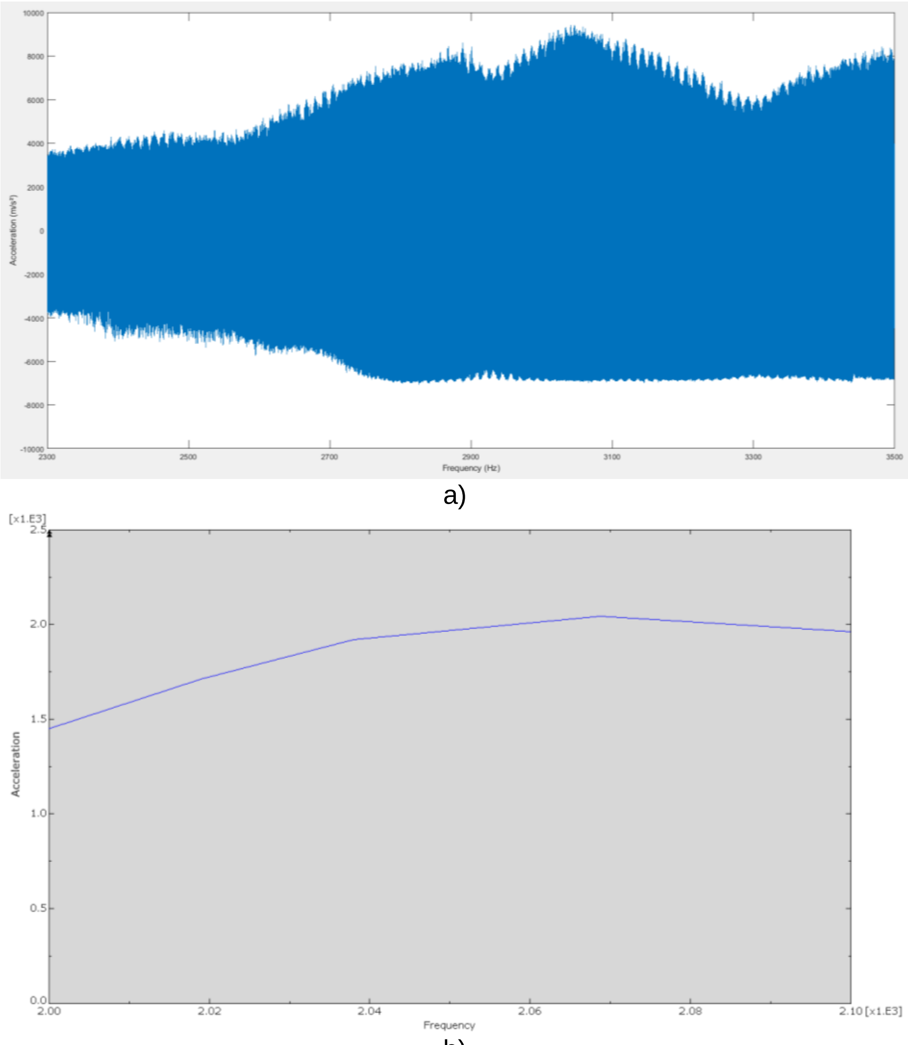

a)

b)

Figure 8.2:17 – a) Experimental and b) numerical acceleration for mode 5 in rotation with all piezoelectric actuators in phase at 6° AOA for second repetition

Complete de-icing was obtained during all the tests performed. In most tests, complete delamination and shedding of the ice was obtained after two consecutive frequency sweeps around the resonant mode. The frequency sweeps were performed from 2300 to 3500 Hz in 20 seconds. This configuration allowed the excitation of the highly damped resonant mode as well as a sufficiently low sweep rate to reach maximum mode deployment. During the first sweep, de-icing of the first and last third of the blade occurred (Figure 8.2:18-a) and de-icing of the center of the blade occurred during the second sweep (Figure 8.2:18-b). In one of the test, de-icing of the first two thirds of the blade de-iced during first sweep (Figure 8.2:19-a) and de-icing of the rest of the blade occurred during the second sweep (Figure 8.2:19-b).

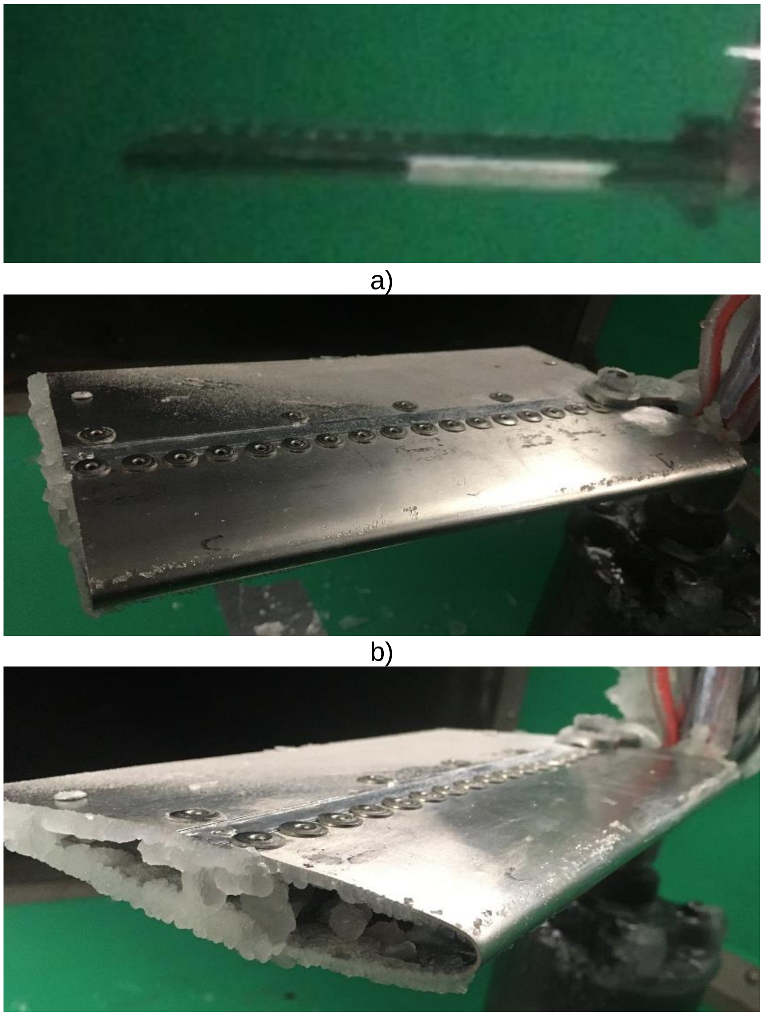

a)

b)

c)

Figure 8.2:18 – a) Partial de-icing after first sweep during a test at 6° AOA, b) and c) complete de-icing after second sweep and test stopped

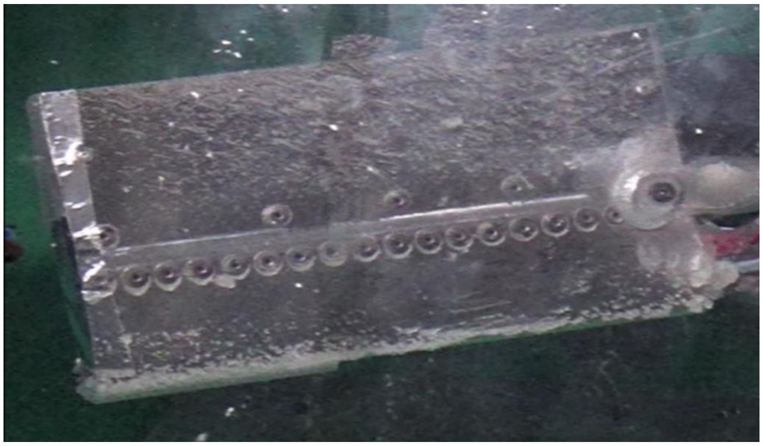

a)

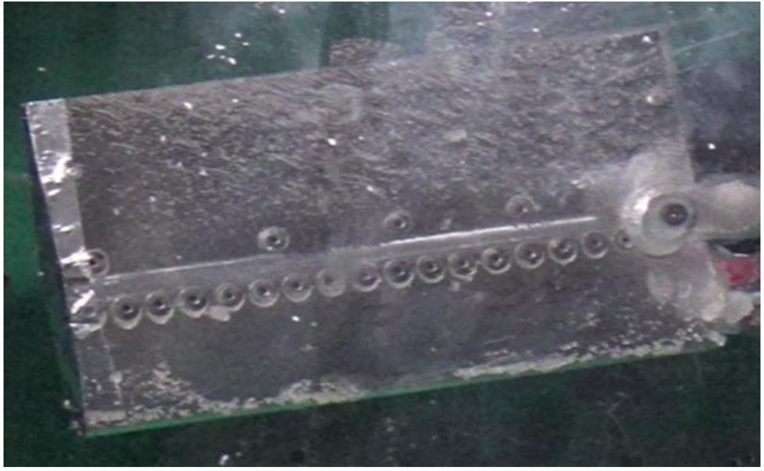

b)

Figure 8.2:19 – a) Partial de-icing after first sweep and b) complete de-icing after second sweep

Results were similar at 0° and 6°. However, due to angle of attack, a longer ridge of ice was obtained under the profile at 6° (Figure 8.2:20). The ice properties of this ridge of ice were different then at the leading edge due to a small accumulation rate. The ice had a very low ice density and was very brittle.

a)

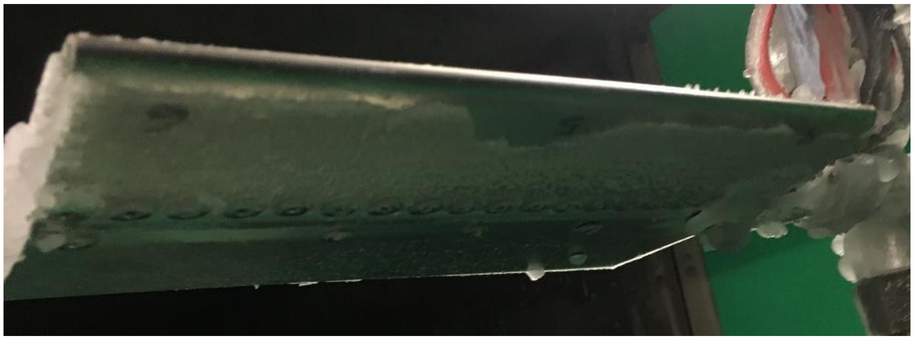

b)

Figure 8.2:20 – Ridge of ice underneath the profile at a) 0° AOA and b) 6° AOA

8.2.6 RESULTS ANALYSIS

8.2.6.1 EXPERIMENTAL VARIABILITY

The experimental variability was calculated from the different test repetitions performed in the wind tunnel. For the static tests, testing was repeated up to three times for two modes. For mode 5, the resonant frequency obtained was 2027 ± 157 Hz and the damping 13 ± 4 %. For the first excitation, with actuators 1, 3, 4, and 6 out of phase with actuators 1 and 2, the delamination voltage was 344 ± 8 Vpp and for the second excitation, all actuators in phase, was 361 ± 9 Vpp. Unfortunately acceleration could not be compared for this mode.

For mode 6, the resonant frequency was obtained at 1927 ± 47 Hz and the damping 18 ± 4 %. For the first excitation, with actuators 1, 3 and 5 out of phase with 2, 4 and 6, the delamination voltage was 390 ± 10 Vpp and acceleration measured 4050 ± 600 m/s².

The resulting variation is presented in Table 8.2:7. The maximum variation, obtained for the damping coefficient, was 31%. This variation was slightly higher than what was observed for the flat plate, but was expected for wind tunnel icing tests compared to cold room accumulation.

Table 8.2:7 – Percentage of variation for static experimental testing for mode 5 and 6

Mode	Excitation	Frequency	Damping	Vpp	Acceleration
5	1-3-4-6/2-5	8%	31%	2%	N/A
	1-2-3-4-5-6			2%	
6	1-3-5/2-4-6	2%	22%	3%	15%
	1-2-3/4-5-6			N/A	N/A

For the rotating setup, tests were performed at 0° and 6°. The results were similar, except for the ridge of ice on the lower surface of the profile, and results were considered as a single test condition for the analysis. The measured resonant frequency was 2495 ± 255 Hz and the damping coefficient was 10 ± 4 %. The voltage for de-icing was 668 ± 18 Vpp. and acceleration measured was 8380 ± 420 m/s². The resulting variation is presented in Table 8.2:8 and the maximum variation obtained was 30% for the damping. This variation was similar for the static test results. The overall test experimental variability could be defined at 31%.

Table 8.2:8 – Percentage of variation for rotating experimental testing

Mode	Frequency	Damping	Vpp	Acceleration
5	10%	30%	3%	5%

8.2.6.2 NUMERICAL MODEL ACCURACY AND STRESS PREDICTION

Experimental validation of the numerical model was partially done due to the limitation of the system. Only one accelerometer could be installed, providing the only measure of vibration of the system. The position of this accelerometer was not optimal for certain modes of vibration. Also, the reliability of the signal transferred through the slip ring and impact of rotation and imbalances on the results were unknown. This made the complete characterization of the vibration of the blade as well as the complete validation of the numerical model impossible. Partial experimental validation was still done using the available information and de-icing was achieved with the setup, proving the proof of concept of the method.

For the static setup, the comparison of the frequency analysis prediction with the experimental results when an ice layer is accumulated at the leading edge are presented in Table 8.2:9. The model accurately predicted the frequencies of the resonant modes within 11% except for the first mode. It seems that in this case the first resonant mode of the structure is heavily impacted by the boundary conditions. For this mode the discrepancy was 43%. During rotation tests, de-icing occurred around 2495 Hz, which was higher than the predicted frequency for mode 5 and frequency of delamination for static tests. This resulted in a discrepancy of 22%. In static mode the profile was tightly held on both sides, which helped creating a more efficient fully clamped boundary condition. In rotation, the profile was only held on one side and could not be held as tight as for the static tests. The vibration of the whole setup caused by the rotation imbalances, could have also impacted the frequency of the resonant mode. Also, even if the ice layer was similar, the ice accumulated in rotation could have affected the resulting frequency.

Table 8.2:9 – Comparison of experimental and numerical frequencies for the static setup

Mode (#)	Numerical Frequency (Hz)	Experimental Frequency (Hz)	Discrepancy (%)
1	559	800	43
2	1136	N/A	N/A
3	1828	N/A	N/A
4	1865	N/A	N/A
5	2038	2019	1
5 rotation	2038	2495	22
6	2149	1918	11

The comparison between the numerical model and experimental acceleration for static experimentation is presented in Table 8.2:10. Damping obtained was very high making the structure highly damped. During a previous project on this subject [62], the significant impact of weak clamped boundary conditions was observed. Most of the modes investigated with the flat plate setup in that previous project could not be observed, or showed very weak asymmetric vibration amplitudes over the plate as well as big frequency offset. Important friction within the plate and the clamping structure was supposed responsible for this phenomenon. This lead to the modification of the clamped boundary conditions for the flat plate setup to the one used in this project, big heavy blocks carefully tightened with multiple bolts and a torquemeter. After this modification, all the investigated resonant modes were found with symmetrical vibration patterns in accordance to numerical predictions at frequencies closer to the predicted frequencies. Even with all the attention that was given to the clamped boundary condition for this setup, it was not possible to recreate an equivalent clamping than for the flat plate setup, which explained to some degree the less clear vibration response. The important friction at the boundary condition, with the highly curved structure and presence of a significant ice accumulation on the profile could have been the reasons for this very high damping . Still, signal of the single accelerometer was not as symmetrical and did not show clear mode definitions in opposition to the flat plate (Figure 8.2:17). This made damping calculation more difficult and even questionable to some degree. While it was still believed that these damping values could be explained, they were on the high end of the possible damping coefficients and limitations of the measurement system should be addressed.

The average difference obtained between the numerical model and experimental results was 52% with a maximum variation of 67%. This was slightly higher than what was observed for the flat plate setup, which was expected. The higher experimental variability, as well as the more complicated nature of the structure explained this slightly higher deviation. Also, it was not possible to recreate the fixed boundary condition at the back of the profile as efficiently as for the flat plate. Finally, the important limitation of the experimental measurement could have affected the accuracy of that measurement. Unlike for the flat plate, the numerical model underpredicted the vibration magnitude for all the cases, which could be cause be an overvaluation of the damping ratio. Table 8.2:10 also shows the shear stress predicted by the numerical model as well as the adjusted value. The numerical model prediction for delamination was between 0.15 and 0.35 MPa, which was slightly out of the 0.20 to 0.90 MPa range obtained previously. This could be explained by the higher discrepancy between the model and experimentation. For the adjusted value, it ranged from 0.32 to 0.90 MPa. Again this was slightly out of the 0.33 to 0.66 MPa value obtained with the flat plate. This change could be attributed to the different accretion regime which was different, but also to the higher variability in the ice accumulation created in wind tunnel. No cracking of the ice layer was predicted by the numerical model and none was obtained experimentally.

Table 8.2:10 – Comparison of the acceleration between the experimental tests and numerical model predictions for static setup

Mode **(Repetition)**	**Acceleration** **(m/s²)**		**Discrepancy** **(%)**	**S12** **(MPa)**	
	Exp.	**Num.**		**Num.**	**Adj.**
5 p* (1)	N/A	600	N/A	0.27	N/A
5 p* (2)	2100	680	67	0.30	0.90
5 (1)	N/A	800	N/A	0.26	N/A
5 (2)	2900	1125	61	0.35	0.90
6 p* (1)	3800	1700	55	0.15	0.33
6 p* (2)	3700	1950	47	0.17	0.32
6 p* (3)	4650	2550	45	0.22	0.40
6 (1)	3300	2100	36	0.20	0.32

*with optimally phased actuators

For the experimental tests in rotation, the comparison when an ice layer is present on the blade is presented in Table 8.2:11. The average difference obtained in rotation was 73% with a maximum variation of 79%. This was higher than for the static tests, which could be explained by the effect of rotation and imbalances. Also, the clamped boundary condition was not as tight with the way the profile was held in the setup. As for the static tests, the numerical model underpredicted the vibration magnitude for all the tests performed. The shear stress predicted by the numerical model as well as the adjusted value were higher than for the static tests. Those values estimated the shear stress limit for de-icing and expulsion of the ice from the surface and not only delamination. To de-ice the blade structure in rotation, the model predicted an adjusted shear stress range of 2.60 to 2.84 MPa. When not considering the numerical discrepancy, the shear stress predicted range was 0.57 to 0.93 MPa.

Table 8.2:11 – Comparison of the acceleration between the experimental tests and numerical model predictions for rotation tests

AOA **(Repetition)**	**Acceleration** **(m/s²)**		**Discrepancy** **(%)**	**S12** **(MPa)**	
	Exp.	**Num.**		**Num.**	**Adj.**
0 (1)	N/A	N/A	N/A	N/A	N/A
0 (2)	8100	2900	64	0.93	2.60
6 (1)	8500	2275	73	0.76	2.84
6 (2)	8000	2045	74	0.68	2.66
6 (3)	8800	2275	74	0.73	2.82
6 (4)	8500	1800	79	0.57	2.69

Partial experimental validation of the numerical model was performed. Unfortunately, the limitations of the measurement system (only one accelerometer, accelerometer position, reliability of the signal, impact of rotation and imbalances on the results) made it very difficult to obtain a proper characterization of the vibration response of the experimental system. Damping values were very high. While still explainable, they should be measured with an improved system in future projects. Partial validation was still done using the available information. However, a full characterization should be done with a different technique like using a laser vibrometer, to complete validation and increase confidence in the results. The numerical model underpredicted the vibration amplitude by up to 67% for static tests and 79% for rotation tests. This discrepancy was slightly higher than for the flat plate, but this was expected due to the more complicated nature of the structure as well as the higher variability of the experimental testing. However, the numerical model was judged satisfying. For the shear stress prediction, the numerical model of the blade was consistent with the flat plate model in predicting delamination. Moreover, the higher discrepancy and different accumulation in wind tunnel resulted in a broader stress range for delamination prediction. In rotation, the shear stress calculated corresponded to the stress for de-icing and shedding of the ice layer from the blade. The value predicted by the model was 3 to 8 times higher than for simple delamination. This new information was used for numerical prediction of a similar blade with a larger span in section 8.3. The limited information obtained and drawbacks of the experimental setup made it difficult to fully validate the model and limited confidence in the results. Modification to the setup should be done to perform a more comprehensive study in order to confirm results and conclusions obtained as well as gathered additional data to complete validation.

8.2.6.3 POWER CONSUMPTION

The power consumption of the system for the de-icing of the blade setup was calculated with the formula provided by the piezoelectric actuator manufacturer [ajouter reference]:

$$P_m = C * f * U_h^2 \tag{45}$$

with P_m the average electrical power, *C* the actuator electrical capacitance, *f* the frequency of excitation and U_h the voltage swing.

The electrical capacitance of the actuators was 45 nF. The average frequency of excitation obtained during the de-icing test was 2495 Hz and the average voltage swing was 668 Vpp. At those conditions, the average power consumption of an actuator was 50 W, meaning a total average power for the six actuators of 300 W.

To compare with thermal de-icing systems, the power density was calculated. The common practice is to consider the first 30% of the chord of the profile to calculate the de-iced area, corresponding to approximately 15% of its surface area. For this blade setup, an iced zone of 22.9 cm (9 inch) spanwise by 4.1 cm (1.6 inch) chordwise was considered, for a total of 93.9 cm^2 (14.5 in^2), which resulted in an average power density of 32 kW/m^2 (21 W/in^2).

When compared to 39 to 43 kW/m^2 (25-28 W/in^2) [51] for a thermal de-icing system, this gave a power reduction up to 25%. While interesting, this power reduction is small to justify the implementation of such a complicated system. De-icing occurred after two complete sweeps of 20 seconds, for a total energy consumption, the product of the power and the sweep duration, of 12 kJ. The sweeps could have been restarted as soon as the first partial de-icing occurred to avoid waste of energy. Since ice removal occurred around the middle of the sweeps, stopping the sweeps after around 5 seconds when the de-icing just occurred would have prevent wasting energy for the second half of the sweep and the energy consumption would have dropped to 3 kJ. This value could be diminished even more with an optimized system targeting more precisely the resonant mode limiting the energy consumption with an instant de-icing. However, this would have require a better setup allowing a complete characterization of the blade vibration.

The blade profile was very small, especially compared to the actuator size. With a longer profile spanwise, it was believed that the blade should have a higher flexibility and vibration would be favored. Also, the actuator used in this study would be more fit to the anti-nodes of the first modes of vibration of a longer blade resulting in more efficient excitation of the structure by the actuators. Finally, the very low angular speed at which de-icing tests were performed as well as the small radius of rotation did not yield tangential speeds representative of the reality. With higher tangential speeds, higher centrifugal forces would have facilitated de-icing. All those factors should contribute to considerably reduce the power consumption of the system. To investigate those assumptions, a full tail rotor blade case was investigated in the next section.

8.3 FULL TAIL ROTOR BLADE CASE

Complete de-icing was achieved with the small blade setup. However power density, while still lower than for a thermal de-icing system, was still high to justify the implementation of such a complicated system. It was concluded that the small span of the structure, large size of the actuators and very low rotation speed and radius were factors impacting negatively power consumption of the system. To test this theory, the numerical model was used to model a full size tail rotor. With its longer span, flexibility of the structure should favor vibration, and anti-nodes size be better suited for the size of the patches used in this project. Moreover, a longer span increases centrifugal force on the ice layer for same rotation speed.

The same extruded shell NACA0012 part cut to 0.045 m used for the small blade model was also used for this model. The sketch was extruded to a span of 0.60 m (Figure 8.2:1-b) and thickness of the shell kept to 0.8 mm (Figure 8.3:1-a). The material was changed to the stainless steel material used for the flat plate which is the material used to build Bell 206 tail rotors. The same mesh elements and element size was used than for the small blade structure. Fully constrained clamped boundary conditions were added to the side of the profile in addition to the one at the back of the profile (Figure 8.3:1-b). Those boundary conditions simulate the capping at each end of the blade.

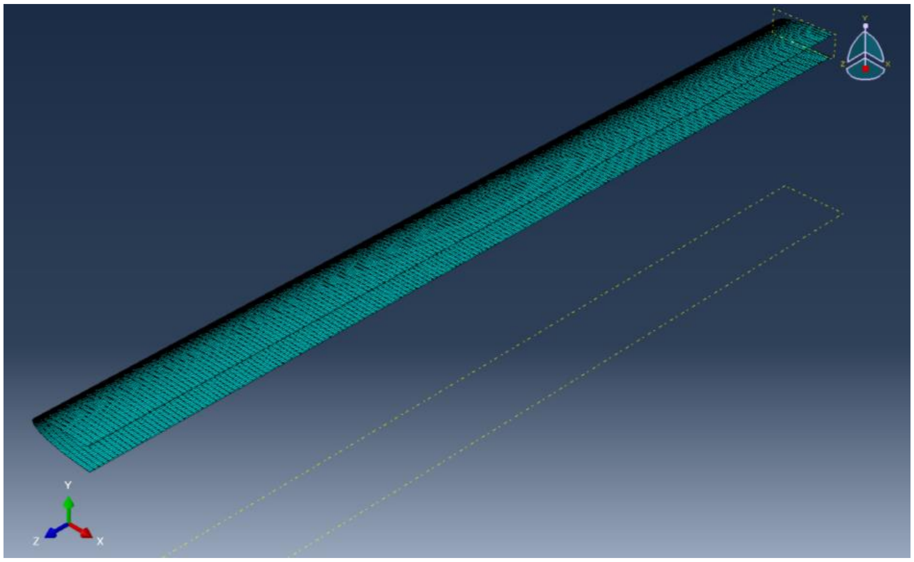

a)

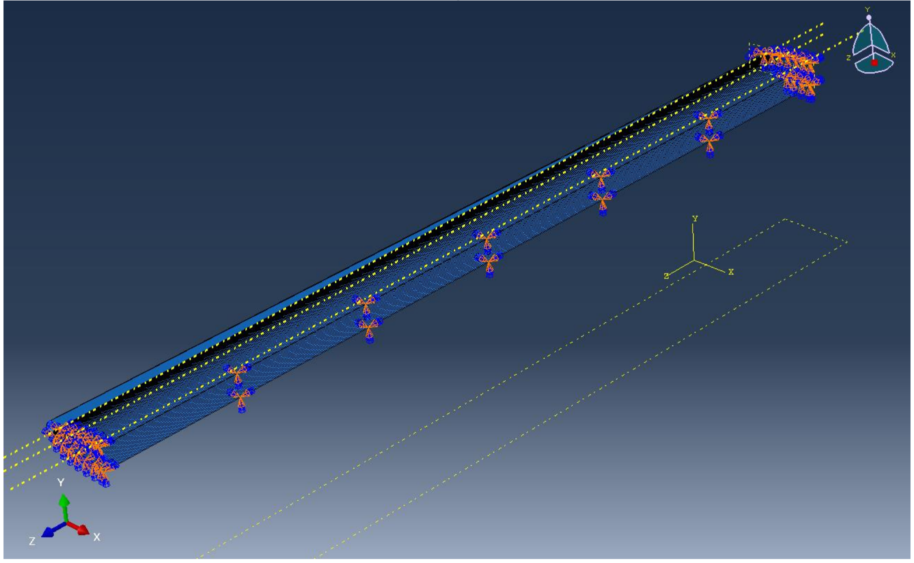

b)

Figure 8.3:1 – a) Blade shell model b) with clamped boundary conditions

The ice layer was also created as a 3D homogenous deformable extruded part. Ice material properties were kept the same as for the other numerical models. The shape of the ice was based on the ice shape obtained with the small blade model and the thickness was set to 6.35 mm (1/4th of an inch) at the tip of the blade, as it is the maximum allowed thickness on a rotorcraft blade. However, the ice layer is susceptible to have a linear thickness decrease along its span towards its root due to the increase in tangential velocity with the increase in radius. To model that phenomenon, the thickness was linearly reduced down to 1 mm at the root of the blade (Figure 8.3:2). The ice was tied to the blade shell structure with a Tie constraint. The element type to mesh the ice part was changed to C3D10 10-node quadratic tetrahedron elements.

Tetrahedral elements can fit better complex geometry but requires more elements to obtain the same accuracy. The element size was increased by a factor 6 to compensate for this.

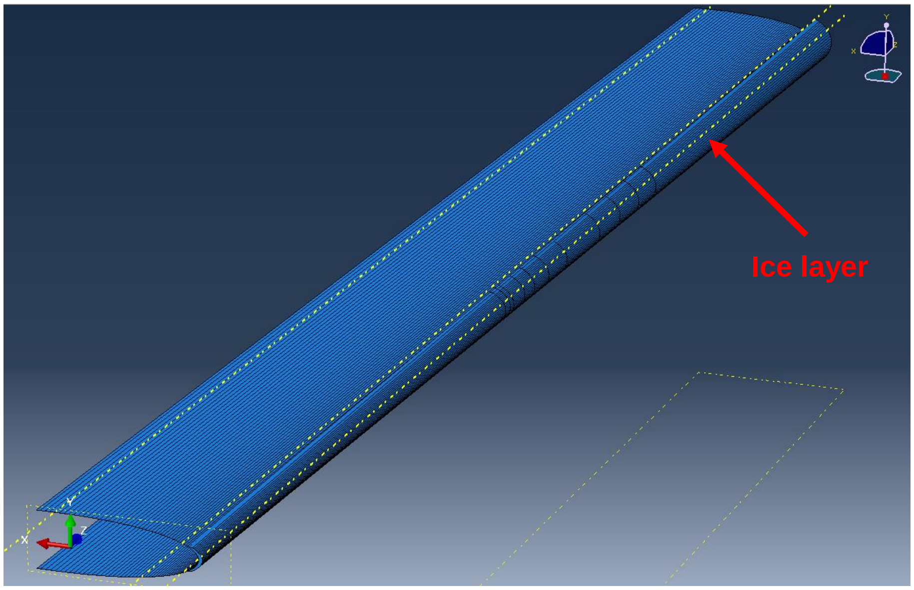

Figure 8.3:2 – Ice layer part with linear thickness increase

8.3.1 FREQUENCY AND DIRECT STEADY-STATE DYNAMICA ANALYSIS

A frequency analysis was first run to calculate the first resonant modes of the iced blade. As for the small blade setup, the first modes were targeted to minimize power consumption (see 8.2.3). Mode 2, 3 and 4 (Figure 8.3:3) were selected for their lower frequency and mode shape similar to successful resonant modes with the small blade setup and proper anti-node size for the actuators.

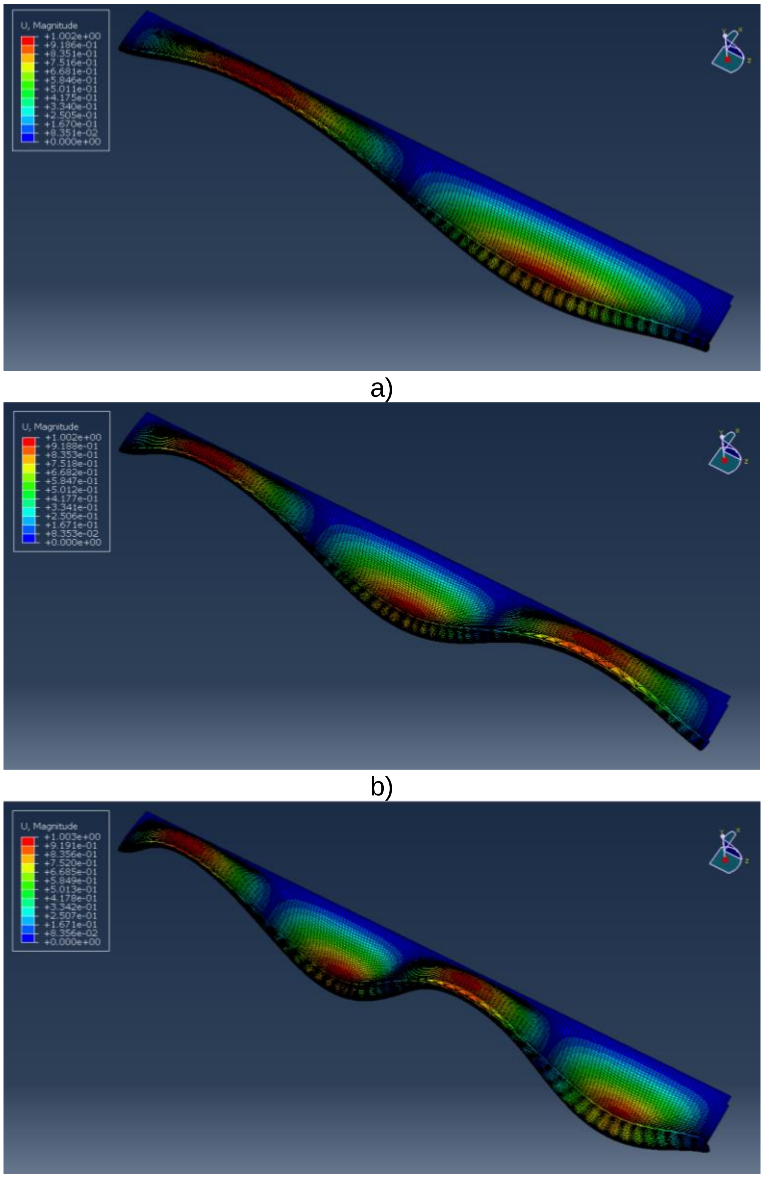

a)

b)

c)

Figure 8.3:3 – Full tail rotor resonant mode 2 (a), 3 (b) and 4 (c)

For each of those modes, PI876.A15 piezoelectric actuator patches were positioned at the center of each anti-nodes on the upper and lower surface. The direct steady-state dynamic analysis was run for each mode with the optimal phasing of the actuators. A damping of 10% was used, which was the average experimental damping coefficient measured for the rotating small blade setup. Even if the material is not the same, this value is deemed acceptable since it is only a rough approximation impacted mainly by the boundary conditions and ice layer, and the results obtained must be treated as such.

For each mode, the voltage peak to peak required to obtain 2.72 MPa of shear stress S12 was determined with the simulation. This corresponded to the average shear stress calculated with the numerical model at complete de-icing of the blade for the small blade setup. Voltages were calculated at each mode for two scenarios, first when taking into account the numerical model average error of -73% into the results (Table 8.3:1) and second without considering numerical model error (Table 8.3:2). Those results assumed the validity of the partial experimental validation of the small blade setup numerical model, similar damping values for the full iced tail rotor blade, a similar numerical discrepancy between experimentation and the full tail rotor blade model (for scenario 1) and similar shear stress values for complete de-icing.

Voltage values are presented for a static case (only piezoelectric actuator de-icing system) and when a centrifugal force was added. For the shear stress resulting of the piezoelectric actuator system excitation, the numerical error was taken into account to adjust the stress for scenario 1. An additional static step was run to determine the shear stress added by the centrifugal load. The centrifugal force was considered at 600 RPM, a conservative tail rotor rotation speeds, the estimated accumulated ice mass of 25 grams and a radius of 0.55 m for a force of 54 N. The shear stress resulting of this force was not adjusted in either scenarios since the numerical error for this is unknown and should be much lower than for complex vibration calculation.

Table 8.3:1 – Voltage prediction by the numerical to obtain similar stress at de-icing than for small blade setup considering same numerical error

Mode	**Frequency (Hz)**	**Voltage for shear stress = 2.72 MPa (Vpp)**	**Voltage for shear stress = 2.72 MPa in rotation (Vpp)**
2	1015	950	675
3	1373	122	87
4	1798	77	55

Table 8.3:2 – Voltage prediction by the numerical to obtain similar stress at de-icing than for small blade setup without considering numerical error

Mode	**Frequency (Hz)**	**Voltage for shear stress = 2.72 MPa (Vpp)**	**Voltage for shear stress = 2.72 MPa in rotation (Vpp)**
2	1015	3510	2500
3	1373	453	323
4	1798	286	205

8.3.2 DE-ICING SCENARIOS AND POWER ESTIMATION

The voltage required for de-icing, based on the shear stress obtained with the small blade setup, were estimated numerically for the full tail rotor case for modes 2, 3 and 4. With this information the power consumption of the system was estimated, as detailed under section 8.2.6.3, for both the case where the experimental error was considered similar to the one for the small blade setup and the case where no experimental error was considered.

For the power density calculation, the span was changed from 22.9 cm (9 inches) to 60 cm (23.6 inches) for a 246 cm² (37.8 in²) surface (see 8.2.6.3). The results, presented in Table 8.3:3 and Table 8.3:4, show the power reduction potential of the system. Those values are simple basic estimate based on the various assumptions presented at previous section and should be considered likewise. They represent best case scenarios within potential voltage range. Also, exact shedding mechanism were not fully investigated and de-icing prediction was based only on maximum shear stress prediction by the numerical model.

Finally, this was for a hollow leading edge of 4.5 cm, which is significantly longer than the 1 cm hollow leading edge of the Bell 206 tail rotor. Despite all this, they show the power reduction potential and they validated the conclusions that power density should be much lower for a larger blade. When the numerical model error was not considered, power density down to 1.1 kW/m² (0.72 W/in²) were estimated, which is significant. Despite the important considerations that must be taken into account when judging those values, this reduction potential justify a deeper investigation of the piezoelectric actuator system integrated to a full tail rotor blade.

Table 8.3:3 – De-icing power estimation based on numerical prediction for full tail rotor considering same numerical error as small blade setup

Mode	Number of actuators	Power without rotation (W)	Power in rotation (W)	Power Density in rotation (W/in²)	Reduction from thermal system (%)
2	4	165	83	2.2	92
3	6	5.5	2.8	0.07	99.7
4	8	3.9	2.0	0.05	99.8

Table 8.3:4 – De-icing power estimation based on numerical prediction for full tail rotor without considering numerical error

Mode	Number of actuators	Power without rotation (W)	Power in rotation (W)	Power Density in rotation (W/in²)	Reduction from thermal system (%)
2	4	2250	1140	30	-8
3	6	76	39	1.03	96
4	8	53	27	0.72	97

8.4 SUMMARY

An experimental setup of a small tail rotor blade, limited in span by the wind tunnel size, was designed and built for wind tunnel testing. A new setup allowing power to be brought to the blade during rotation was developed and allow testing of the piezoelectric actuator de-icing system to be tested in rotation for the first time with the contribution of the centrifugal force. The experimental tests were successful and complete de-icing of the blade was obtained. Power consumption was calculated and showed a 25% reduction as compared to electrothermal systems. A numerical model was also developed and use to investigate stresses. However, with the lack of measurement capabilities very limited validation could be performed.

It was then estimated that the power reduction could be much more significant for a longer blade similar to a real tail rotor blade due to the size of the actuators, greater flexibility and higher centrifugal force. The numerical model was modified to the actual span of a real tail rotor and the first resonant modes were investigated. Results have confirmed those assumptions predicting power reductions above 97%. Even if these results are preliminary results based on different assumptions and simplification, it still shows great potential and that it is worth pursuing the investigation. It is possible that this kind of excitation can impact the fatigue life of the structure and aeroelastic stability. This should be investigated in a next study.

CONCLUSION

In the first chapter of this thesis, it was clearly demonstrated that the industry is in need of new alternative ice protection systems with low power consumptions, which is even more of paramount importance when it comes to smaller rotorcraft. Vibration based de-icing has been investigated using piezoelectric actuators to excite the resonant frequencies of structures. First, a numerical model of a simple flat plate structure has been developed. Preliminary simulations run with this model have allowed the design and integration of piezoelectric actuators for de-icing research to a flat plate experimental setup. They have provided the necessary information for actuator positioning and phasing of the actuator patches for optimal mode deployment. A numerical model of the final setup was elaborated with the optimal positions of the piezoelectric actuator patches obtained from the preliminary simulations and meshed with piezoelectric elements. A physical experimental setup was also built in accordance with the numerical model for experimental validation using a scanning laser vibrometer. The numerical model was used for resonant frequency and mode shape calculations with a frequency analysis. The experimental setup confirmed the results with a maximum variation of 14%.

Following this investigation, direct steady-state dynamic analysis were performed to predict vibration amplitudes of the plate. Electric boundary conditions were applied to the actuators, and vibration of the plate resulted from the piezoelectric actuators excitation. The experimental results validated the model when the plate was optimally excited with an average error of 20% and a maximal error obtained of 43%. This deviation was explained by the experimental repeatability of the test, as well as by the assumption of the numerical model for boundary conditions and bonding of the actuators. However, when the plate was not correctly excited for a mode, the prediction of the numerical data were not as accurate. Piezoelectric actuators were too large for two of the resonant modes investigated during this validation, which resulted in a less symmetric and optimal vibration of the plate experimentally. This was not totally accounted for by the numerical model and explains the overprediction of vibration amplitudes of the model for those two modes. This was not a concern since the numerical model was developed to design and predict optimal excitation of structures for de-icing purposes. The results also confirmed the conclusions obtained with the numerical model on optimal phasing of the piezoelectric actuators in function of each resonant mode shape. This comprehensive study allowed to develop a numerical model for a simple flat plate and a better understanding and optimization of the actuators driving strategies for the design and instrumentation of piezoelectric-based de-icing system and was the subject of an original paper published in a peer reviewed journal [84].

After the development of the numerical model, vibration response of the flat plate structure to frequency sweep excitations was studied. The results have shown that a minimum number of excitation cycles was required for the plate to reach maximum magnitude of vibration during a frequency sweep. If the frequency sweep rate was too high, the resonant modes excited did not reach maximum vibration amplitudes. As the sweep duration was increased (lower sweep rate), the vibration of the plate tended to reach the value of the steady-state excitation, where maximum mode deployment was obtained. No other effects were observed during frequency sweep tests, meaning that steady-state was the optimal activation for de-icing. Frequency sweeps, if done at a proper sweeping rate, can achieve the same results as steady-state activation and for lower frequencies, lower sweep rates are required to reach the same percentage of the steady-state value.

To validate those conclusions, a camera was installed in the cold room and resonant frequencies of the structure at which breaking of the ice layer occurred during frequency sweeps were determined. The use of the camera has allowed to identify two frequencies at which cracking occurred and two frequencies at which delamination occurred. Testing was subsequently performed at fixed frequency in steady-state activation at the four frequencies obtained. The tests have proven that it is possible to obtain cracking and delamination of the ice layer on the flat plate in steady-state activation, without sweeping, which confirmed the conclusions that maximum acceleration and mode deployment is obtained in steady-state mode and that adjacent modes excited during sweeping are not required to help cracking and delamination. It also pointed out the importance of correctly determining which mode can lead to de-icing and the exact frequency of the resonant mode to achieve de-icing. De-icing was obtained in steady-state activation, which was not successful in the previous works done on the subject in the laboratory [62] [63]. During those studies, de-icing in steady-state mode was tried by using frequencies selected arbitrarily from their mode shapes and accelerometers were not used to their full potential to identify the actual frequency of the mode once ice was accumulated. The ice layer accumulations on the plate modify the stiffness of the structure and the frequencies of the resonant modes. Repeatability of the ice layer accumulation creates variation in the resulting resonant frequency for each mode between each ice accumulation, making it impossible to determine the exact frequency without measuring it. If the excitation is not done at the exact frequency, acceleration and stress generation will be sub-optimal, only a small fraction of those obtained at the exact frequency and de-icing will not occur. This explained the lack of success from previous studies: even if steady-state mode is the optimal activation, it is less practical and harder to achieve without the use of the right tools. Frequency sweeps were used to find frequencies where ice breaking occurred, showing the necessity of developing a numerical model and limit criteria to determine the resonant modes susceptible of generating de-icing in order to use steady-state activation without frequency sweeps.

Results have also showed that breaking of the ice layer affects the bending stiffness of the ice/plate structure. This change in stiffness lowers the frequency of the resonant modes. Performing frequency sweep backwards, from the highest frequency to the lowest, should be more effective for de-icing by activating multiple time the same resonant mode. Sweeping at proper sweep rate could be performed from highest to lowest frequency for more efficiency by re-exciting the same mode multiple time in a single sweep. This work on transient and frequency sweep excitation was published in an original paper in a peer reviewed journal [85].

An ice layer was added to the flat plate numerical model and frequency analysis and direct steady-state dynamic analysis were performed to predict the structural natural frequencies, vibration amplitudes and stresses generated in the ice layer. Experimental validation was performed with the experimental test setup in a cold room. The test variation was established at 26% and the average numerical error of the model was 20% with a maximum error of 41%. The two types of ice breaking were investigated during the experimental testing (cracking within the ice layer and delamination of the ice layer from the flat plate structure). Numerical model predicted an average of 1.04 MPa in normal stress in the ice layer for cracking which is in accordance with literature. For delamination of the ice layer, numerical model calculated two significant stresses at the bottom of the ice layer, a shearing stress S23 and a normal stress S33. The average shearing stress value predicted by the model was 0.46 MPa, which was right within the literature range for adhesion of ice on steel and also for shear stress obtained in other studies at the laboratory. The average value obtained for normal stress S33 was 0.69 MPa, which was larger than S23. However, even if no value was found in literature for adhesion of ice on steel in tension, a paper established that in tensile experiments, adhesive strength of ice in tension is at minimum 15 times greater than in shearing experiments. This was explained by the presence of a liquid-like layer at the interface which hold the ice and substrate together by surface tension forces. This indicated that S23 was the limiting stress, but more experimentation could be done on the subject. The stress distribution of the different stresses for delamination cases where concentrated on the edges of the bottom layer of the ice accumulation. Negligible stresses were obtained at the center of the ice layer and concentrated rapidly close to the edges. This result was in accordance with a shear model developed in the literature that showed the same distribution pattern and concluded that shear stress is concentrated on the edges of the ice and delamination starts off from edges and maximum shear stress emerges on the new edges until complete delamination. Stress limit criteria were determined from the prediction of the model for all the modes tested and the numerical model was used, as a proof of concept, to find modes susceptible to generate ice breaking within the voltage limit of the piezoelectric actuators and to predict the voltage range within which breaking should occur. Four modes were found and tested, revealing that the numerical model was successful in predicting ice breaking and voltage range.

Finally, a new numerical model of a small blade structure was developed using results and conclusions obtained for the flat plate structure to perform numerical simulation and experimentation of de-icing on a rotating blade structure. The numerical model was done for both static tests and tests in rotation. Experimentation was performed with a small blade structure prototype in wind tunnel. Validation of the numerical model was difficult due to lack of measurement on the blade with the limitations of the systems. With the time remaining in the project and pandemic situation, it was not possible to develop a more robust measurement system for the prototype. Still, with the information gathered during testing, partial validation was performed. The numerical model predicted vibration magnitude with an average difference of 52% and a maximum variation of 67% for static tests. This was slightly higher than for the flat plate setup, which was expected due to the higher experimental variability, more complicated nature of the structure and less representative boundary conditions. As experienced in a previous study on the project, the weaker boundary conditions are believed to be responsible for much of this variation and worse results than for the flat plate. For the experimental tests in rotation, the average difference obtained was 73% with a maximum variation of 79%, which was higher than for the static tests. For both the static and tests in rotation, the numerical model underpredicted the vibration magnitude for all the tests performed. The shear stress predicted by the numerical model as well as the adjusted value in rotation estimated the shear stress limit for de-icing and expulsion of the ice from the surface. The value predicted by the model was 3 to 8 times higher than for simple delamination. Power consumption was calculated using information provided by the actuator manufacturer. Power density was evaluated at 21 W/in^2, as compared to 28 W/in^2 for actual thermoelectric systems. It was estimated that the power could be greatly reduced for a longer blade which should have a higher flexibility and that vibration would be favored with the actuator used more fit to the anti-nodes of the first modes of vibration of a longer blade. Also a greater radius would yield higher centrifugal force.

To investigate those assumptions, a full tail rotor blade case was investigated numerically. This investigation confirmed those conclusions and showed the potential of the method when applied to such a blade, even if the results obtained were simple basic estimate based on various assumptions and should be considered likewise. They represented best case scenarios within potential voltage range. Also, they were obtained for a hollow leading edge of 4.5 cm, which is significantly longer than the 1 cm hollow leading edge of the Bell 206 tail rotor. When the numerical model error was not considered, power densities down to 0.72 W/in^2 were estimated, which is a significant decrease, and this potential alone justify a deeper investigation of the piezoelectric actuator system integrated to a full tail rotor blade.

Actually, there is no ice protection systems available for small rotorcraft and very few researches have been done on a piezoelectric vibration based de-icing system with mitigated results. This research has allowed to fill in the lack of knowledge on actuator positioning, actuator excitation, levels and types of stress required for different ice breaking and de-icing under dynamic excitation. It has also provided a comprehensive validated numerical model, including piezoelectric actuators and ice, to the scientific community to assist in the design of such systems, which is not limited to rotorcraft application. Such a model did not exist before. A new innovative experimental setup of powered rotating blade has also been developed which will allow unique wind tunnel testing capabilities at the laboratory in order to test piezoelectric systems in rotation, as well as electrothermal and coatings. Three scientific papers have been published in MDPI Aerospace Journal (peer reviewed) and are now available on-line and have been referenced throughout this thesis. A fourth one is also in preparation at the moment of redaction of this thesis. This all demonstrate the originality and contribution of this research.

RECOMMANDATIONS

Following this comprehensive investigation of the use of piezoelectric actuators for ice protection system, it is recommended to pursue the investigation with a full tail rotor prototype. In order to do so, the first step recommended is to use the numerical model for the design of new optimal piezoelectric actuators. The flat plate and small blade prototype setup have shown the paramount important of the proper size and geometry of the actuator used in such a system. The piezoelectric material used can also be investigated with the model. Other types of actuators, like preloaded or piston-like actuators, must also be considered. At the beginning of this research project, it was quickly realized that there was a lack of information for actuator manufacturer to design optimal actuators. With the numerical model developed and results obtained during this investigation, it is strongly believed that there should be sufficient data now to allow the design of such actuators.

It is also recommended to design an improved measurement and operation system for the testing and validation of a full tail rotor prototype. This would allow to perform a complete characterization of the vibration of a full blade prototype in order to obtain a comprehensive experimental validation of the model and confirm or improve the results obtained during the investigation on the small blade structure. At the end of this project, a partial study of a blade structure was performed with acceptable results, but for a new project, a better system must be designed. Also, the operation system to gathered measurements as well as excite the actuators must be designed to facilitate the process.

The exact shedding mechanism were not fully investigated and de-icing prediction was based only on maximum shear stress prediction by the numerical model. Despite all this, stresses obtained for cracking and delamination were within the literature values found in the literature. They also showed the power reduction potential and they validated the conclusions that power density should be much lower for a larger blade. However, it is recommended that those mechanism be fully investigated in a specific project exclusively on this topic. For cracking, the brittle cracking theory should be investigated experimentally and numerically, while for delamination, cohesive elements could be used numerically. The delamination process obtained in this study should be validated. In order to do so, non-linear explicit analysis have to be used. This project could also investigate the difference between delamination and de-icing, both for the stresses involved as well as the phenomena involved.

This kind of excitation could impact the fatigue life of the structure and its aeroelastic stability. This should be investigated in a next study.

Finally, the centrifugal force in the numerical model should be investigated to ensure the validity of the results. A simple pressure force was used in this project to add to the stress in the ice layer. This practice should be verified experimentally on its own. This could be done using the Spinning Rotor Blade setup in the wind tunnel without any other systems involved. The stresses involved could then be compared and validated.

REFERENCES

1. Flight Safety Foundation, *Inflight Icing and the Helicopter - Results of a U.S. Army investigation into the unique hazards facing rotary wing operations in the winter environment offers timely tips for all helicopter flight crews.* Helicopter Safety, 1990. **16**(6): p. 4.
2. Simpson, M.P. and R. P.M., *Certification and Operation of Helicopters in Icing Environments.* Journal of Aircraft, 1998. **Vol. 35**(6): p. 936-941.
3. Ramanathan, S., *An Investigation on the Deicing of Helicopter Blades Using Shear Horizontal Guided Waves*, in *Engineering Science and Mechanics*. 2005, Pennsylvania State University. p. 189.
4. Palacios, J.L., E.C. Smith, and J.L. Rose. *Investigation of an Ultrasonic Ice Protection System for Helicopter Rotor Blades*. in *64th Annual Forum Proceedings - AHS International*. 2008. Montreal, Quebec.
5. Venna, S.V., Y.-J. Lin, and G. Botura, *Piezoelectric Transducer Actuated Leading Edge De-Icing with Simultaneous Shear and Impulse Forces.* Journal of Aircraft, 2007. **Vol. 44**(2): p. 509-515.
6. Kandagal, S.B. and K. Venkatraman, *Piezo-actuated Vibratory Deicing of a Flat Plate*, in *AIAA/ASME/ASCE/AHS/ASC Structure Dynamics, and Materials Conference*. 2005: Austin, Texas. p. 3907-3914.
7. Gent, R.W., N.P. Dart, and J.T. Cansdale, *Aircraft icing.* Philosophical Transactions of the Royal Society of London. Series A: Mathematical, Physical and Engineering Sciences, 2000. **358**(1776): p. 2873-2911.
8. Schulson, E., *The structure and mechanical behavior of ice.* JOM Journal of the Minerals, Metals and Materials Society, 1999. **51**(2): p. 21-27.
9. Gold, L.W., *On the elasticity of ice plates.* Canadian Journal of Civil Engineering, 1988. **15**(6).
10. Fletcher, N.H., *The Chemical Physics of Ice.* Science, 1970. **169**(3947).
11. Petrovik, J.J., *Review Mechanical properties of ice and snow.* Journal of Materials Science, 2003. **38**.
12. Haynes, F.D., *Effect of Temperature on the Strength of Snow-Ice*. 1978, Department of the Army, Cold Regions Research and Engineering Laboratory, Corps of Engineers: Hanover, New Hampshire. p. 27.
13. J.H. Currier, E.M.S., *The tensile strength of ice as a function of grain size.* Acta Metallurgica, 1982. **30**(8).
14. Michel, B., *Ice Mechanics*. 1978: Les presses de l'Université Laval.
15. Weibull, W. *A Statistical Theory of the Strength of Materials*. 1939. **151**, 1-45.
16. J.P. Dempsey, S.J.D., R.M. Adamson and S.V. Mulmule, *Scale effects on the in-situ tensile strength and fracture of ice Part I: Large grained freshwater ice at Spray Lakes Reservoir, Alberta.* International Journal of Fracture, 1999. **95**(325).
17. Mohamed, A.M.A. and M. Farzaneh, *An experimental study on the tensile properties of atmospheric ice.* Cold Regions Science and Technology, 2011. **68**(3): p. 91-98.
18. Berthouex, P.M. and L.C. Brown, *Statistics for Environmental Engineers*. Second ed. 2002: Lewis Publishers. 512.
19. Kermani, M., Farzaneh, M., Gagnon, R., *Compressive strength of atmospheric ice.* Cold Regions Science and Technology, 2007. **49**(3).
20. Farid, H., A. Saeidi, and M. Farzaneh, *An atmospheric ice empirical failure criterion.* Cold Regions Science and Technology (under press), 2016.
21. Farid, H., A. Saeidi, and M. Farzaneh, *Prediction of failure in atmospheric ice under triaxial compressive stress.* Cold Regions Science and Technology, 2017. **138**.
22. Ryzhkin, I.A. and V.F. Petrenko, *Physical Mechanisms Responsible for Ice Adhesion.* The Journal of Physical Chemistry B, 1997. **101**(32): p. 6267-6270.
23. Petrenko, V.F. and S. Peng, *Reduction of ice adhesion to metal by using self-assembling monolayers (SAMs).* Canadian Journal of Physics, 2003. **81**(1-2): p. 387-393.
24. Zou, M., et al., *Effects of surface roughness and energy on ice adhesion strength.* Applied Surface Science, 2011. **257**(8): p. 3786-3792.

25. Faraday, M., *Note on Regelation.* Proceedings of the Royal Society of London, 1859. **10**(ArticleType: research-article / Full publication date: 1859 - 1860 /): p. 440-450.
26. Jellinek, H.H.G., *Liquid-like (transition) layer on ice.* Journal of Colloid and Interface Science, 1967. **25**(2): p. 192-205.
27. Rice, J.R. and G.C. Sih, *Plane problems of cracks in dissimilar media.* Journal of applied mechanics, 1965. **32**: p. 418-423.
28. Scavuzzo, R.J. and L.C. Mamerto, *Structural properties of impact ices accreted on aircraft structures*. 1987, NASA. p. 57.
29. Chu, M.C. and R.J. Scavuzzo, *Adhesive shear strength of impact ice.* AIAA Journal, 1991. **29**(11): p. 1921-1926.
30. Fortin, G., A. Beisswenger, and J. Perron, *Centrifuge Adhesion Test to Evaluate Icephobic Coatings*, in *2nd AIAA Atmospheric and Space Environments Conference*. 2010, AIAA: Toronto, ON. p. 1-11.
31. Fortin, G. and J. Perron, *Spinning Rotor Blade Tests in Icing Wind Tunnel*, in *1st AIAA Atmospheric and Space Environments Conference*. 2009, AIAA: San Antonio, Texas. p. 1-16.
32. Akitegetse, C., *Approche numérique et expérimentale pour l'amélioration d'une méthode de mesure de la force d'adhérence de la glace par l'utilisation de films piezoélectriques*, in *DSA*. 2007, Université du Québec à Chicoutimi. p. 137.
33. Meuler, A.J., et al., *Relationships between Water Wettability and Ice Adhesion.* ACS Applied Materials & Interfaces, 2010. **2**(11): p. 3100-3110.
34. Knuth, T.D., *Ice Adhesion Strength Modeling Based on Surface Morphology Variations*, in *Aerospace Engineering*. 2015, Penn State University. p. 198.
35. Laforte, J.-L., M.-A. Allaire, and D. Asselin, *État de l'art du déglaçage des conducteurs et des câbles aériens*. 1994, Groupe de recherche en ingénierie de l'environnement atmosphérique GRIEA, Université du Québec à Chicoutimi: Chicoutimi, Québec. p. 107 (seulement xix p.).
36. Jellinek, H.G., *Ice adhesion.* Canadian Journal of Physics, 1962. **40**(10): p. 1294-1309.
37. Mehran, M.R., *Numerical and experimental studies of the mechanical behaviour at the ice/aluminium interface = Études numérique et expérimentale du comportement mécanique à l'interface glace/aluminium*, in *DSA*. 2007, Université du Québec à Chicoutimi. p. 157.
38. Nixon, W.A. and E.M. Schulson, *The Fracture Toughness of Ice Over a Range of Grain Sizes.* Journal of Offshore Mechanics and Arctic Engineering, 1988. **110**: p. 192-196.
39. L. Swedlow, J., *On Griffith's theory of fracture*. Vol. 1. 1965. 210-216.
40. Schulson, E., et al., *Fractography of ice*. Vol. 8. 1989. 1193-1194.
41. Schulson, E., P. N. Lim, and R. W. Lee, *A brittle to ductile transition in ice under tension*. Vol. 49. 1984. 353-363.
42. Zant, B. and J. Planas, *Fracture and Size Effect in Concrete and Other Quasi-Brittle Materials*. 1998.
43. L Anderson, T., *Fracture mechanics : fundamentals and applications / T. L. Anderson*. 1985: CRC Press.
44. Tryde, P., *Physics and Mechanics of Ice*. 1979, Symposium Copenhagen, Technical University of Denmark: Springer-Verlag Berlin Heidelberg.
45. E. Hillerborg, A., M. E. Modéer, and P.E. Petersson, *Analysis of Crack Formation and Crack Growth by Means of Fracture Mechanics and Finite Elements*. Vol. 6. 1976. 773-781.
46. Evans, P.H.a.M., M S,, *Microcracking and stress-strain curves for concrete in tension.* Materials and Structures (RILEM), 1968(No. 1): p. 61-64.
47. Hillerborg, A., M. Modéer, and P.E. Petersson, *Analysis of crack formation and crack growth in concrete by means of fracture mechanics and finite elements.* Cement and Concrete Research, 1976. **6**(6): p. 773-781.
48. ABAQUS. Available from: http://abaqusdoc.ucalgary.ca/v6.9/books/usb/default.htm?startat=pt03ch06s03at09.html.
49. Coffman Jr, H.J., *Helicopter Rotor Icing Protection Methods.* Journal of the American Helicopter Society, 1987. **Vol. 32**(2): p. 34-39.
50. Thomas, S.K., R.P. Cassoni, and C.D. MacArthur, *Aircraft anti-icing and de-icing techniques and modeling.* Journal of Aircraft, 1996. **33**(5): p. 841-854.
51. Goraj, Z., *An Overview of the Deicing and Antiicing*, in *24th International Congress of the Aeronautical Sciences*. 2004: Yokohama, Japan.
52. Feher, L.E.a.M.T. *High frequency microwave anti/de- icing system for carbon reinforced airfoil structures*. in *The International Society for Optical Engineering*. 2001.

53. WW Transport Inc.; Available from: www.weepingwings.com.
54. Hill, E., et al., *Investigations of Performance of Pneumatic Deicing Boots, Surface Ice Detectors and Scaling of Intercycle Ice*. 2006, Office of Aviation Research and Development.
55. NASA, *Analysis and tests for design of an electro-impulse de-icing system*. 1985.
56. Cox & Company, I.; Available from: www.coxandco.com/emeds.htm.
57. Boldmethod. Available from: www.boldmethod.com/blog/lists/2018/02/types-of-deicing-systems-and-advantages-and-disadvantages.
58. Zhu, Y., et al., *Numerical simulation and experimental validation of tailored wave guides for ultrasonic de-icing on aluminum plates*. 2010.
59. Quinlan, P. and C. Laforte, *Proof of Concept Testing of a Piezo Ice Protection System*. 2009, Anti-Icing Materials International Laboratory: University of Quebec at Chicoutimi. p. 59.
60. Palacios, J.L., et al., *Ultrasonic Shear and Lamb Wave Interface Stress for Helicopter Rotor Deicing Purposes*, in *47th Structures, Structural Dynamics and Materials Conference*. 2006: Newport, Rhode Island (USA).
61. Palacios, J., et al., *Global Ultrasonic Shear Wave Anti-Icing Actuator for Helicopter Blades*. Vol. 3. 2007.
62. Harvey, D., *Modélisation numérique d'un système de protection contre le givre par éléments piézoélectriques avec validation expérimentale*, in *Département des sciences appliquées*. 2012, Université du Québec à Chicoutimi. p. 297.
63. Villeneuve, E., et al., *Piezoelectric De-Icing System for Rotorcraft.* Journal of American Helicopter Society, 2015. **60**(4): p. 12.
64. Azizi, B.Y., *Finite Element Modeling of Macro Fiber Composite Actuators with Application to Wing De-icing*. 2014, Embry-Riddle Aeronautical University-Daytona Beach. p. 58.
65. Habibi, H., et al., *Simulation of an electro-mechanical ice protection system for aircraft structure based on ultrasonic guided wave*. 2016.
66. Budinger, M., et al., *Ultrasonic Ice Protection Systems: Analytical and Numerical Models for Architecture Tradeoff*. Vol. 53. 2016. 1-11.
67. Pommier-Budinger, V., et al., *Analysis of Piezoelectric Ice Protection Systems Combined with Ice-Phobic Coatings*. 2016.
68. Kalkowski, M., T. Waters, and E. Rustighi, *Removing surface accretions with piezo-excited high-frequency structural waves*. 2015.
69. Zhu, Y. and Q. Li, *Numerical Simulation and Experiment of the Piezoelectric De-Icing System*. 2015.
70. Jong, M.d., *A database to enable discovery and design of piezoelectric materials.* Nature, 2015.
71. Villeneuve, E., et al., *Piezoelectric De-Icing System for Rotorcraft.* Journal of American Helicopter Society, October 2015. **60**(4): p. 12.
72. Physik Instrumente, *DuraAct Patch Transducer Datasheet*. 2012.
73. Tian Bai, C., Z., Bo, M., Kai, L., Chengxiang, Z., *Vibration de-icing method with piezoelectric actuators.* Journal of vibroengineering, 2015. **17**(1): p. 61-73.
74. University, P., *Single Degree of Freedom harmonically forced vibration.* Structural Dynamics, 2016: p. 8.
75. Hejazi, V., K. Sobolev, and M. Nosonovsky, *From superhydrophobicity to icephobicity: forces and interaction analysis.* Scientific reports, 2013. **3**.
76. Ling, E.J.Y., et al., *Reducing Ice Adhesion on Nonsmooth Metallic Surfaces: Wettability and Topography Effects.* ACS applied materials & interfaces, 2016. **8**(13): p. 8789-8800.
77. Starostin A., V.V., Barkay Z., Legchenkova I., Danchuk V., Bormashenko E.,, *Drop-wise and film-wise water condensation processes occurring on metallic micro-scaled surfaces.* Applied Surface Science, 2018. **444**: p. 604-609.
78. Guerin, F., et al., *Analytical Model Based on Experimental Data of Centrifuge Ice Adhesion Tests with Different Substrates.* Cold Regions Science and Technology, 2016. **121**(C): p. 93-99.
79. Hardesty Work Jr., A., *The measurement of the adhesion of glaze ice*, in *Mechanical Enginerring*. 2018, University of Louisville: Faculty of the J.B. Speed School of Engineering of the University of Louisville. p. 269.
80. Brassard, J.D., et al., *Nano-micro structured superhydrophobic zinc coating on steel for prevention of corrosion and ice adhesion.* J Colloid Interface Sci, 2015. **447**(0): p. 240-7.
81. Villeneuve, E. and J. Perron, *Icing Wind Tunnel Certification Tests in Accordance with SAE ARP5905 and AIR4906*. 2012, AMIL. p. 80.

82. SAE International, *Calibration and Acceptance of Icing Wind Tunnels*. 2003.
83. SAE International, *Droplet Size Instrumentation Used in Icing Facilities*. 1995.
84. Eric Villeneuve, C.V., Sebastian Ghinet, *Numerical and experimental investigation of the design of a piezoelectric de-icing system for small rotorcraft part 1/3: Development of a flat plate numerical model with experimental validation.* Aerospace, 2020.
85. Eric Villeneuve, C.V., Sebastian Ghinet, *Numerical and experimental investigation of the design of a piezoelectric de-icing system for small rotorcraft part 2/3: Investigation of transient vibration during frequency sweeps and optimal piezoelectric actuator excitation.* Aerospace, 2020.